NASA
Technical
Paper
2071

October 1982

Experimental Trim Drag Values and Flow-Field Measurements for a Wide-Body Transport Model With Conventional and Supercritical Wings

Peter F. Jacobs

NASA

NASA
Technical
Paper
2071

1982

Experimental Trim Drag Values and Flow-Field Measurements for a Wide-Body Transport Model With Conventional and Supercritical Wings

Peter F. Jacobs
Langley Research Center
Hampton, Virginia

NASA
National Aeronautics
and Space Administration

**Scientific and Technical
Information Branch**

SUMMARY

The purpose of the present study was to determine if advanced supercritical wings incur higher trim drag values at cruise conditions than current wide-body technology wings. Significantly higher trim drag would lessen the performance benefits to be gained from the aerodynamically advanced supercritical wings. Relative trim drag increments were measured in an experimental wind-tunnel investigation conducted in the Langley 8-Foot Transonic Pressure Tunnel. The tests utilized a high-aspect-ratio supercritical wing and a current wide-body wing, in conjunction with five different horizontal tail configurations, mounted on a representative wide-body fuselage. The three low-tail and two T-tail configurations were chosen to measure the effects of horizontal tail size, location, and camber on the trim drag increments for the two wings. Longitudinal force and moment data (for a range of center-of-gravity (c.g.) positions) and flow-field measurements are presented at a Mach number of 0.82 and design cruise lift coefficients for the wide-body and supercritical wings of 0.45 and 0.55, respectively. The data indicate that the supercritical wing configurations do not have significantly higher trim drag than the wide-body wing configurations, when each configuration is compared at the c.g. position which results in minimum trim drag, regardless of static margin. The wide-body wing had lowest trim drag increments for tail uploads, and the supercritical wing had lowest increments with slight tail downloads. A reduction in both tail size and static stability produced trim drag reductions for both wings. The cambered tails had higher trim drag increments than the symmetrical tails for both wings, and the low-tail configurations had higher trim drag increments than the T-tail configurations. The increase in performance (lift-drag ratio) for the supercritical wing over the wide-body wing was approximately 11 percent for both the optimum low-tail and T-tail configurations.

INTRODUCTION

The advent of fuel shortages and higher fuel prices has had a tremendous impact on the aviation industry. Aircraft designed in the 1950's and 1960's, when fuel was relatively inexpensive, are not as profitable today when flown at the speeds for which they were designed. Consequently, aircraft and engine manufacturers have been challenged to build more fuel efficient aircraft. Within the National Aeronautics and Space Administration's Aircraft Energy Efficiency (ACEE) Program, research is being conducted in the areas of advanced aerodynamics, laminar flow, composite structures, and active control systems in order to develop the technology which will design the next generation of transport aircraft. The overall goal of the ACEE Program is to reduce the drag of transport aircraft by 50 percent.

The development of advanced supercritical airfoils by NASA (ref. 1) has led to energy efficient transport aircraft wings (refs. 2 and 3) which have higher lift-drag ratios, thicker airfoil sections, less sweep, and higher aspect ratios than wings for current wide-body aircraft. Another characteristic of these advanced wings is an increased nose-down pitching moment caused by camber in the aft portion of the supercritical airfoils. The increased pitching moment is of concern if the drag penalty required for trim significantly reduces the performance benefits of the advanced wings.

Because of inherent static stability requirements, the aerodynamic center (a.c.) of most current subsonic transport aircraft is located aft of the center of gravity (c.g.). This arrangement necessitates a download on the horizontal tail for trim, which in turn forces the wing to produce more lift. The induced drag of the tail and the extra induced drag of the wing constitute a major part of the trim drag, and if the aircraft is flying near its drag-divergence Mach number, the trim drag penalty can be large. Advances in the area of active control technology will allow the next generation of jet transport aircraft to fly with relaxed static stability. It will then be possible to have a smaller, lighter horizontal tail or a c.g. further aft. Either or both would result in smaller trim drag penalties (refs. 4 to 6).

The objective of the present experimental investigation was to assess the trim drag of a high-aspect-ratio supercritical wing configuration relative to the trim drag of a current wide-body transport configuration for a range of c.g. positions. In order to have a direct comparison of the two wings, each wing was tested on a fuselage which closely simulated the fineness ratios of current wide-body aircraft (fig. 1). Each wing was tested in conjunction with five different horizontal tails, and the trim drag for each configuration was determined at a cruise Mach number of 0.82. The three low-tail and two T-tail configurations were designed to measure the effects of horizontal tail location, size, and camber on the trim drag for the two wings.

In addition to the force and moment data for these configurations, local flow angles and Mach numbers in the vicinity of the tails were measured with a yawhead rake. The localized flow fields near the tails provide important information on the interaction of the different wings and tails of this investigation.

SYMBOLS

The longitudinal aerodynamic characteristics presented in this paper are referred to the stability axis system. Force and moment data have been reduced to conventional coefficient form based on the trapezoidal planform geometry of the wing used for each configuration. The moment-reference center for the wide-body wing is $0.35\bar{c}$, and the moment-reference center for the supercritical wing is $0.33\bar{c}$. All dimensional values are given in both the International System of Units (SI) and U.S. Customary Units. All measurements and calculations were made in U.S. Customary Units.

A aspect ratio, b^2/S

a speed of sound, m/sec (ft/sec)

b wing span, 116.12 cm (45.72 in.) for wide-body wing and 134.54 cm (52.97 in.) for supercritical wing

C_D drag coefficient, $\frac{\text{Drag}}{q_\infty S}$

C_L lift coefficient, $\frac{\text{Lift}}{q_\infty S}$

C_m pitching-moment coefficient, $\frac{\text{Pitching moment}}{q_\infty S\bar{c}}$

C_T tail volume coefficient, $\ell_T S_T/\bar{c}S_W$

c	local streamwise chord, cm (in.)
$\bar{c}$	wing mean aerodynamic chord, 18.22 cm (7.175 in.) for wide-body wing and 14.58 cm (5.742 in.) for supercritical wing
$H_1,\ldots,H_5$	horizontal tails 1 through 5
$i_{H_1},\ldots,i_{H_5}$	Incidence of horizontal tails 1 through 5, measured from fuselage waterline, positive with tail trailing edge down, deg
L/D	lift-drag ratio
ℓ_T	tail arm, distance from c.g. to a.c. of tail, cm (in.)
M	Mach number
p	local static pressure, Pa (lb/ft^2)
p_t	total pressure, Pa (lb/ft^2)
p_1,p_2	pressure measured at yawhead tube 1 and 2, respectively, Pa (lb/ft^2)
q	dynamic pressure, Pa (lb/ft^2)
R	universal gas constant
R'	resultant velocity vector (see fig. 36)
R_n	Reynolds number
S	reference area, 0.193 m^2 (2.075 ft^2) for wide-body wing and 0.185 m^2 (1.988 ft^2) for supercritical wing
T	absolute temperature, °R
t	local maximum wing or tail thickness, cm (in.)
U_∞	free-stream velocity in x-direction, m/sec (ft/sec)
u,v,w	velocity perturbation in x-, y-, and z-direction, respectively, m/sec (ft/sec)
V	three-dimensional velocity vector
V_1,V_2	vertical tails 1 and 2
x	streamwise distance, cm (in.)
y	spanwise distance, measured normal to model plane of symmetry, cm (in.)
z	vertical distance, measured normal to x, cm (in.)
α	angle of attack, referred to fuselage waterline, deg
Γ	dihedral of wing or tail, deg

γ ratio of specific heat at constant pressure to specific heat at constant volume

Δ incremental value

ΔC_D trim drag increment, $(C_D)_{\text{wing-body-vert. and horiz. tail}} - (C_D)_{\text{wing-body-vert. tail}}$

ε downwash angle, deg

ε' local streamwise wing section incidence angle, referred to fuselage waterline, positive for leading edge up, deg

θ, σ, ϕ angles between vectors of flow field (see fig. 36), deg

Λ sweep angle of wing or tail, deg

λ taper ratio of wing or tail trapezoidal planform

Subscripts:

avg average value of interpolated α values (used to calculate $\Delta\varepsilon/\Delta\alpha$ in figs. 28 and 29)

ℓ lower surface of airfoil

T horizontal or vertical tail

t total conditions (i.e., conditions that would exist if the gas were brought to rest isentropically)

u upper surface of airfoil

W wing

∞ free-stream conditions

Abbreviations:

a.c. aerodynamic center

c.g.,C.G. center of gravity

F.S. fuselage station

MAC mean aerodynamic chord

SCW supercritical wing

EXPERIMENTAL APPARATUS AND PROCEDURES

Test Facility

This investigation was conducted in the Langley 8-Foot Transonic Pressure Tunnel (ref. 7). This facility is a continuous-flow single-return rectangular slotted-throat tunnel. Tunnel controls allow independent variation of Mach number, density, stagnation temperature, and dew point. The test section is approximately 2.2 m (7.1 ft) square (same cross-sectional area as that of a circle with a 2.4-m (8-ft) diameter). The upper and lower walls are slotted axially, to permit the test-section Mach number to be changed continuously throughout the transonic speed range. The slotted top and bottom walls each have an average open ratio of approximately 0.06. The stagnation pressure in the tunnel can be varied from a minimum of 0.25 atmosphere (1 atmosphere = 0.101 MN/m^2) at all Mach numbers to a maximum of approximately 2.00 atmospheres at Mach numbers less than 0.40. At transonic Mach numbers, the maximum stagnation pressure that can be obtained is about 1.5 atmospheres.

Model Description

Drawings of the model are shown in figures 1, 2, and 3. Photographs of the model in the Langley 8-Foot Transonic Pressure Tunnel are shown in figures 4 and 5.

Fuselage.- The fuselage described in reference 2 was used for this investigation. The fuselage is 125.88 cm (49.56 in.) long and has a maximum diameter of 14.58 cm (5.74 in.). For both wings, the wing lower surface was faired into the fuselage to provide a relatively flat bottom which extended from near the leading edge to approximately 15.24 cm (6.0 in.) aft of the trailing edge.

Wings.- Planform details for the wide-body wing are shown in figure 1. The wing has 35° sweep at the quarter-chord, 7.5° dihedral inboard and 5.5° dihedral outboard, an aspect ratio of 6.99, and a trapezoidal planform area of 0.193 m^2 (2.075 ft^2). Twist and thickness distributions are presented in figures 6 and 7, respectively. This wing was designed for a cruise Mach number of 0.84 and a lift coefficient of 0.45.

Planform details for the supercritical wing are shown in figure 1. The wing has 30° sweep at the quarter-chord, 5° dihedral, an aspect ratio of 9.80, and a trapezoidal planform area of 0.185 m^2 (1.988 ft^2). Twist and thickness distributions are presented in figures 6 and 7, respectively. The airfoil sections used in this wing were designed for a two-dimensional lift coefficient of 0.7. The three-dimensional effects of sweep, finite span, inboard modifications (ref. 2), and fuselage interference reduce the lift obtainable for this wing to a design lift coefficient of 0.55 at a cruise Mach number of 0.81.

Tails.- The latest technology NASA supercritical airfoils (ref. 8) were used for all horizontal and vertical tail surfaces. Departing from the previously used method of designing airfoils (an iterative experimental procedure), the tail airfoils in this investigation were designed with the two-dimensional airfoil code of reference 9. The airfoils developed with this code follow the three principal guidelines of references 10 and 11. These guidelines produce airfoils with reduced strength shock waves, little flow separation, and reduced drag. The airfoils used for the horizontal and vertical tails are shown in figure 8. Planform details for the tails used in this investigation are presented in table 1 and coordinates are presented in tables 2 to 4.

The planform shapes of the vertical tail and the three horizontal tails for the low-tail configuration are shown in figure 2. The two smaller horizontal tails, designated H_1 and H_3, utilize the 10-percent-thick cambered and symmetrical airfoils, respectively. The larger horizontal tail H_2 also utilizes the cambered airfoil. The vertical tail V_1 has a 10-percent-thick symmetrical airfoil section.

The planform shapes of the vertical tail and two horizontal tails for the T-tail configuration are shown in figure 3. Horizontal tails H_4 and H_5 have cambered and symmetrical 10-percent-thick airfoil sections, respectively. The T-tail vertical tail V_2 has a 12-percent-thick symmetrical airfoil section.

The tails were designed to have approximately the same tail volume coefficients as for current aircraft. Tail volume coefficient is a measure of the contribution of the tail to the overall stability level of the configuration and is defined as $C_T = \frac{\ell_T S_T}{\bar{c} S_W}$. In the design of the tails, the c.g. was set at $0.25\bar{c}$. This point occurs at the same fuselage station for both wings. Therefore, the tail arm ℓ_T was the same for both wings. In addition, the wing planform area was nearly the same for each wing. The tail volume coefficients for each wing differ because the mean aerodynamic chord $\bar{c}$ for the wide-body configuration is larger than for the supercritical wing configuration. The tails designed for this investigation were not optimized for either wing, but were representative of current aircraft and allowed comparisons of the trim drag characteristics of the two wings to be made.

The tail area listed in table 1 for the horizontal tails is the trapezoidal area extended to the fuselage center line, but for the vertical tails, the area shown is exposed area. Neglecting tail dihedral, horizontal tails H_1, H_3, H_4, and H_5 have the same geometry and planform. Tail H_2, which is slightly larger than the other horizontal tails, was designed to have the same exposed area and tail volume coefficient as T-tails H_4 and H_5.

Both horizontal tail configurations were designed with incidence blocks to allow variation of the tail-plane incidence from -4° to 4° in 0.5° increments. The tails rotated about an axis through the quarter-chord of the mean aerodynamic chord of each tail and perpendicular to the fuselage axis. Filler plugs covered the tail attachments for the tail-off configurations.

Boundary-Layer Transition Strips

The transition location of the boundary layer was fixed for all model components with carborundum grit set in a plastic adhesive. The transition strips were 0.127 cm (0.05 in.) wide and were sized by the techniques of reference 12. Transition strip patterns for the wide-body and supercritical wings are presented in figures 9 and 10, respectively. The aft positions of the grit on the upper surface of the wings were determined from analysis of oil flow photographs (ref. 13) of each configuration near its drag-rise Mach number and cruise lift coefficient. The aft grit locations on the wing were used to simulate a higher effective Reynolds number by producing a thinner boundary layer (ref. 14). Boundary-layer transition strips of No. 120 carborundum grit were located 0.3c back from the leading edges on the upper and lower surfaces of all the horizontal and vertical tails. In addition, a transition strip of No. 120 carborundum grit was located 2.54 cm (1.00 in.) from the nose of the fuselage.

Measurements

Aerodynamic force and moment data were obtained with a six-component electrical strain-gage balance. The quoted accuracy of the balance is 0.5 percent of the full-scale values (normal force, 2500 lb; axial force, 200 lb; pitching moment, 3500 in-lb; rolling moment, 2000 in-lb; yawing moment, 2000 in-lb; and side force, 500 lb). The repeatability of the data was generally better than the quoted accuracy, however. Several configurations were repeated at different times during the test, and drag coefficient values repeated to within 0.0002. Because of the large number of model configurations, the amount of data required, and wind-tunnel scheduling problems, four separate tunnel entries were required for this investigation. An offset in the drag values for the second entry was discovered near the end of the testing. This offset affects only the data for the wide-body wing with horizontal tail H_2. Although the absolute values of the drag data are in question, the incremental values due to tail incidence changes are not affected.

An accelerometer attached to the balance block was used to measure angle of attack. Static pressures were measured in the model along the sting cavity by using differential-pressure transducers referenced to tunnel plenum static pressure. Two yawhead rakes were used to measure the cross-flow and downwash components of the flow field in the vicinity of the horizontal tails. Details of the rake and its calibration are presented in the appendix.

Corrections

The angle of attack of the model was corrected for flow angularity in the tunnel test section. This correction was obtained from upright and inverted tests of the baseline configurations. Drag data presented herein have been adjusted to correspond to the condition of free-stream static pressure acting in the balance chamber and at the base of the fuselage. No correction to the data has been made to account for lift interference effects. Also, the frontal area of the model was sufficiently small to avoid having to correct Mach number for wind-tunnel blockage effects (ref. 15).

Test Conditions

Throughout the entire test, stagnation temperature was maintained at 322 K (120°F), and the air was dried until the dew point was sufficiently low to prevent condensation effects. Data were taken at Mach numbers of 0.60, 0.80, 0.82, 0.84, 0.86, and 0.90. Only the data at $M_\infty = 0.82$ are presented in this report because the trim drag at cruise conditions was of primary importance. Data at $M_\infty = 0.82$ are slightly beyond the design Mach number for the supercritical wing and slightly less than the design Mach number for the wide-body wing; however, the best data comparison is possible at this Mach number since neither wing is favored. The test conditions at $M_\infty = 0.82$ were $R_n = 16.4 \times 10^6$/m (5.0×10^6/ft) and $q_\infty = 40$ kPa (839 lb/ft^2).

PRESENTATION OF RESULTS

The results of this investigation are presented in the following figures:

RESULTS AND DISCUSSION

The longitudinal data were initially reduced to coefficient form by using the quarter-chord of the mean aerodynamic chord ($\bar{c}/4$) as the c.g. location. Analyis of the data showed that the longitudinal stability parameter $\Delta C_m/\Delta C_L$ was too large; this resulted in unrealistically stable cruise configurations for both the wide-body and supercritical wings. Due to a longer tail arm, the T-tail configurations had even greater static margins than the low-tail configurations. Normally, wide-body aircraft at cruise conditions fly with a static margin of approximately 7 to 8 percent. The uncambered low-tail H_3 was considered to be closest to the horizontal tails on actual wide-body aircraft; therefore, the c.g. for the wide-body configurations was moved aft to provide a static margin of approximately 7 percent for tail H_3 at cruise conditions. The c.g. for the supercritical wing configurations was also moved back to provide a similar static margin for the H_3 tail at cruise conditions. The c.g. for all the wide-body configurations was fixed at $0.35\bar{c}$ and for all the supercritical wing configurations was fixed at $0.33\bar{c}$. The longitudinal aerodynamic data presented in figures 11 to 16 have been reduced using these two c.g.'s.

Force and Moment Data

Several important trends are evident from the aerodynamic force and moment data.

C_L vs α .- From the variation of lift coefficient with angle of attack (figs. 11 and 14), it can be seen that at low lift coefficients all the horizontal tails are producing downloads for the tail incidences tested. The tail download causes a net loss of lift when compared with the wing-body-vertical tail configurations at the same angle of attack. At some higher angle, however, the wide-body configurations experience an upload on the tail. The point at which the configuration with a horizontal tail produces more total lift than for the wing-body-vertical tail configuration depends on the horizontal tail incidence and airfoil section. The supercritical wing has a higher stall angle of attack than the wide-body wing, and in only a few instances at very high lift coefficients do the horizontal tails on supercritical wing configurations experience an upload.

C_D vs C_L .- The effect of a tail upload on performance can be seen from the variation of drag coefficient with lift coeffficient (figs. 12 and 15). With an upload on the tail, the wing can be at a lower angle of attack to achieve the same total lift. Lowering the angle of attack of the wing reduces the drag for the configuration. The wide-body wing data show this tendency for the configurations with tail uploads at higher angles of attack. For the supercritical wing configurations, the horizontal tails usually trim with downloads even at higher angles of attack. Therefore, while the drag values for the supercritical wing configurations with horizontal tails approach the values for the wing-body-vertical tail configuration, they do not become less.

It should be noted that the T-tail vertical tail produces more drag than the low-tail vertical tail (figs. 12(a), 12(d), 15(a), and 15(d)), which is mainly due to a 2-percent difference in thickness between the two tails. The leading- and trailing-edge fairings at the tip of the T-tail vertical tail were not specifically optimized for minimum drag and some local flow separation may be present. However, for the purposes of this investigation, the difference in absolute drag level of the baseline configurations (wing-body-vertical tail) is of secondary importance compared with the trim drag increments for each horizontal tail.

C_m vs C_L .- The static longitudinal stability characteristics of the wide-body and supercritical wing configurations are shown in figures 13 and 16. The low-tail configurations for both wings are heavily influenced by the downwash and wake of the wings. The three low-tail configurations (figs. 13(a), 13(b), 13(c), 16(a), 16(b), and 16(c)) all tend to pitch up at lift coefficients beyond the cruise lift coefficient, regardless of the wing involved. Notice that the tails are more effective in conjunction with the supercritical wing (i.e., the increment in C_m due to tail incidence changes is greater).

The T-tail configurations (figs. 13(d), 13(e), 16(d) and 16(e)) are more stable than the low-tail configurations mainly due to a longer tail arm. The supercritical wing shows much less tendency to pitch up than the wide-body wing with tails H_4 and H_5; in fact, the supercritical wing configurations pitch down sharply at the higher lift coefficients. It was anticipated that the yawhead rake data would provide some insight into this anomaly; however, no definite cause-effect relationship has been identified from the available data. Also, it is not known whether the T-tail configurations for the supercritical wing would trim out again at even higher lift coefficients and develop classic "deep stall" problems (refs. 16 and 17).

Trim Drag

From the data presented in figures 11 to 16, it is possible to construct trimmed drag polars for each combination of wing and horizontal tail at a fixed c.g. (stability level). Another way of presenting the data is to assume that each configuration can be trimmed at any desired lift coefficient by moving the c.g. Moving the c.g. position causes the data for C_m versus C_L to be rotated, and by choosing the proper c.g. position, a trim point will result for any tail incidence angle at any desired lift coefficient within the range of the data taken. The resulting plots present the variation of trimmed drag coefficient with c.g. position for a fixed lift coefficient. Because of the interest in relaxed static stability and its effect on trim drag, the latter method was chosen to present the data from this investigation. Data for the wide-body and supercritical wing configurations are presented in figures 17 and 18, respectively. Data for the corresponding wing-body-vertical tail configurations are plotted with centered symbols. The drag increment between each horizontal tail configuration and the corresponding wing-body-vertical tail configuration at the same lift coefficient is called the trim drag increment, and it represents the total drag increment due to the addition of the horizontal tail, including skin friction.

Measuring the trim drag increments experimentally requires a large number of model configuration changes and many hours in the wind tunnel. It would be helpful if these increments could be calculated with a simple theoretical procedure. In the past decade, numerous attempts have been made to calculate trim drag increments analytically (refs. 18 to 27). The various methods used to calculate trim drag tend to produce differing opinions on whether a tail upload or download results in lower trim drag. None of these simplified methods are capable of handling compressibility effects, which may occur at transonic speeds and can be on the order of one-half the total trim drag. The simplified methods do indicate interesting trends which may be useful as a starting point for tail design, however. In general, most methods agree that for an arbitrary wing, a rearward movement of the c.g. or a longer tail arm results in smaller loads and reduced trim drag. Also, the mutual interference between the flow fields of the wing and the tail can be an important factor on trim drag. A wing at an angle of attack which produces high induced drag benefits from an upload on the tail. As previously mentioned, an upload on the tail unloads the wing

and can result in significant trim drag savings. The same wing at a lower angle of attack or a higher aspect-ratio wing at the same angle of attack which produces less induced drag may not require an upload on the tail. In fact, a downloaded tail in the presence of sufficient wing downwash causes the tail lift vector to be rotated in a forward direction; this results in a "tail thrust" component which reduces trim drag. The trim drag increments for each wing at its design point are summarized in figures 19 and 20, and in general substantiate these trends.

Wide-body wing.- The wide-body wing (fig. 19) has more induced drag than the supercritical wing due to its smaller aspect ratio, and the symmetrical tails H_3 and H_5 show definite trim drag advantages for small tail uploads. However, as the tail upload gets larger, the induced drag on the horizontal tail increases and the trim drag increments get larger. The cambered tails H_2 and H_4 show an increase in trim drag with tail uploads, probably because the tails were built with the airfoils "upside down" (inverse camber) in anticipation of tail downloads for trim. Obviously, these cambered tails are not efficient at producing uploads and have higher trim drag increments than the symmetrical tails. The behavior of horizontal tail H_1 is dissimilar to the other tails. For some small range of tail incidence, H_1 first experiences reduced trim drag increments due to tail thrust on a downloaded tail. As the tail load becomes more positive, the tail thrust component disappears and the trim drag increases. For further small increases in tail upload, the induced drag of the wide body is reduced until the point at which the cambered tail becomes inefficient at producing uploads. It is not understood why the larger cambered tail H_2 does not follow this same trend, however. Nevertheless, after the difference in skin friction is accounted for, the smaller tail H_1 has a minimum trim drag increment 0.0006 less than that for the larger tail H_2. Both T-tails, H_4 and H_5 have smaller trim drag increments than any of the low-tail configurations. The symmetrical T-tail H_5 has a minimum trim drag increment which is 0.0003 less than its skin-friction increment, which implies that the upload on the tail has significantly reduced the induced drag on the wide-body wing. The c.g. positions for neutral stability are indicated for each tail configuration in figure 19. At their minimum trim drag points, the tail configurations have positive static margins of at least 7 percent.

Supercritical wing.- The supercritical wing produces minimum trim drag increments with a tail download or less of a tail upload than for the wide-body wing. The more negative tail incidence angles required for trim (fig. 20), in conjunction with greater downwash, substantiate this trend. Data for the low-tail configurations are similar for both wings. The large cambered tail H_2 has the highest trim drag increments, followed by the smaller cambered tail H_1 and the symmetrical tail H_3. Apparently, there was too much camber in tails H_1 and H_2 to generate the small tail downloads required for trim. Again, the cambered tails may experience reduced trim drag due to tail thrust $\left(i_{H_1} = -2° \text{ and } i_{H_2} = -1.5°\right)$. The tail thrust is lost as the c.g. moves aft slightly and the tail incidence angles become more positive. Then as the c.g. moves further aft and the tail downloads become smaller, the induced drag on the wing is reduced, which lowers the trim drag. The large cambered tail H_2 also has an increase in trim drag at $i_{H_2} = -2°$; this may be due to greater induced drag on the tail itself for this highly downloaded case. To a varying extent, the tails show reduced trim drag increments as the c.g. is moved aft. Both T-tails have less trim drag than the low-tail configurations. Although H_4 and H_5 have trim drag increments equal to their skin-friction values, the

symmetrical tail H_5 would appear to have even lower trim drag if the data were extrapolated to a more aft c.g. position.

The most important information to be gained from the increments presented in figures 19 and 20 is that the supercritical wing can be trimmed without a large increase in trim drag compared with the wide-body wing. The c.g. positions for minimum trim drag are further aft for the supercritical wing configurations than for the wide-body wing configurations. A stability augmentation system may be required for the supercritical wing configurations in order to fly at the aft c.g. positions. However, the technology needed to fly a transport aircraft with relaxed static stability is available and has been demonstrated in flight (ref. 28).

Each of the horizontal tails has a minimum trim drag increment for the range of tail incidences tested. If one subtracts the minimum value for each horizontal tail for the wide-body wing configurations from the value for the corresponding tail for the supercritical wing configurations, the differences are $\Delta C_D = 0.0003$, -0.0001, 0.0001, 0.0001, and 0.0003 for tails H_1 through H_5, respectively. The maximum increase in trim drag coefficient is $\Delta C_D = 0.0003$, which is less than 1 percent of the total drag of the supercritical wing at cruise conditions ($M_\infty = 0.82$ and $C_L = 0.55$). This means that the performance gains for the supercritical wing are not significantly eroded when a tail is added.

Cruise Performance

The cruise performance (L/D) for the five tail configurations with each wing is presented in figure 21. The increases in L/D for the supercritical wing over the wide-body wing with just the low-tail vertical and T-tail vertical tails are 10.9 percent and 11.8 percent, respectively. When the horizontal tails are added, the increases in L/D for the supercritical wing with the optimum low-tail and T-tail incidences are 11.2 and 11.3 percent, respectively. The lift-drag ratios for the best T-tail configuration (H_5) are lower than those for the best low-tail configuration (H_3) because of the higher drag for the T-tail vertical tail.

Yawhead Rake Data

A photograph of the yawhead rake used with the low-tail configurations is shown in figure 22 and a drawing of the rake is shown in figure 23. The three static-pressure tubes located between the yawheads are used to calculate local Mach number. Photographs of the rake installations for the low-tail and T-tail configurations are presented in figures 24 and 25, respectively.

The rakes were centered vertically on the horizontal tail reference planes at the root of the horizontal tails for the low-tail and T-tail configurations. Rake data were taken at two spanwise locations for each configuration (figs. 26 and 27).

Downwash.- Downwash data for the two wings are presented in figures 28 and 29. In addition to the variation of downwash with angle of attack, the rate of change of downwash with angle of attack $\Delta\varepsilon/\Delta\alpha$ is also plotted. It can be shown (ref. 29) that the rate of change of downwash with angle of attack $\Delta\varepsilon/\Delta\alpha$ has an effect on the stability of the configuration. The tail contribution to stability is proportional to $1 - (\Delta\varepsilon/\Delta\alpha)$. A positive increase in $\Delta\varepsilon/\Delta\alpha$ reduces the contribution of the tail to the overall stability level. Data for the bottom yawhead of the wide-body low-

tail configuration are not presented in figure 28(a) because plugged tubes gave incorrect pressure measurements.

The rake data show that for the portions of the flow field measured, the T-tail configurations are located in an area of greater downwash than the low-tail configurations and have a fairly linear change in downwash with yawhead position. This effect is described in references 30 and 31 and is caused by the flow field converging toward the wake of the wing. The result is an increase in the downwash above the wake and a decrease in the downwash below the wake. As expected, the supercritical wing has higher levels of downwash at a given angle of attack for both the low-tail and T-tail configurations due to its higher design lift coefficient and lift-curve slope.

From the nonlinearity of the values of $\Delta\varepsilon/\Delta\alpha$, it is apparent that the wing wake influences the low-tail configurations significantly more than the T-tail configurations. The dynamic pressure in the wake of the wing is less than free stream and can adversely affect the performance of the tail, as was shown in the trim drag data previously presented.

Flow-field velocity vectors.- From the yawhead rake data, it is possible to compute components of the flow in the directions of all three axes as well as the local Mach number. The resultant three-dimensional flow-field velocity vectors have been projected onto a plane perpendicular to the free-stream flow direction in figures 30 to 33 to show the cross-flow components of the flow with the corresponding local Mach numbers. The viewpoint is one looking downstream at the left-hand tails. Flow angles for the bottom yawhead of the wide-body low-tail configuration are not presented in figure 30 because plugged tubes gave incorrect pressure measurements. Local Mach numbers are not presented for the top yawhead for the supercritical wing low-tail configuration (fig. 32). For this run, the center total-pressure tube was partially plugged; this gives small Mach number errors. The flow-field velocity vectors shown for this yawhead were computed by using the erroneous Mach numbers. However, since the pressure differences at a fixed angle have only a small variation with Mach number in the rake calibration, the error in the computed flow angle is insignificant. (See appendix.)

The low-tail data (figs. 30 and 32) show a definite cross flow toward the body due to the closure angle of the fuselage. The position of the wing wake can be tracked by watching the local Mach numbers decrease as the angle of attack increases. A steady movement of the wake vertically is shown, as well as local flow separation for angles of attack greater than 5°. The influence of the wing wake is more apparent for the supercritical wing due to the thicker airfoils used.

In contrast to the low-tail data, the T-tail data (figs. 31 and 33) show an outward cross-flow component which is due to the flow field of the T-tail vertical tail. The local Mach numbers inboard are also higher for the same reason. It should be noted that both T-tail rake positions for the wide-body wing were further forward than for the supercritical wing (fig. 27); this resulted in a greater influence from the flow field of the vertical tail and higher local Mach numbers. Since the horizontal tail is above the wing wake, the local Mach numbers are fairly constant with angle of attack for the T-tail configurations.

SUMMARY OF RESULTS

The purpose of the present study was to determine if advanced supercritical wings incur higher trim drag values at cruise conditions than current wide-body technology wings. In order to measure relative trim drag increments at cruise conditions, an experimental wind-tunnel investigation was conducted in the Langley 8-Foot Transonic Pressure Tunnel utilizing a high aspect-ratio supercritical wing and a current wide-body wing in conjunction with five different tail configurations mounted on a representative wide-body fuselage. The three low-tail and two T-tail configurations were designed to measure the effects of horizontal tail size, location (height), and camber on the trim drag increments for the two wings.

The results of this investigation may be summarized as follows:

1. The trim drag values for the supercritical wing configurations were not significantly higher than for the wide-body configurations. Minimum trim drag values for the supercritical wing configurations occurred at center of gravity (c.g.) positions further aft (lower static margins) than for the wide-body wing.

2. The wide-body wing had lower trim drag values with horizontal tail uploads. Conversely, the high-aspect-ratio supercritical wing had lower trim drag values with small downloads on the tail.

3. Both wings showed a reduction in trim drag for the smaller cambered low tail H_1 compared with the large cambered tail H_2.

4. For the range of tail incidences tested, the cambered tails H_1 and H_4 had higher minimum trim drag increments than the corresponding symmetrical tails H_3 and H_5. The inverse camber was inefficient for producing the uploads required to trim the wide-body configurations, and there was probably too much camber to generate the small downloads required to trim the supercritical wing configurations.

5. The T-tail configurations for both wings had lower trim drag increments than the low-tail configurations since they were not in the wake of the wing where the dynamic pressures were less than free stream.

6. The best performance for both wings was achieved with the symmetrical low tail H_3 and the best T-tail was the symmetrical tail H_5. The addition of a horizontal tail lowers the maximum lift-drag ratio (L/D) for each wing, but the improvement in L/D for the supercritical wing over the wide-body wing remains approximately 11 percent for the optimum low tail and T-tail configurations.

Langley Research Center
National Aeronautics and Space Administration
Hampton, VA 23665
August 12, 1982

APPENDIX

YAWHEAD RAKE DESIGN AND CALIBRATION

Two yawhead rakes were used to measure the local flow angles and Mach numbers in the vicinity of the horizontal tails. The rakes were attached to the sting aft of the model. Each rake had four five-tube yawheads like those shown in references 32 and 33, which measure both the downwash and cross-flow components of the local flow field.

The principle behind the yawhead rake is illustrated in figure 34. This cutaway view shows three total-pressure tubes with a 90° angle between the faces of the outside tubes. If the local flow angle is inclined at an angle ε to the yawhead axis, then the pressure measured by tube 1 p_1 is greater than the pressure measured by tube 2 p_2. The difference in pressure $p_1 - p_2$ is proportional to the flow angle ε. The rake is calibrated by inclining it at a known angle to the flow and measuring the difference in pressures between the opposite tubes of the yawhead. Then when taking data, the measured pressure difference at the yawheads can be related back to a flow angle.

The calibration of the yawhead rakes was performed with the tunnel empty. The rakes were attached to the sting as far forward as possible to reduce any influence from the front of the sting. The calibration consisted of running through an angle-of-attack sweep at Mach numbers from 0.55 to 0.90. The top and bottom tubes of each yawhead were calibrated with the rake in its normal vertical orientation. To calibrate the left and right tubes of each yawhead, the rake was rotated 90° and a similar angle-of-attack sweep was taken for each Mach number. The pressure differences for each set of opposing tubes were then nondimensionalized by dividing by the local dynamic pressure at each yawhead. Each yawhead for both rakes then had a three-dimensional calibration table of $\frac{\Delta p}{q}$ versus ε or σ for six different free-stream Mach numbers. Because the local static- and total-pressure measurements varied with the angle of attack of the rake, the local Mach numbers measured for each yawhead were less than the free-stream values. This effect is described in reference 32. Local Mach number correction tables were set up for each yawhead to eliminate this problem. The tables consisted of an incremental Mach number to be added to each yawhead at each vertical calibration angle. There was a different table for each free-stream calibration Mach number. The procedure for correcting local Mach number and flow angle was as follows:

1. Calculate the local downwash angle ε, using the erroneous local Mach number value when interpolating in the calibration tables

2. Find the local Mach number correction, using ε calculated in step 1 and the free-stream Mach number for interpolation in the local Mach number correction table

3. Add the local Mach number correction found in step 2 to the local Mach number measured in step 1

4. Recompute the flow angles ε and σ using the corrected local Mach number when interpolating in the calibration tables

APPENDIX

As a check, the new procedure was used to compute flow angles and local Mach numbers for the calibration runs. The computed flow angles and local Mach numbers compared quite closely to the known calibration values.

The yawhead rakes had a fairly linear variation of pressure difference $\Delta p/q$ with flow angle, and there was little change in the calibrations with Mach number (fig. 35). Therefore, small errors in the measurement of local Mach number do not have a major effect on flow angle calculations.

The resultant velocity vectors plotted in figures 30 to 33 are the projection of the three-dimensional flow-field velocity vectors at each yawhead projected onto a plane perpendicular to the free-stream flow direction. From figure 36, it can be shown that the resultant velocity vector can be calculated if the downwash angle ε, the cross-flow angle σ, and the magnitude of the three-dimensional flow vector V are known. Assuming this is true, R' and the angle with respect to the y-axis ϕ can be calculated as follows:

$$v = \tan \sigma \, (U_\infty + u) \tag{A1}$$

$$w = \tan \varepsilon \, (U_\infty + u) \tag{A2}$$

$$R' = \sqrt{v^2 + w^2} \tag{A3}$$

Substituting equations (A1) and (A2) into equation (A3) gives

$$R' = (U_\infty + u) \sqrt{\tan^2 \sigma + \tan^2 \varepsilon} \tag{A4}$$

Also, notice that

$$\tan \theta = \frac{R'}{U_\infty + u} \tag{A5}$$

Substituting equation (A4) into equation (A5) gives

$$\tan \theta = \sqrt{\tan^2 \sigma + \tan^2 \varepsilon} \tag{A6}$$

and

$$\theta = \tan^{-1} \sqrt{\tan^2 \sigma + \tan^2 \varepsilon} \tag{A7}$$

It can also be shown that

$$R' = V \sin \theta \tag{A8}$$

Since V, σ, and ε are known, R' can be computed. From figure 36, notice that

$$\tan \phi = \frac{w}{v} \tag{A9}$$

Substituting equations (A1) and (A2) into equation (A9) gives

$$\tan \phi = \frac{\tan \varepsilon}{\tan \sigma} \tag{A10}$$

and finally

$$\phi = \tan^{-1} \frac{\tan \varepsilon}{\tan \sigma} \tag{A11}$$

As previously mentioned, ε and σ can be determined from the pressure differences across the opposite tubes of the yawhead (fig. 34). The magnitude of V must be determined from the local static pressure p and the local pressure p_t. Assuming that at the rake the flow is isentropic (no shock waves), adiabatic (no heat transfer), and behaves like a perfect gas, equations (29b), (44), and (46) from reference 34 can be used to calculate V as follows:

$$\frac{p}{p_t} = \left(1 + \frac{\gamma - 1}{2} M^2\right)^{-\gamma/(\gamma-1)} \tag{A12}$$

where equation (A12) is equation (44) from reference 34. Solving this equation for the local Mach number M gives

$$M = \sqrt{\frac{2}{\gamma - 1}\left(\frac{p_t}{p}^{(\gamma-1)/\gamma} - 1\right)} \tag{A13}$$

Other useful equations are

$$\frac{a}{a_t} = \frac{1}{\sqrt{1 + \frac{\gamma - 1}{2} M^2}} \tag{A14}$$

$$a_t = \sqrt{\gamma R T_t} \tag{A15}$$

where equations (A14) and (A15) are equations (46) and (29b) from reference 34 and R is the gas constant, and Mach number is defined as

$$M = \frac{V}{a} \tag{A16}$$

Rewriting equation (A14) gives

$$a = \frac{a_t}{\sqrt{1 + \frac{\gamma - 1}{2} M^2}} \tag{A17}$$

Substituting equations (A15) and (A16) into equation (A17) gives

$$\frac{V}{M} = \frac{\sqrt{\gamma R T_t}}{\sqrt{1 + \frac{\gamma - 1}{2} M^2}} \tag{A18}$$

Finally, solving the magnitude of the local three-dimensional flow vector V gives

$$V = \frac{M\sqrt{\gamma R T_t}}{\sqrt{1 + \frac{\gamma - 1}{2} M^2}} \tag{A19}$$

REFERENCES

1. Whitcomb, Richard T.: Review of NASA Supercritical Airfoils. ICAS Paper No. 74-10, Aug. 1974.

2. Bartlett, Dennis W.: Wind-Tunnel Investigation of Several High Aspect-Ratio Supercritical Wing Configurations on a Wide-Body-Type Fuselage. NASA TM X-71996, 1977.

3. Bartlett, Dennis W.; and Patterson, James C., Jr.: NASA Supercritical-Wing Technology. NASA TM-78731, 1978.

4. Pope, G. G.: Prospects for Reducing the Fuel Consumption of Civil Aircraft. Proceedings - Energy and Aerospace, Royal Aeronaut. Soc. and American Inst. Aeronaut. & Astronaut. Soc., 1978.

5. Urie, D. M.; and Reaser, J. S.: Aerodynamic Development of a Small Horizontal Tail for an Active Control Relaxed Stability Transport Application. A Collection of Technical Papers - AIAA/Atmospheric Flight Mechanics Conference for Future Space Systems, Aug. 1979, pp. 224-231. (Available as AIAA Paper 79-1653.)

6. Hofmann, L. Gregor; and Clement, Warren F.: Vehicle Design Considerations for Active Control Application to Subsonic Transport Aircraft. NASA CR-2408, 1974.

7. Schaefer, William T., Jr.: Characteristics of Major Active Wind Tunnels at the Langley Research Center. NASA TM X-1130, 1965.

8. Bobbitt, Percy J.: Modern Fluid Dynamics of Subsonic and Transonic Flight. AIAA-80-0861, May 1980.

9. Bauer, Frances; Garabedian, Paul; Korn, David; and Jameson, Antony: Supercritical Wing Sections II. Volume 108 of Lecture Notes in Economics and Mathematical Systems, Springer-Verlag, 1975.

10. Harris, Charles D.: Aerodynamic Characteristics of the 10-Percent-Thick NASA Supercritical Airfoil 33 Designed for a Normal-Force Coefficient of 0.7. NASA TM X-72711, 1975.

11. Harris, Charles D.: Aerodynamic Characteristics of a 14-Percent-Thick NASA Supercritical Airfoil Designed for a Normal-Force Coefficient of 0.7. NASA TM X-72712, 1975.

12. Braslow, Albert L.; and Knox, Eugene C.: Simplified Method for Determination of Critical Height of Distributed Roughness Particles for Boundary-Layer Transition at Mach Numbers From 0 to 5. NACA TN 4363, 1958.

13. Loving, Donald L.; and Katzoff, S.: The Fluorescent-Oil Film Method and Other Techniques for Boundary-Layer Flow Visualization. NASA MEMO 3-17-59L, 1959.

14. Blackwell, James A., Jr.: Preliminary Study of Effects of Reynolds Number and Boundary-Layer Transition Location on Shock-Induced Separation. NASA TN D-5003, 1969.

15. Brooks, Joseph D.: Some Anomalies Observed in Wind-Tunnel Tests of a Blunt Body at Transonic and Supersonic Speeds. NASA TN D-8237, 1976.

16. Taylor, Robert T.; and Ray, Edward J.: Deep-Stall Aerodynamic Characteristics of T-Tail Aircraft. Conference on Aircraft Operating Problems, NASA SP-83, 1965, pp. 113-121.

17. Taylor, Robert T.; and Ray, Edward J.: Factors Affecting the Stability of T-Tail Transports. J. Aircr., vol. 3, no. 4, July-Aug. 1966, pp. 359-364.

18. McKinney, Linwood W.; and Dollyhigh, Samuel M.: Some Trim Drag Considerations for Maneuvering Aircraft. J. Aircr., vol. 8, no. 8, Aug. 1971, pp. 623-629.

19. Goldstein, S. E.; and Combs, C. P.: Trimmed Drag and Maximum Flight Efficiency of Aft Tail and Canard Configurations. AIAA Paper No. 74-69, Jan.-Feb. 1974.

20. Lutze, F. H., Jr.: Reduction of Trimmed Drag. Proceedings of the NASA/Industry/University General Aviation Drag Reduction Workshop, Jan Roskam, ed., Univ. of Kansas, July 1975, pp. 307-318. (Available as NASA CR-145627.)

21. Larrabee, E. E.: Trim Drag in the Light of Munk's Stagger Theorem. Proceedings of the NASA/Industry/University General Aviation Drag Reduction Workshop, Jan Roskam, ed., Univ. of Kansas, July 1975, pp. 319-329. (Available as NASA CR-145627.)

22. Lamar, John E.: Minimum Trim Drag Design for Interfering Lifting Surfaces Using Vortex-Lattice Methodology. Vortex-Lattice Utilization, NASA SP-405, 1976, pp. 89-111.

23. McLaughlin, Milton D.: Calculations, and Comparison With an Ideal Minimum, of Trimmed Drag for Conventional and Canard Configurations Having Various Levels of Static Stability. NASA TN D-8391, 1977.

24. Laitone, E. V.: Ideal Tail Load for Minimum Aircraft Drag. J. Aircr., vol. 15, no. 3, Mar. 1978, pp. 190-192.

25. Shevell, Richard S.: Comment on "Ideal Tail Load for Minimum Aircraft Drag." J. Aircr., vol. 15, no. 9, Sept. 1978, p. 639.

26. Sachs, Gottfried: Minimum Trimmed Drag and Optimum c.g. Position. J. Aircr., vol. 15, no. 8, Aug. 1978, pp. 456-459.

27. Lutze, Frederick H., Jr.: Trimmed Drag Considerations. J. Aircr., vol. 14, no. 6, June 1977, pp. 544-546.

28. Hays, A. P.; Beck, W. E.; Morita, W. H.; Penrose, B. J.; Skarshaug, R. E.; and Wainfan, B. S.: Integrated Technology Wing Design Study. NASA CR-3586, 1982.

29. Dommasch, Daniel O.; Sherby, Sydney S.; and Connolly, Thomas F.: Airplane Aerodynamics, Fourth ed. Pitman Pub. Corp., c.1967.

30. Silverstein, Abe; and Katzoff, S.: Experimental Investigation of Wind-Tunnel Interference on the Downwash Behind an Airfoil. NACA Rep. 609, 1937.

31. Silverstein, Abe; Katzoff, S.; and Bullivant, W. Kenneth: Downwash and Wake Behind Plain and Flapped Airfoils. NACA Rep. 651, 1939.

32. Bryer, D. W.; and Pankhurst, R. C.: Pressure-Probe Methods for Determining Wind Speed and Flow Direction. Her Majesty's Stationery Office (London), 1971.

33. Dudzinski, Thomas J.; and Krause, Lloyd N.: Flow-Direction Measurement With Fixed-Position Probes. NASA TM X-1904, 1969.

34. Ames Research Staff: Equations, Tables, and Charts for Compressible Flow. NACA Rep. 1135, 1953. (Supersedes NACA TN 1428.)

TABLE 1.- TAIL PARAMETERS

Tail	Airfoil	S_T		b_T		$\Lambda_{c/4}$, deg	λ	A	Γ, deg	C_T	
		m^2	(ft^2)	cm	in.					Wide body	SCW
Low tail											
H_1	0.10 t/c, cambered	0.05	0.55	42.52	16.74	32.5	0.35	3.54	10	0.69	0.90
H_2	.10 t/c, cambered	.07	.70	49.78	19.60	32.5	.31	3.82	10	.86	1.12
H_3	.10 t/c, symmetrical	.05	.55	42.52	16.74	32.5	.35	3.54	10	.69	.90
V_1	.10 t/c, symmetrical	.04	.42	25.40	10.0	35.0	.35	1.65		.51	.67
T-tail											
H_4	0.10 t/c, cambered	0.05	0.56	43.13	16.98	32.5	0.35	3.59	-3	0.84	1.09
H_5	.10 t/c, symmetrical	.05	.56	43.13	16.98	32.5	.35	3.59	-3	.84	1.09
V_2	.12 t/c, symmetrical	.04	.47	17.78	7.0	45.0	.70	.72		.52	.68

TABLE 2.- COORDINATES FOR 10-PERCENT-THICK SYMMETRICAL AIRFOIL

x/c (a)	$(z/c)_u$	$(z/c)_\ell$	x/c (a)	$(z/c)_u$	$(z/c)_\ell$
0.000	0.00000	0.00000	0.510	0.04810	-0.04810
.002	.00760	.00760	.520	.04780	-.04580
.005	.01160	.01160	.530	.04740	-.04740
.010	.01550	.01550	.540	.04700	-.04700
.020	.02070	.02070	.550	.04650	-.04650
.030	.02430	.02430	.560	.04600	-.04600
.040	.02700	.02700	.570	.04550	-.04550
.050	.02920	-.02920	.580	.04490	-.04490
.060	.03110	-.03110	.590	.04430	-.04430
.070	.03280	-.03280	.600	.04360	-.04360
.080	.03430	-.03430	.610	.04280	-.04280
.090	.03570	-.03570	.620	.04200	-.04200
.100	.03690	-.03690	.630	.04110	-.04110
.110	.03800	-.03800	.640	.04020	-.04020
.120	.03900	-.03900	.650	.03920	-.03920
.130	.04000	-.04000	.660	.03820	-.03820
.140	.04090	-.04090	.670	.03715	-.03715
.150	.04170	-.04170	.680	.03610	-.03610
.160	.04250	-.04250	.690	.03505	-.03505
.170	.04320	-.04320	.700	.03400	-.03400
.180	.04390	-.04390	.710	.03295	-.03295
.190	.04450	-.04450	.720	.03190	-.03190
.200	.04510	-.04510	.730	.03085	-.03085
.210	.04560	-.04560	.740	.02980	-.02980
.220	.04610	-.04610	.750	.02875	-.02875
.230	.04660	-.04660	.760	.02770	-.02770
.240	.04700	-.04700	.770	.02665	-.02665
.250	.04740	-.04740	.780	.02560	-.02560
.260	.04780	-.04780	.790	.02455	-.02355
.270	.04810	-.04810	.800	.02350	-.02350
.280	.04840	-.04840	.810	.02245	-.02245
.290	.04870	-.04870	.820	.02140	-.02140
.300	.04900	-.04900	.830	.02035	-.02035
.310	.04920	-.04920	.840	.01930	-.01930
.320	.04940	-.04940	.850	.01825	-.01825
.330	.04960	-.04960	.860	.01720	-.01720
.340	.04970	-.04970	.870	.01615	-.01615
.350	.04980	-.04980	.880	.01510	-.01510
.360	.04990	-.04990	.890	.01405	-.01405
.370	.05000	-.05000	.900	.01300	-.01300
.380	.05000	-.05000	.910	.01195	-.01195
.390	.05000	-.05000	.920	.01090	-.01090
.400	.05000	-.05000	.930	.00985	-.00985
.410	.05000	-.05000	.940	.00880	-.00880
.420	.04990	-.04990	.950	.00775	-.00775
.430	.04980	-.04980	.960	.00670	-.00670
.440	.04970	-.04970	.970	.00565	-.00565
.450	.04960	-.04960	.980	.00460	-.00460
.460	.04940	-.04940	.990	.00355	-.00355
.470	.04920	-.04920	1.000	.00250	-.00250
.480	.04900	-.04900			
.490	.04870	-.04870			
.500	.04840	-.04840			

[a]Coordinates are same for upper and lower surfaces.

TABLE 3.- COORDINATES FOR 10-PERCENT-THICK CAMBERED AIRFOIL

x/c (a)	$(z/c)_u$	$(z/c)_\ell$	x/c (a)	$(z/c)_u$	$(z/c)_\ell$
0.000	0.0000	0.0000	0.510	0.0488	-0.0460
.002	.0076	-.0076	.520	.0485	-.0454
.005	.0116	-.0116	.530	.0482	-.0447
.010	.0155	-.0155	.540	.0479	-.0440
.020	.0207	-.0207	.550	.0476	-.0432
.030	.0242	-.0242	.560	.0472	-.0423
.040	.0269	-.0269	.570	.0468	-.0413
.050	.0291	-.0291	.580	.0464	-.0403
.060	.0310	-.0310	.590	.0459	-.0392
.070	.0327	-.0327	.600	.0454	-.0381
.080	.0342	-.0342	.610	.0449	-.0369
.090	.0355	-.0356	.620	.0443	-.0357
.100	.0368	-.0369	.630	.0437	-.0344
.110	.0379	-.0381	.640	.0431	-.0331
.120	.0389	-.0392	.650	.0425	-.0317
.130	.0399	-.0402	.660	.0418	-.0303
.140	.0408	-.0411	.670	.0411	-.0289
.150	.0416	-.0420	.680	.0404	-.0275
.160	.0424	-.0428	.690	.0396	-.0261
.170	.0431	-.0435	.700	.0388	-.0247
.180	.0438	-.0442	.710	.0380	-.0233
.190	.0444	-.0449	.720	.0372	-.0219
.200	.0450	-.0455	.730	.0363	-.0205
.210	.0456	-.0460	.740	.0354	-.0191
.220	.0461	-.0465	.750	.0345	-.0177
.230	.0466	-.0470	.760	.0336	-.0163
.240	.0470	-.0474	.770	.0326	-.0149
.250	.0474	-.0478	.780	.0316	-.0135
.260	.0478	-.0481	.790	.0306	-.0121
.270	.0481	-.0484	.800	.0296	-.0107
.280	.0484	-.0487	.810	.0285	-.0093
.290	.0487	-.0489	.820	.0274	-.0079
.300	.0489	-.0491	.830	.0263	-.0065
.310	.0491	-.0493	.840	.0252	-.0051
.320	.0493	-.0494	.850	.0241	-.0038
.330	.0495	-.0495	.860	.0229	-.0025
.340	.0496	-.0496	.870	.0217	-.0013
.350	.0497	-.0497	.880	.0205	-.0002
.360	.0498	-.0497	.890	.0193	.0008
.370	.0499	-.0497	.900	.0180	.0017
.380	.0500	-.0497	.910	.0167	.0025
.390	.0500	-.0496	.920	.0154	.0031
.400	.0500	-.0495	.930	.0141	.0035
.410	.0500	-.0494	.940	.0127	.0036
.420	.0500	-.0492	.950	.0113	.0034
.430	.0500	-.0490	.960	.0098	.0029
.440	.0499	-.0488	.970	.0083	.0022
.450	.0498	-.0485	.980	.0067	.0012
.460	.0497	-.0482	.990	.0050	-.0001
.470	.0496	-.0478	1.000	.0032	-.0017
.480	.0494	-.0474			
.490	.0492	-.0470			
.500	.0490	-.0465			

[a]Coordinates are same for upper and lower surfaces.

TABLE 4.- COORDINATES FOR 12-PERCENT-THICK SYMMETRICAL AIRFOIL

x/c (a)	$(z/c)_u$	$(z/c)_\ell$	x/c (a)	$(z/c)_u$	$(z/c)_\ell$
0.000	0.00000	0.00000	0.510	0.05772	-0.05772
.002	.00912	-.00912	.520	.05736	-.05736
.005	.01392	-.01392	.530	.05688	-.05688
.010	.01860	-.01860	.540	.05640	-.05640
.020	.02484	-.02484	.550	.05580	-.05580
.030	.02916	-.02916	.560	.05520	-.05520
.040	.03240	-.03240	.570	.05460	-.05460
.050	.03504	-.03504	.580	.05388	-.05388
.060	.03732	-.03732	.590	.05316	-.05316
.070	.03939	-.03939	.600	.05232	-.05232
.080	.04119	-.04119	.610	.05136	-.05136
.090	.04282	-.04282	.620	.05040	-.05040
.100	.04428	-.04428	.630	.04932	-.04932
.110	.04560	-.04560	.640	.04824	-.04824
.120	.04680	-.04680	.650	.04704	-.04704
.130	.04800	-.04800	.660	.04584	-.04584
.140	.04908	-.04908	.670	.04458	-.04458
.150	.05004	-.05004	.680	.04332	-.04332
.160	.05100	-.05100	.690	.04206	-.04206
.170	.05184	-.05184	.700	.04080	-.04080
.180	.05268	-.05268	.710	.03954	-.03954
.190	.05340	-.05340	.720	.03828	-.03828
.200	.05412	-.05412	.730	.03702	-.03702
.210	.05472	-.05472	.740	.03576	-.03576
.220	.05532	-.05532	.750	.03450	-.03450
.230	.05592	-.05592	.760	.03324	-.03324
.240	.05640	-.05640	.770	.03198	-.03198
.250	.05688	-.05688	.780	.03072	-.03072
.260	.05736	-.05736	.790	.02946	-.02946
.270	.05772	-.05772	.800	.02820	-.02820
.280	.05808	-.05808	.810	.02694	-.02694
.290	.05844	-.05844	.820	.02568	-.02568
.300	.05880	-.05880	.830	.02442	-.02442
.310	.05904	-.05904	.840	.02316	-.02316
.320	.05928	-.05928	.850	.02190	-.02190
.330	.05952	-.05952	.860	.02064	-.02064
.340	.05964	-.05964	.870	.01938	-.01938
.350	.05976	-.05976	.880	.01812	-.01812
.360	.05988	-.05988	.890	.01686	-.01686
.370	.06000	-.06000	.900	.01560	-.01560
.380	.06000	-.06000	.910	.01434	-.01434
.390	.06000	-.06000	.920	.01308	-.01308
.400	.06000	-.06000	.930	.01182	-.01182
.410	.06000	-.06000	.940	.01056	-.01056
.420	.05988	-.05988	.950	.00930	-.00930
.430	.05976	-.05976	.960	.00804	-.00804
.440	.05964	-.05964	.970	.00678	-.00678
.450	.05952	-.05952	.980	.00552	-.00552
.460	.05928	-.05928	.990	.00426	-.00426
.470	.05904	-.05904	1.000	.00300	-.00300
.480	.05880	-.05880			
.490	.05844	-.05844			
.500	.05808	-.05808			

[a]Coordinates are same for upper and lower surfaces

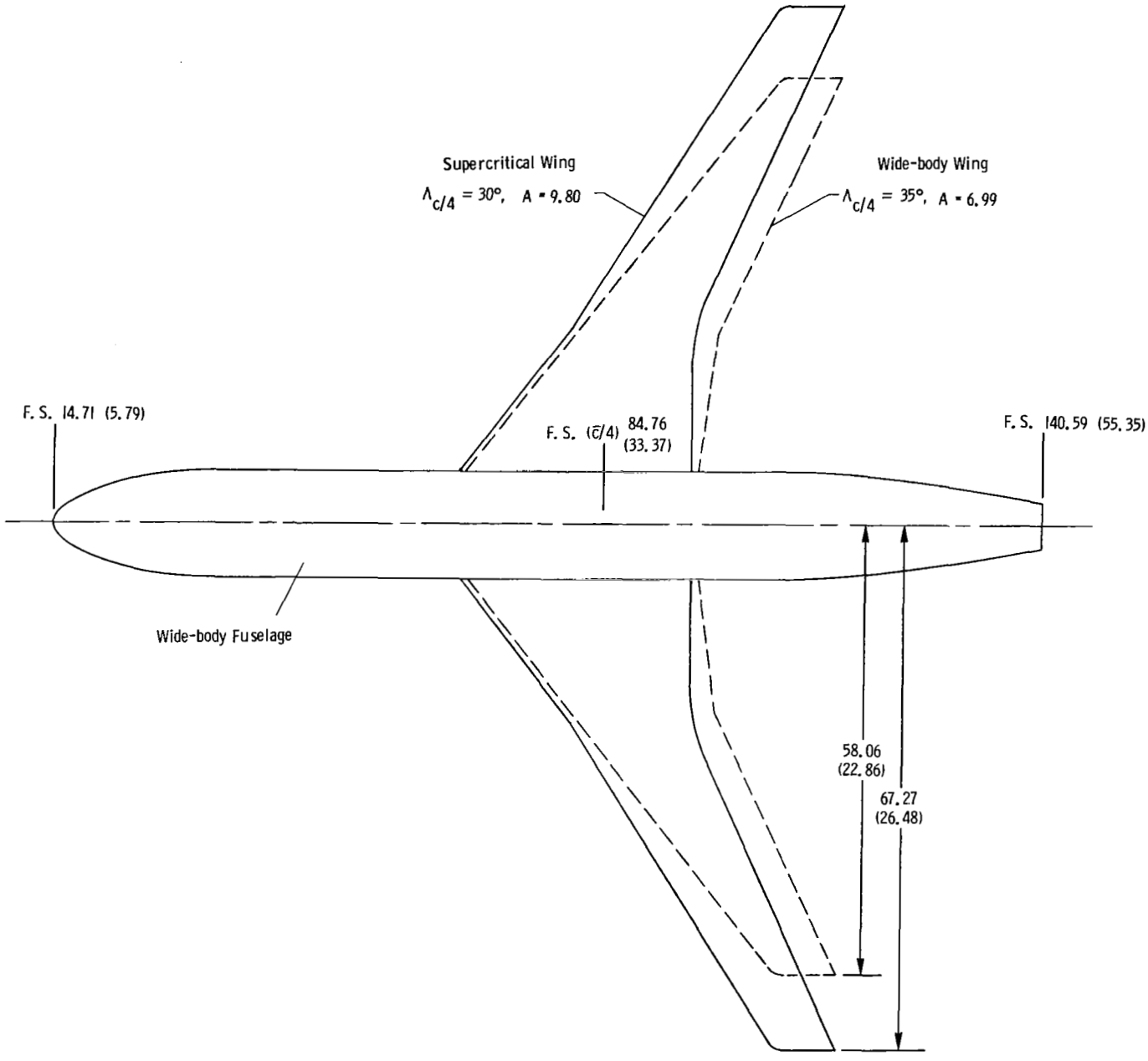

Figure 1.- Wing planforms on fuselage.

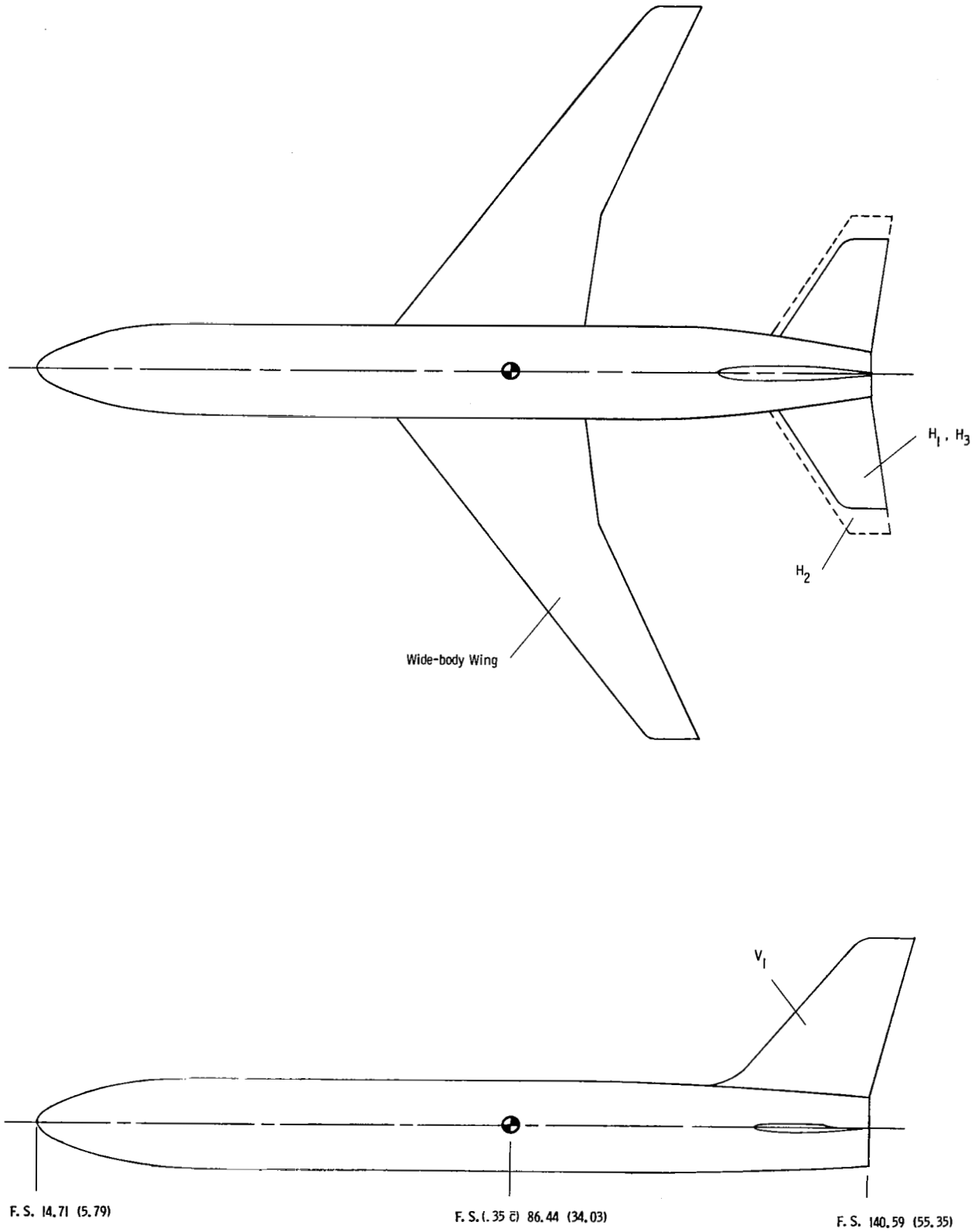

Figure 2.- Low-tail configurations.

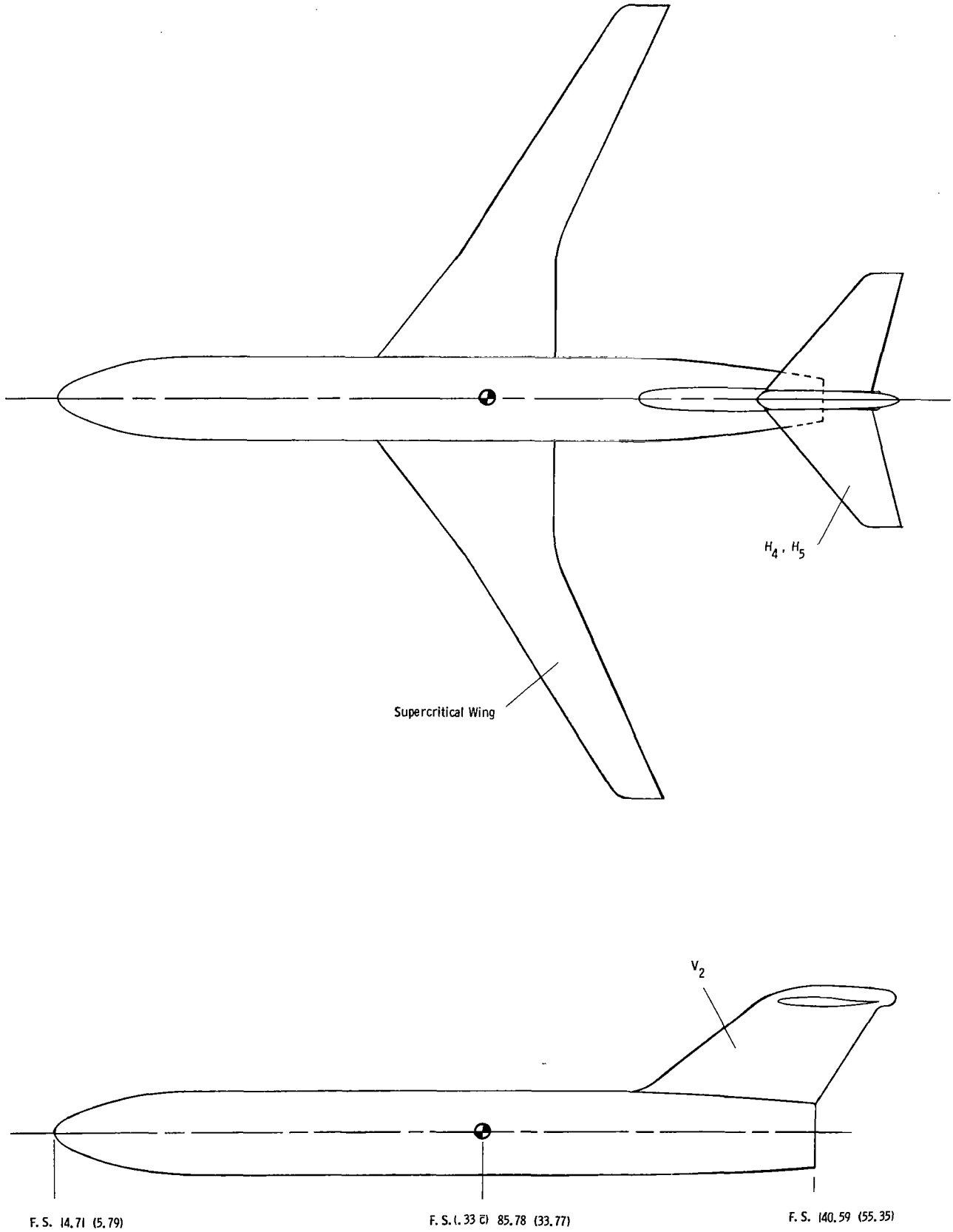

Figure 3.- T-tail configurations.

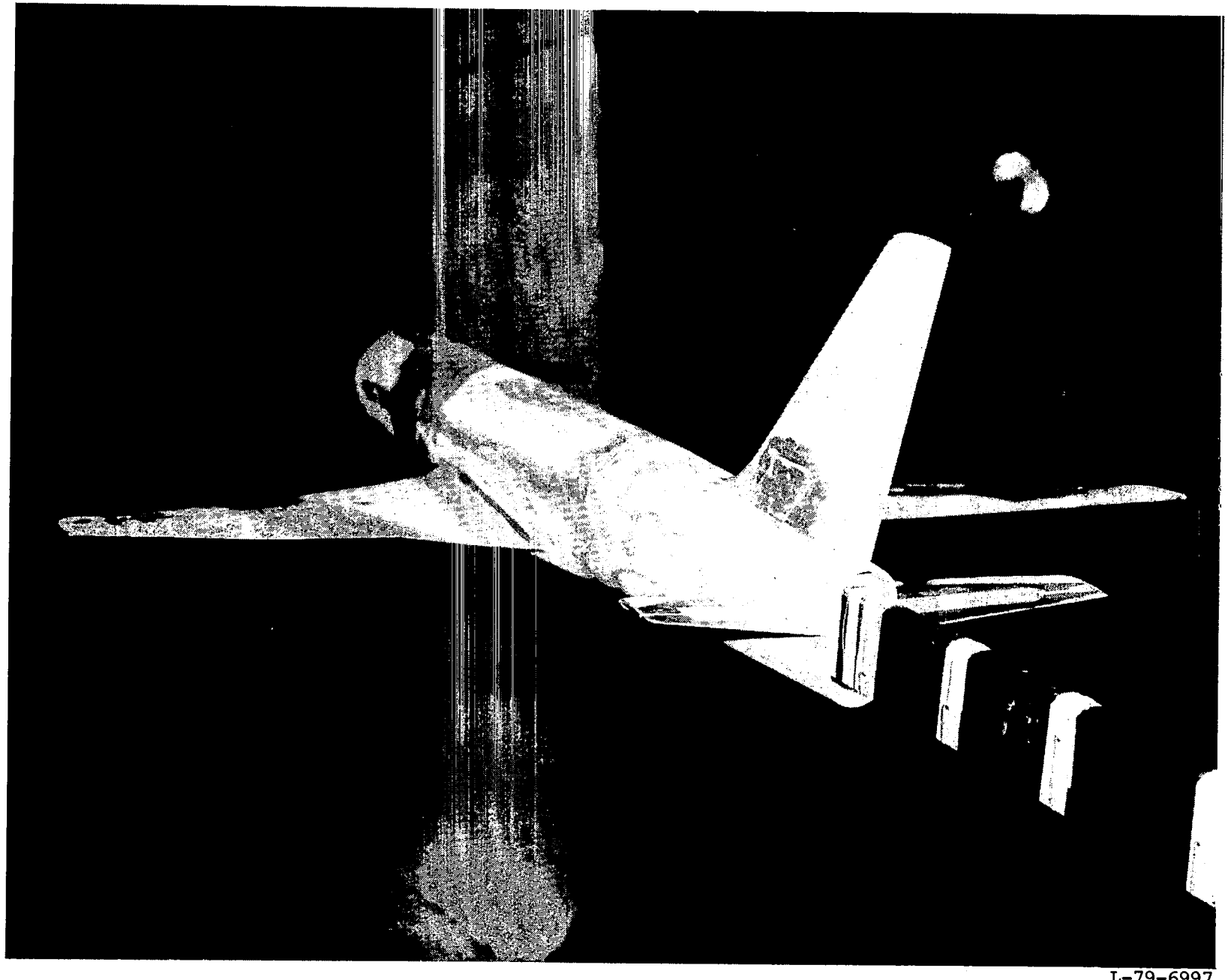

L-79-6997

Figure 4.- Typical low-tail configuration.

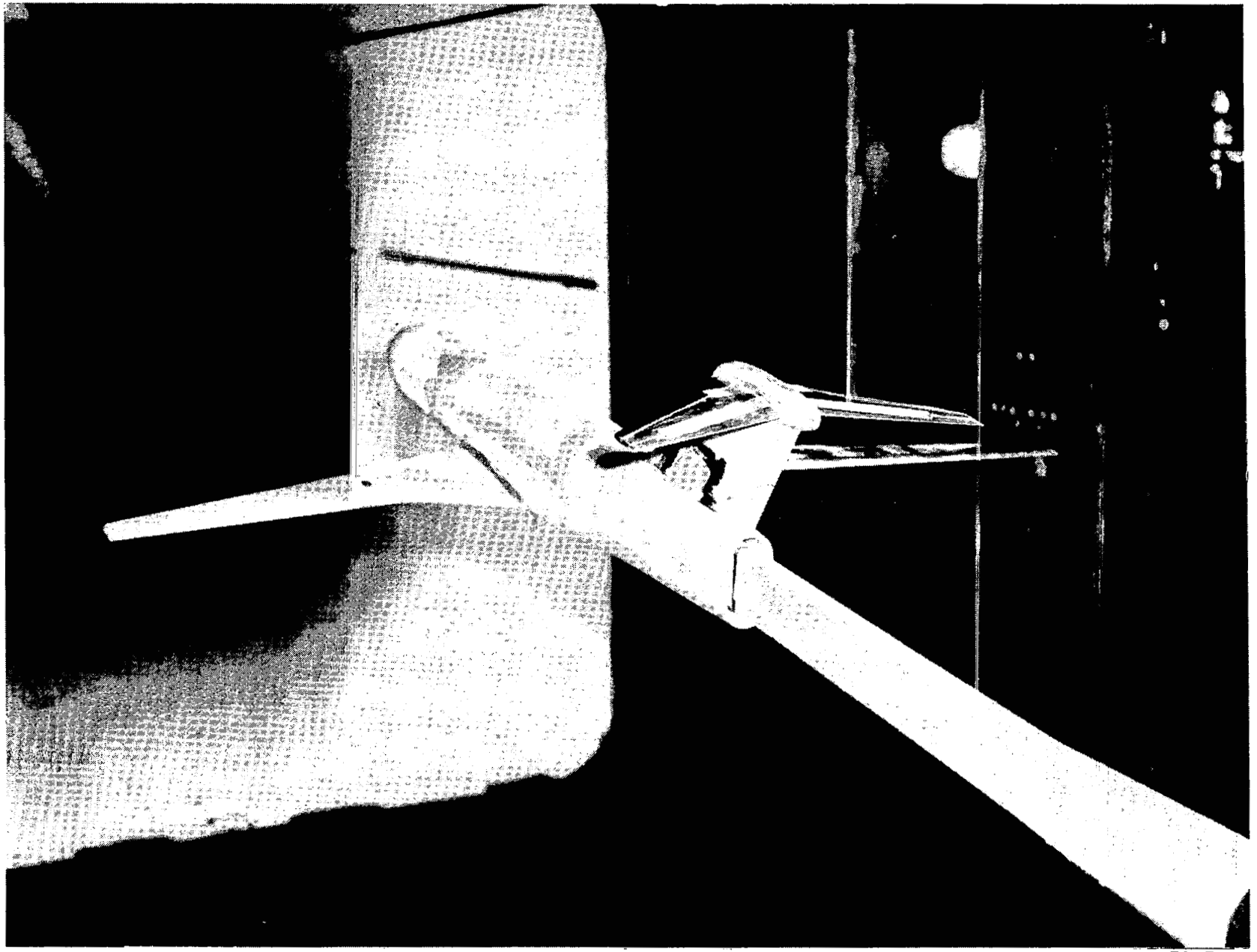

L-79-7861

Figure 5.- Typical T-tail configuration.

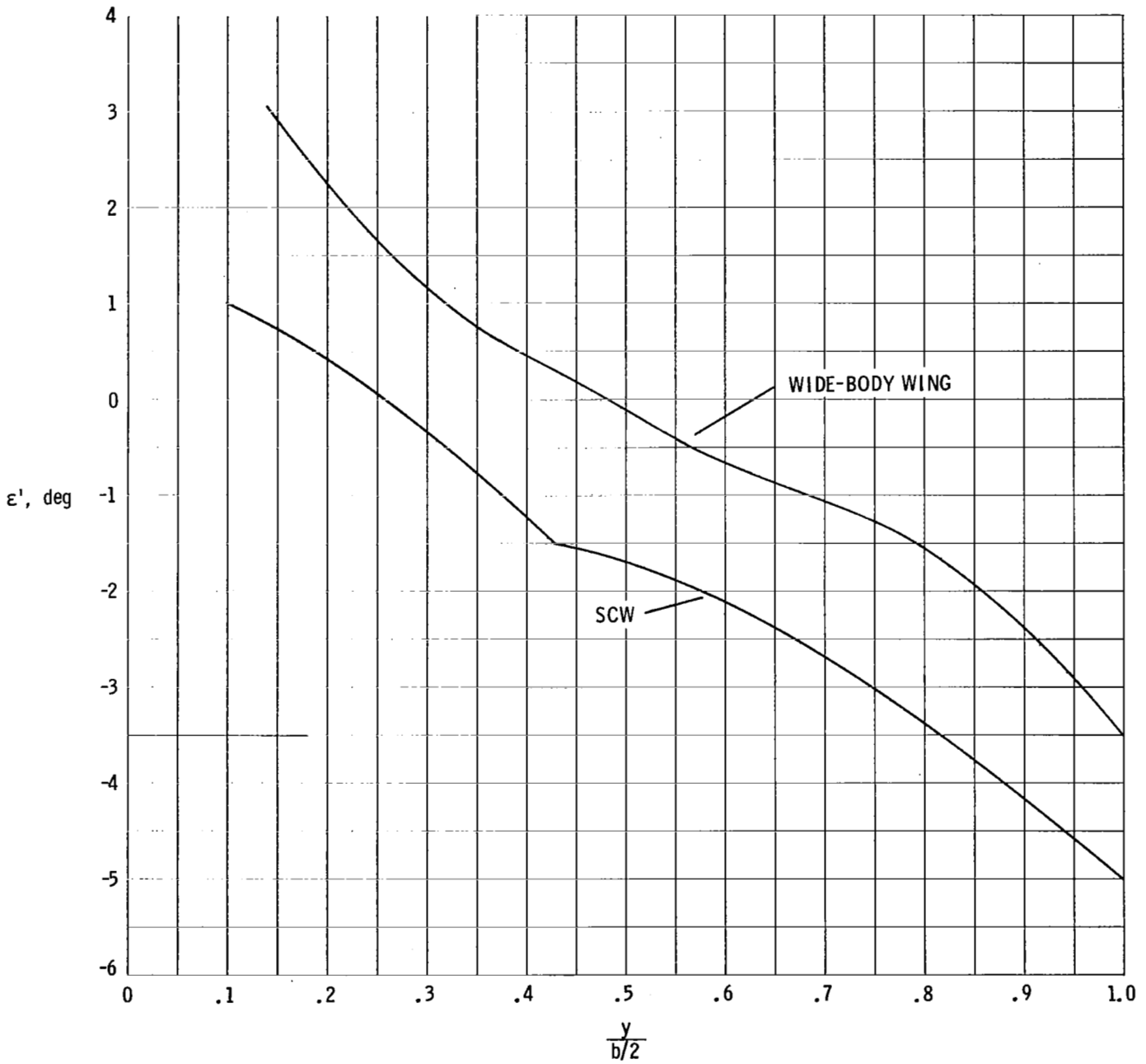

Figure 6.- Twist distribution for both wings.

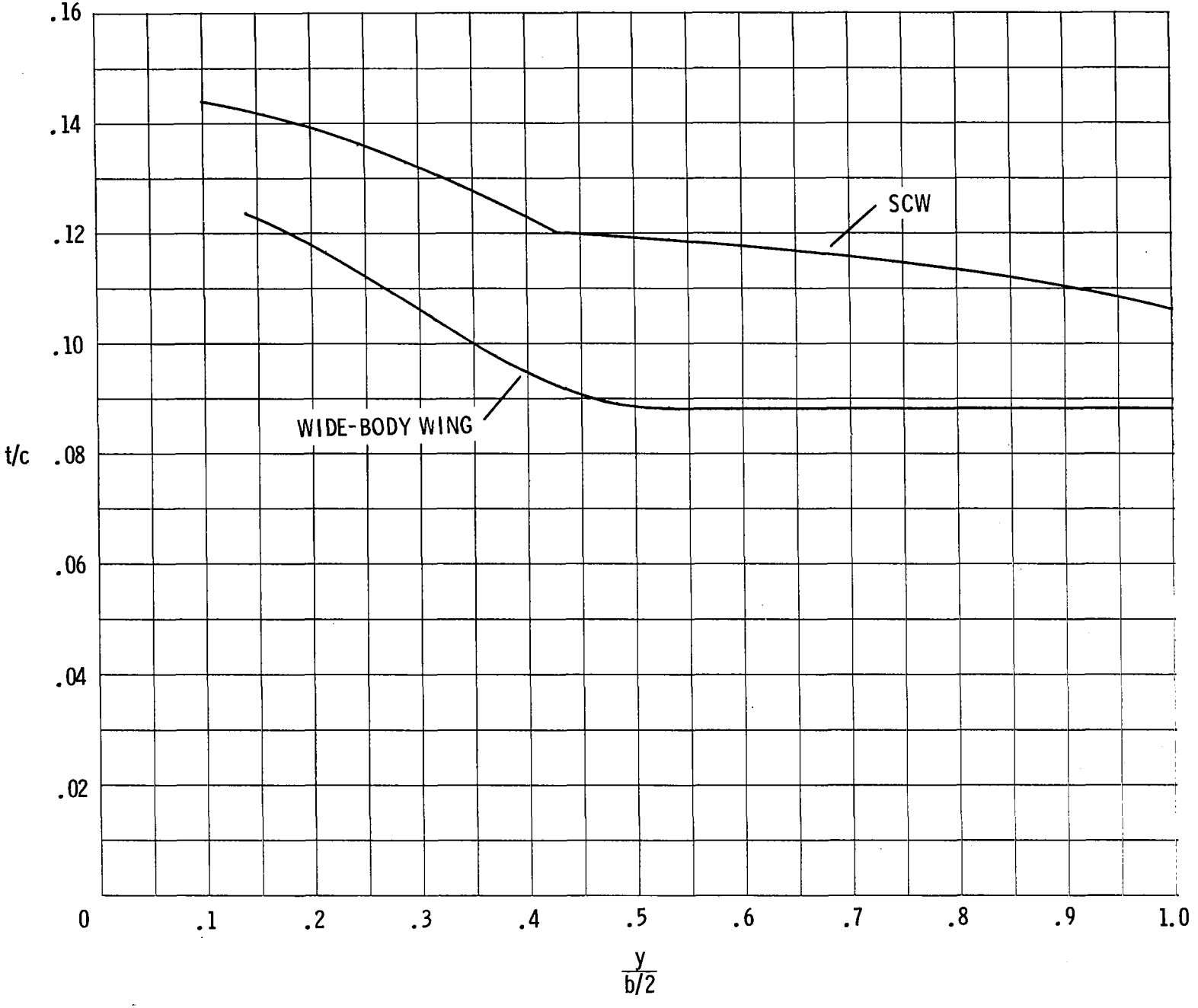

Figure 7.- Thickness distribution for both wings.

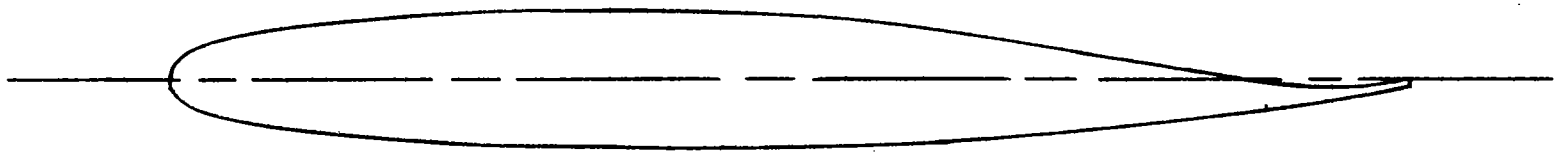

10-percent-thick cambered

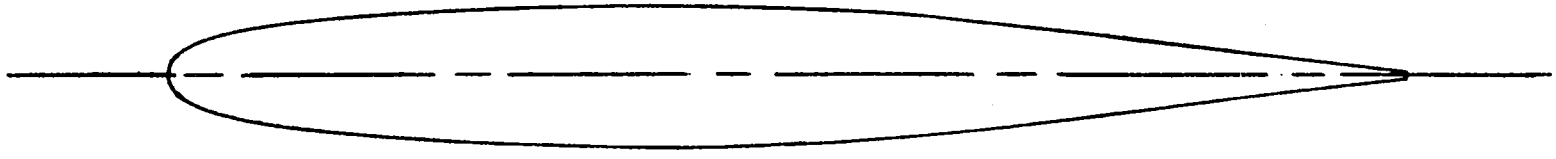

10-percent-thick symmetrical

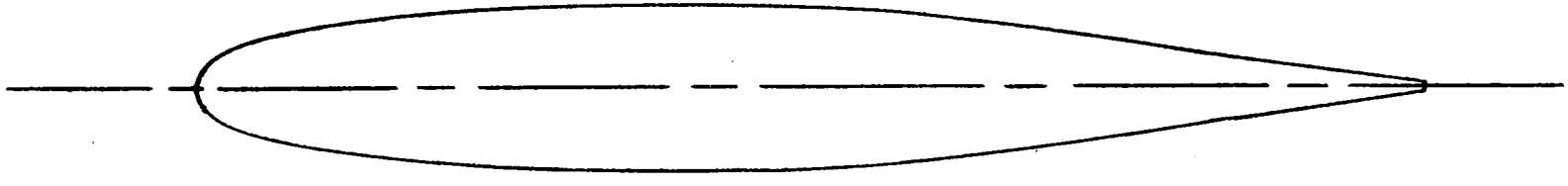

12-percent-thick symmetrical

Figure 8.- Supercritical airfoil sections used for horizontal and vertical tails.

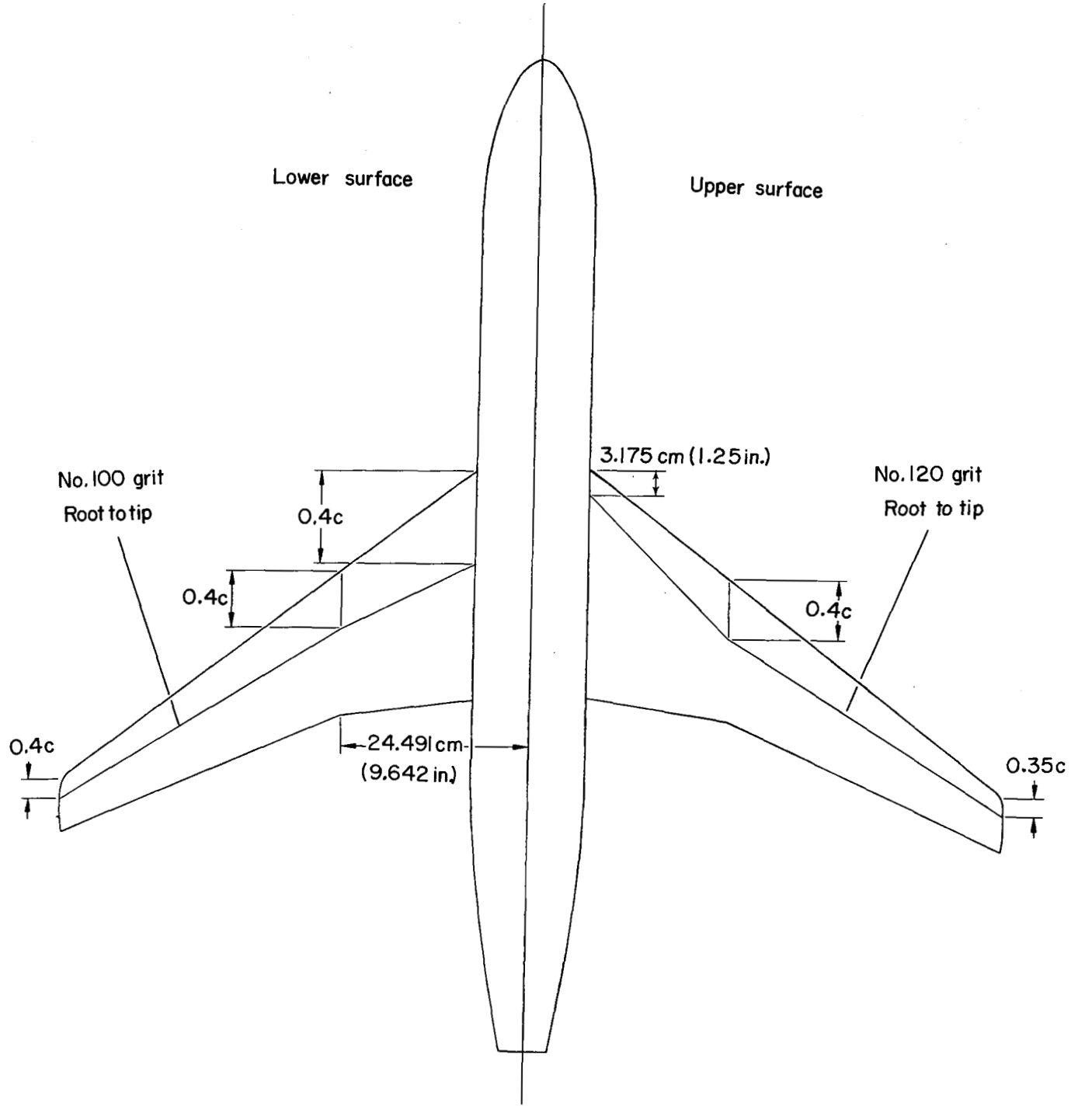

Figure 9.- Boundary-layer transition strip patterns for the wide-body wing.

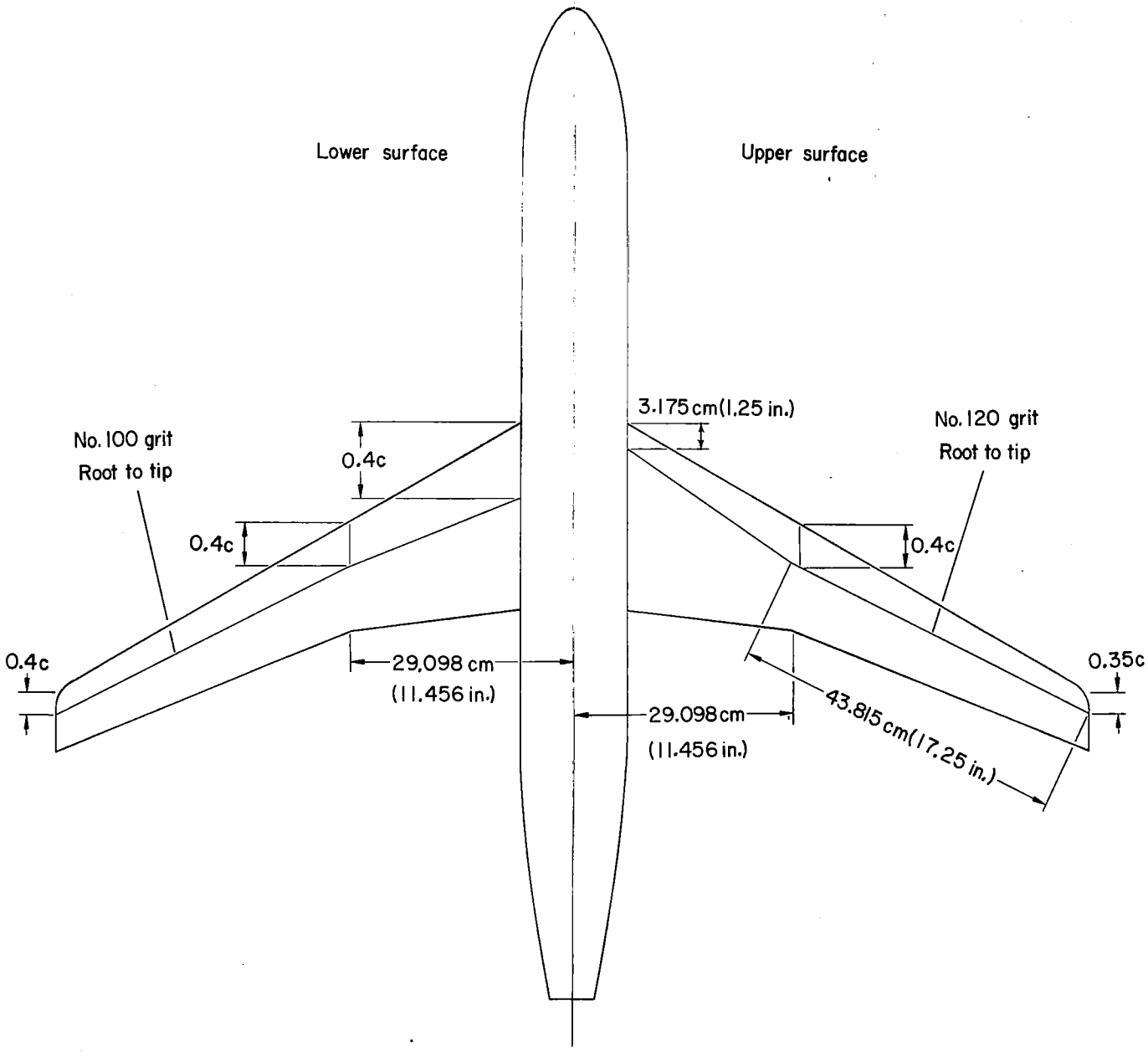

Figure 10.- Boundary-layer transition strip patterns for the supercritical wing.

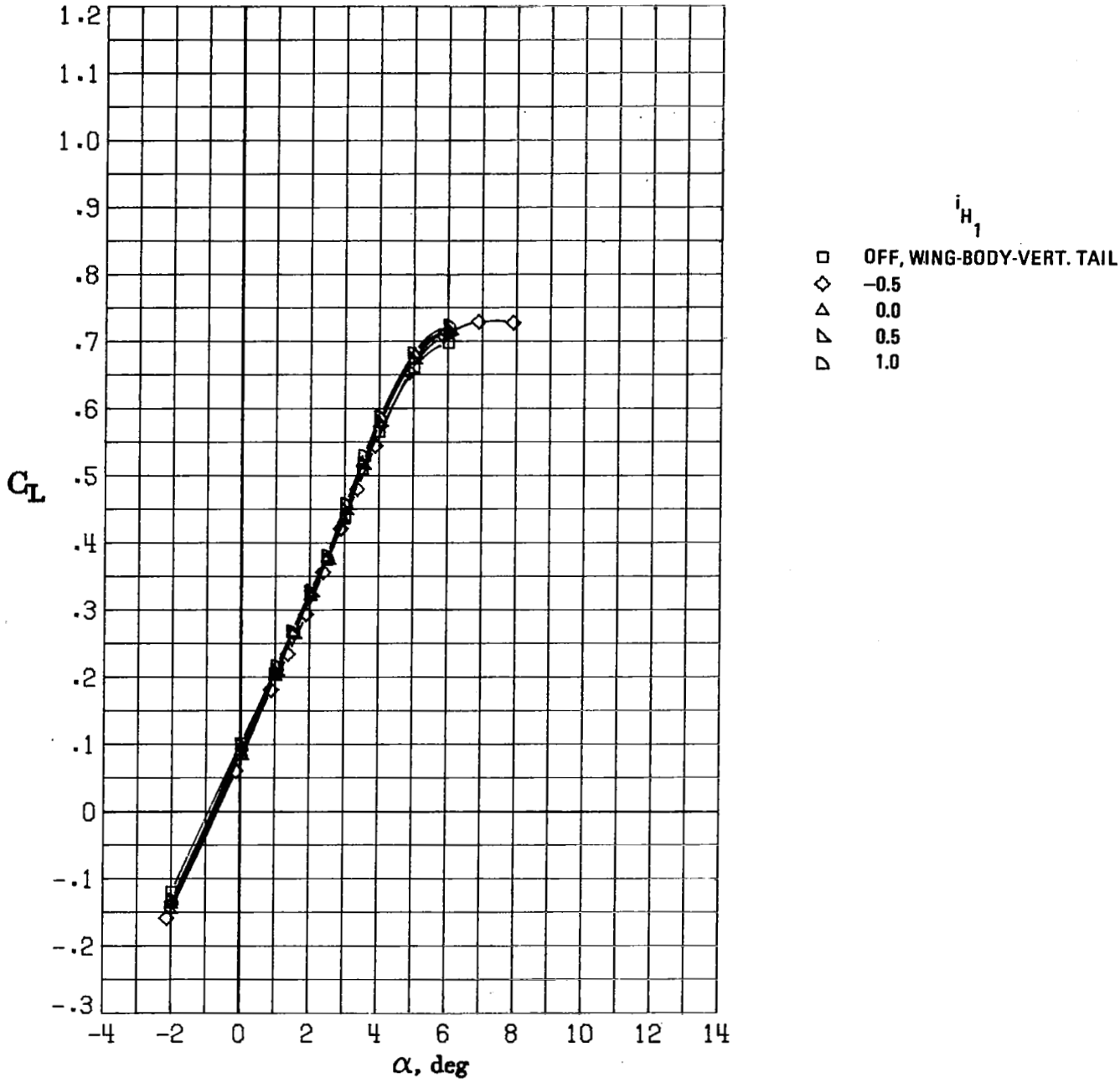

(a) H_1.

Figure 11.- Variation of lift coefficient with angle of attack for wide-body wing configuration at $M_\infty = 0.82$.

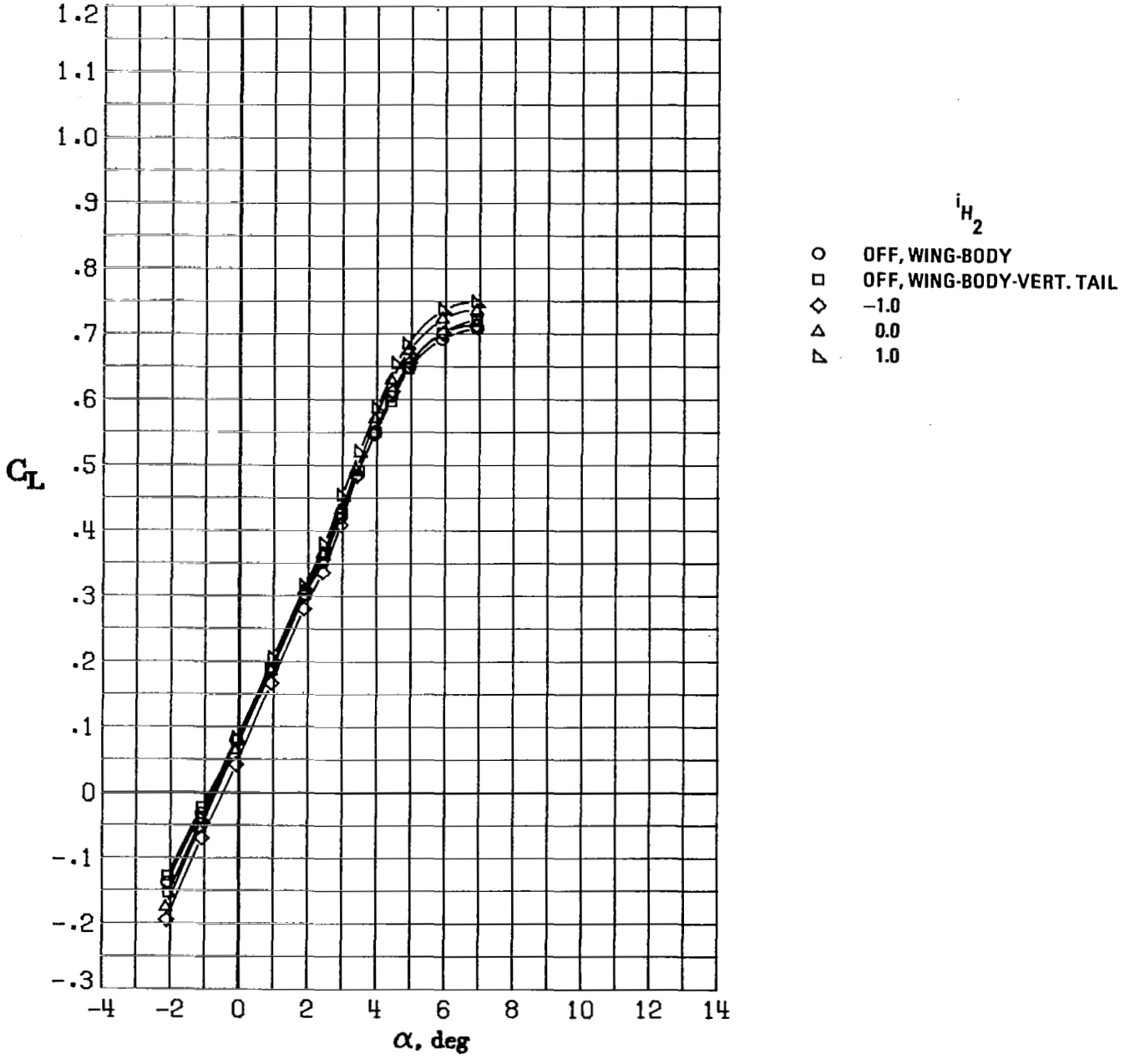

(b) H_2.

Figure 11.- Continued.

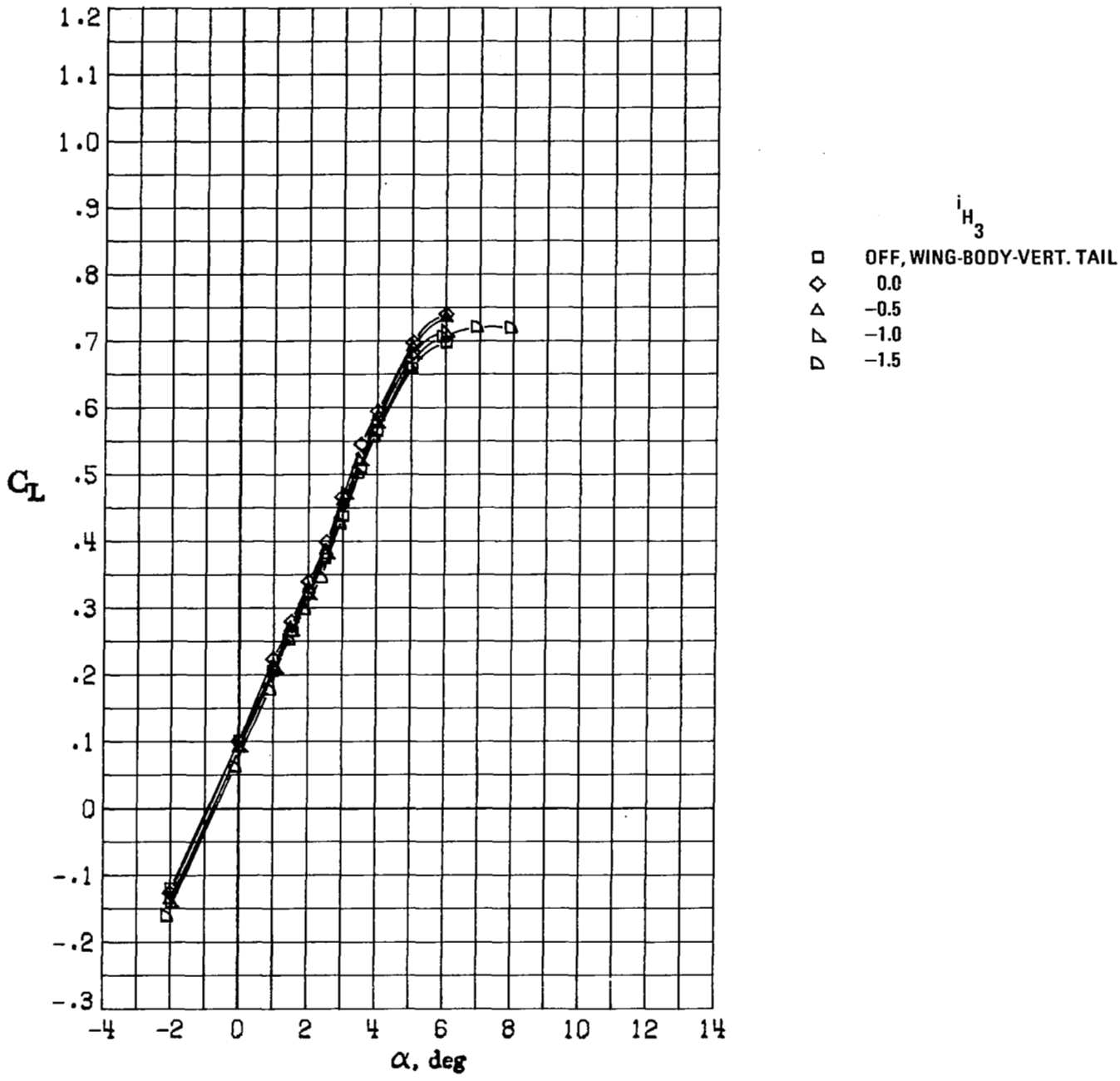

(c) H_3.

Figure 11.- Continued.

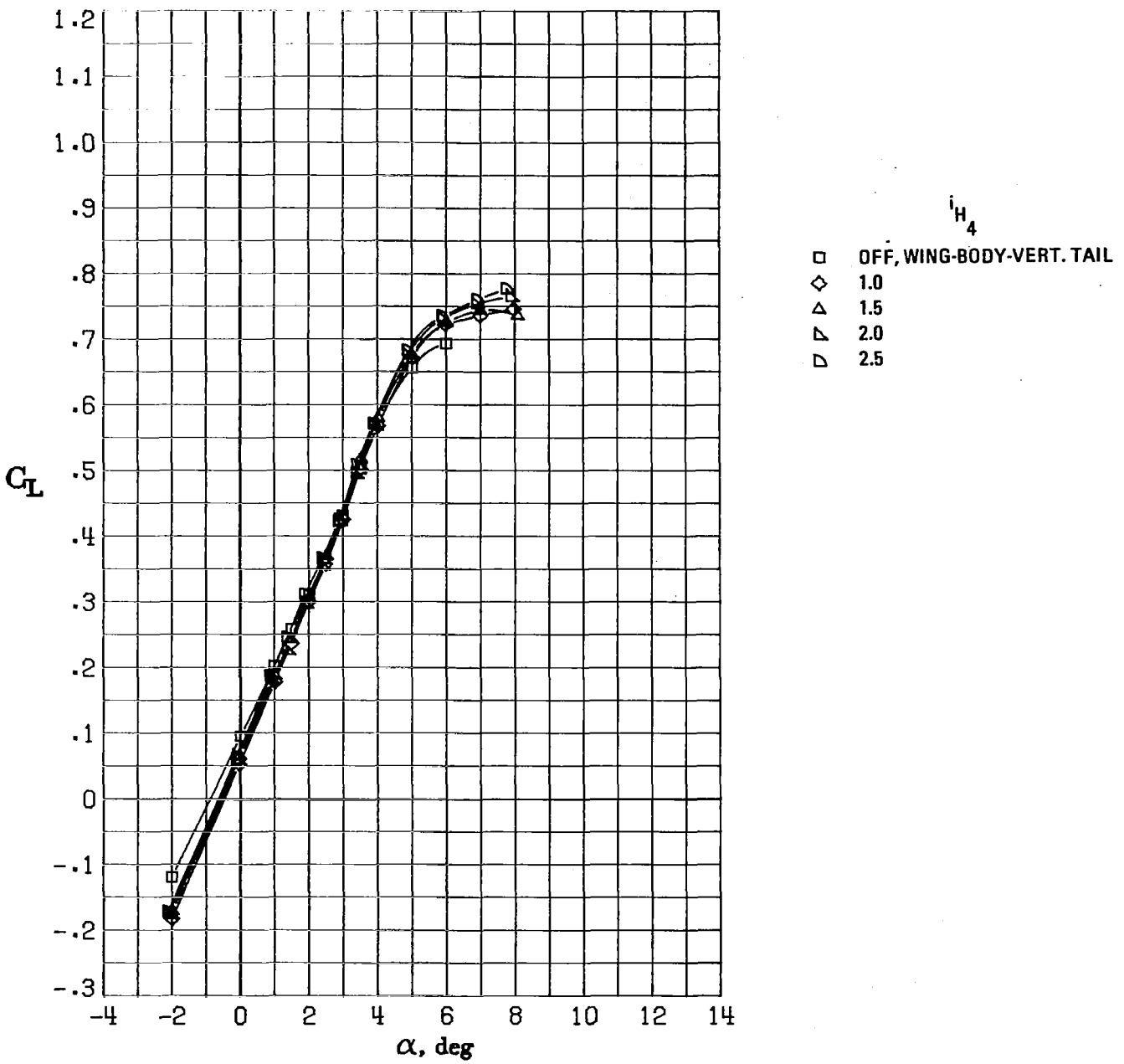

(d) H_4.

Figure 11.- Continued.

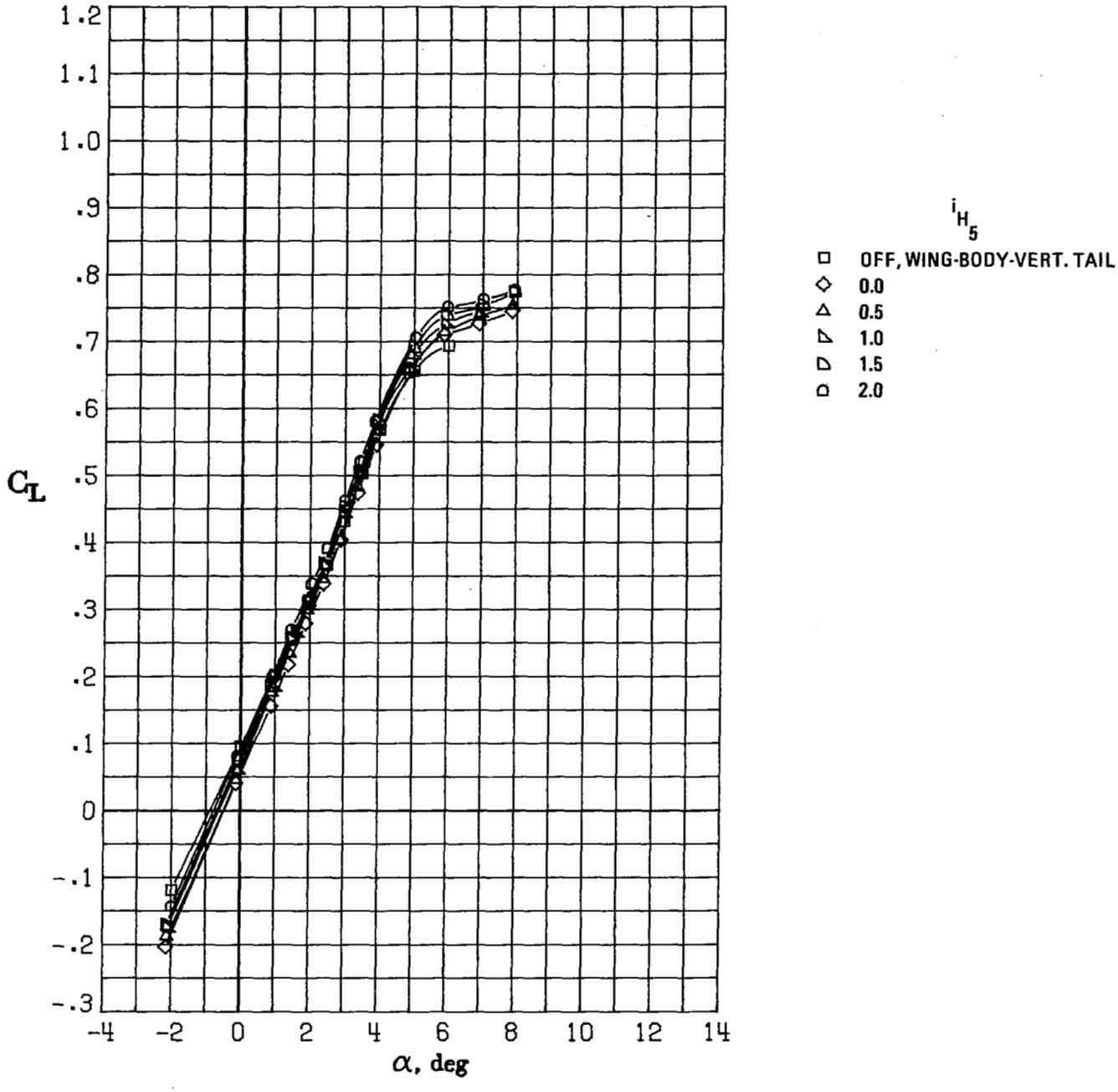

(e) H_5.

Figure 11.- Concluded.

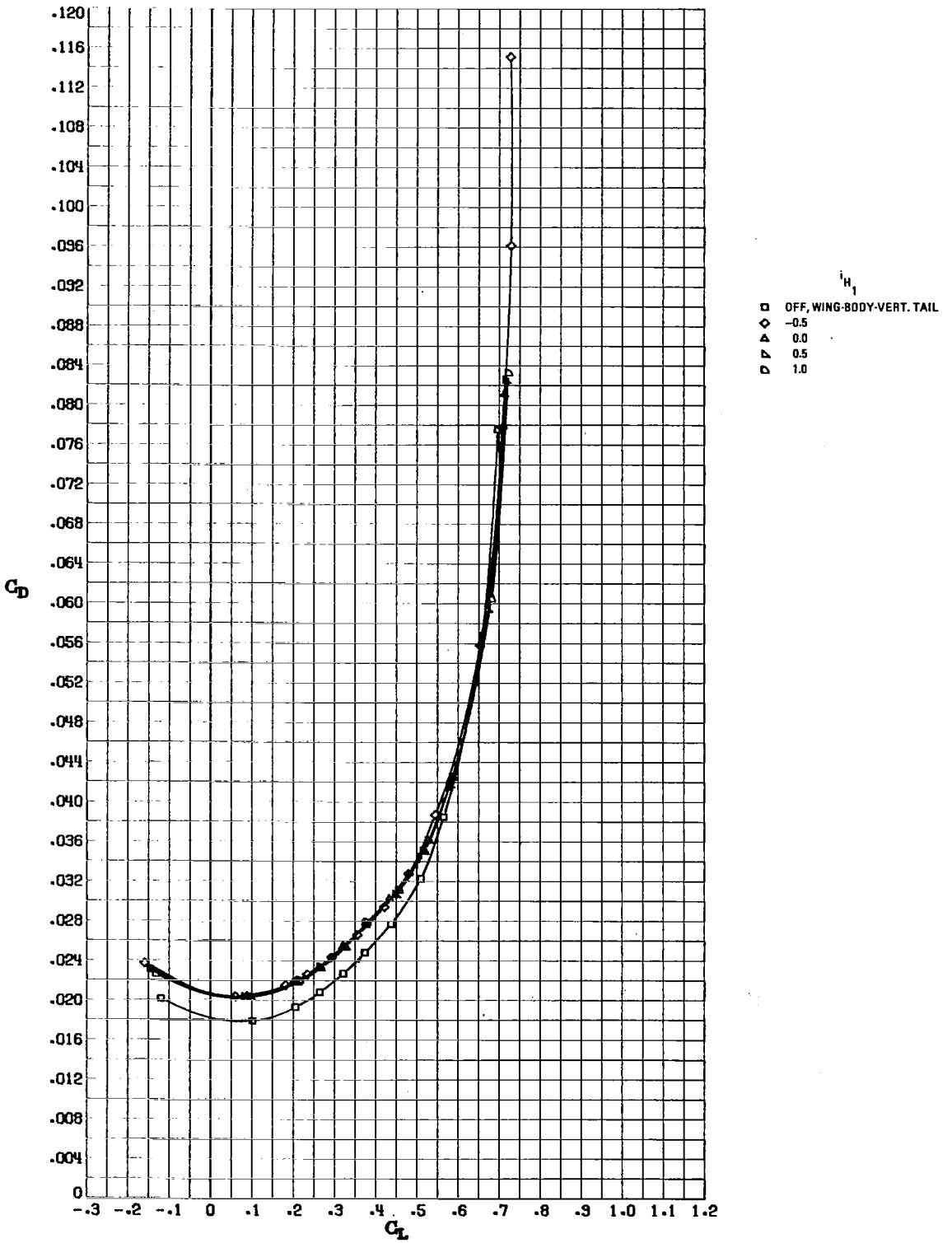

(a) H_1.

Figure 12.- Variation of drag coefficient with lift coefficient for wide-body wing configuration at $M_\infty = 0.82$.

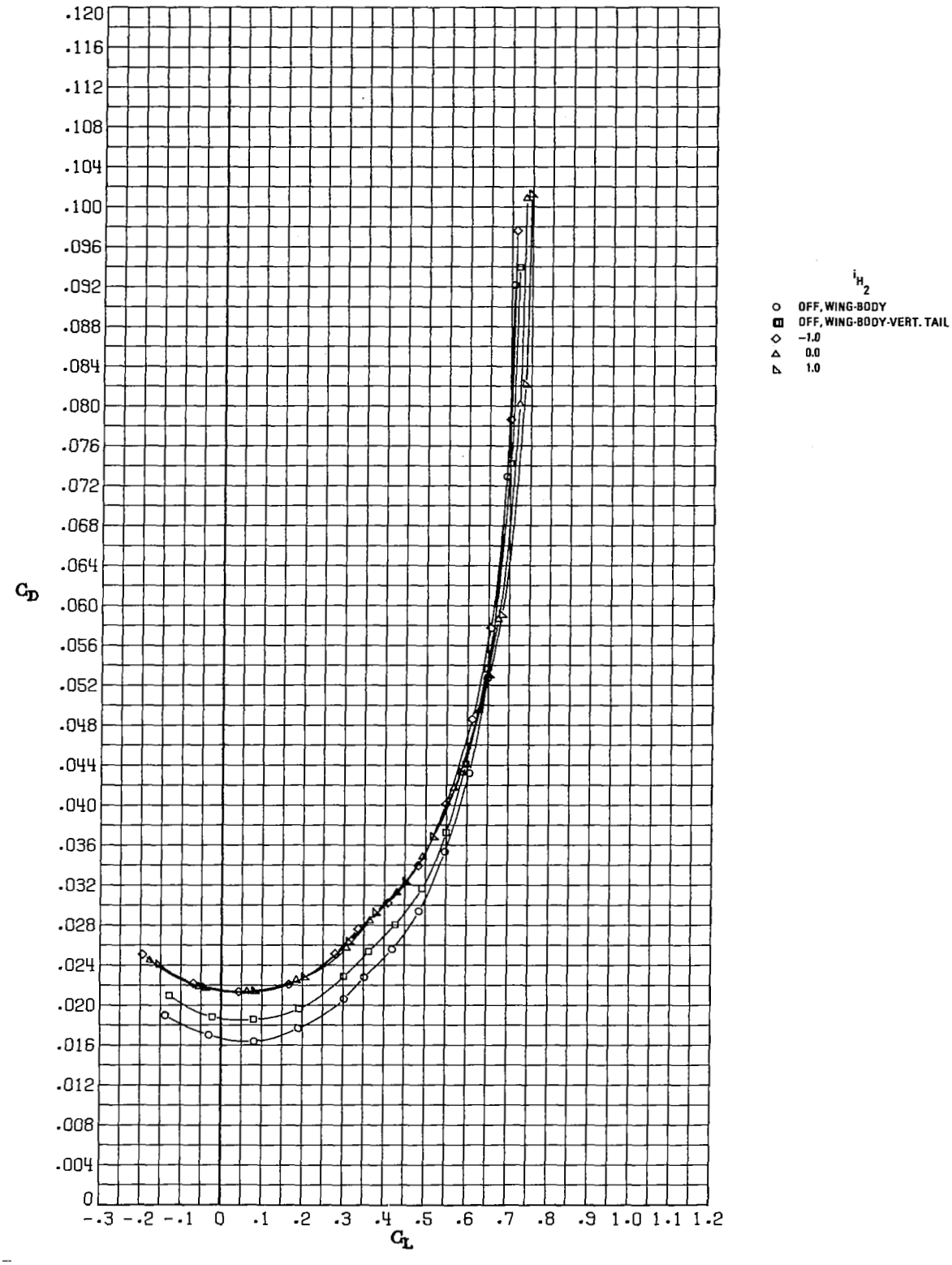

(b) H_2.

Figure 12.- Continued.

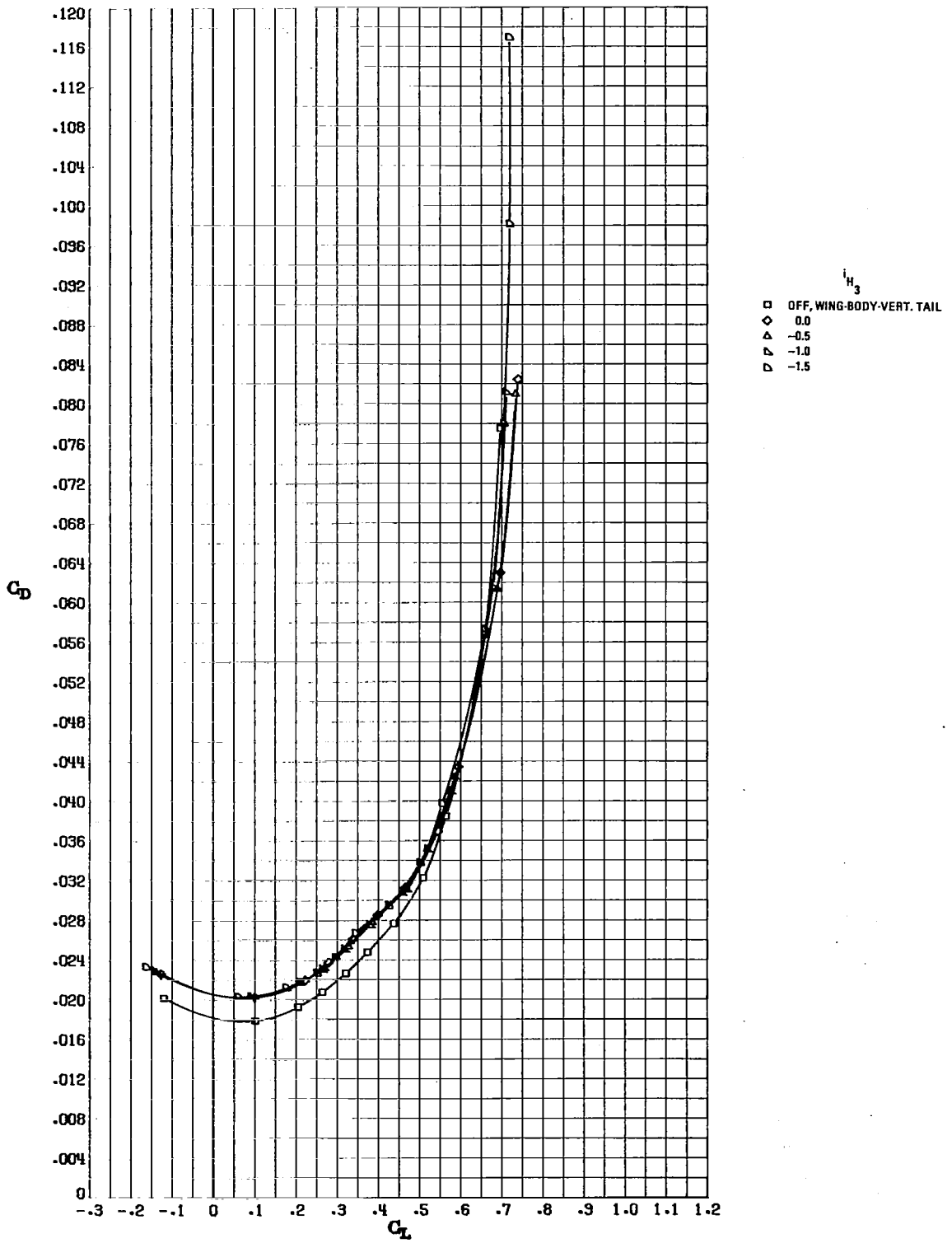

(c) H_3.

Figure 12.- Continued.

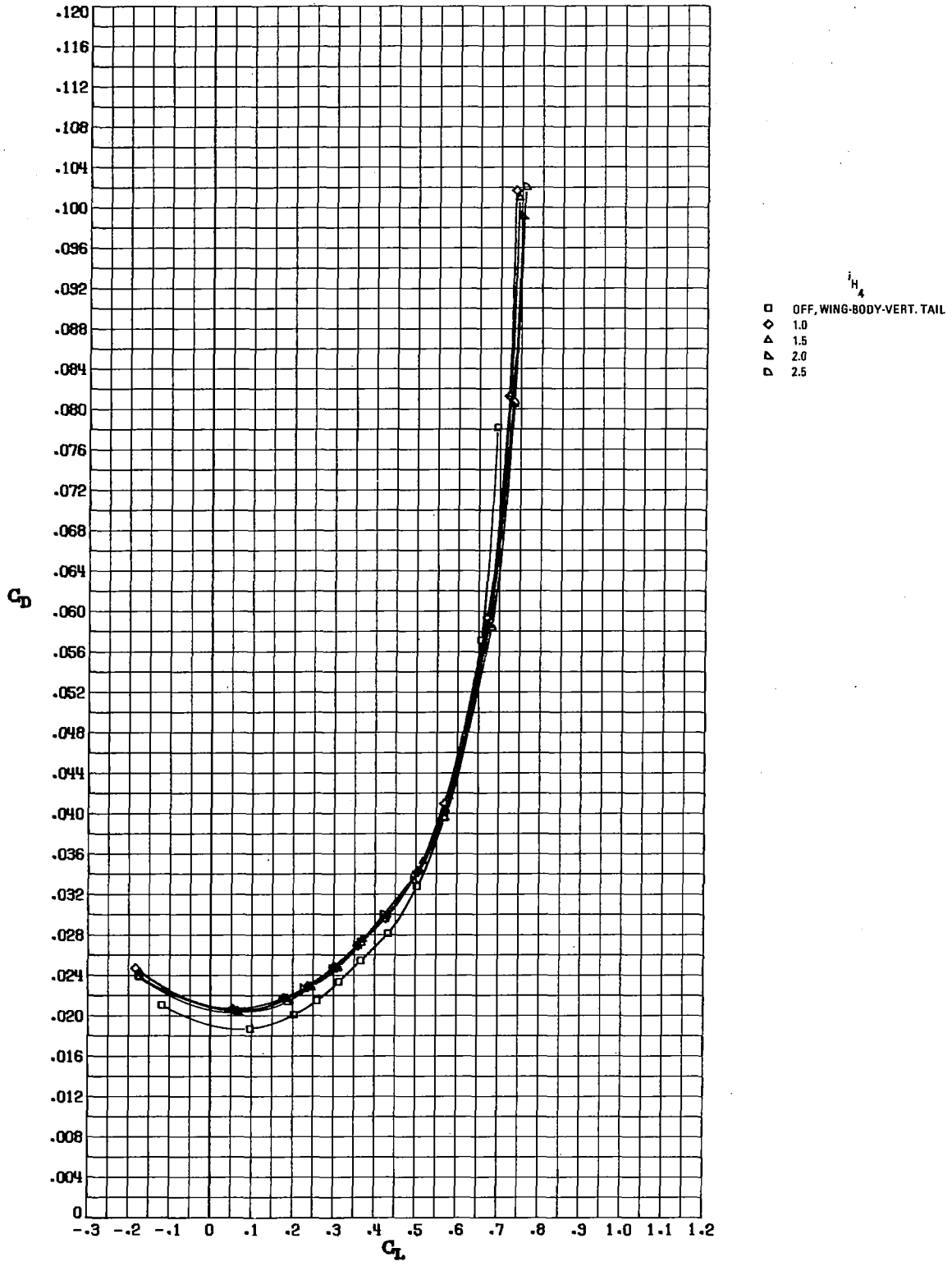

(d) H_4.

Figure 12.- Continued.

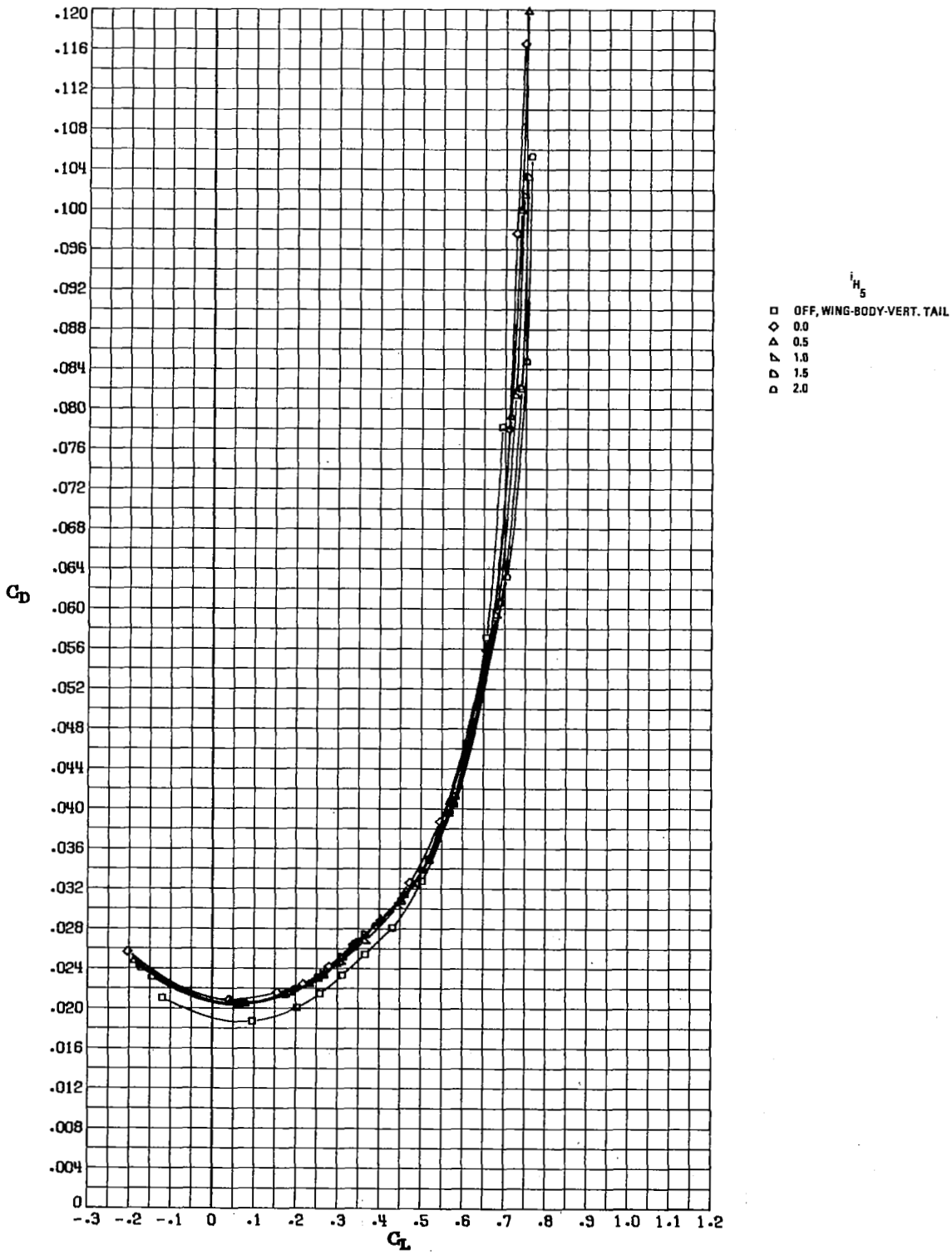

(e) H_5.

Figure 12.- Concluded.

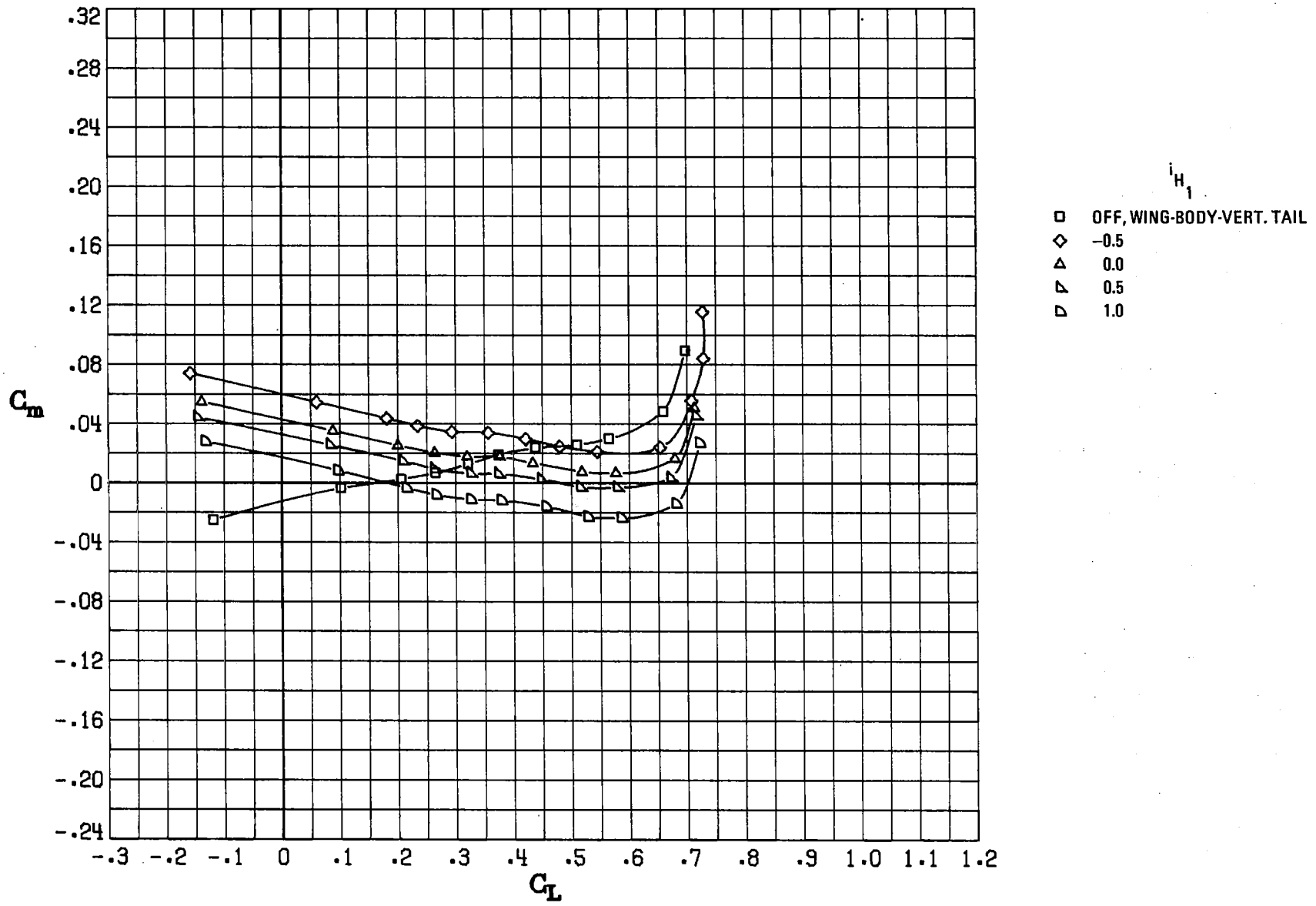

(a) H_1.

Figure 13.- Variation of pitching-moment coefficient with lift coefficient for wide-body wing configuration at $M_\infty = 0.82$ with c.g. = $0.35\bar{c}$.

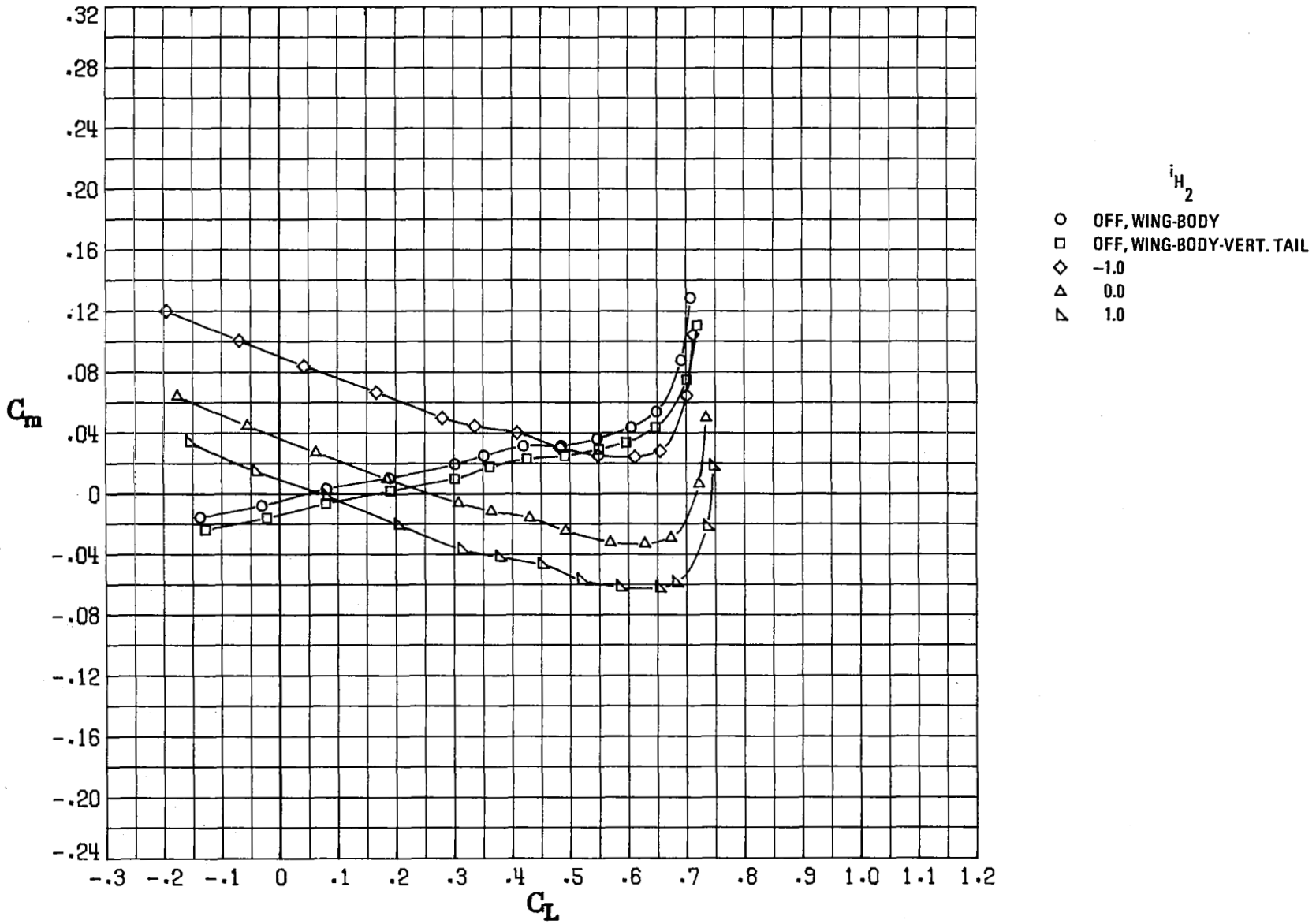

(b) H_2.

Figure 13.- Continued.

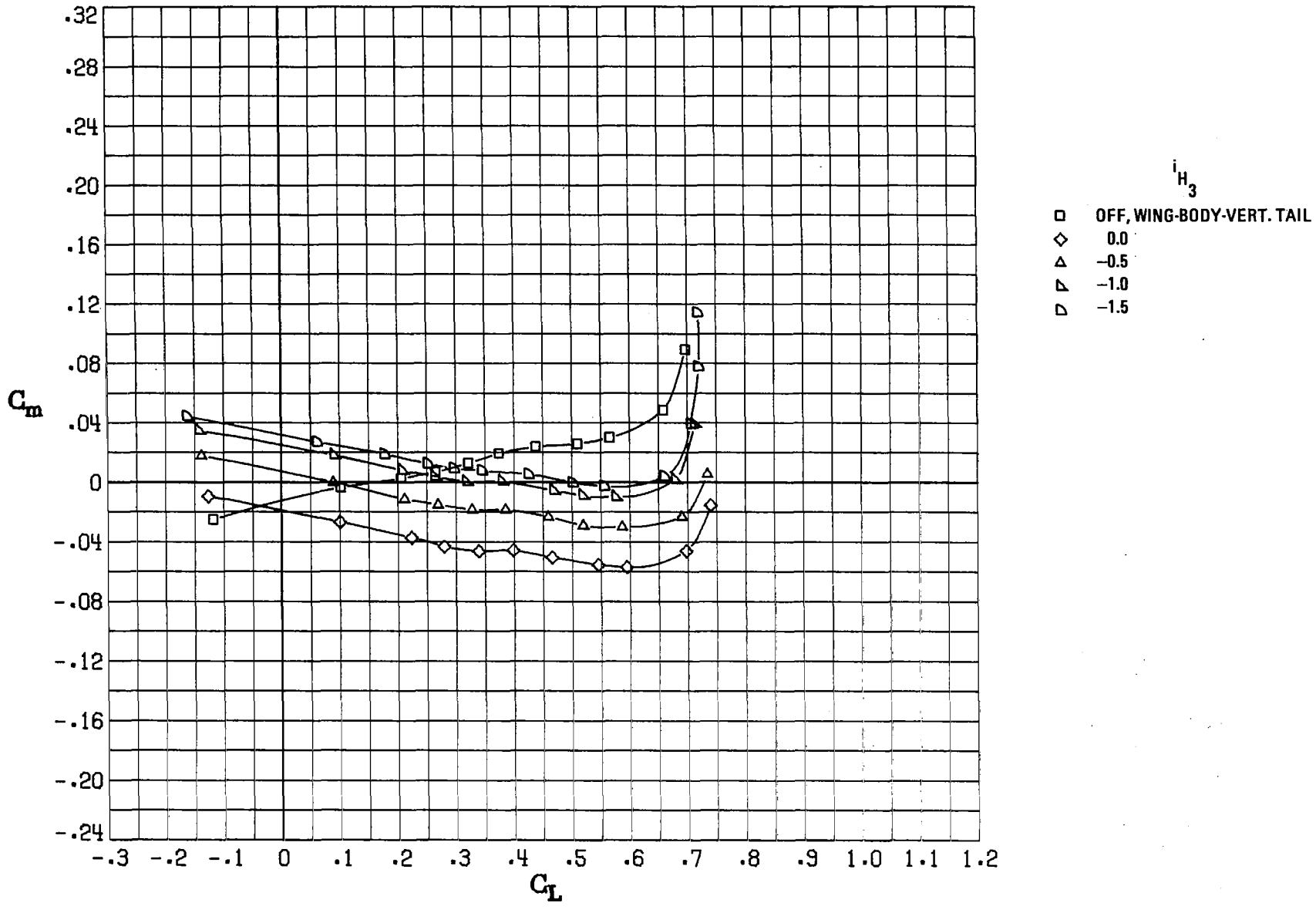

(c) H_3.

Figure 13.- Continued.

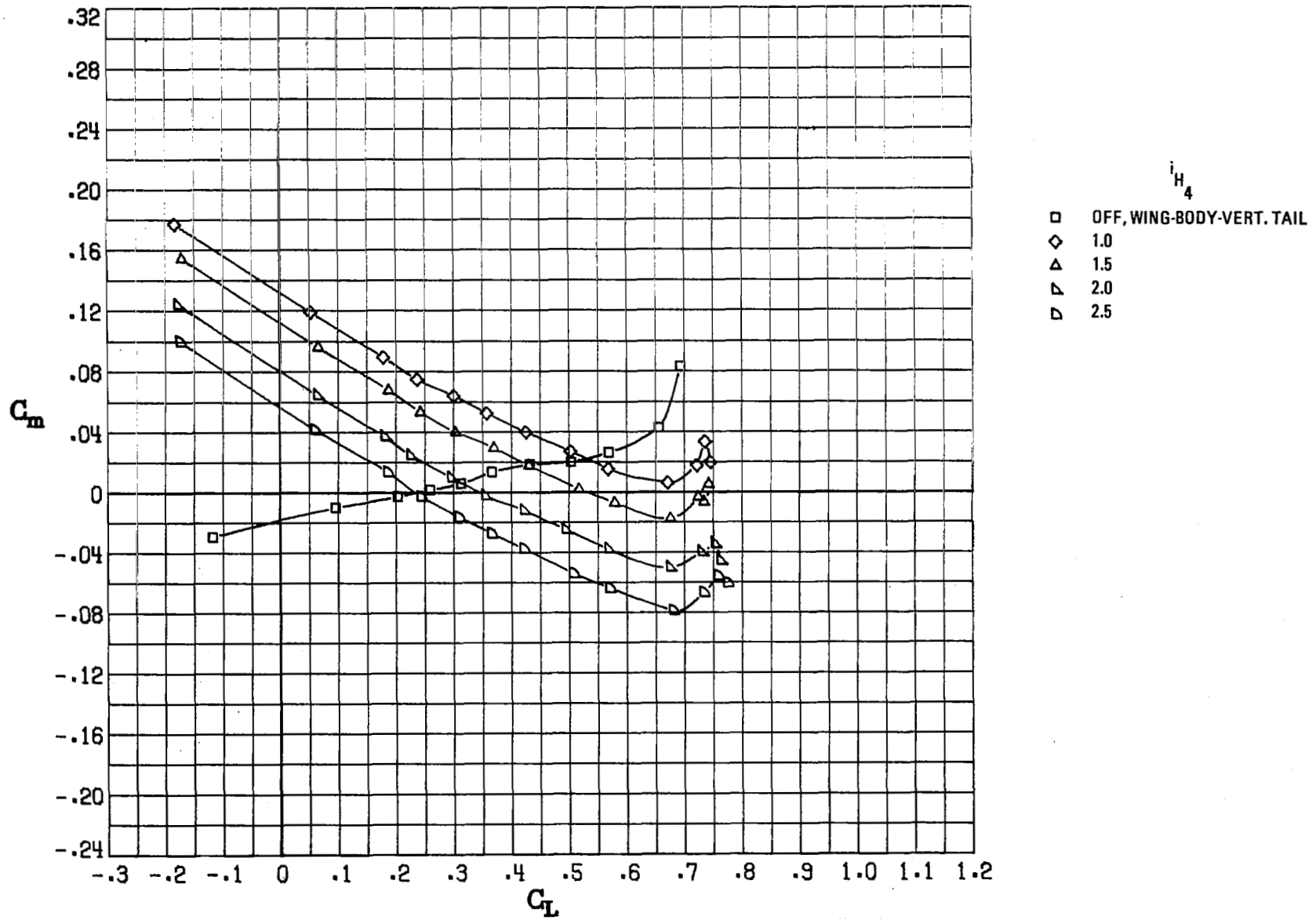

(d) H_4.

Figure 13.- Continued.

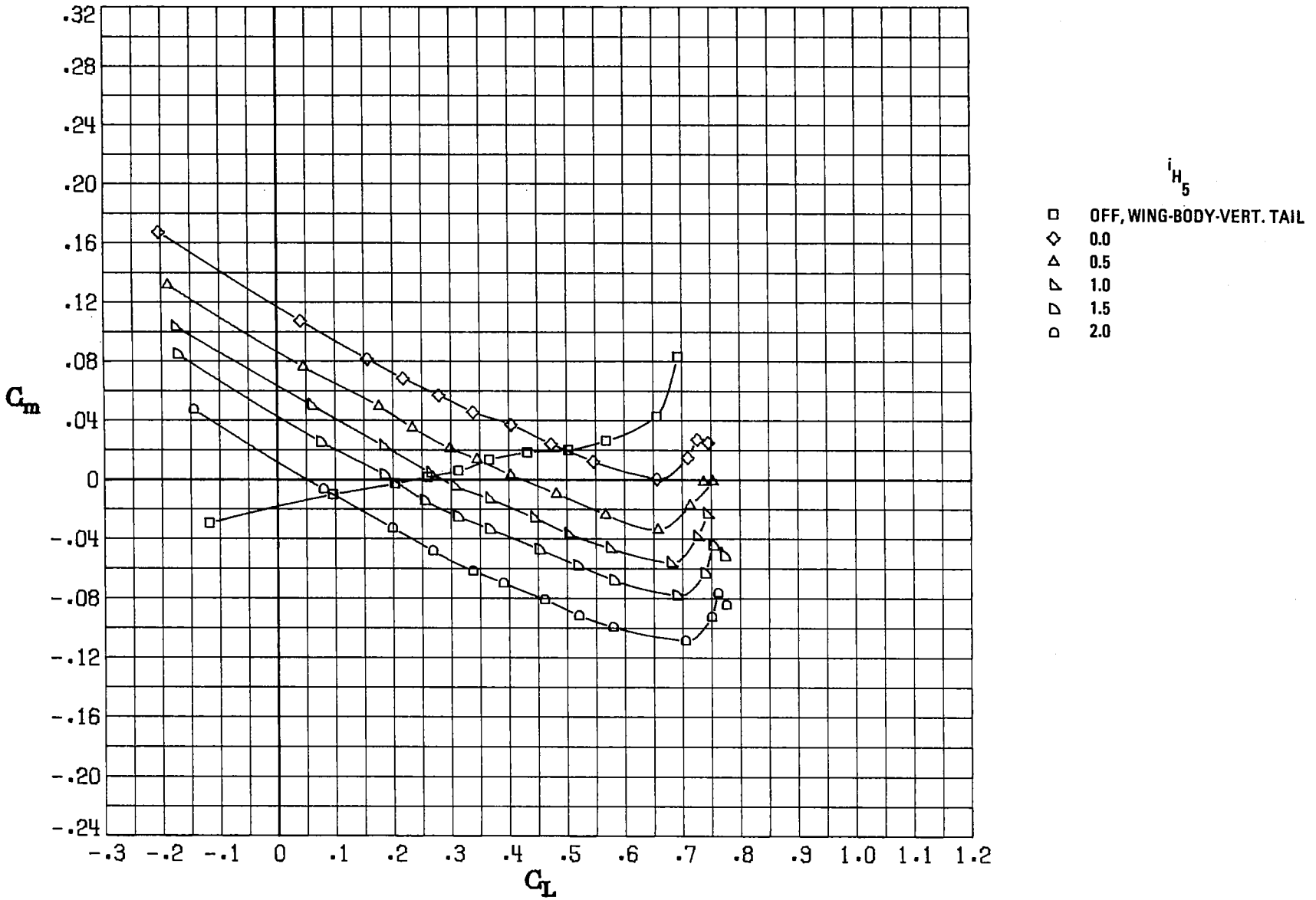

(e) H_5.

Figure 13.- Concluded.

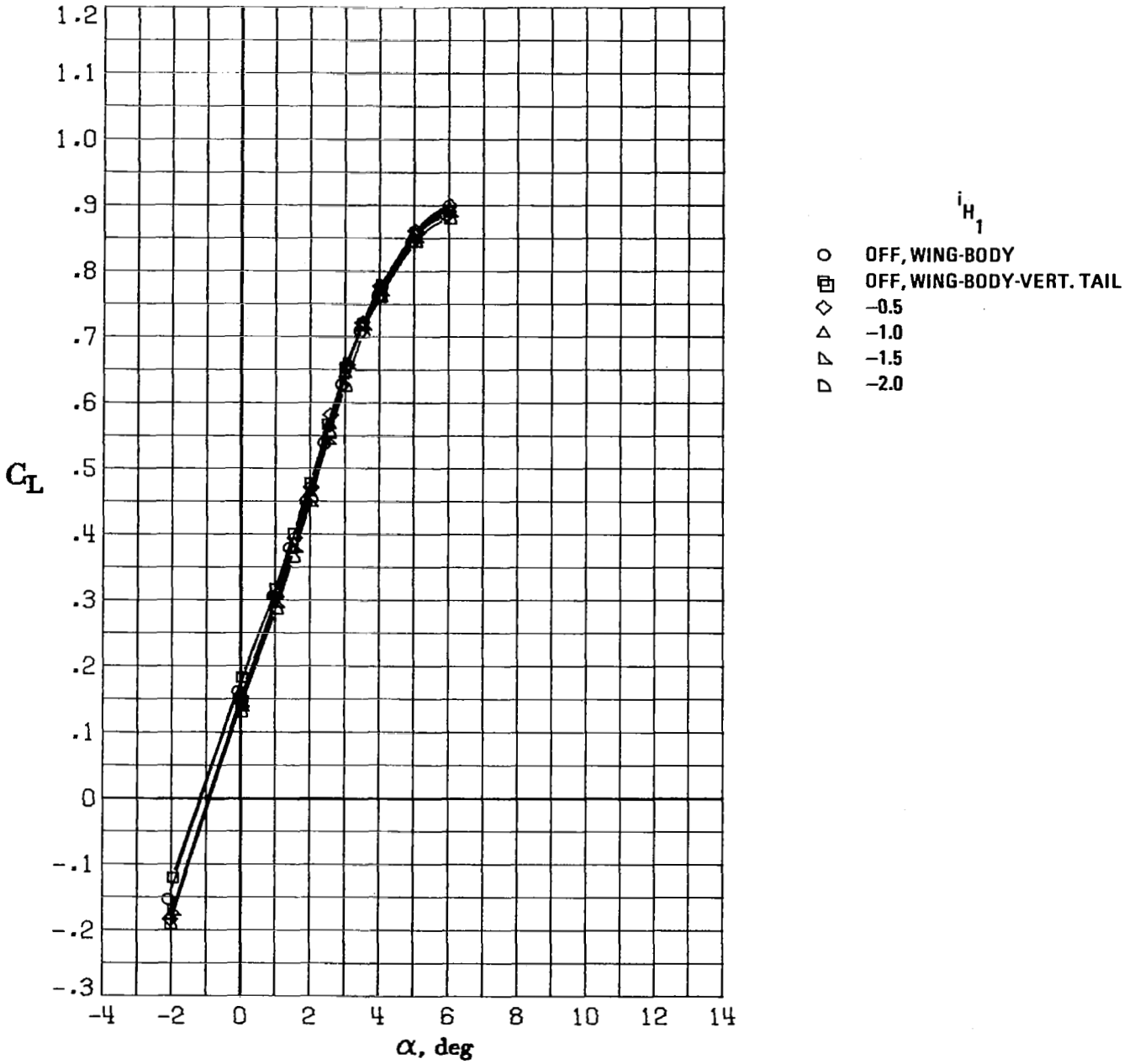

(a) H_1.

Figure 14.- Variation of lift coefficient with angle of attack for supercritical wing configuration at $M_\infty = 0.82$.

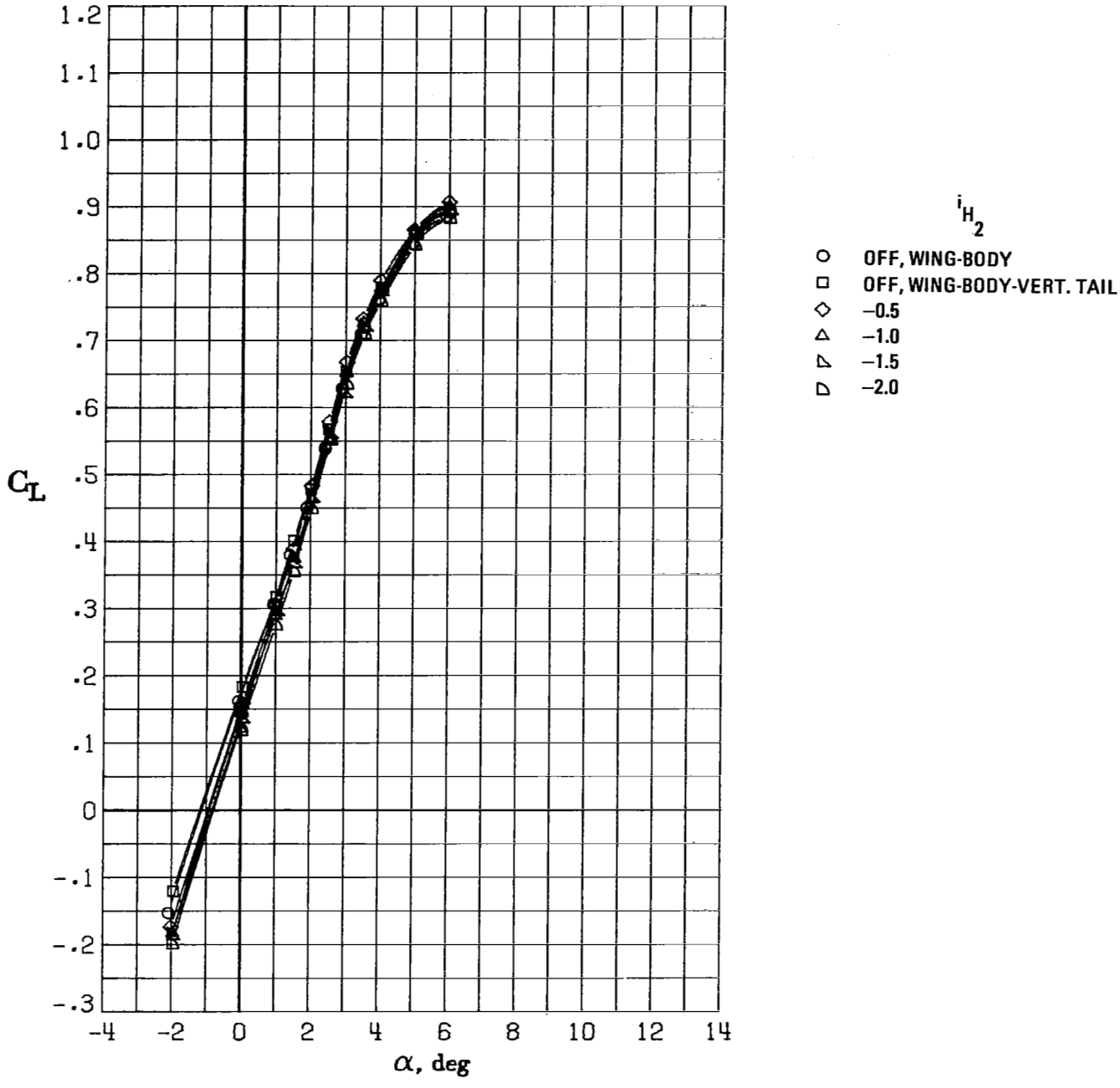

(b) H_2.

Figure 14.- Continued.

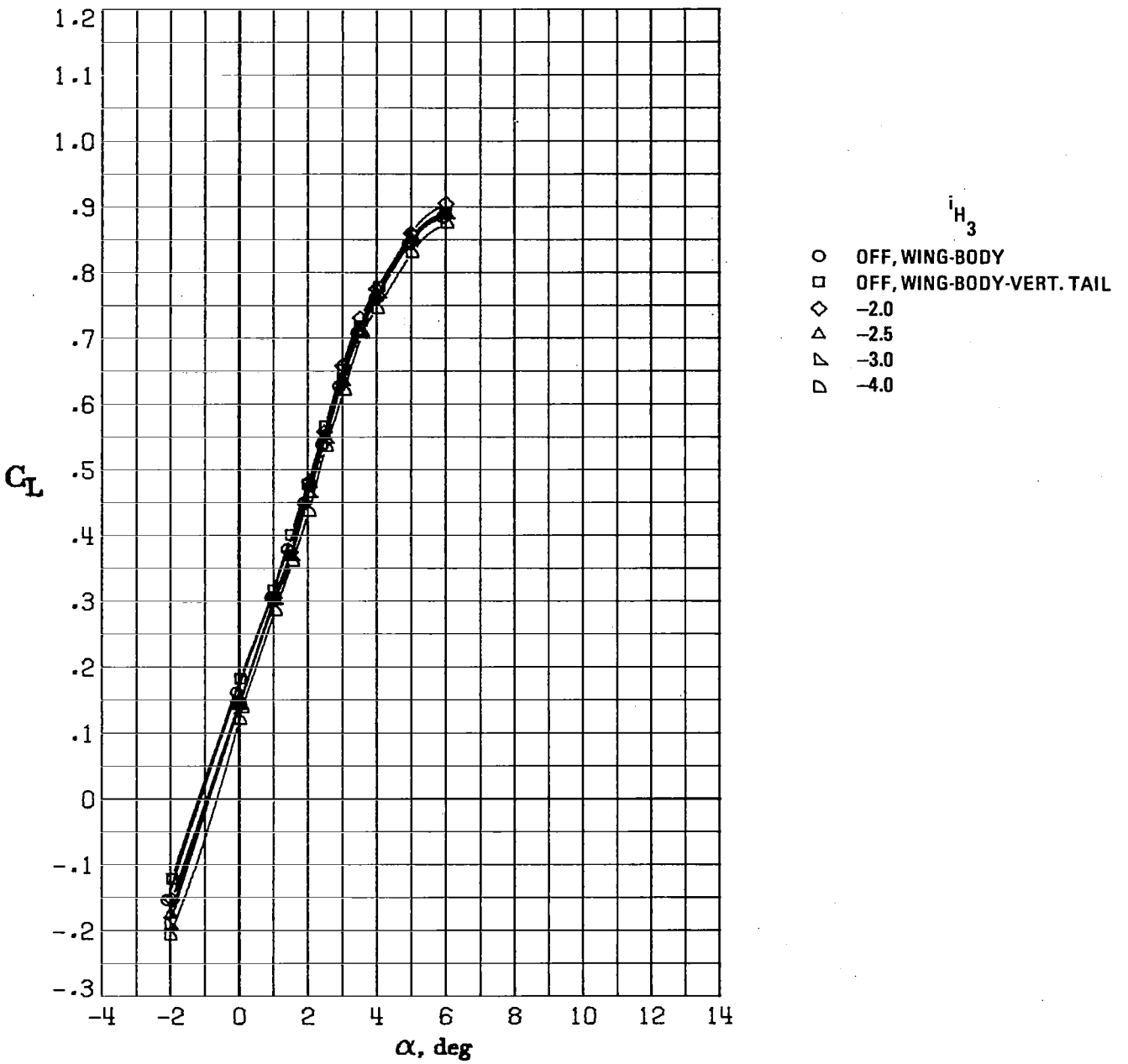

(c) H_3.

Figure 14.- Continued.

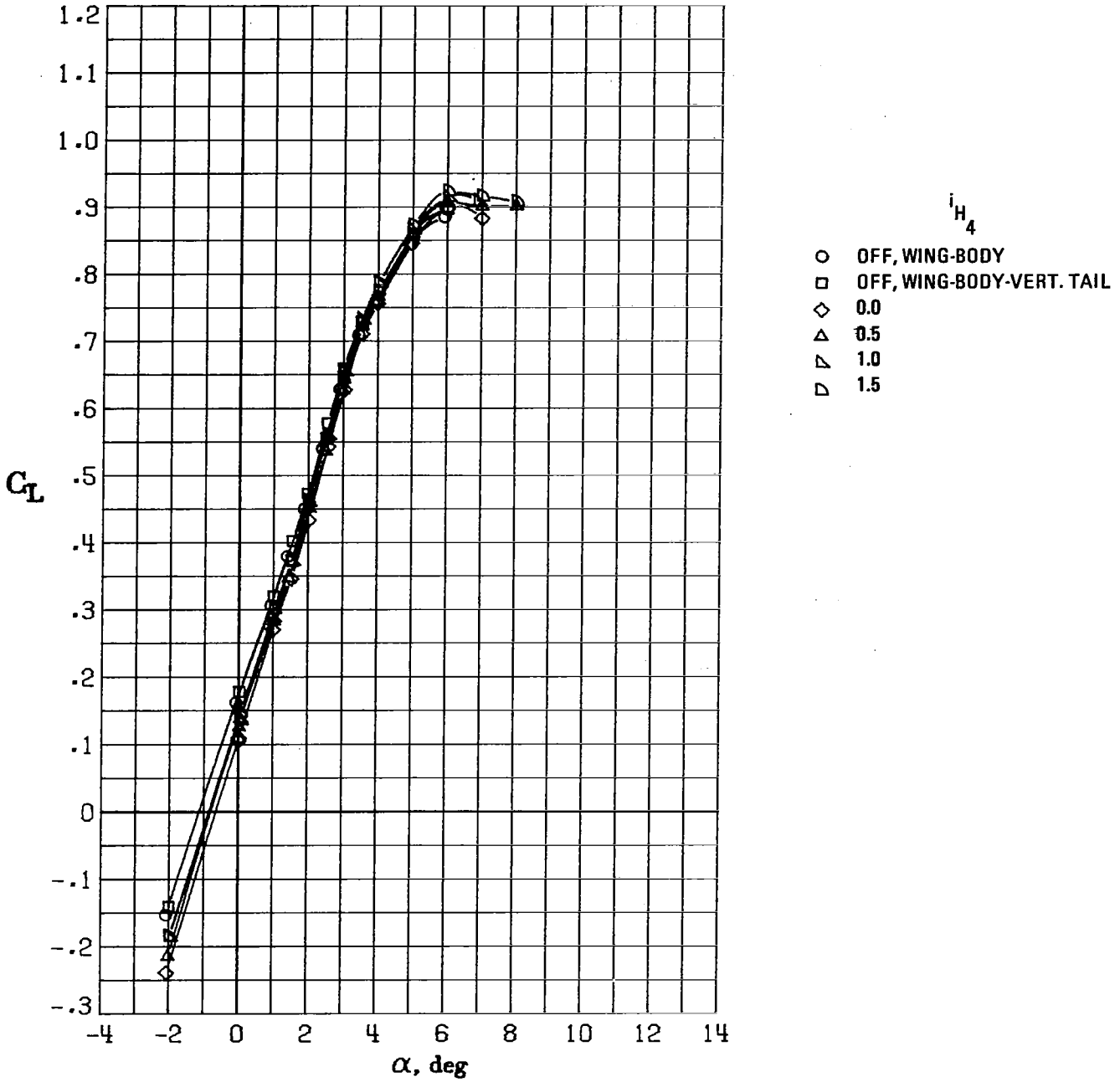

(d) H_4.

Figure 14.- Continued.

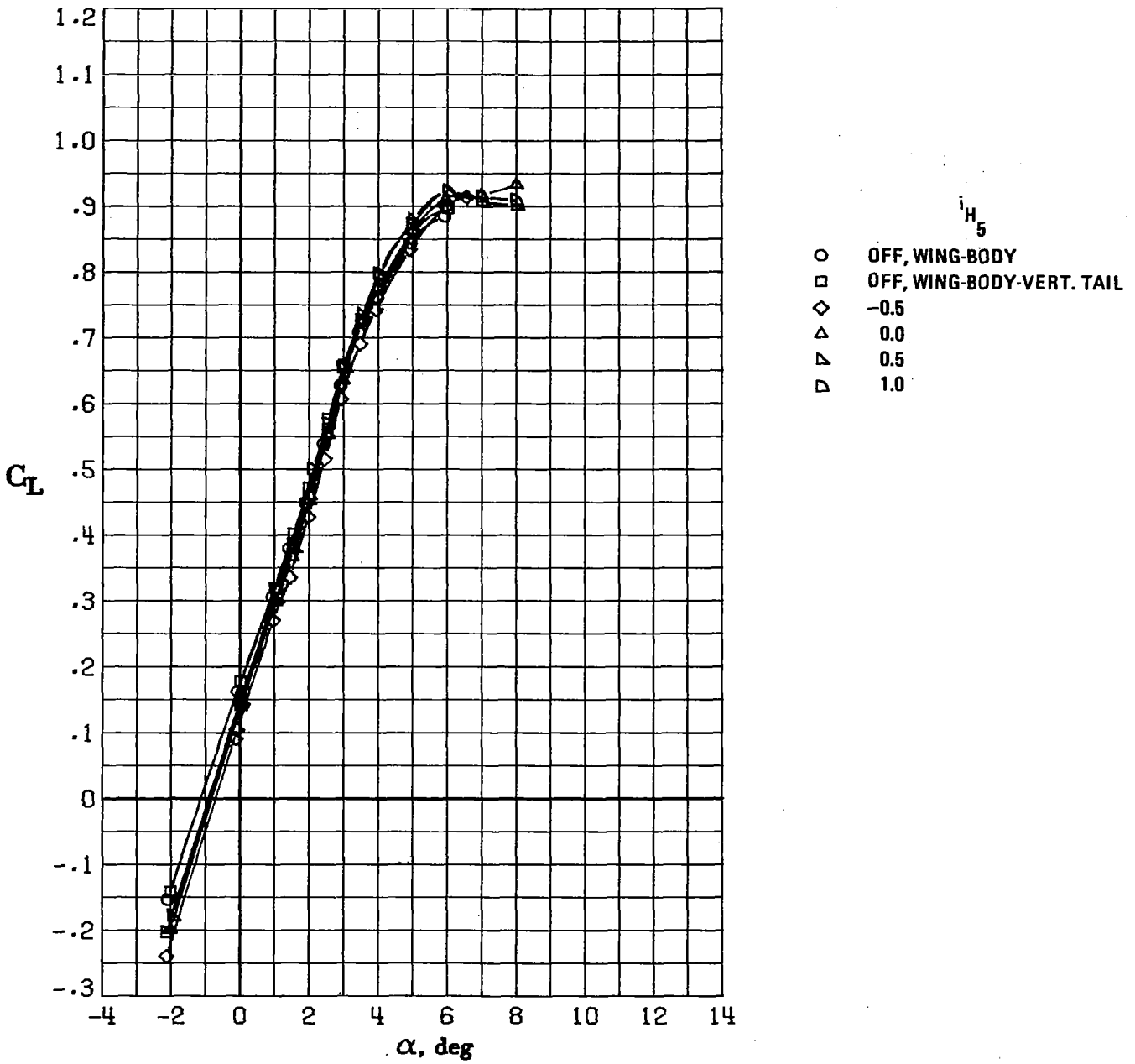

(e) H_5.

Figure 14.- Concluded.

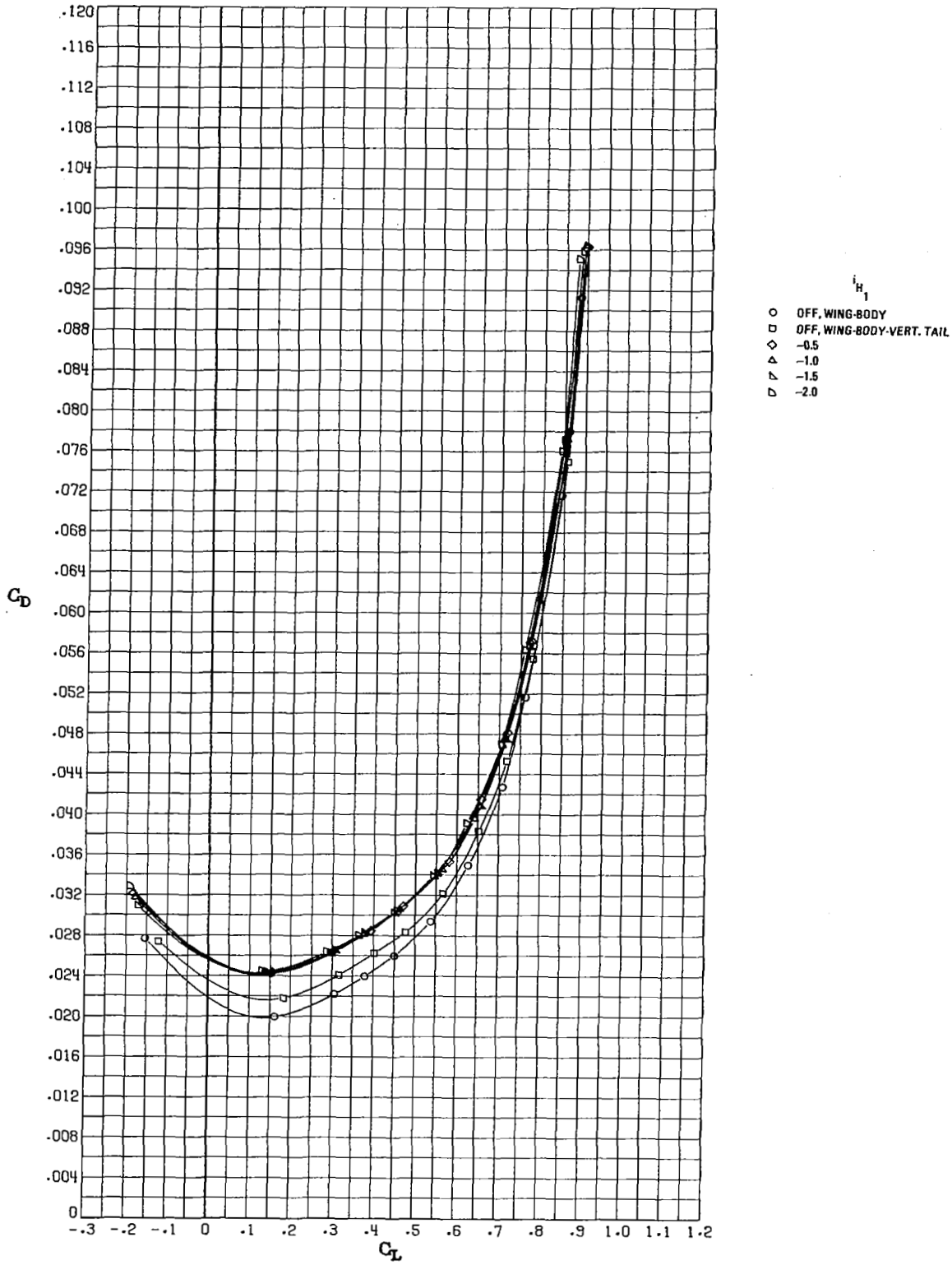

(a) H_1.

Figure 15.- Variation of drag coefficient with lift coefficient for supercritical wing configuration at $M_\infty = 0.82$.

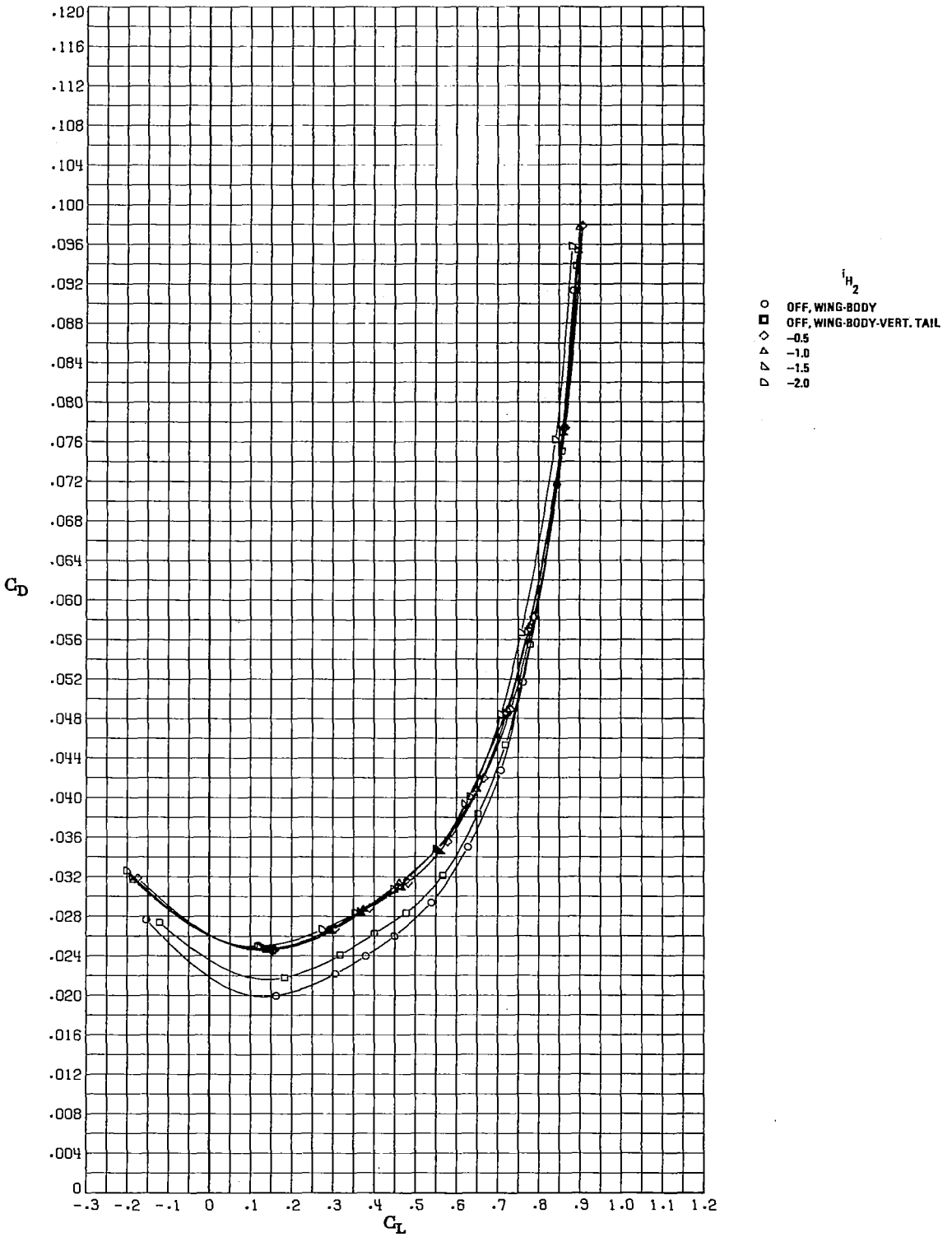

(b) H_2.

Figure 15.- Continued.

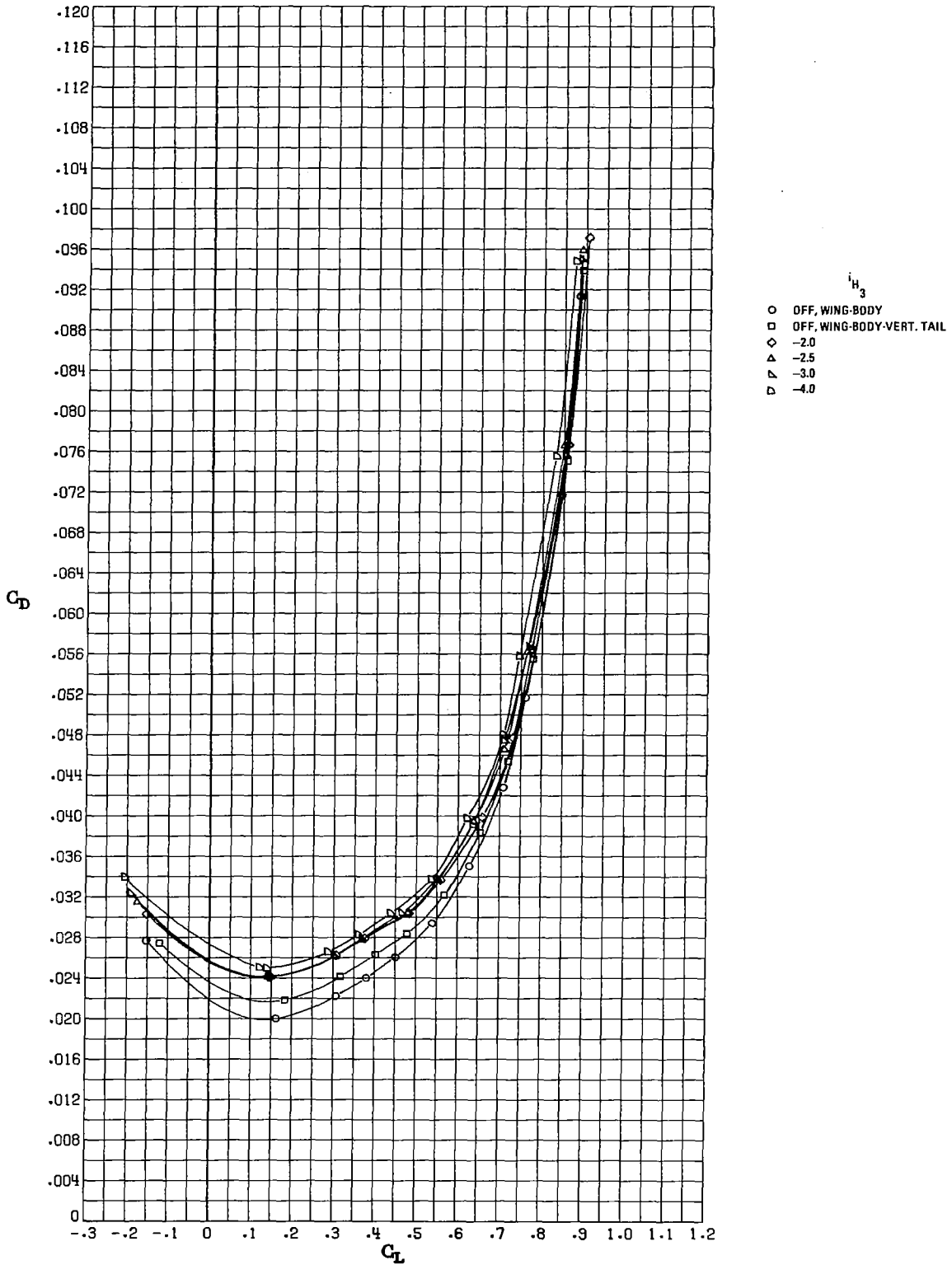

(c) H_3.

Figure 15.- Continued.

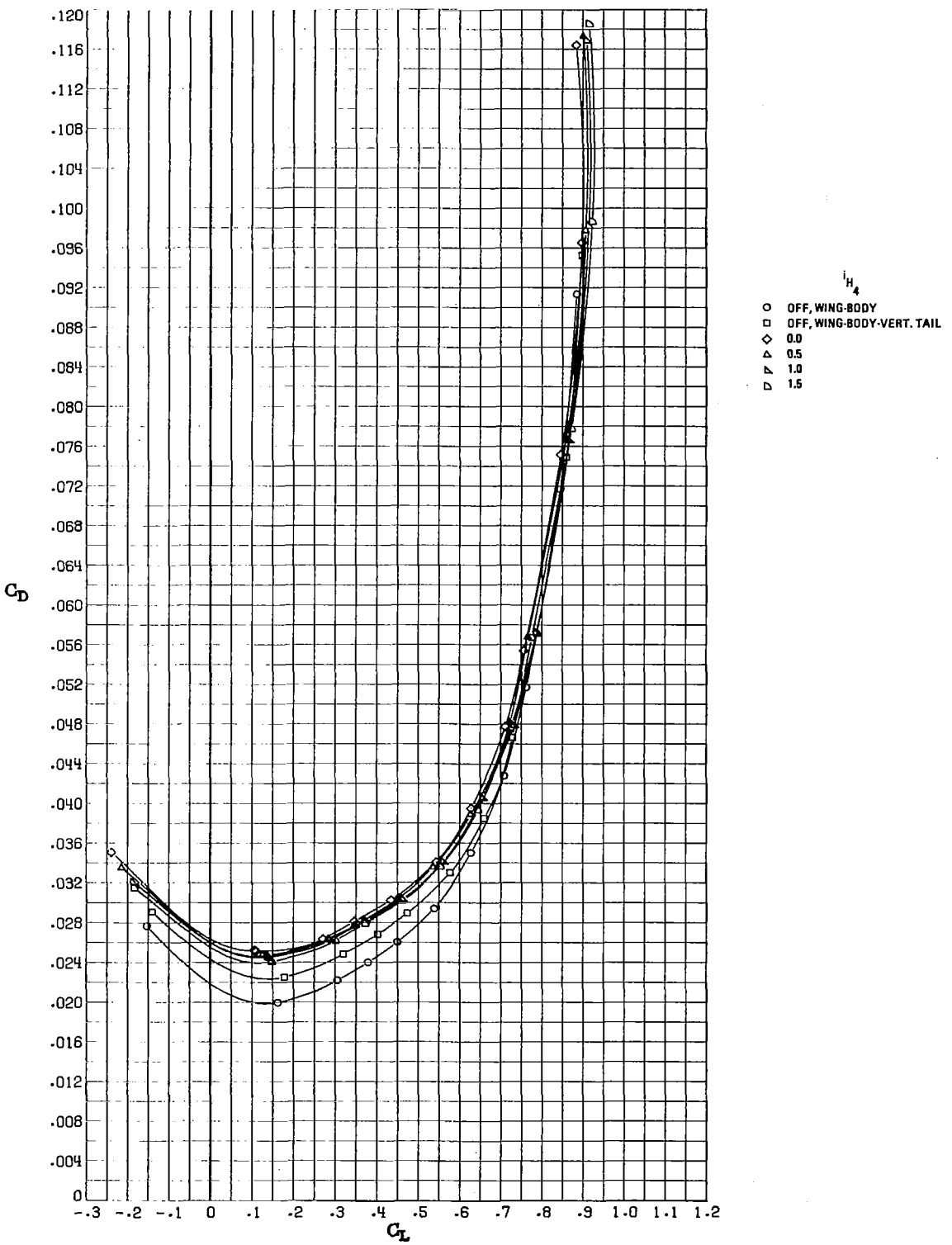

(d) H_4.

Figure 15.- Continued.

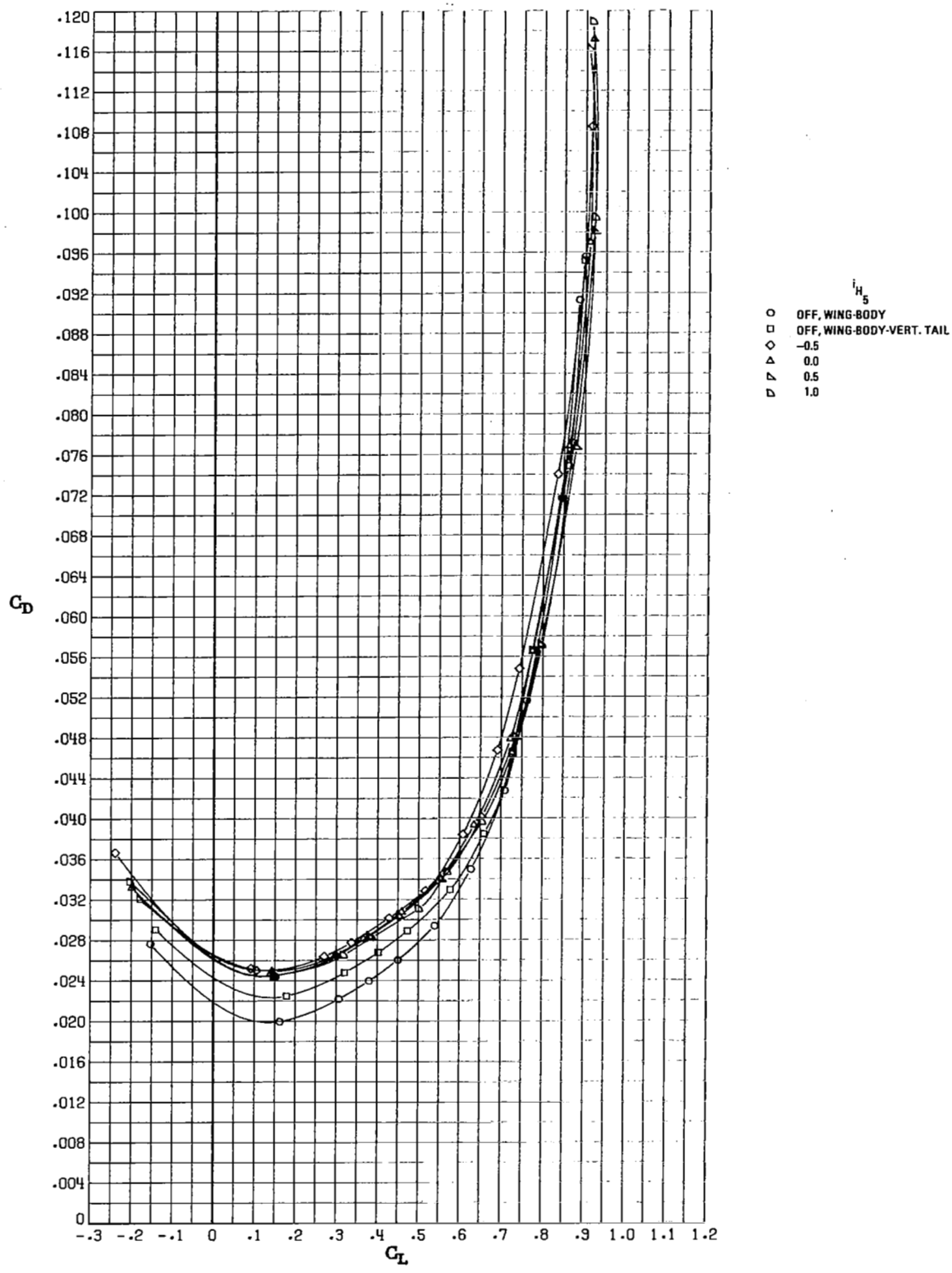

(e) H_5.

Figure 15.- Concluded.

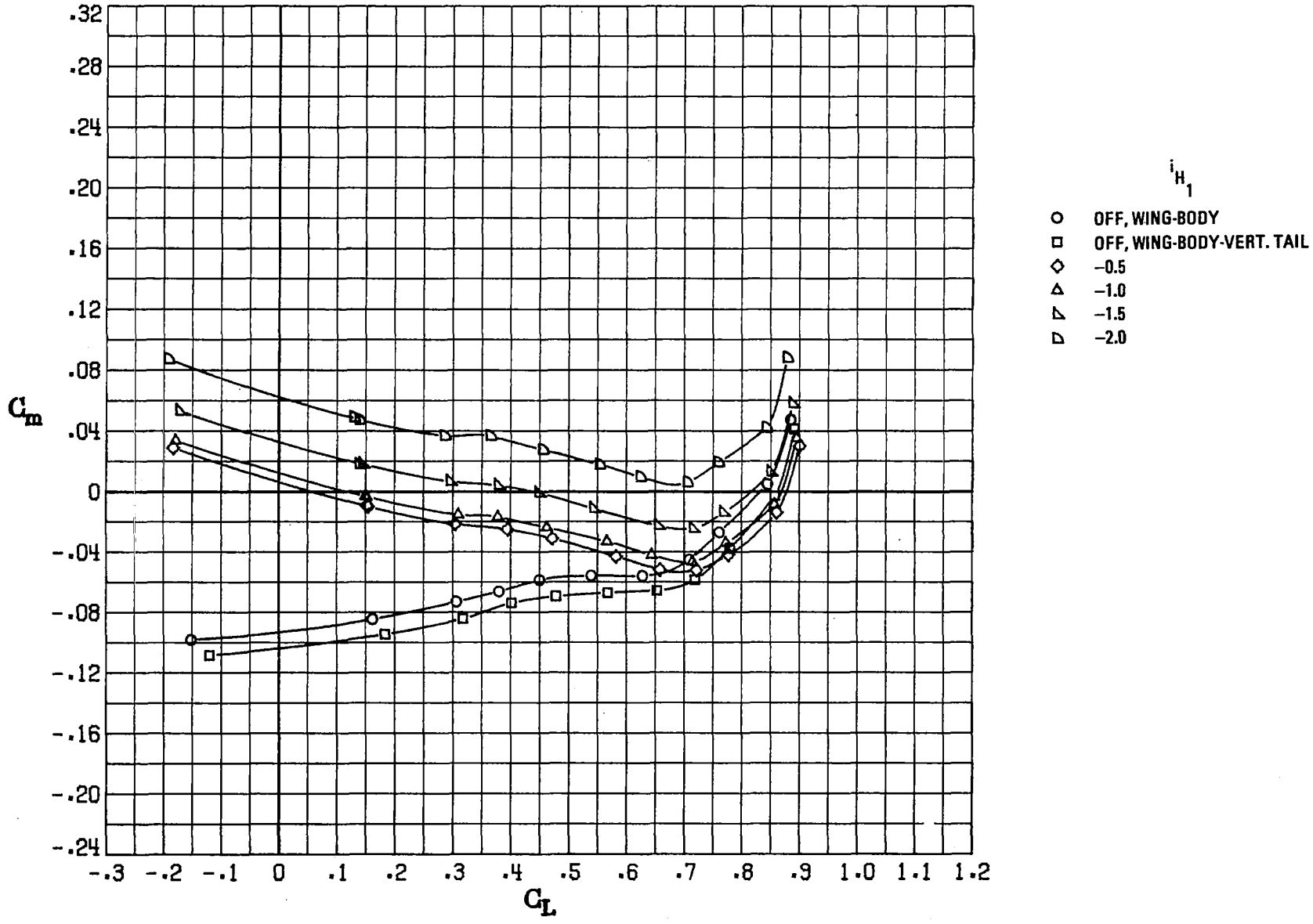

(a) H_1.

Figure 16.- Variation of pitching-moment coefficient with lift coefficient for supercritical wing configuration at $M_\infty = 0.82$ with c.g. = $0.33\bar{c}$.

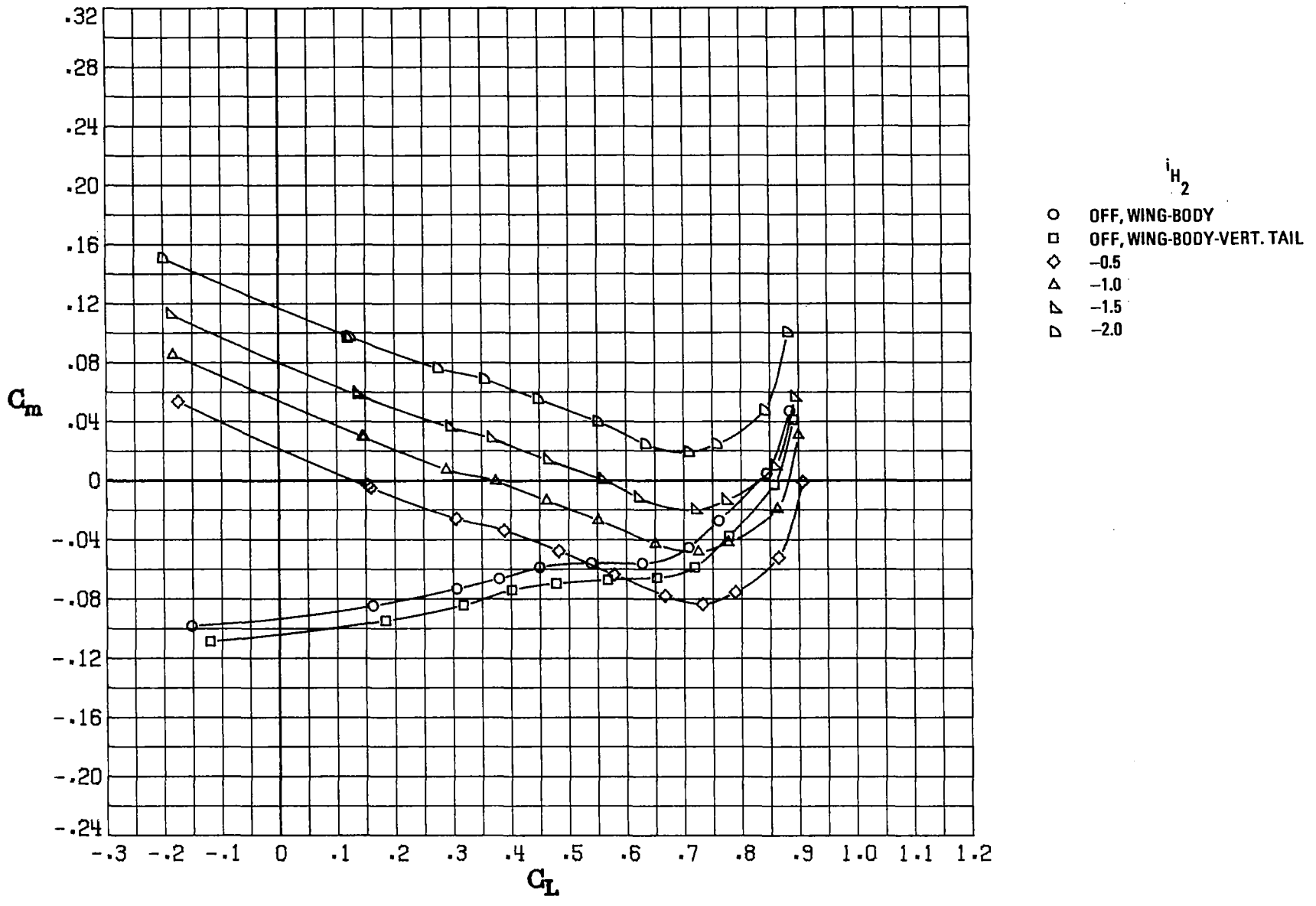

(b) H_2.

Figure 16.- Continued.

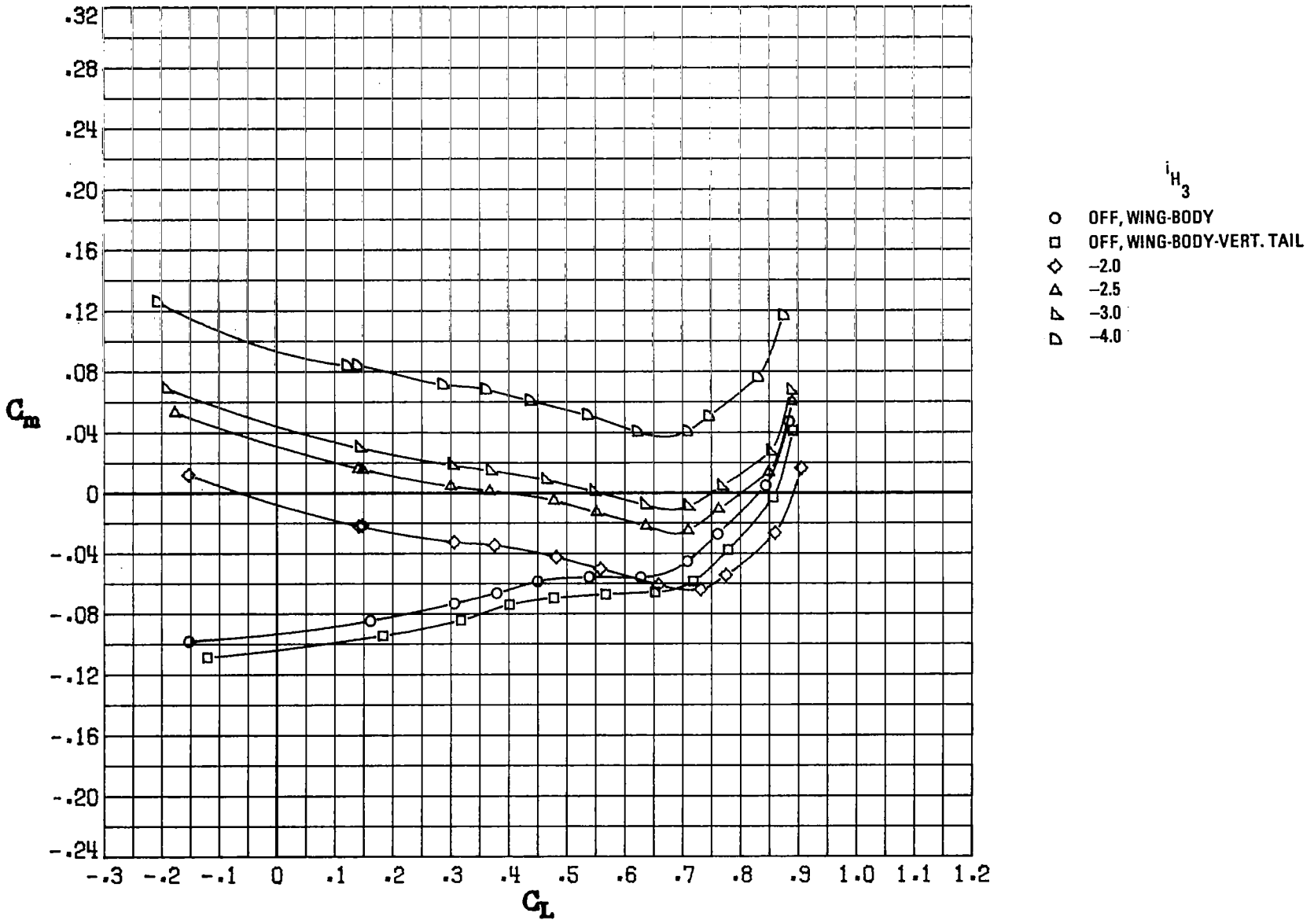

(c) H_3.

Figure 16.- Continued.

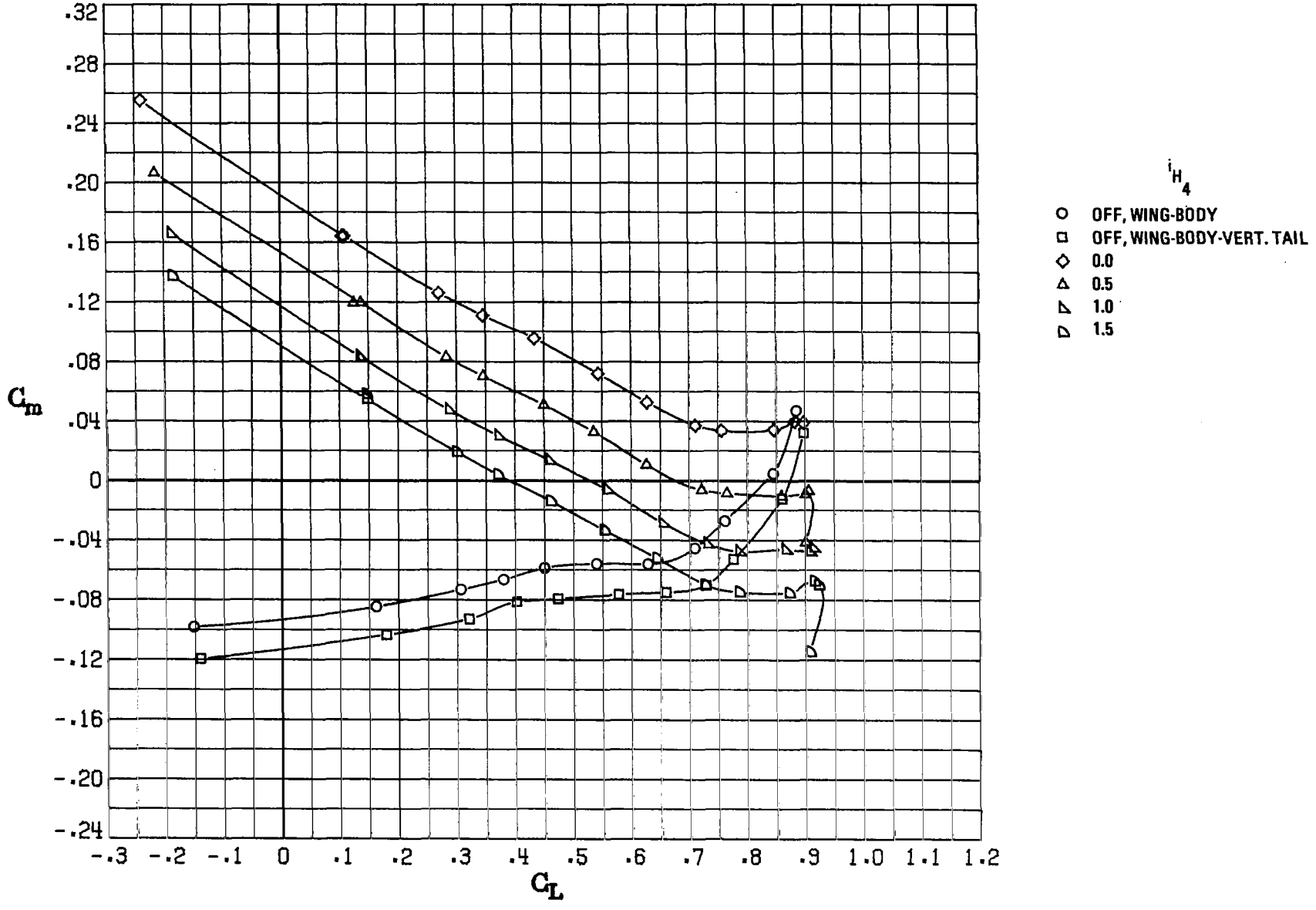

(d) H_4.

Figure 16.- Continued.

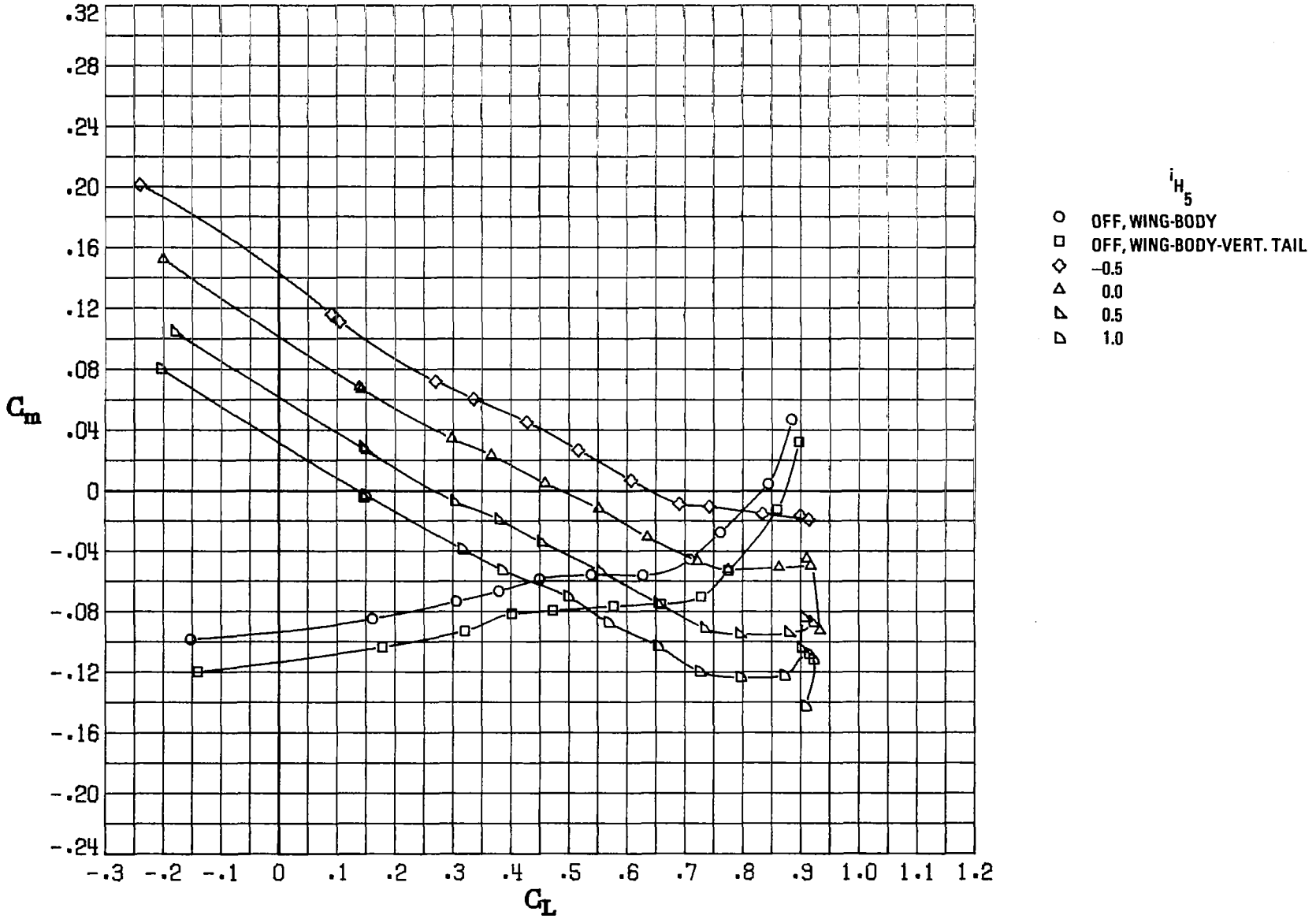

(e) H_5.

Figure 16.- Concluded.

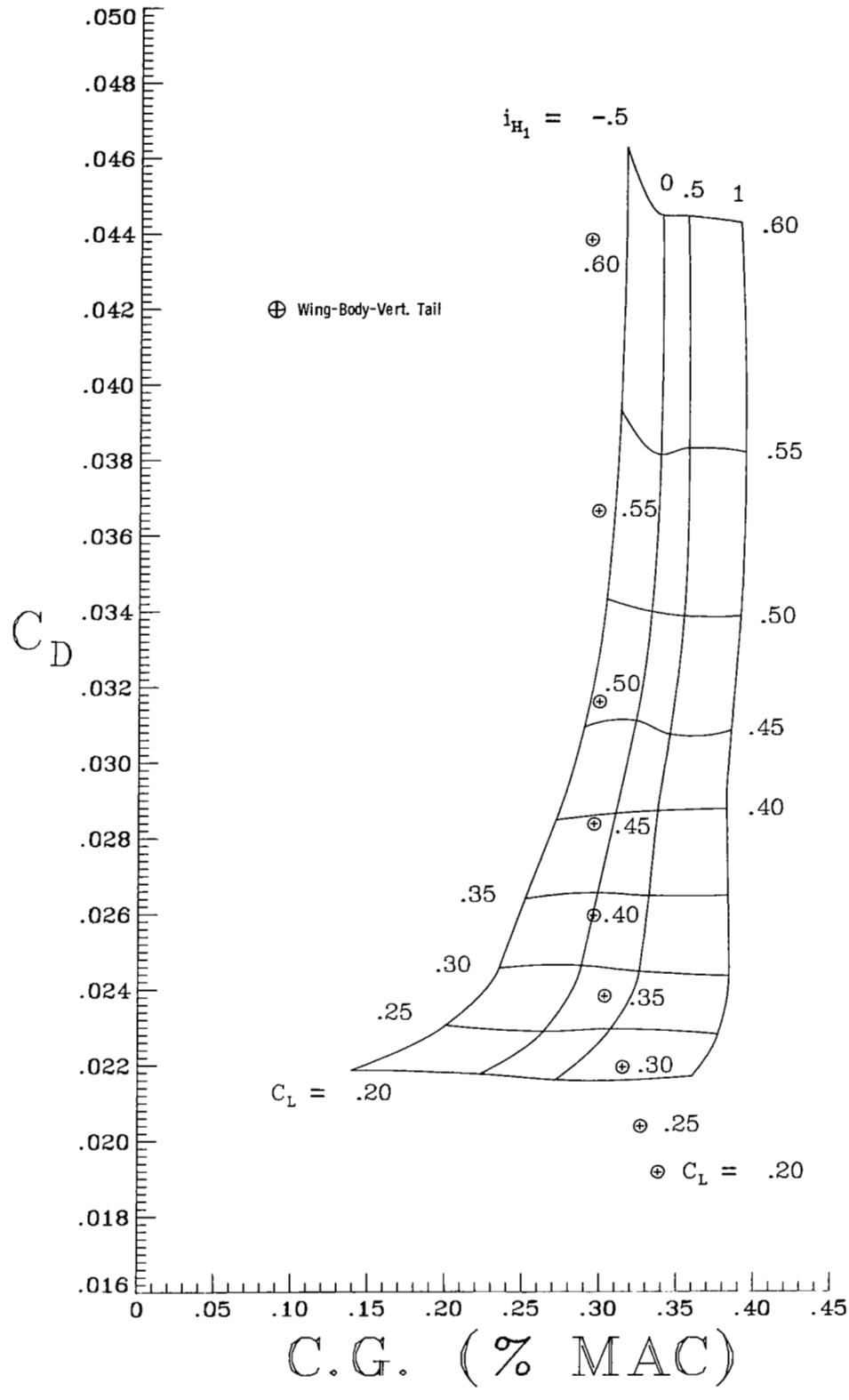

(a) H_1.

Figure 17.- Variation of trimmed drag coefficient with c.g. position for wide-body wing configuration at M_∞ = 0.82.

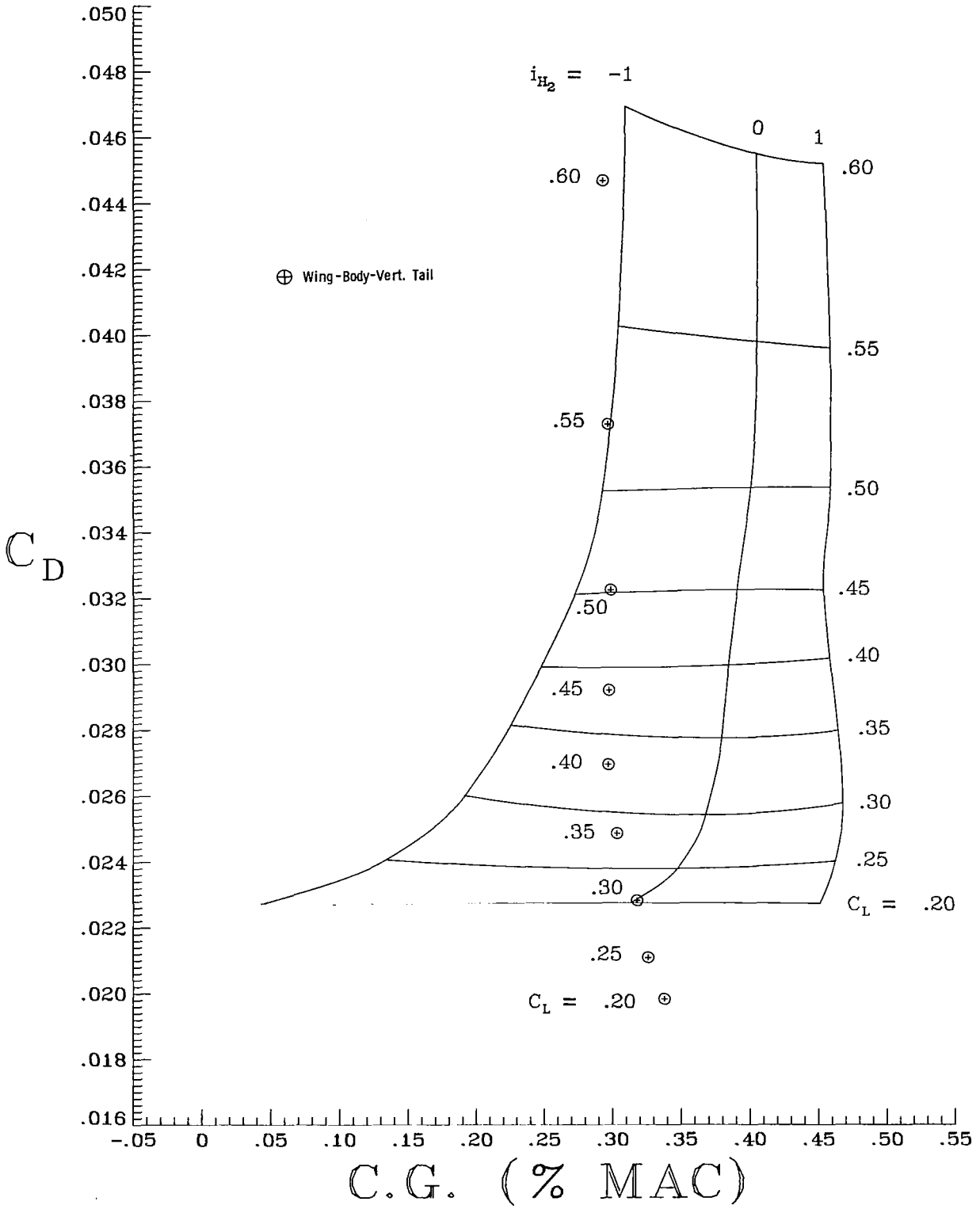

(b) H_2.

Figure 17.- Continued.

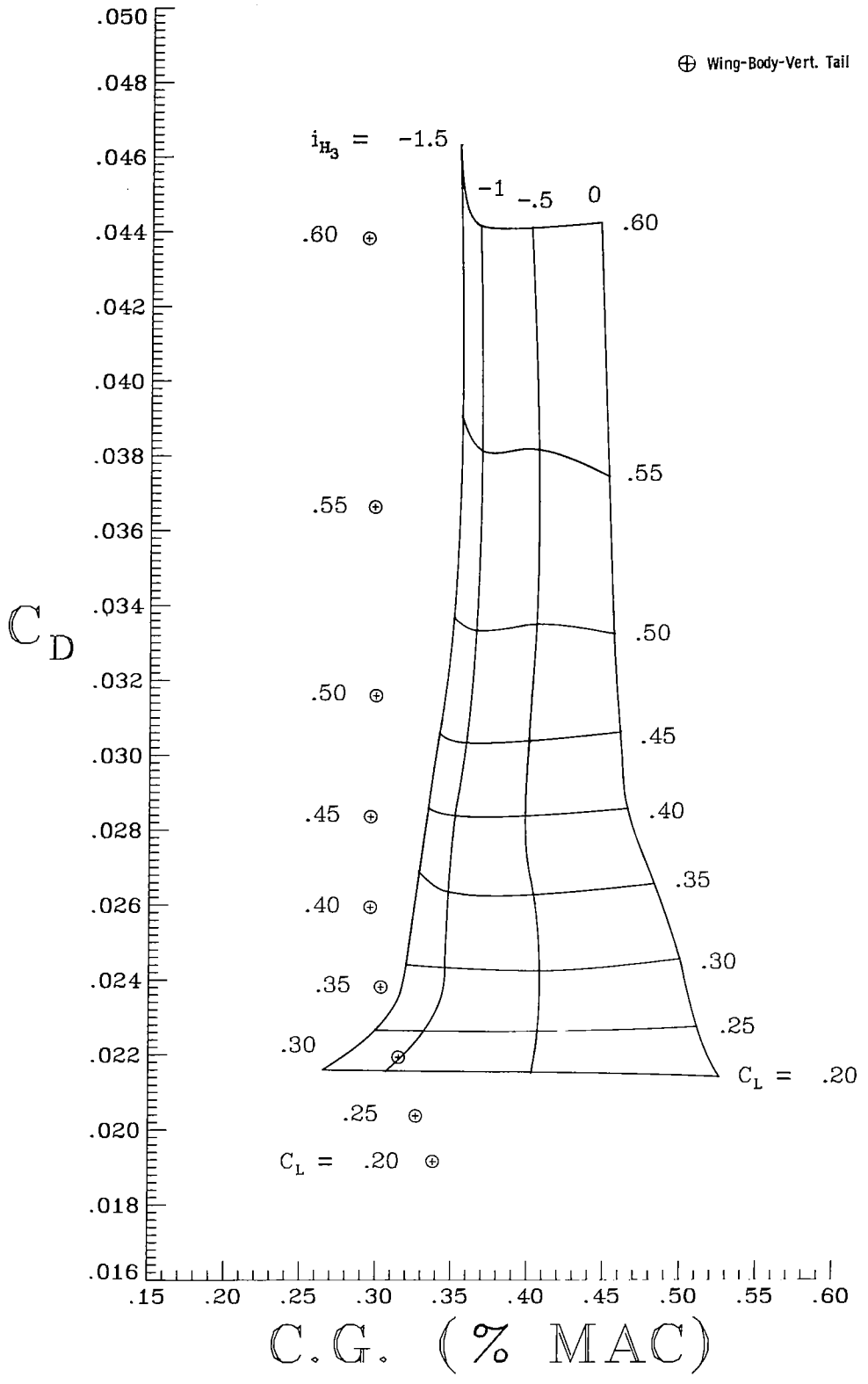

(c) H_3.

Figure 17.- Continued.

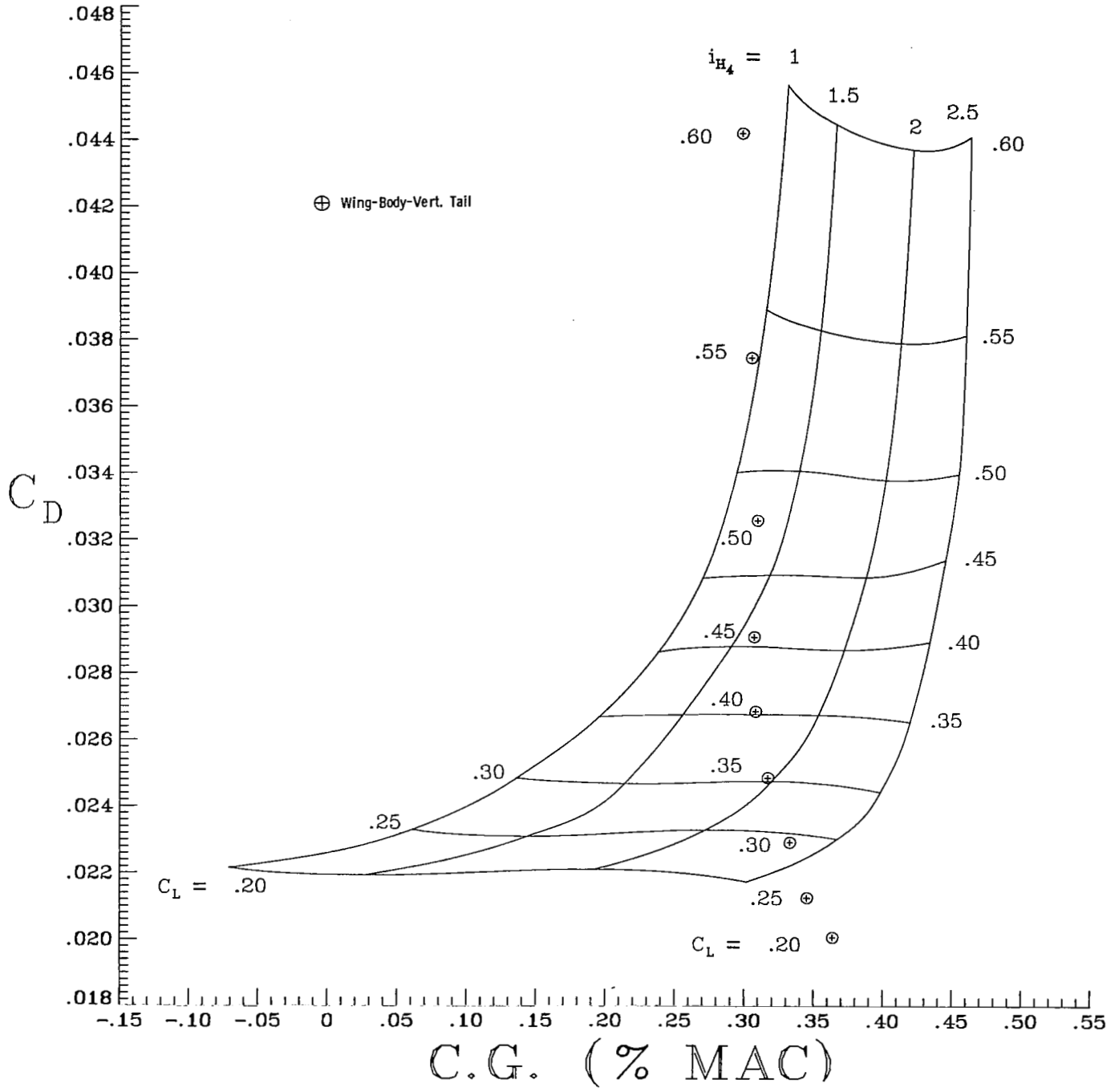

(d) H_4.

Figure 17.- Continued.

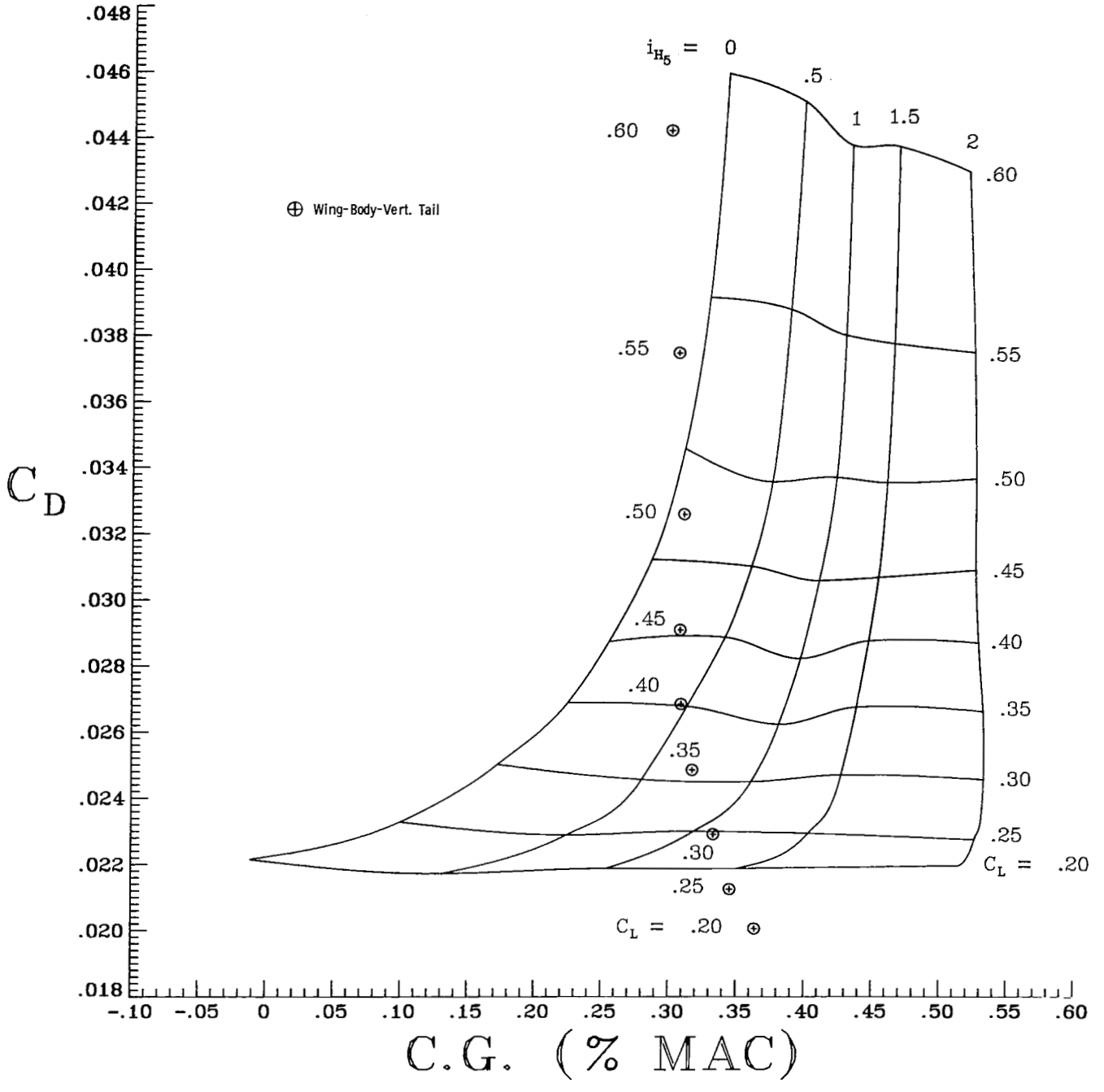

(e) H_5.

Figure 17.- Concluded.

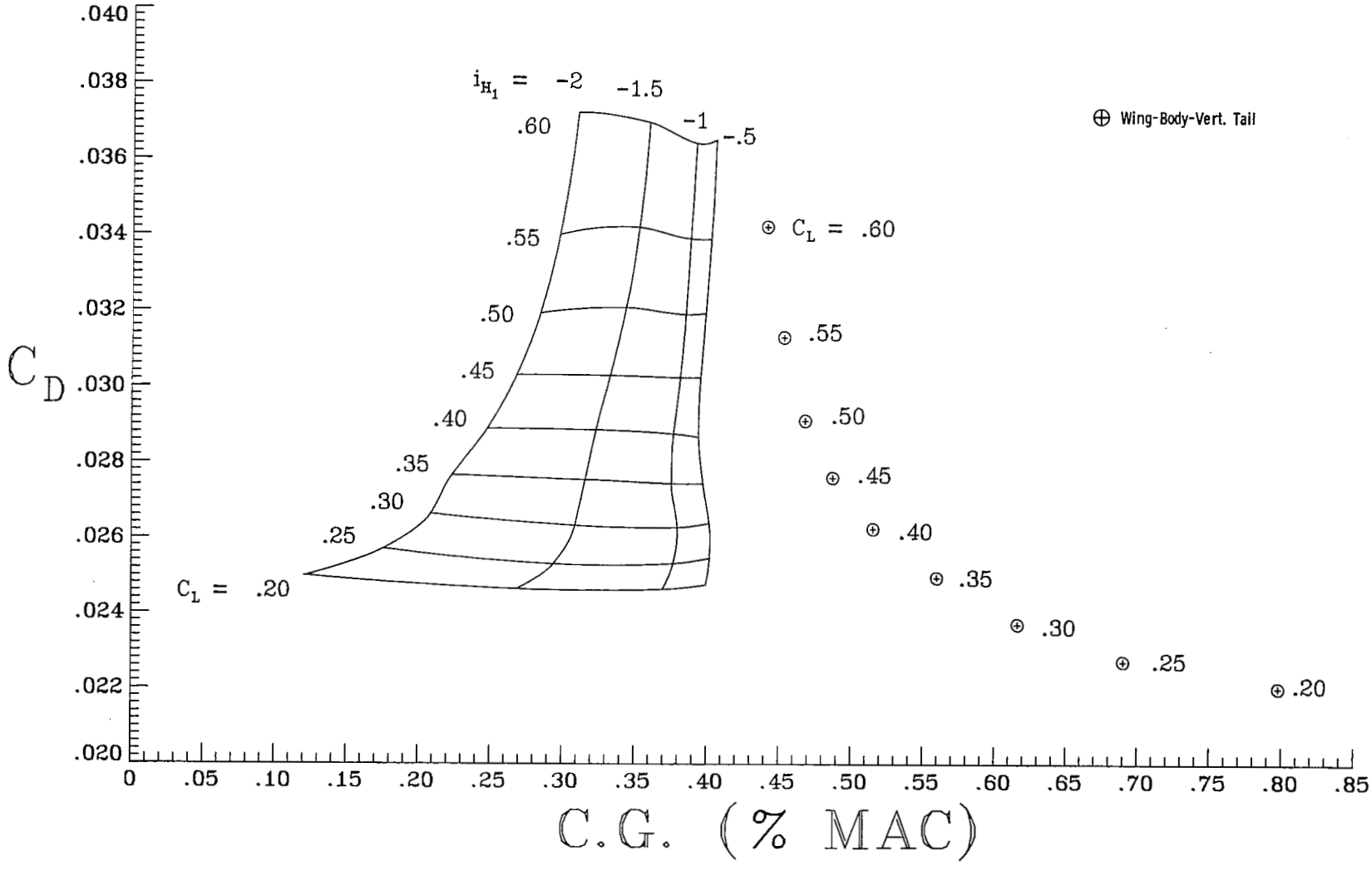

(a) H_1.

Figure 18.- Variation of trimmed drag coefficient with c.g. position for supercritical wing configuration at $M_\infty = 0.82$.

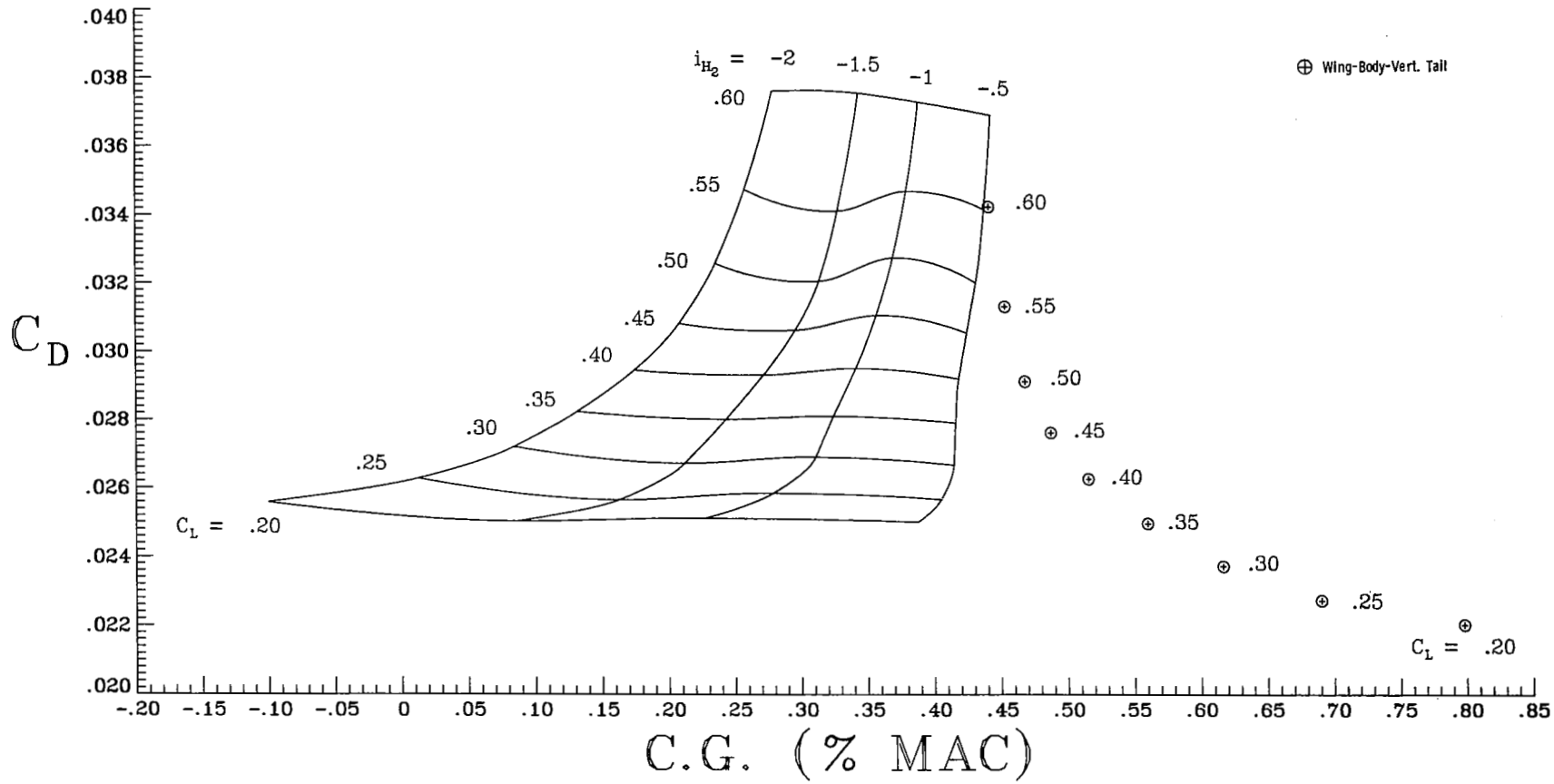

(b) H_2.

Figure 18.- Continued.

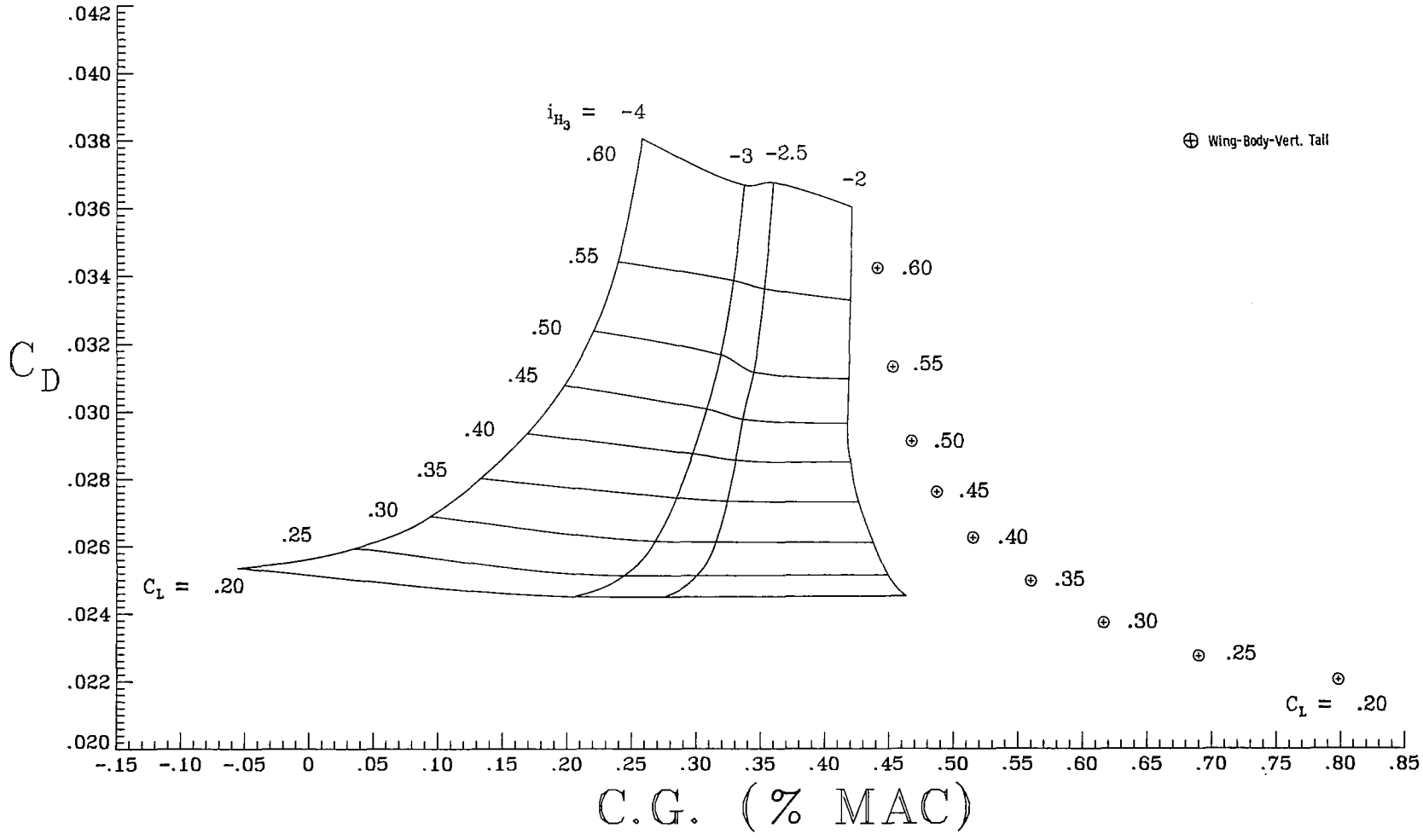

(c) H_3.

Figure 18.- Continued.

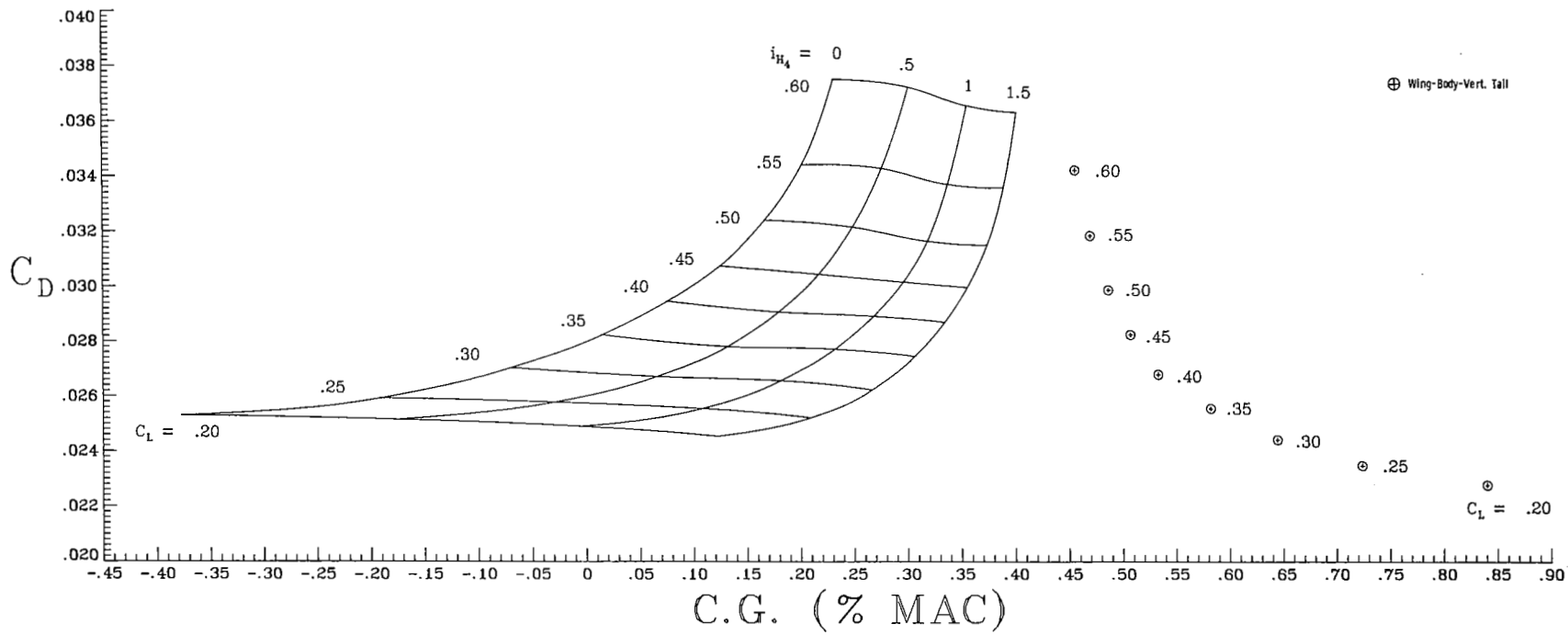

(d) H_4.

Figure 18.- Continued.

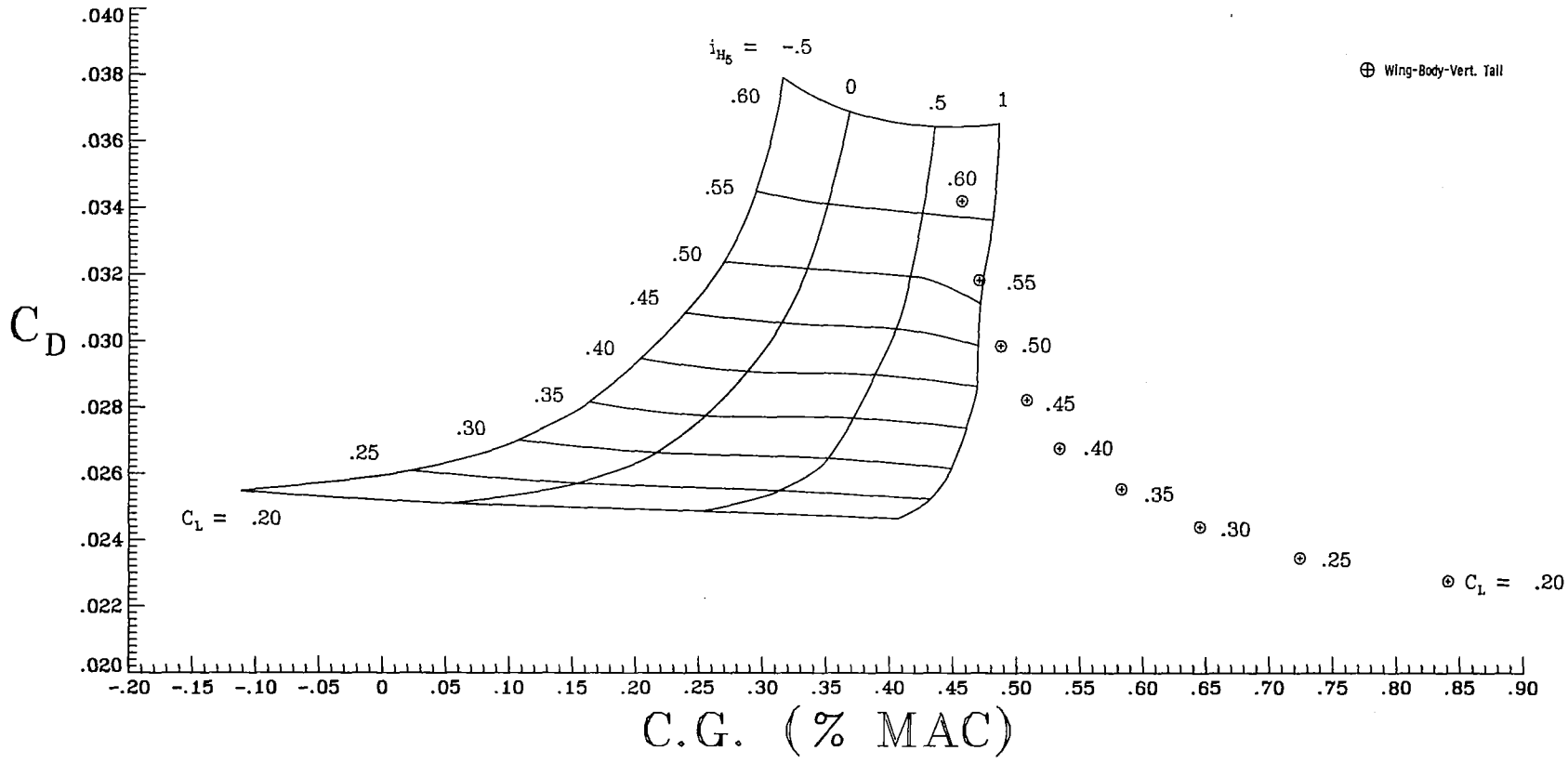

(e) H_5.

Figure 18.- Concluded.

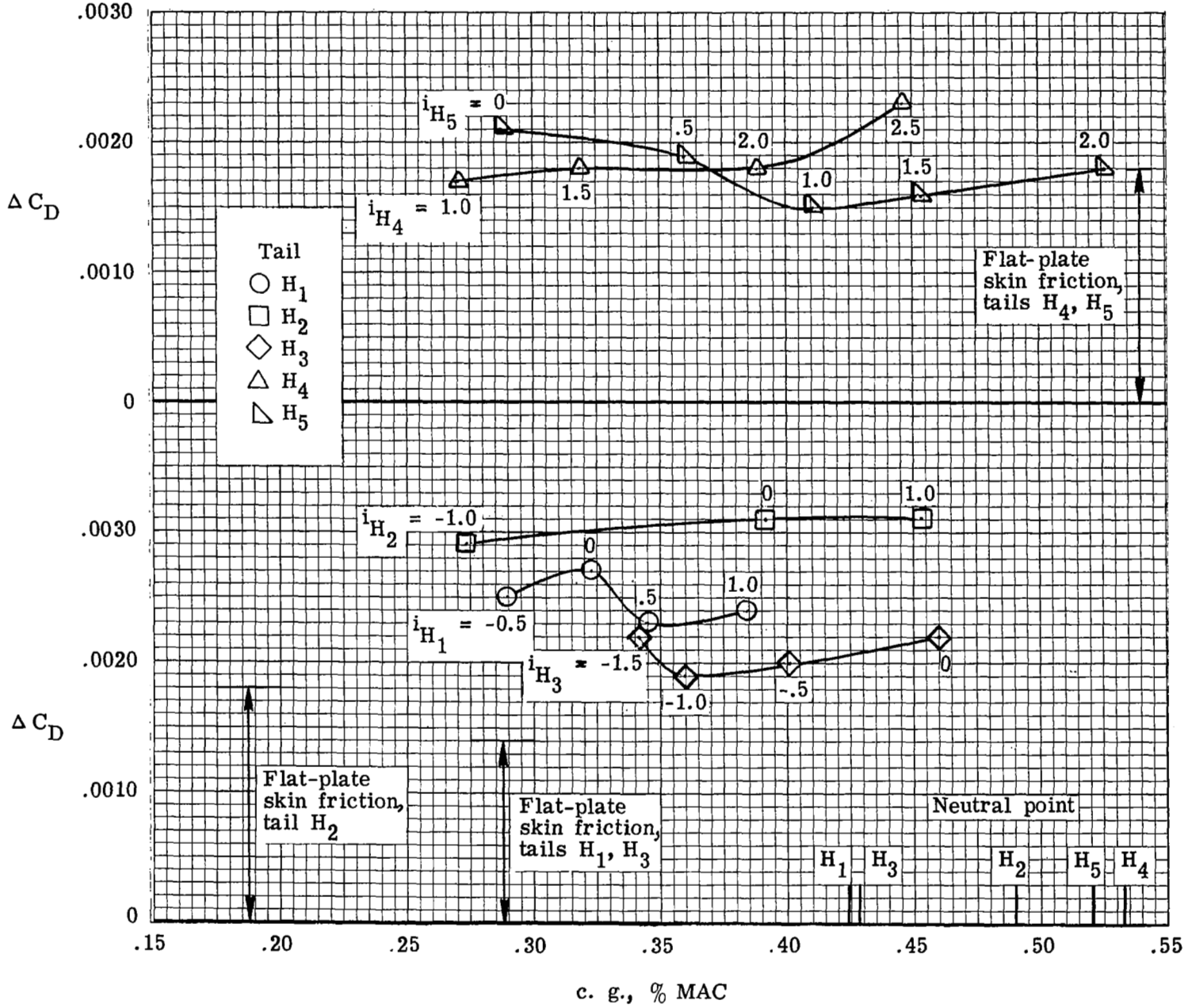

Figure 19.- Variation of trim drag increment with c.g. position for wide-body wing configurations at $M_\infty = 0.82$ and $C_L = 0.45$.

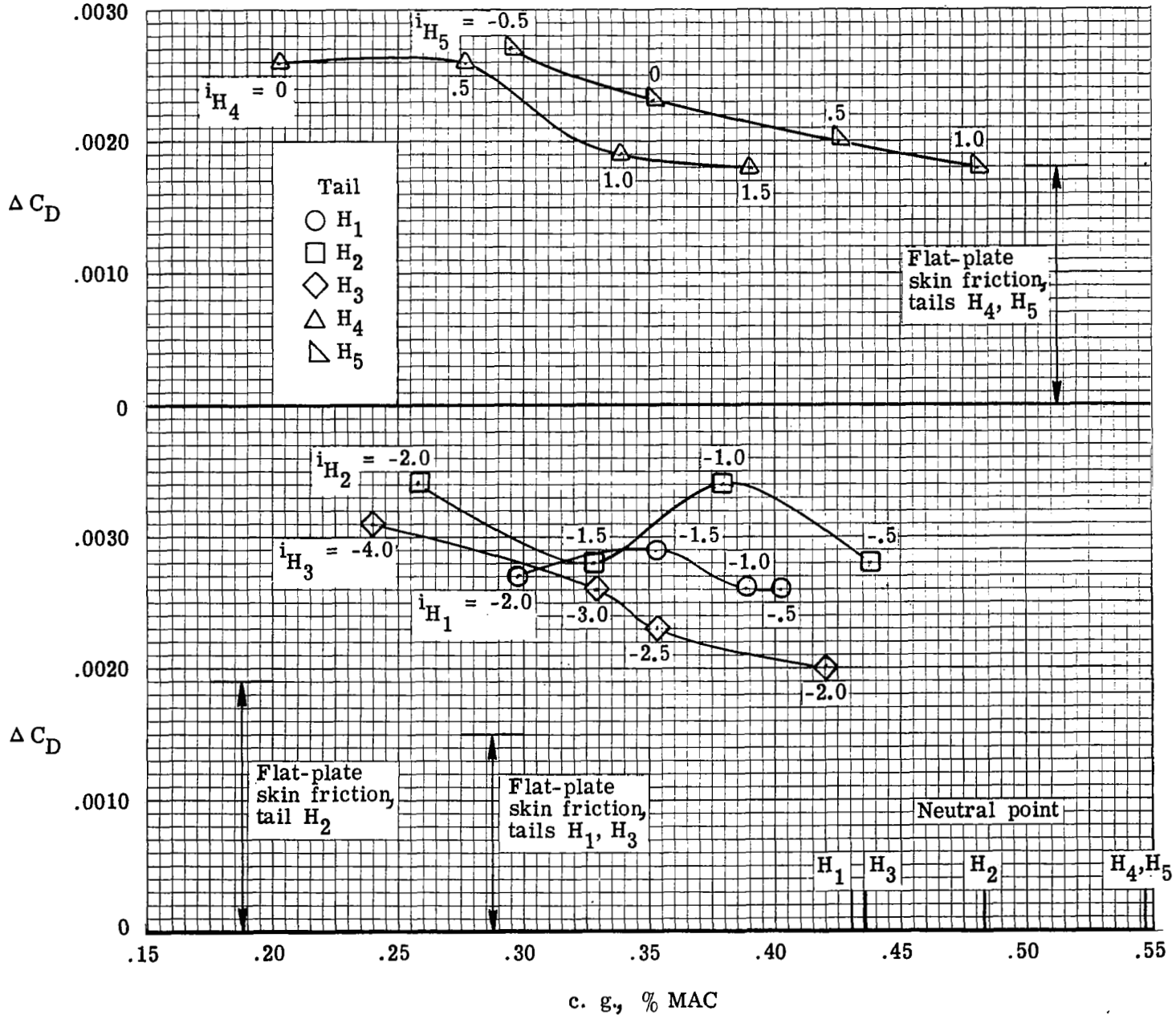

Figure 20.- Variation of trim drag increment with c.g. position for supercritical wing configurations at $M_\infty = 0.82$ and $C_L = 0.55$.

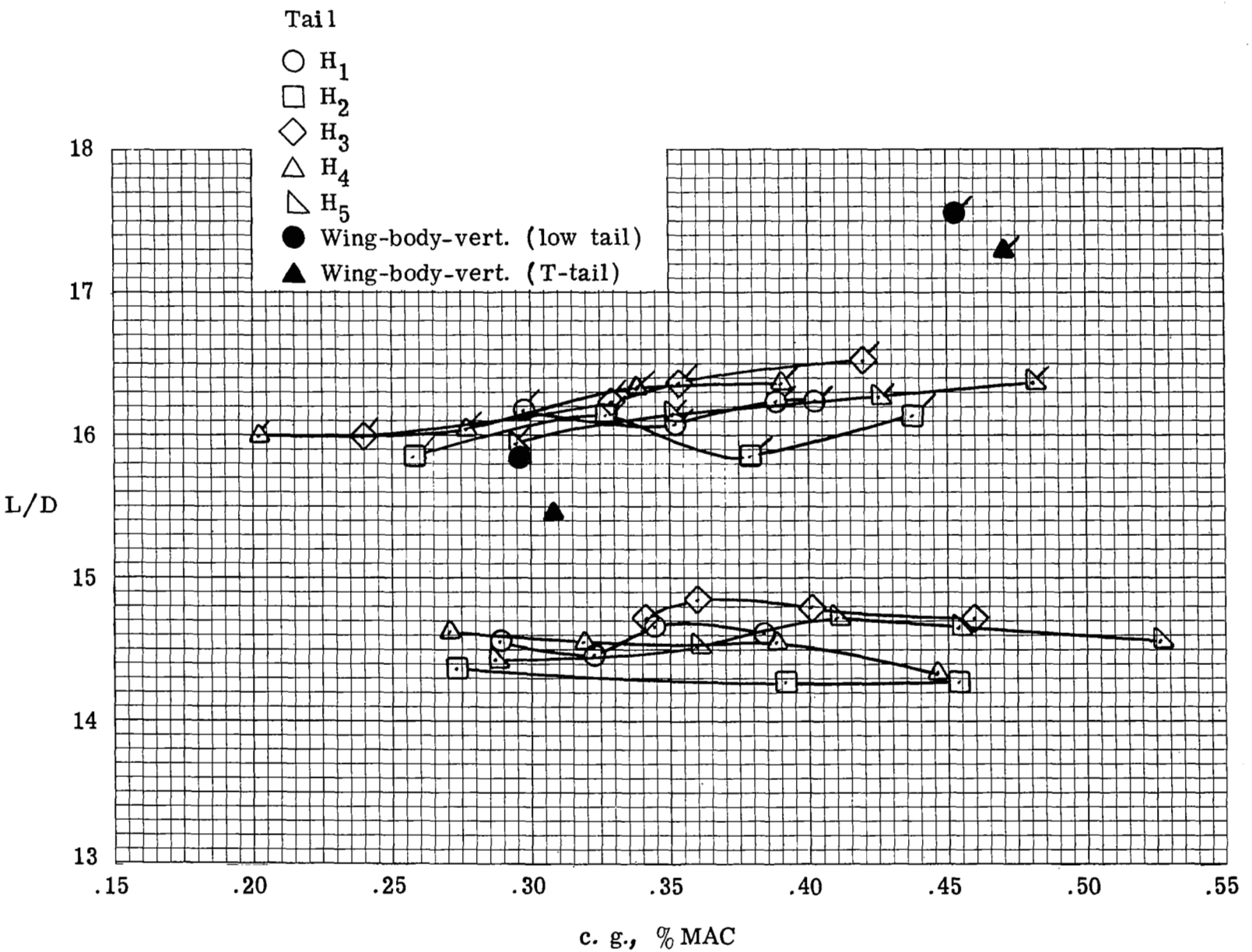

Figure 21.- Variation of lift-drag ratio with c.g. position for both wings at their cruise lift coefficients and $M_\infty = 0.82$. Symbols with ticks represent values for SCW.

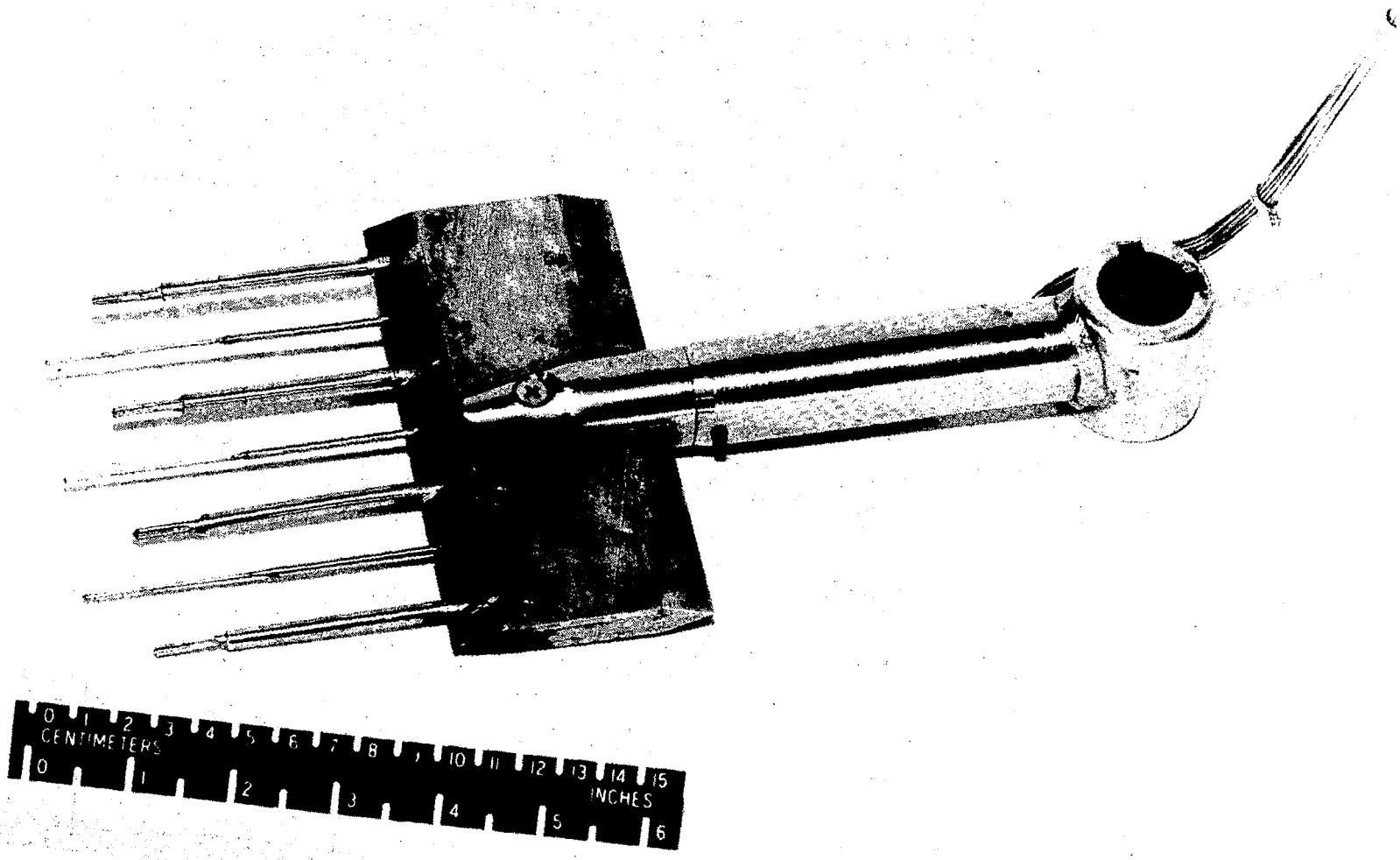

Figure 22.- Yawhead rake for low-tail configurations. L-81-8167

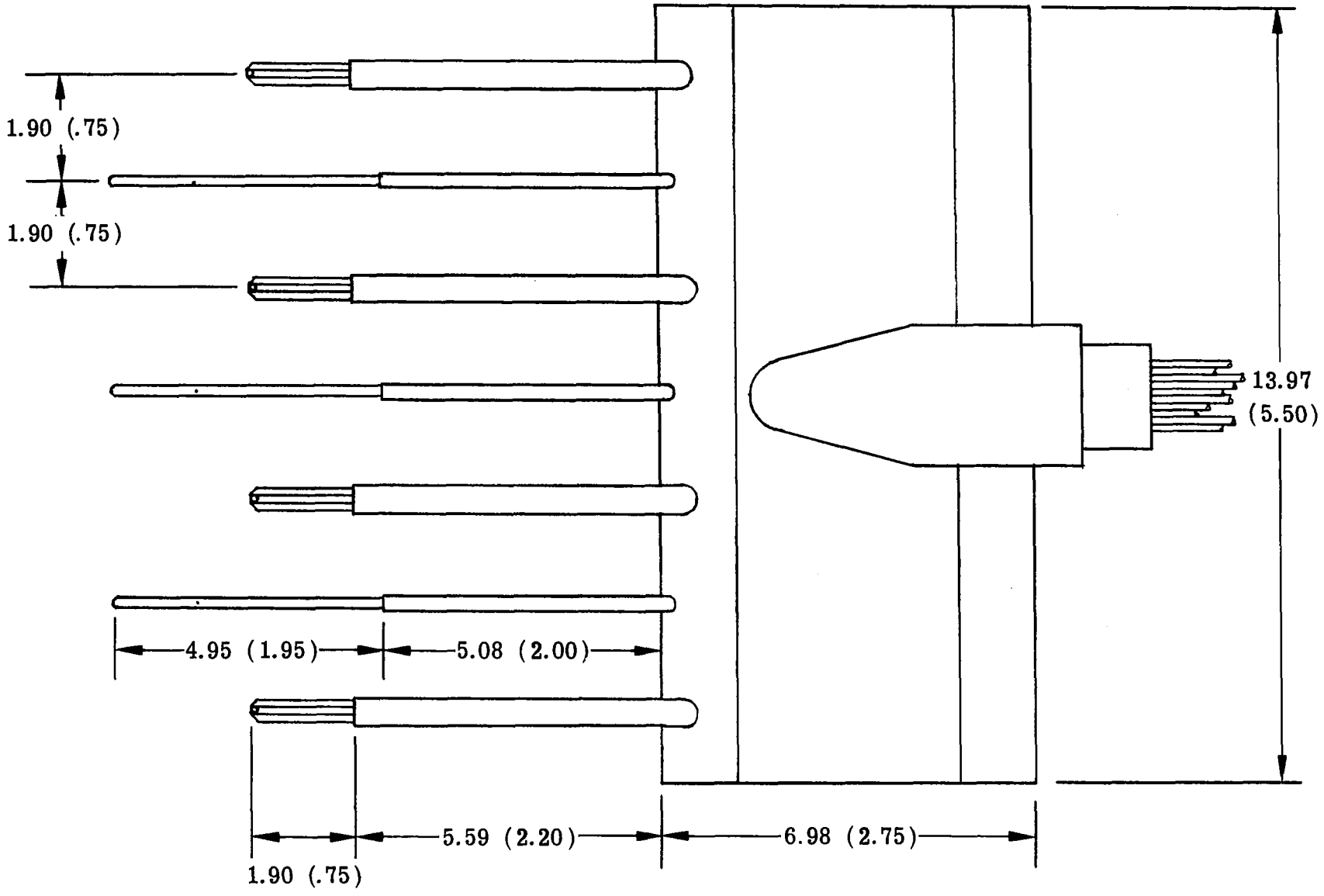

Figure 23.- Yawhead rake details.

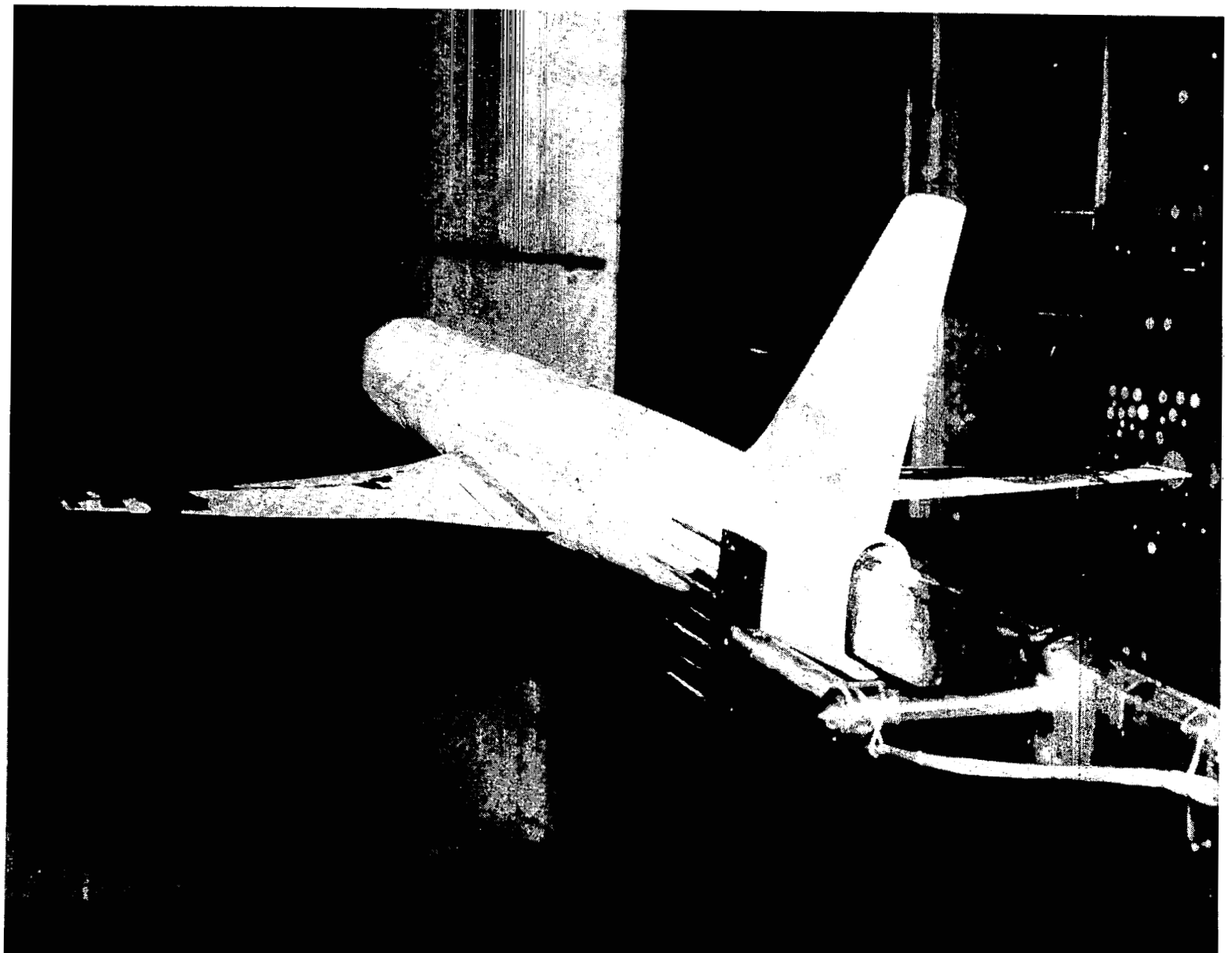

L-80-6816

Figure 24.- Typical yawhead rake installation for low-tail configurations.

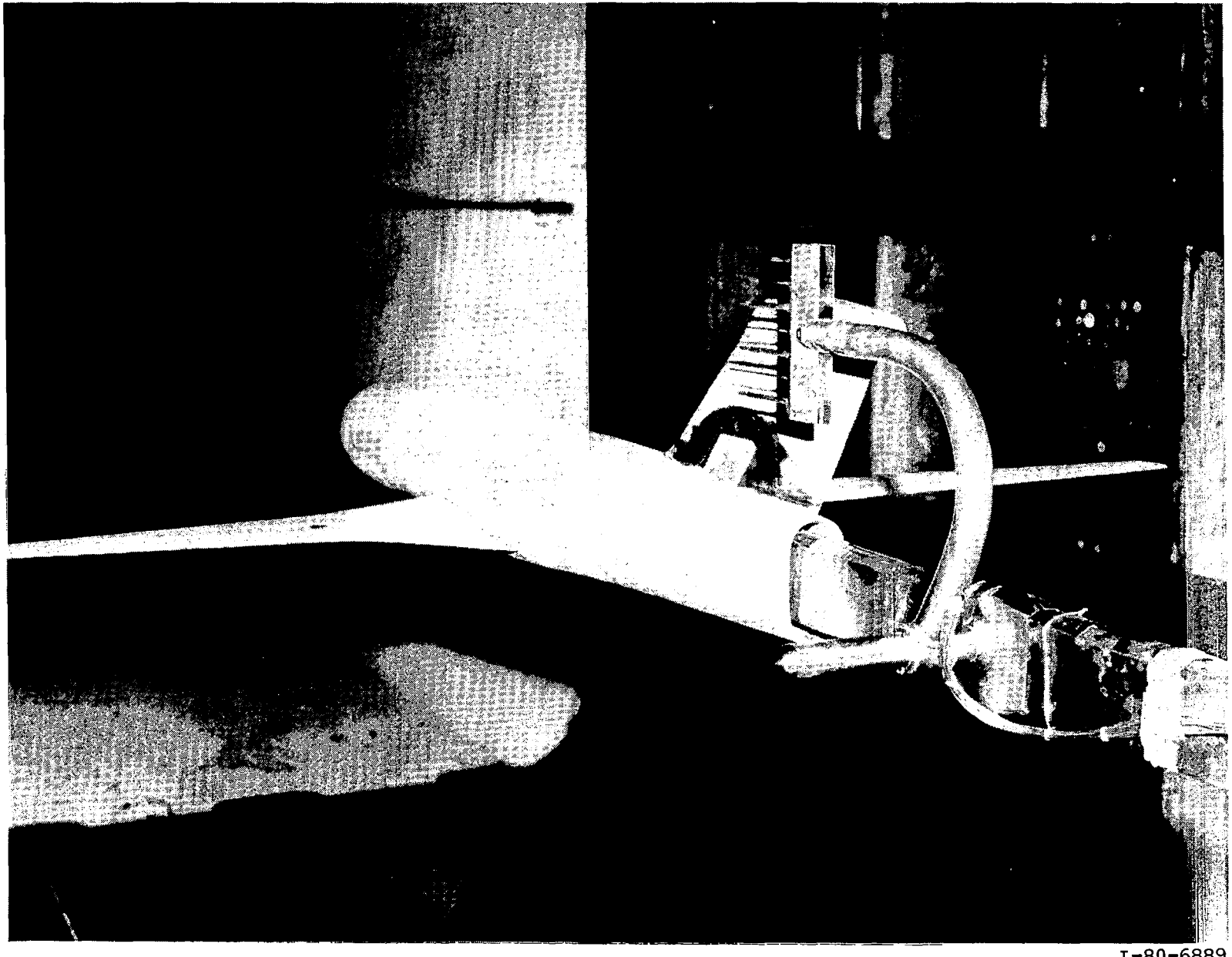

L-80-6889

Figure 25.- Typical yawhead rake installation for T-tail configurations.

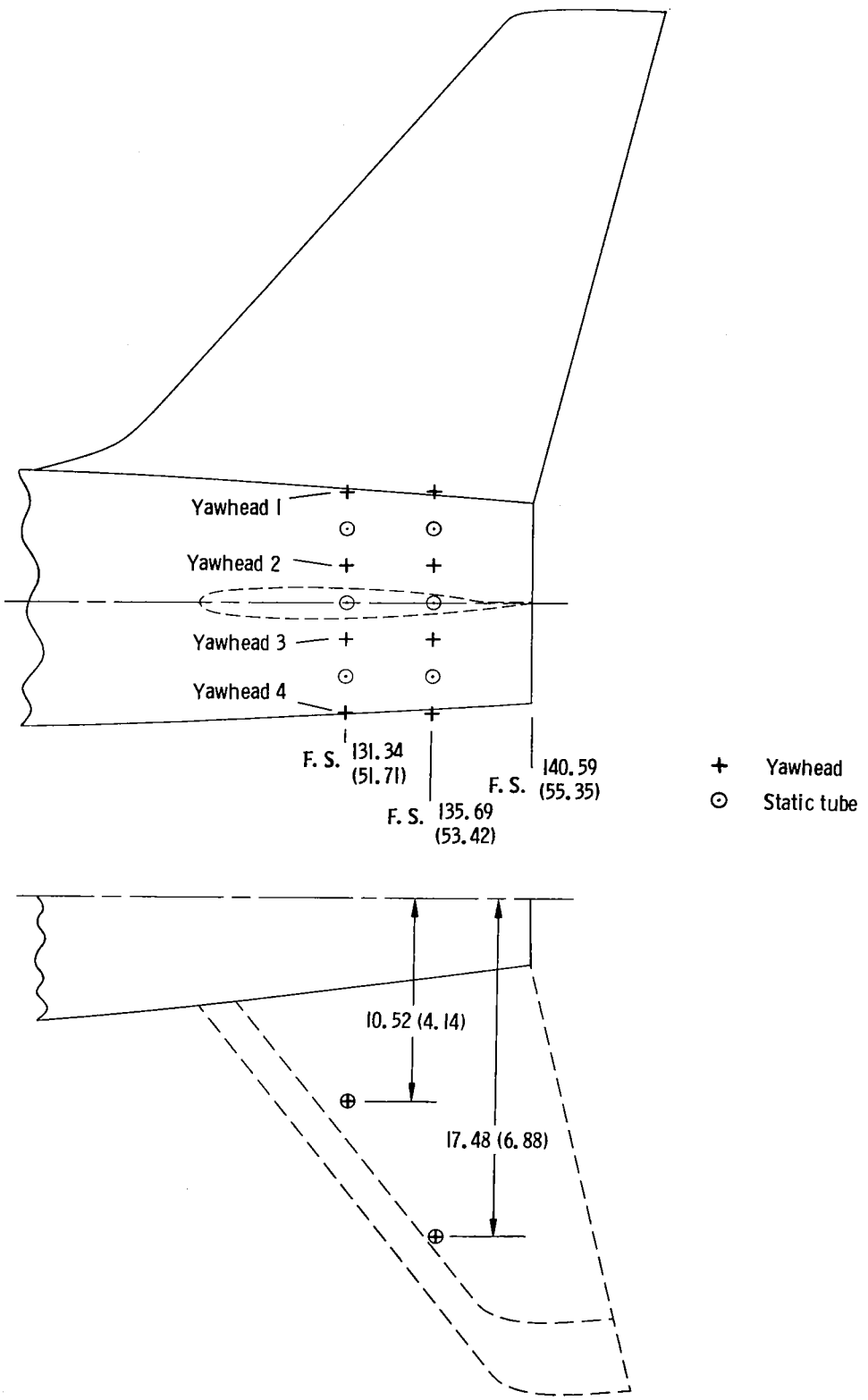

Figure 26.- Yawhead rake data positions for low-tail configurations.

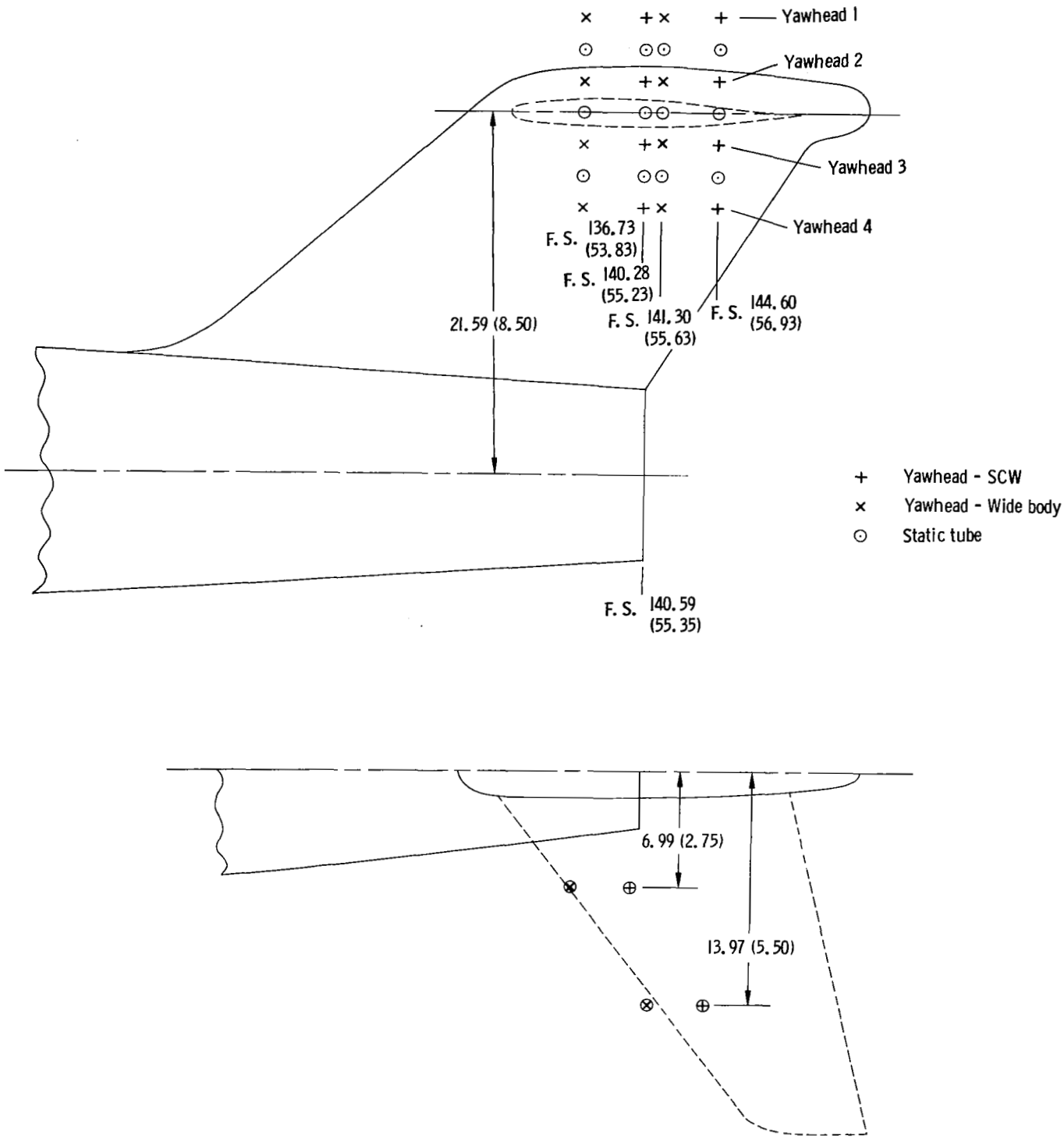

Figure 27.- Yawhead rake data positions for T-tail configurations.

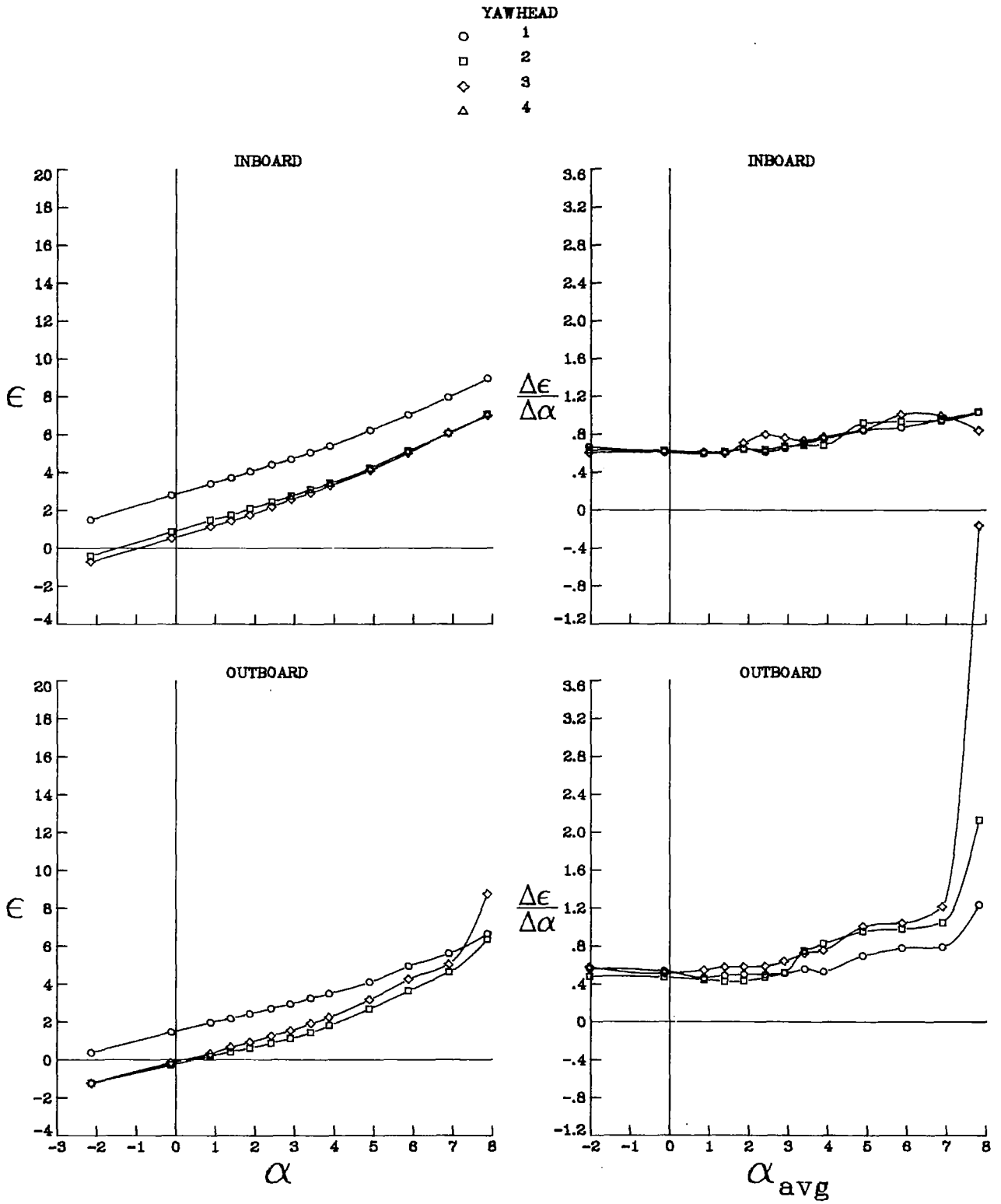

(a) Low-tail configurations.

Figure 28.- Variation of downwash angle and $\Delta\epsilon/\Delta\alpha$ with angle of attack for wide-body wing configurations at $M_\infty = 0.82$.

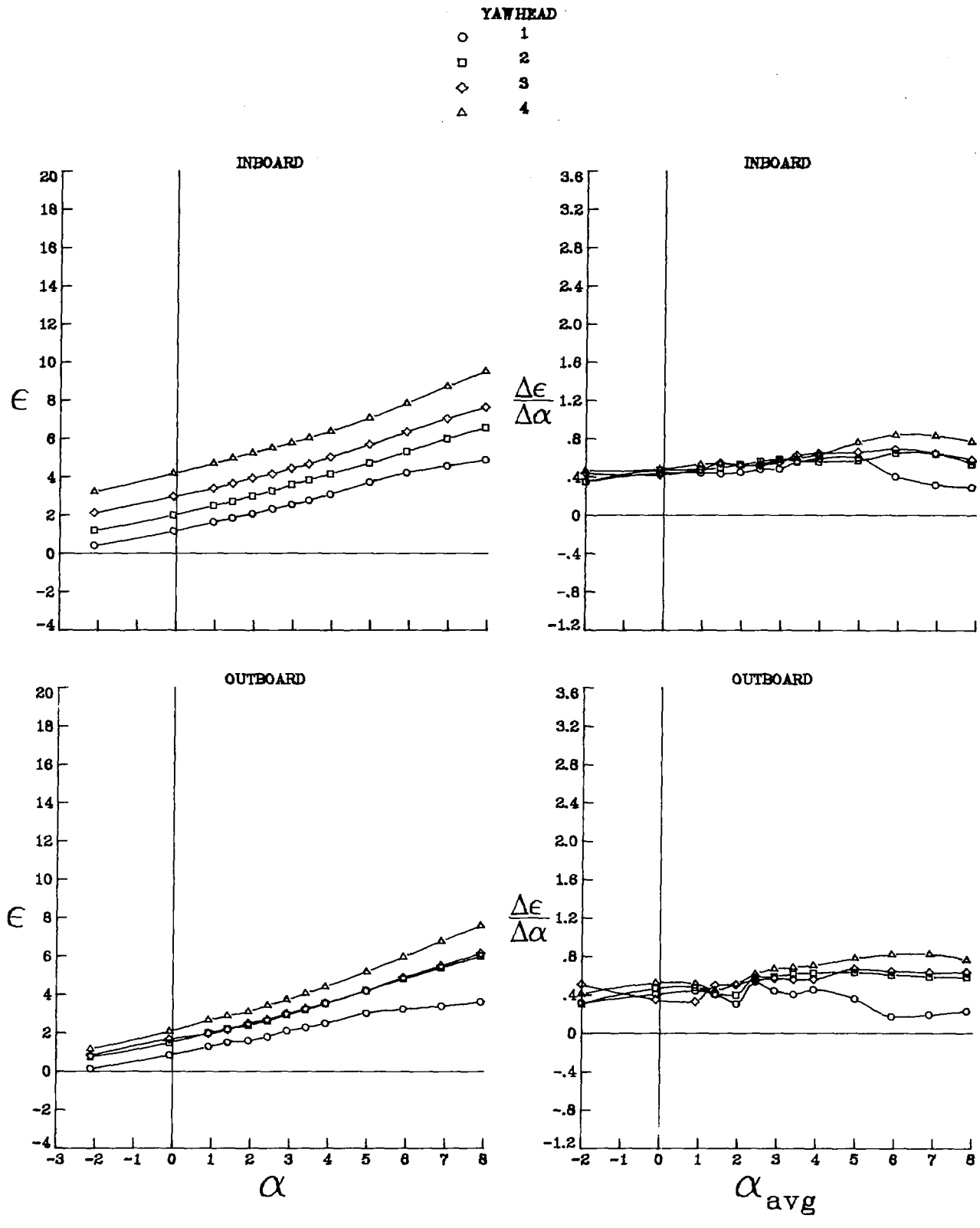

(b) T-tail configurations.

Figure 28.- Concluded.

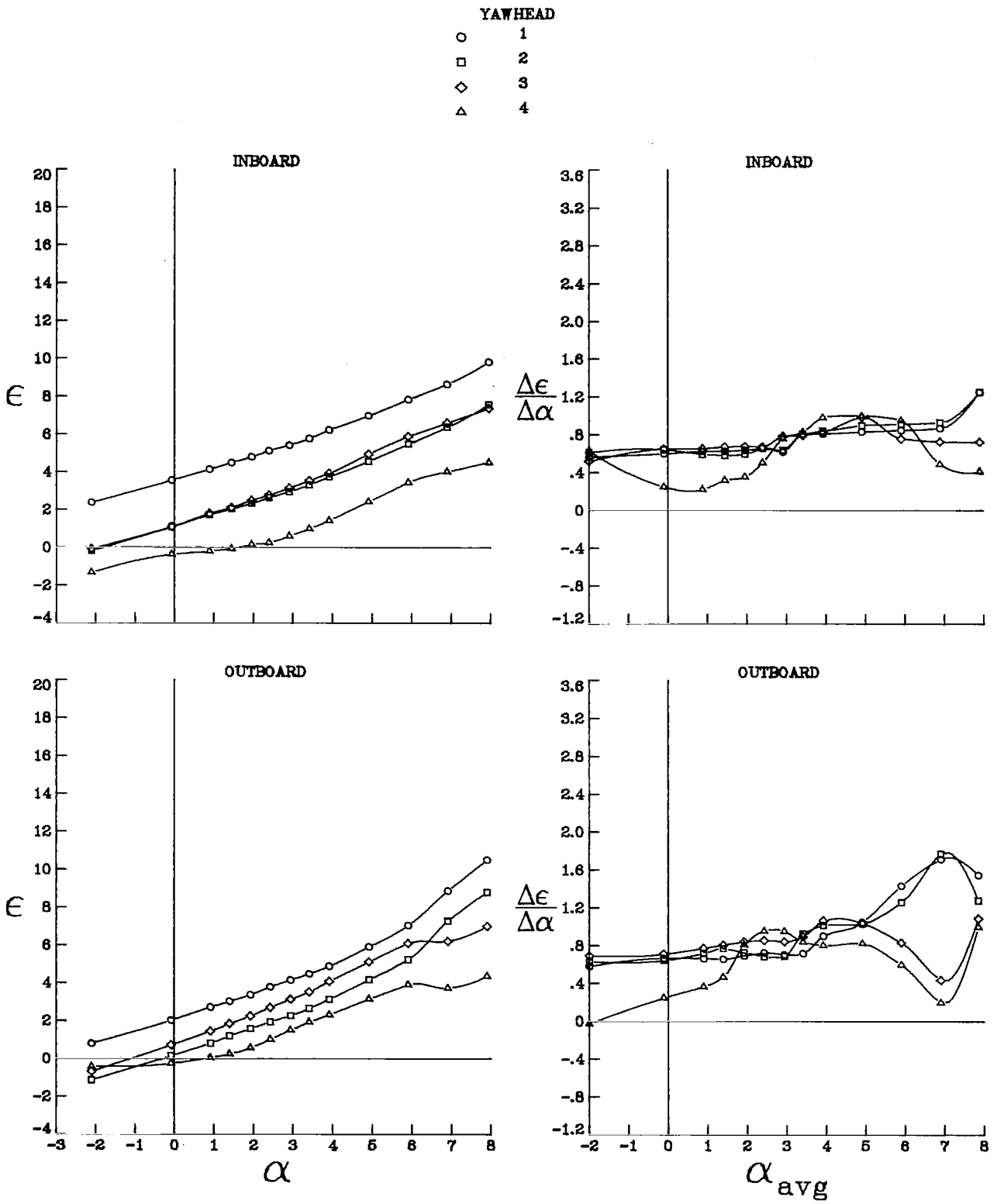

(a) Low-tail configurations.

Figure 29.- Variation of downwash angle and $\Delta\varepsilon/\Delta\alpha$ with angle of attack for supercritical wing configurations at $M_\infty = 0.82$.

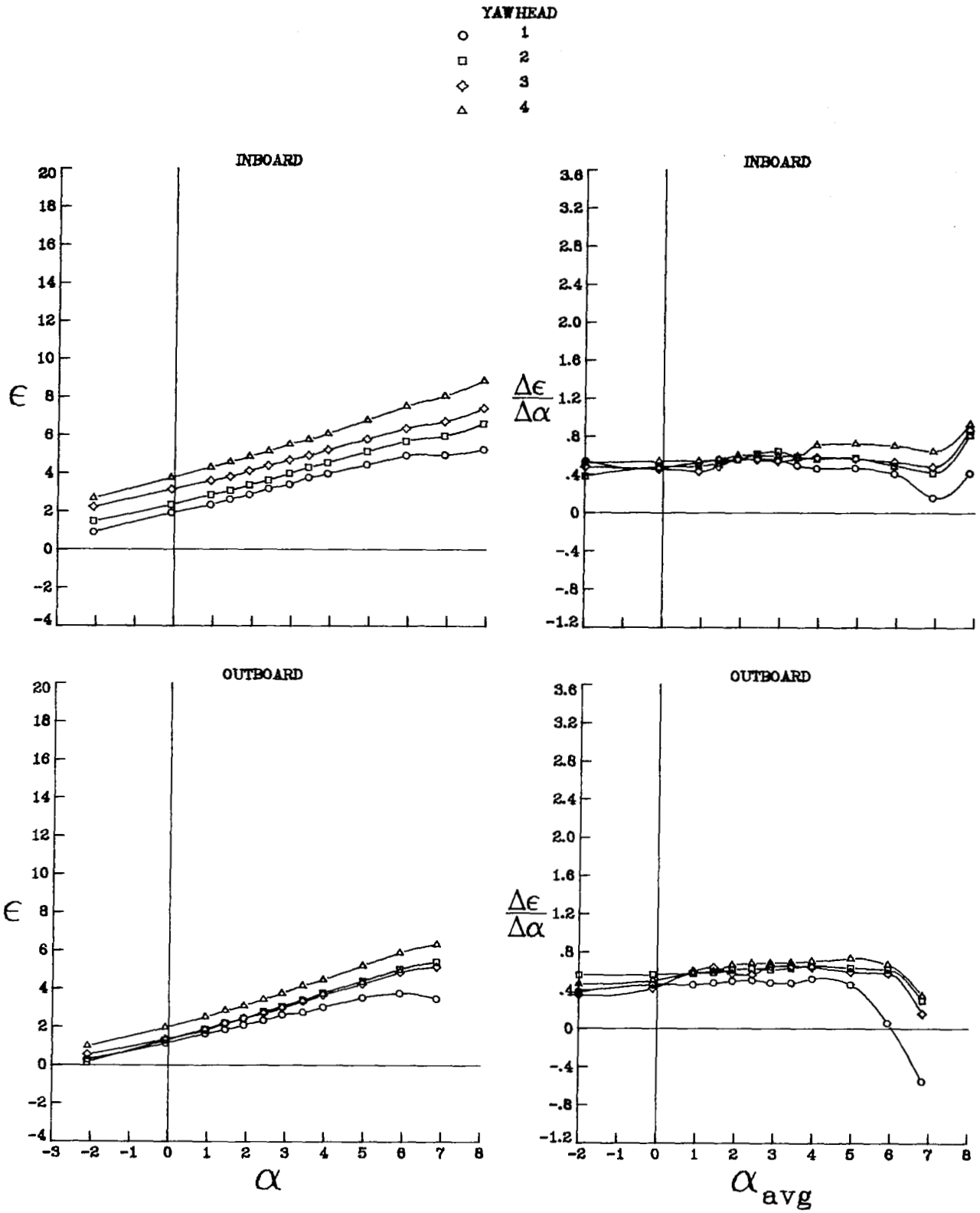

(b) T-tail configurations.

Figure 29.- Concluded.

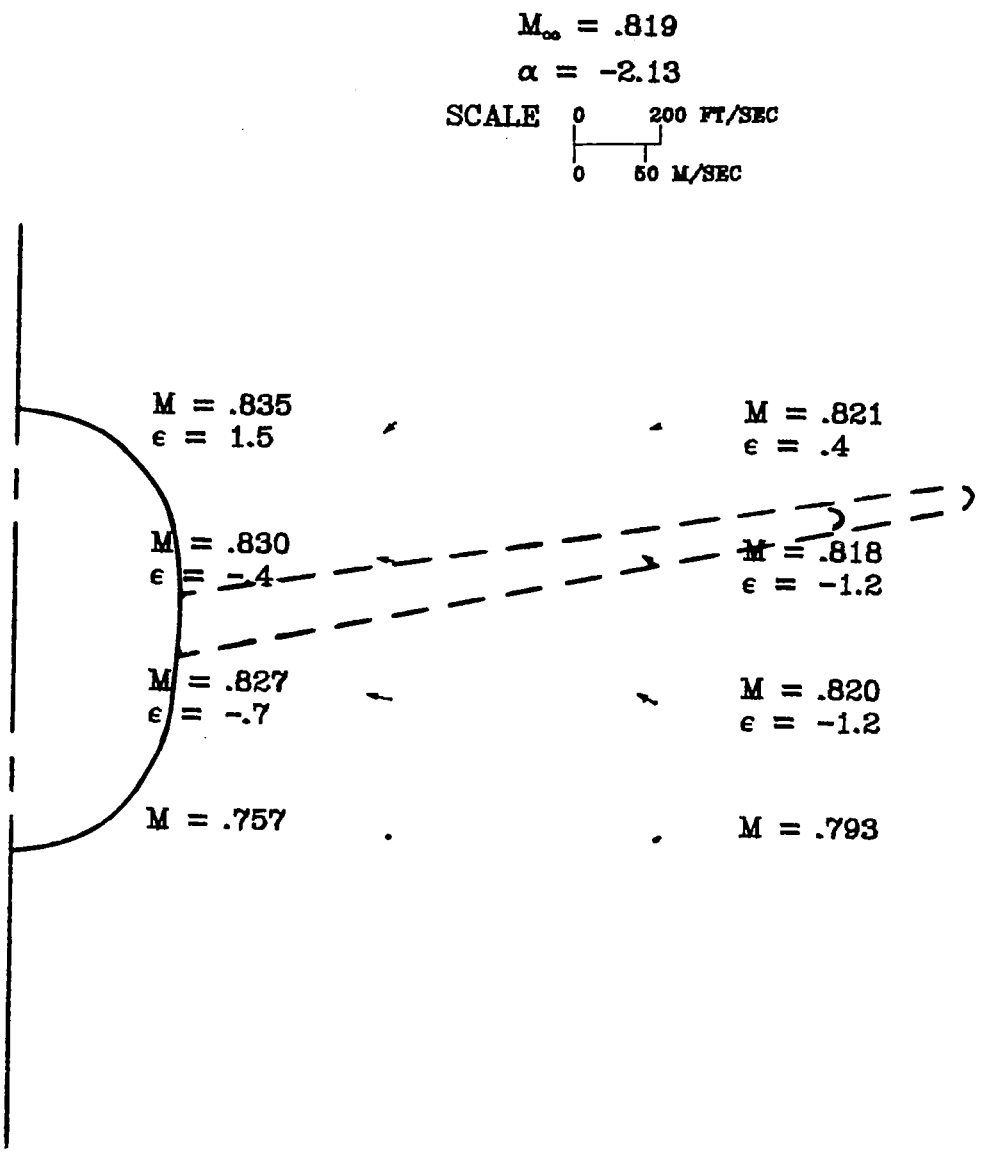

Figure 30.- Local Mach numbers and flow-field velocity vectors behind the wide-body wing with low-tail configuration.

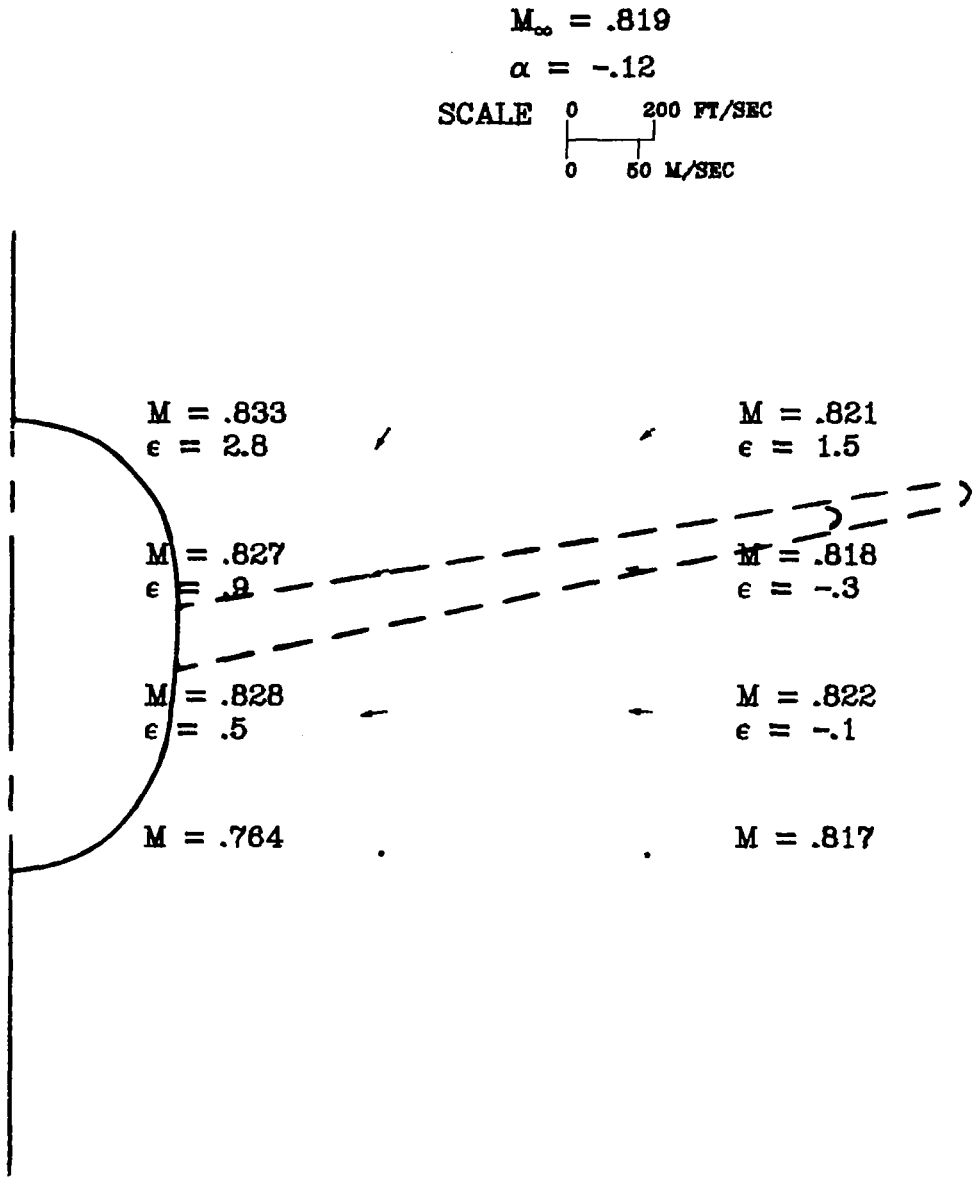

Figure 30.- Continued.

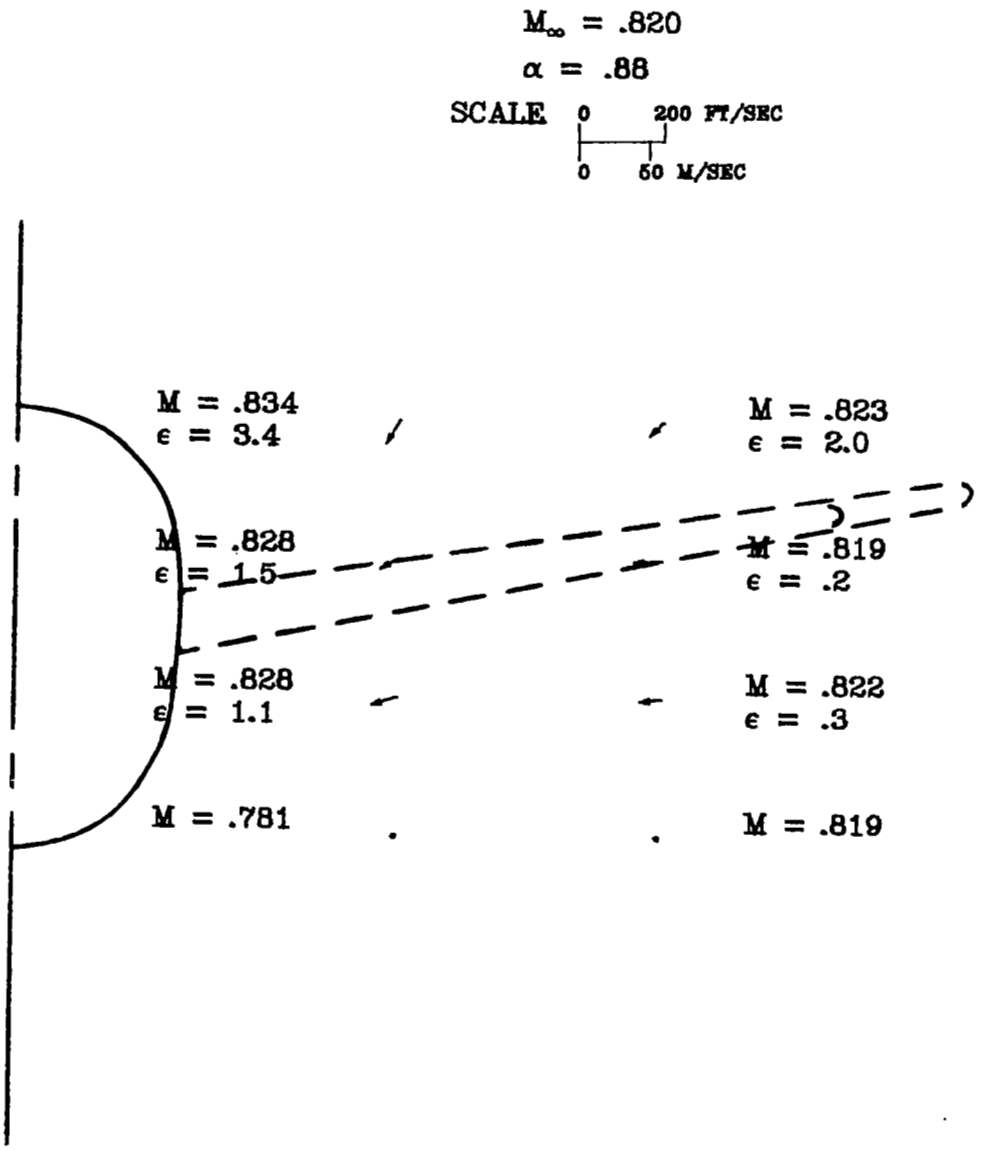

Figure 30.- Continued.

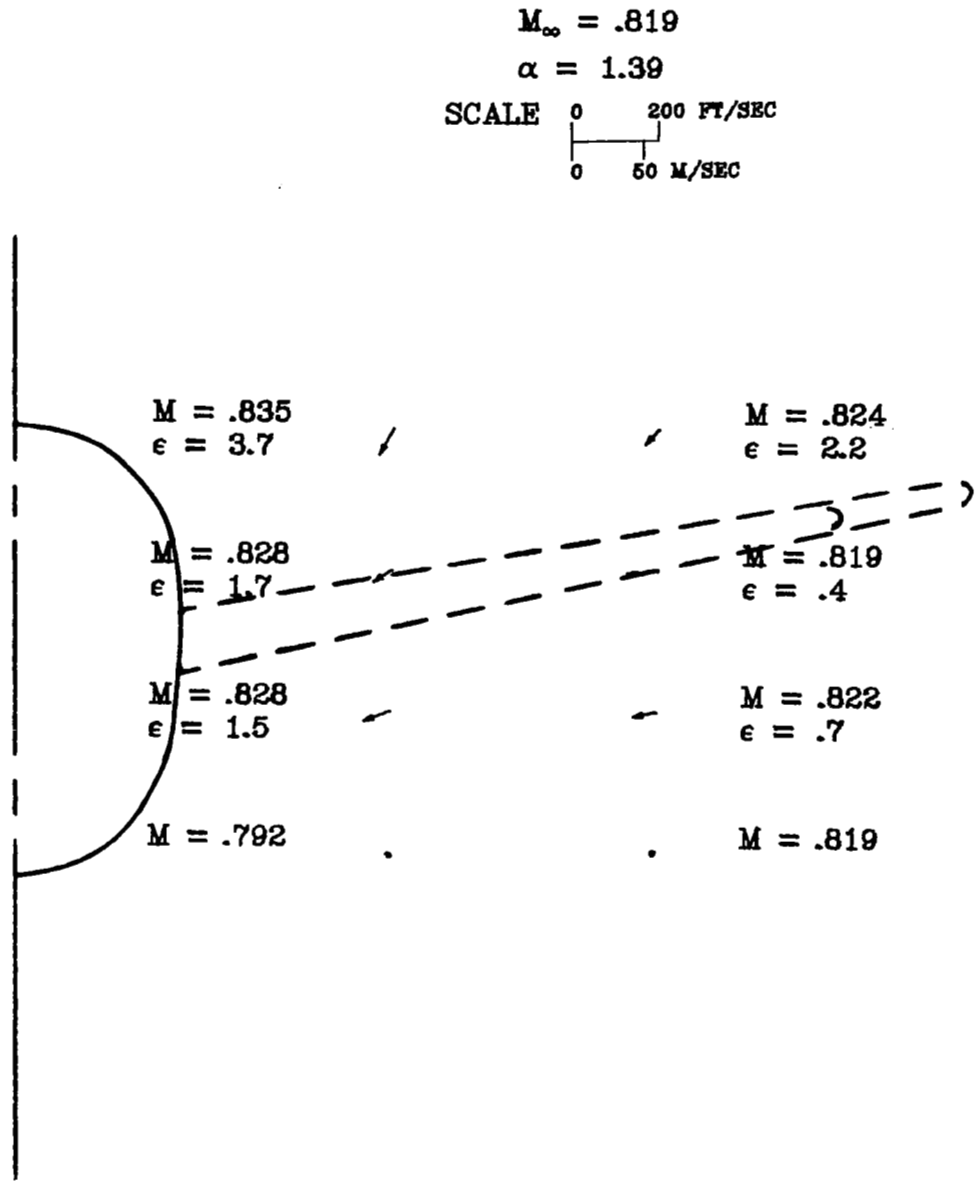

Figure 30.- Continued.

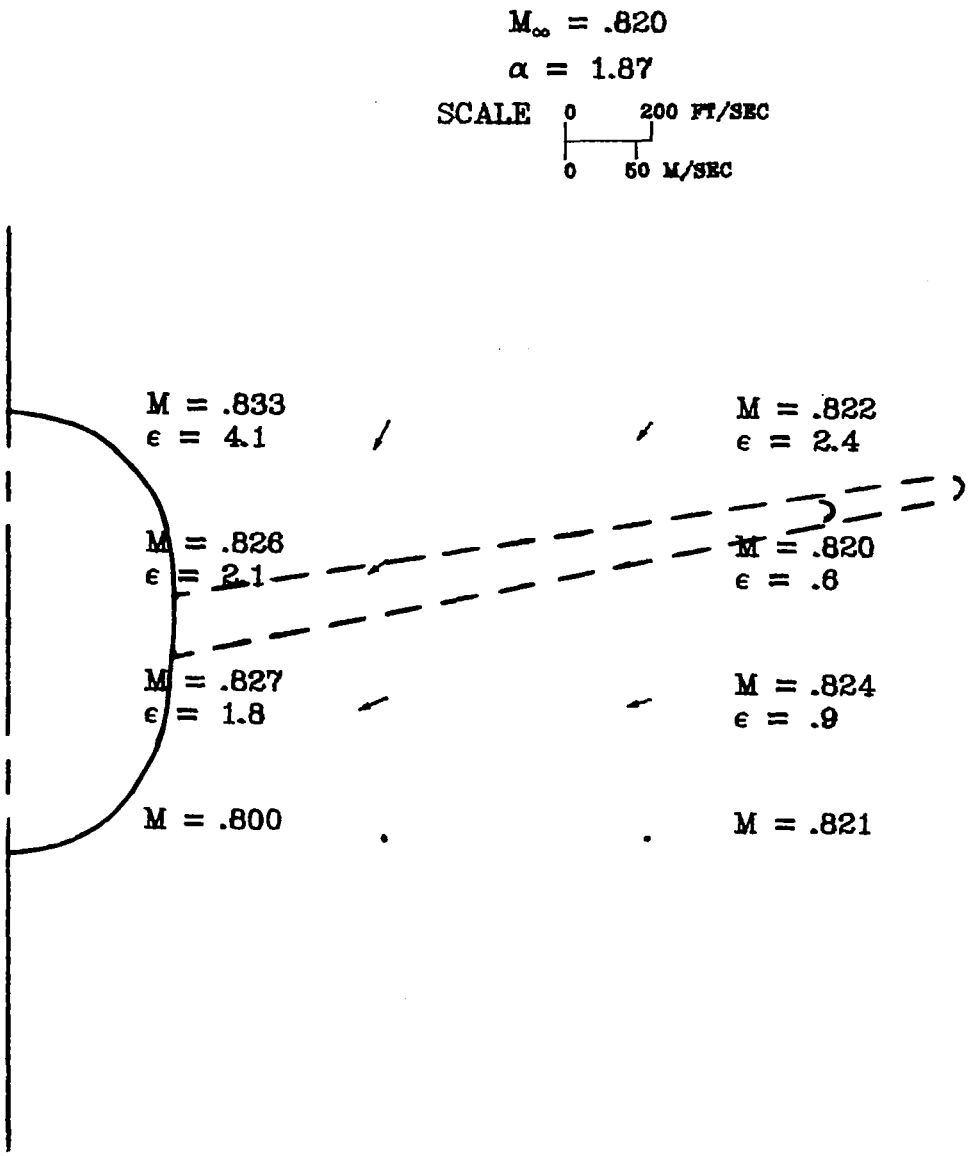

Figure 30.- Continued.

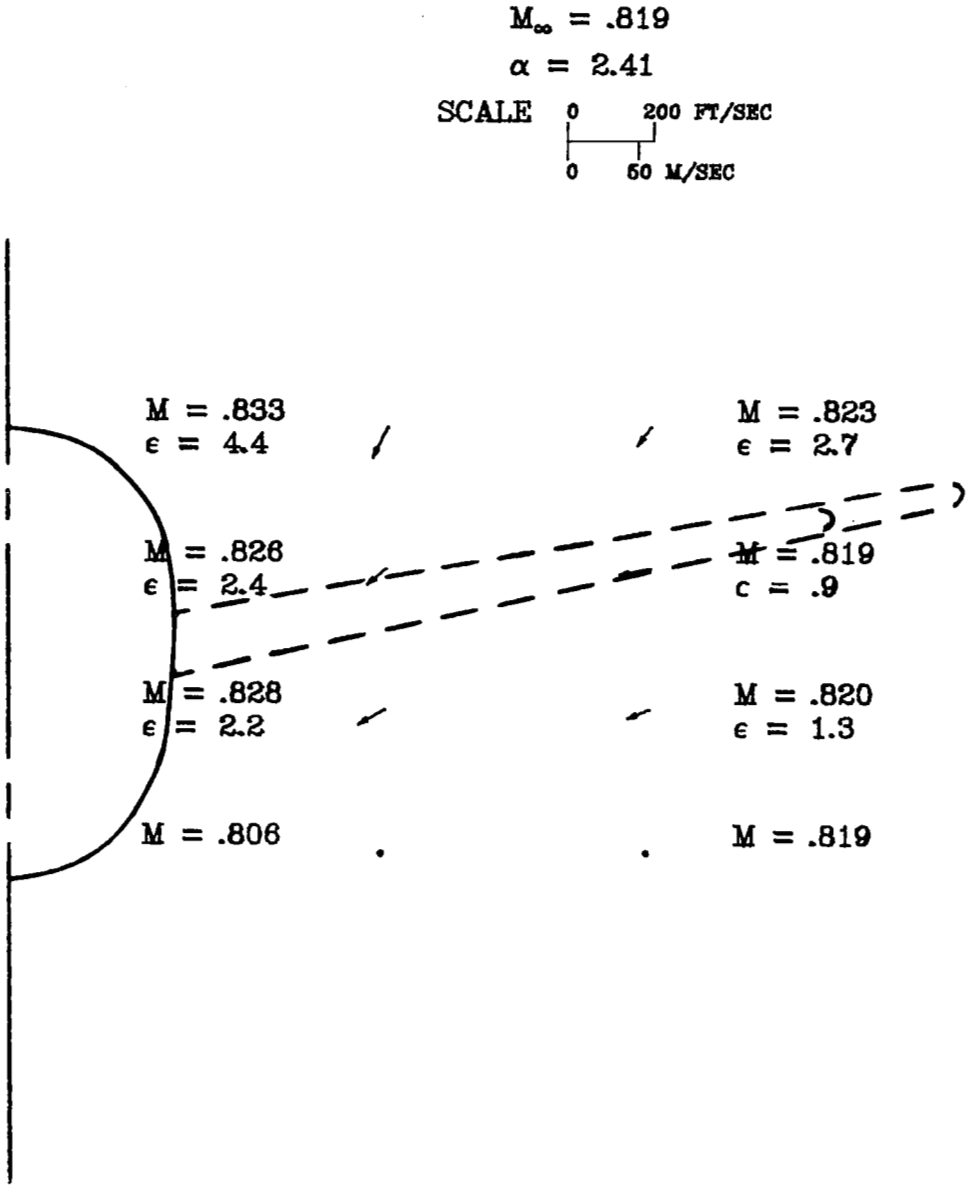

Figure 30.- Continued.

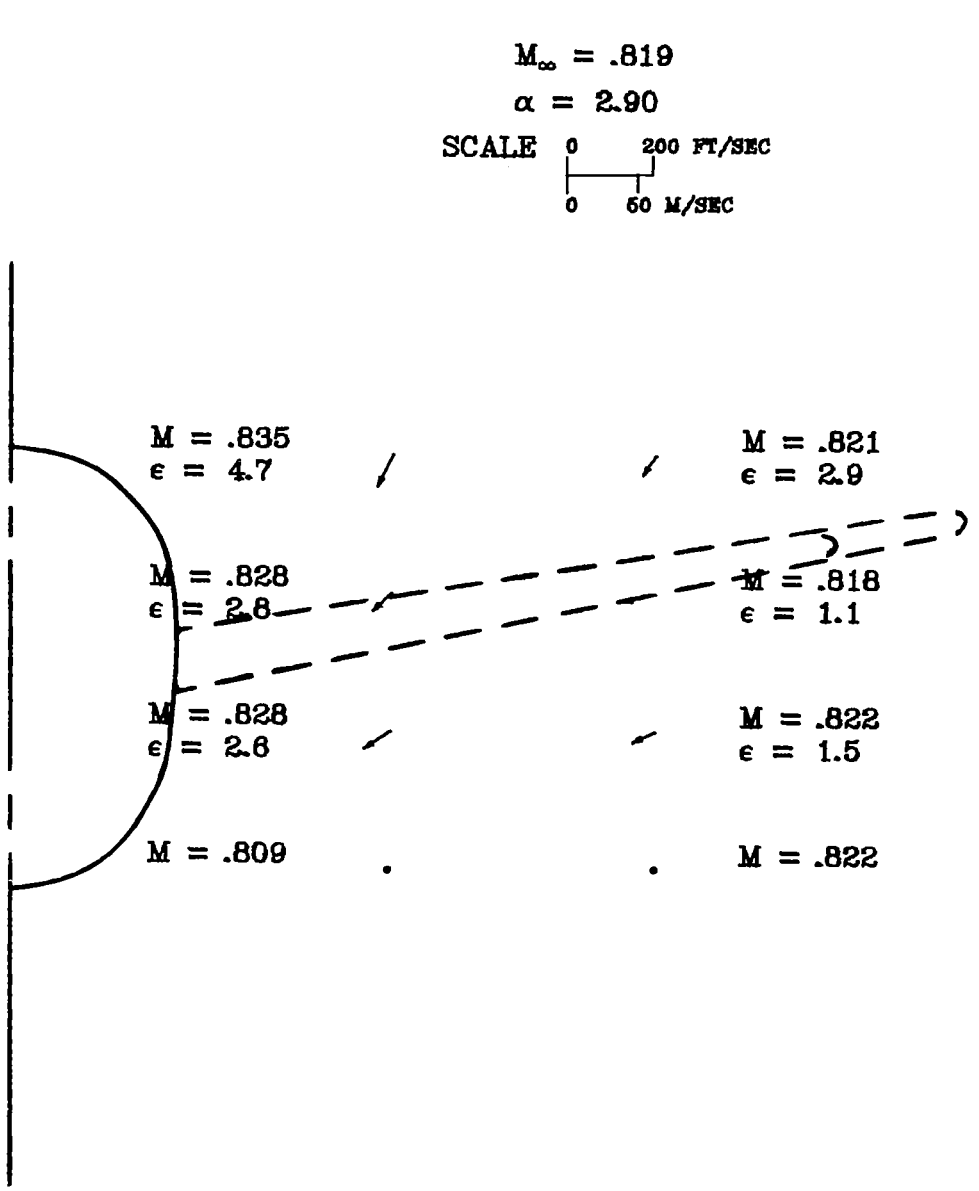

Figure 30.- Continued.

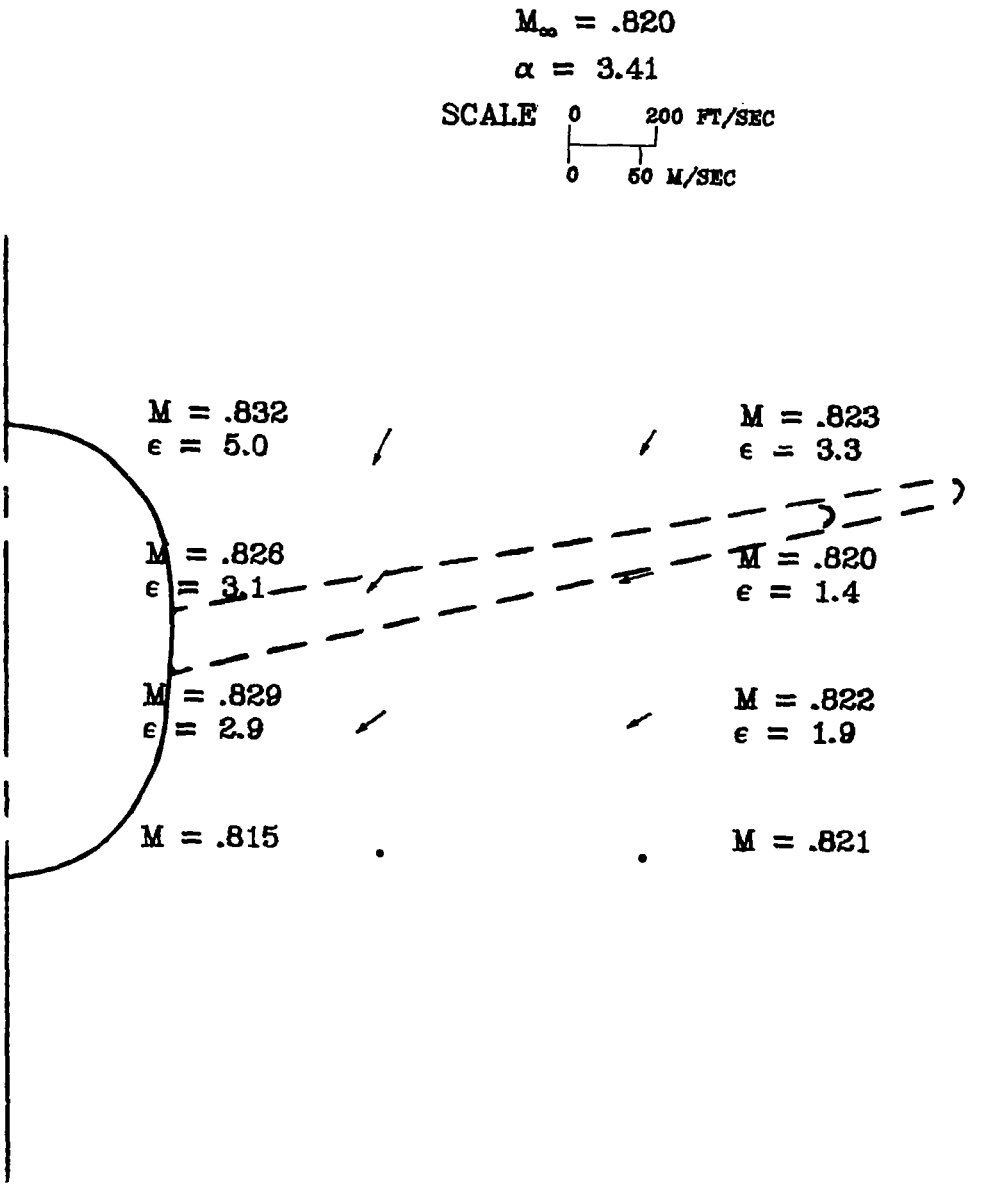

Figure 30.- Continued.

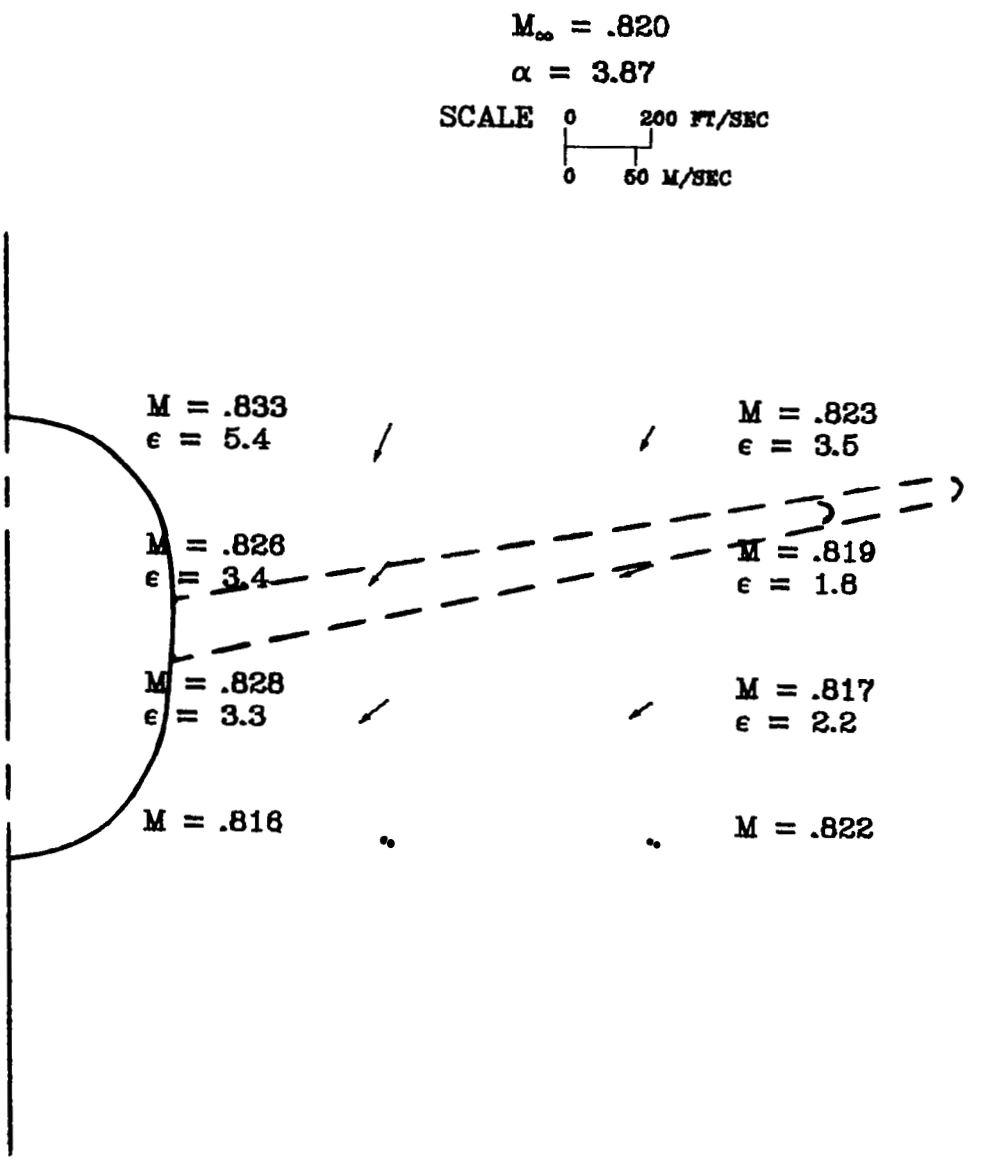

Figure 30.- Continued.

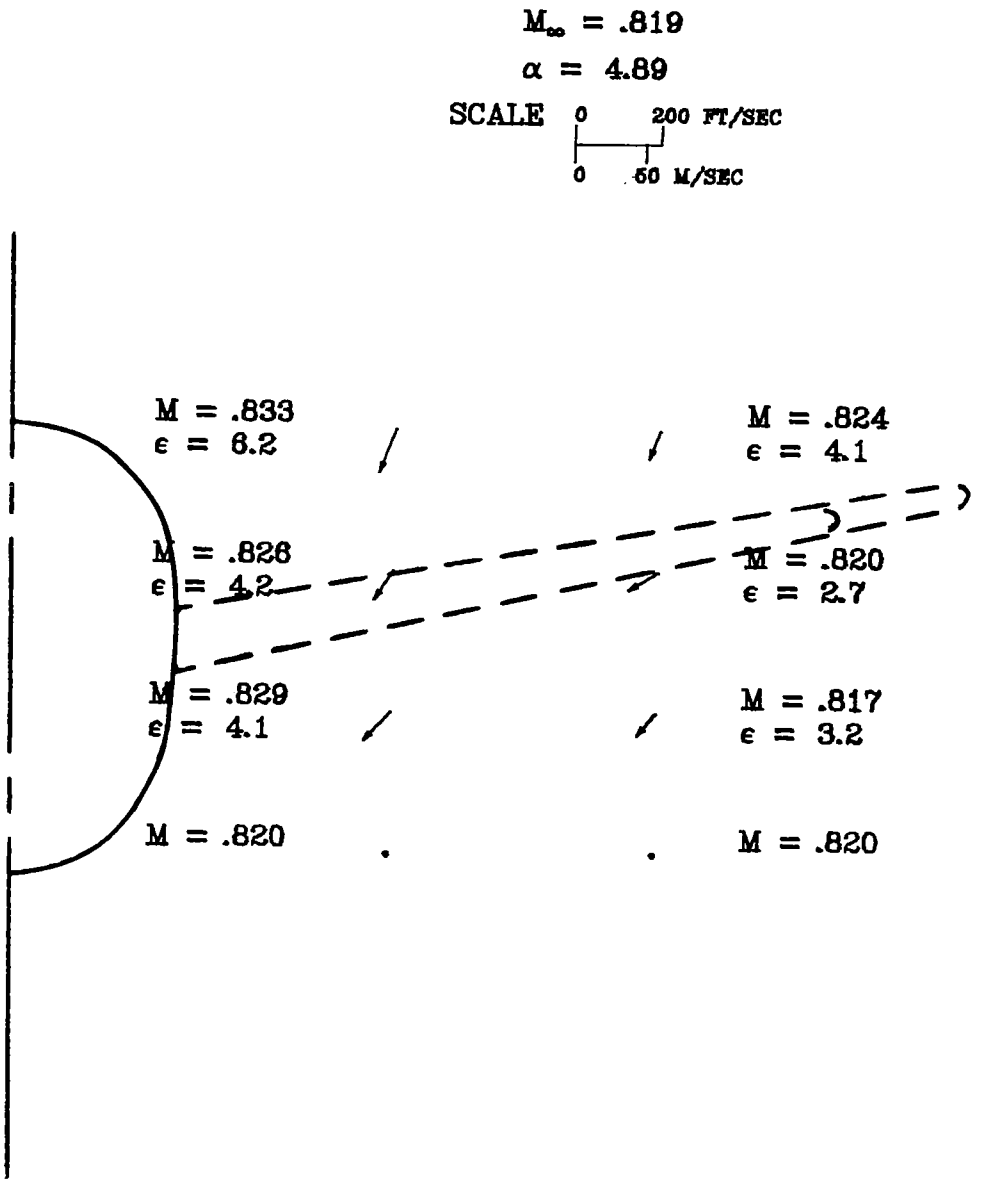

Figure 30.- Continued.

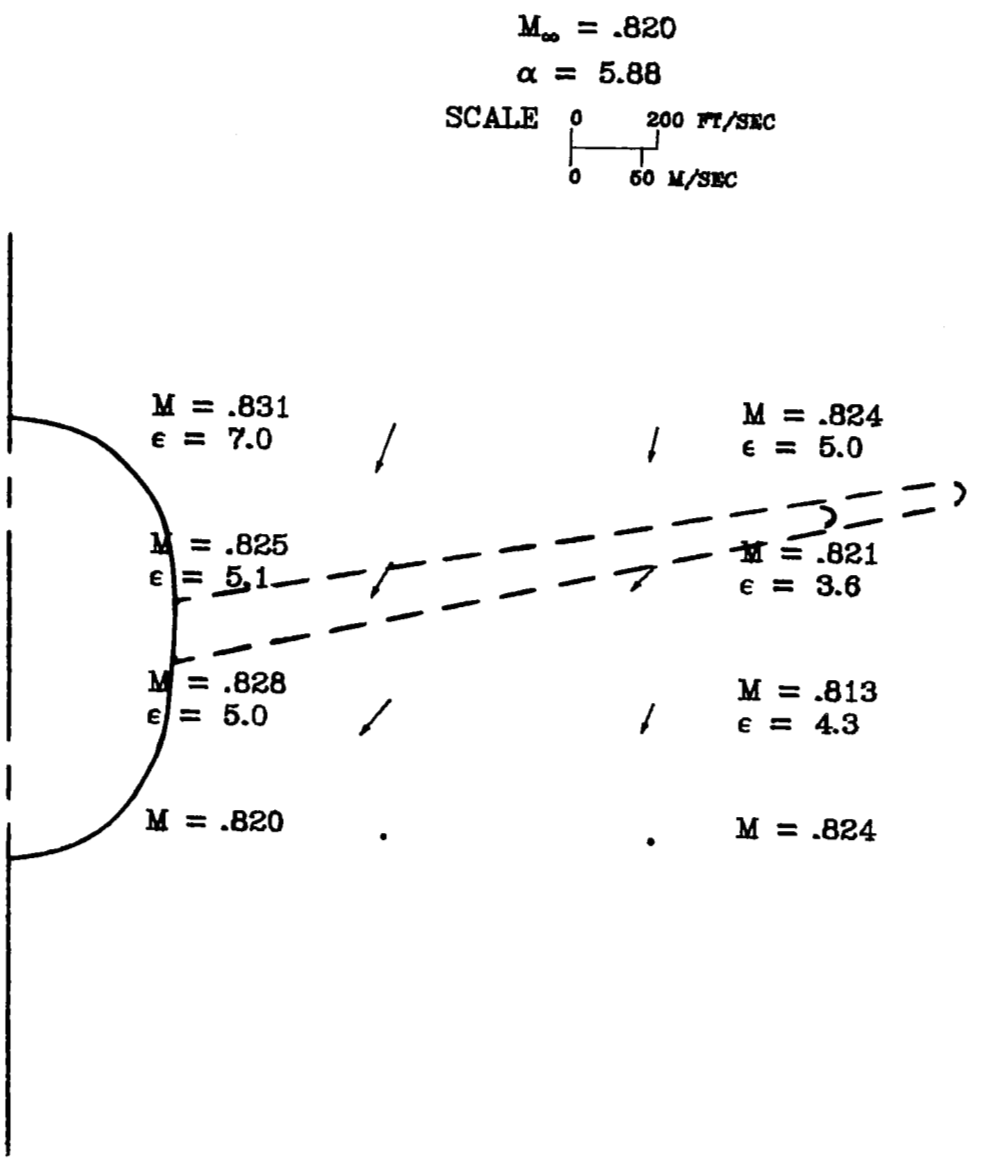

Figure 30.- Continued.

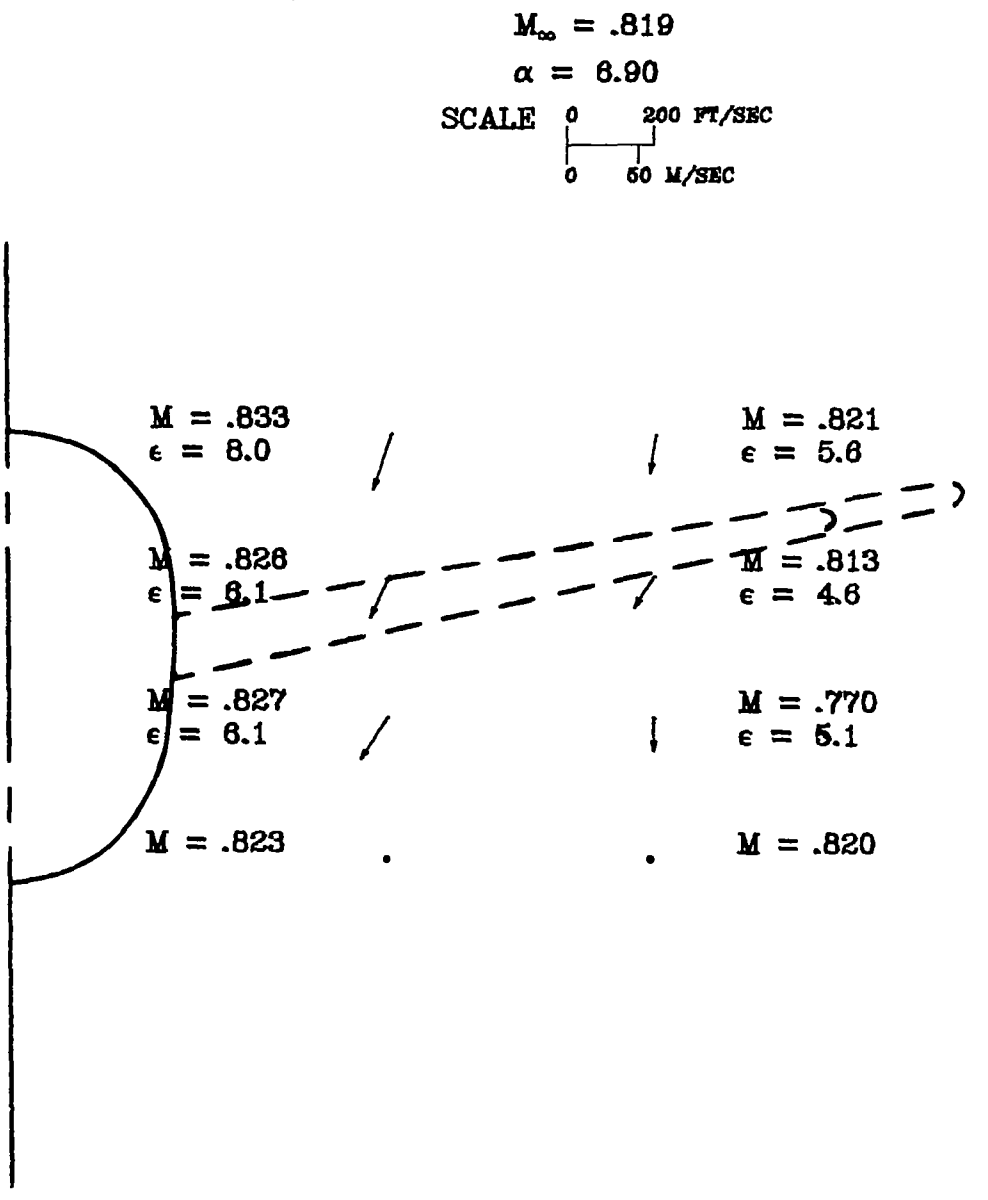

Figure 30.- Continued.

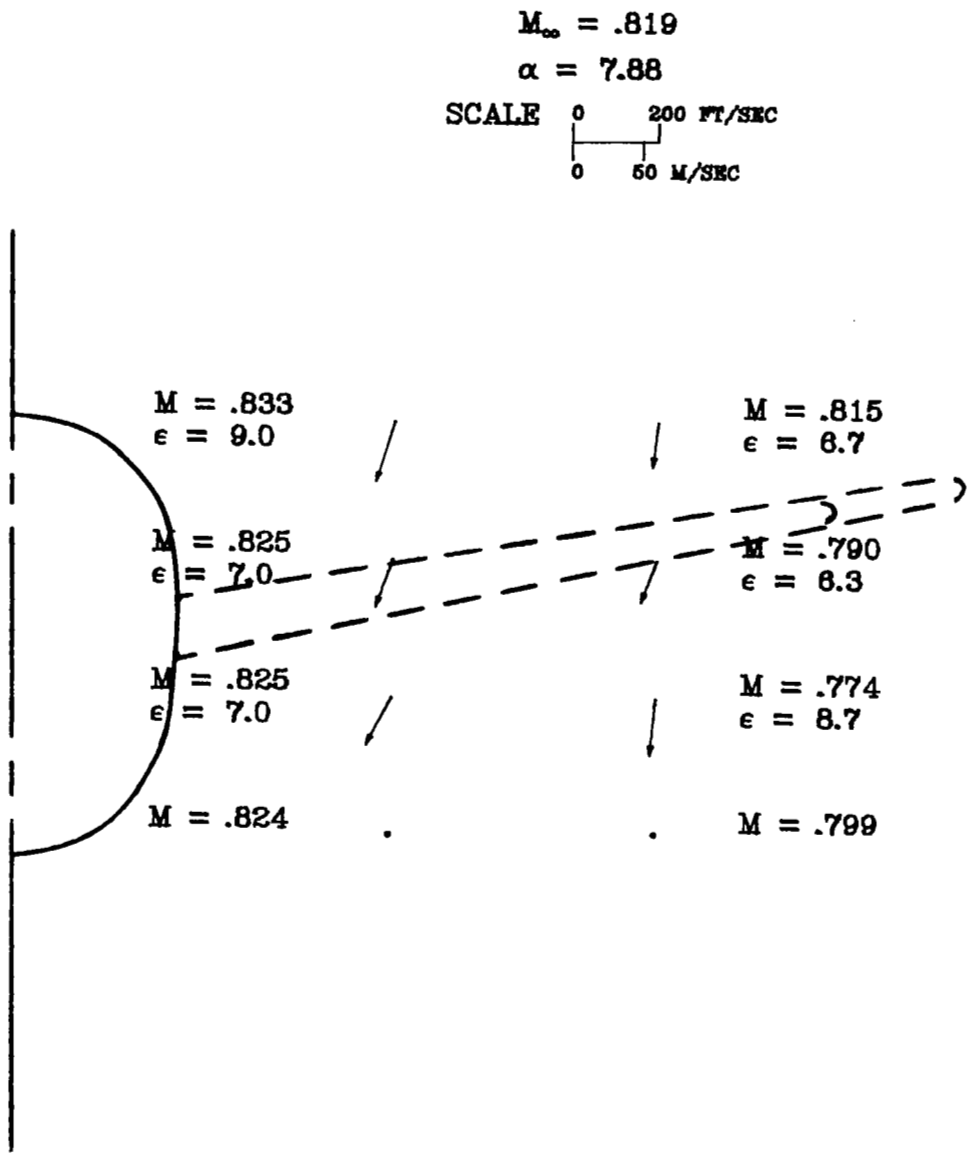

Figure 30.- Concluded.

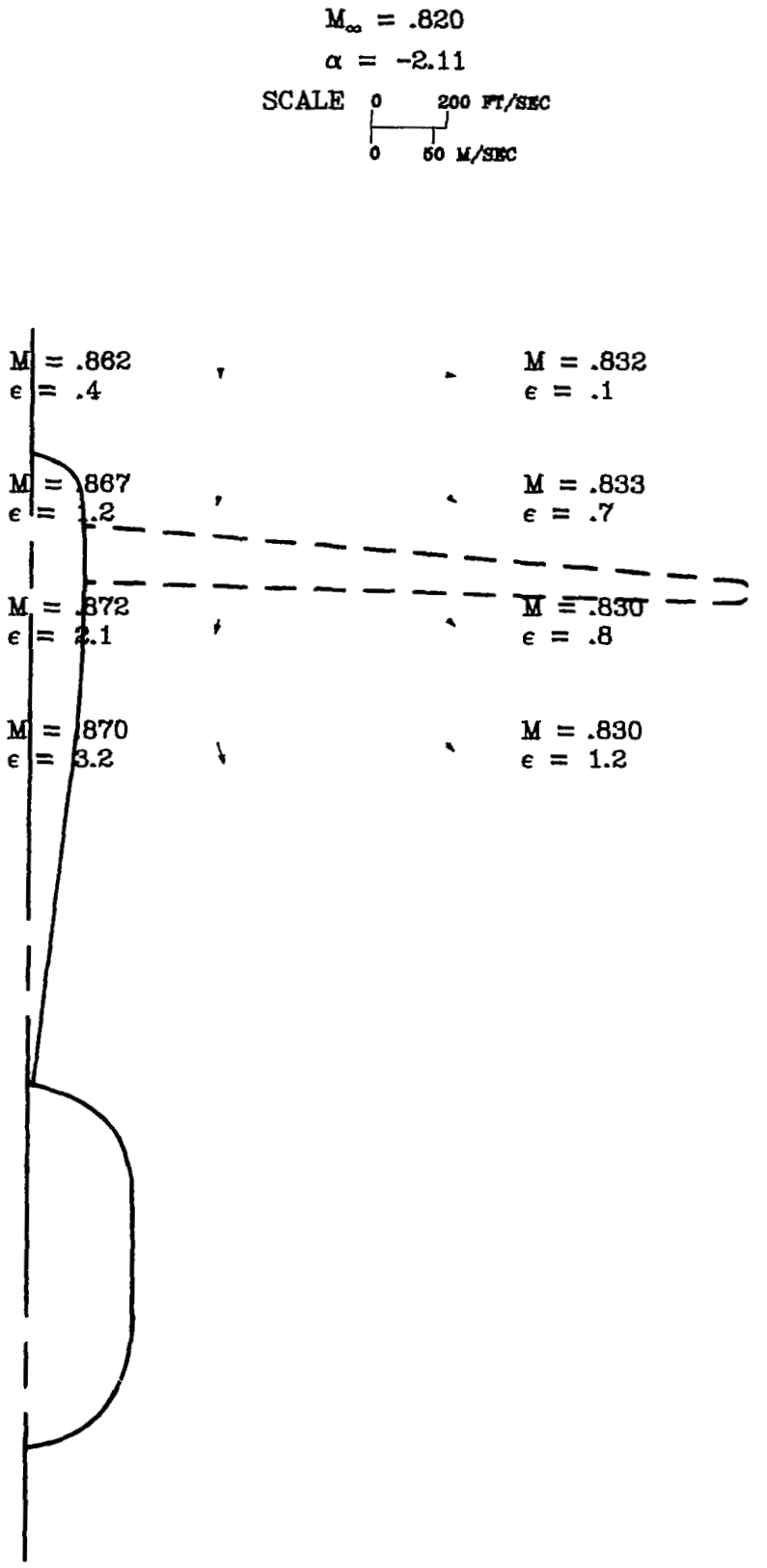

Figure 31.- Local Mach numbers and flow-field velocity vectors behind the wide-body wing with T-tail configuration.

$M_\infty = .820$

$\alpha = -.09$

SCALE 0 200 FT/SEC

0 50 M/SEC

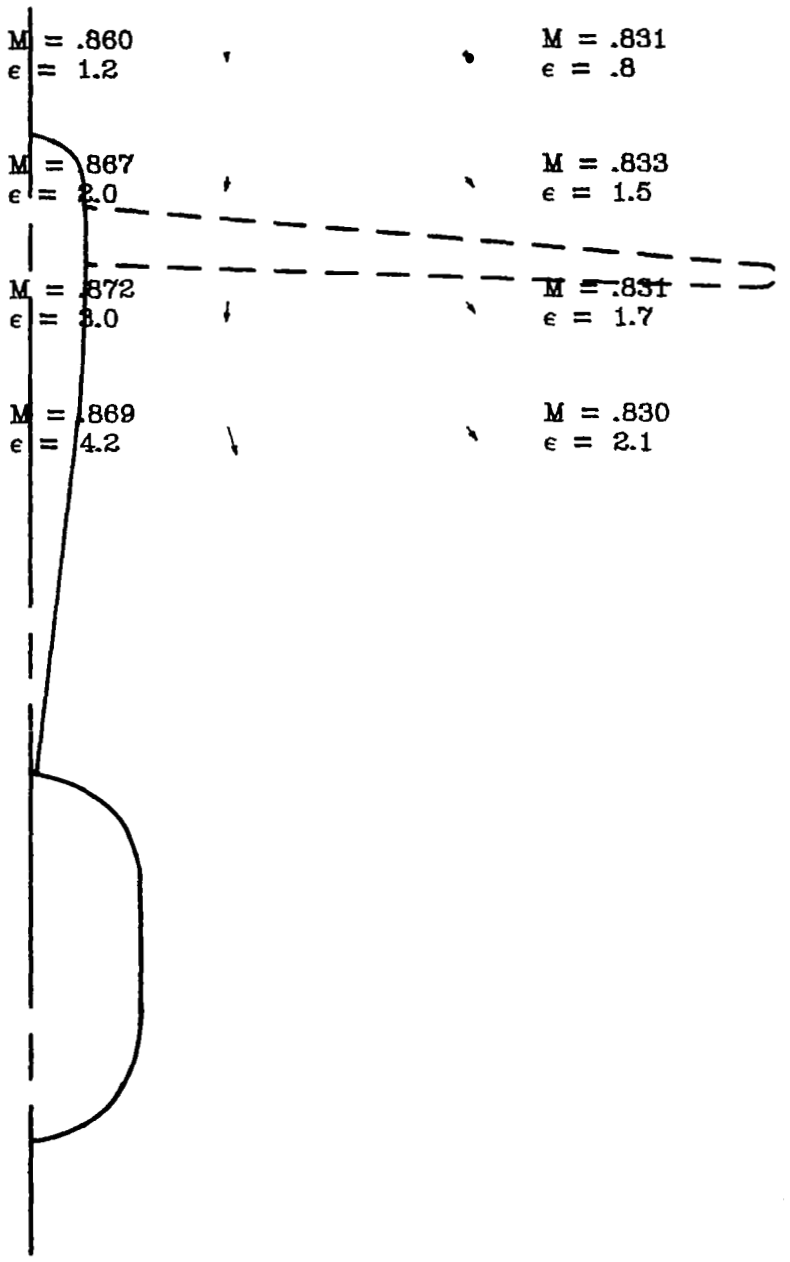

Figure 31.- Continued.

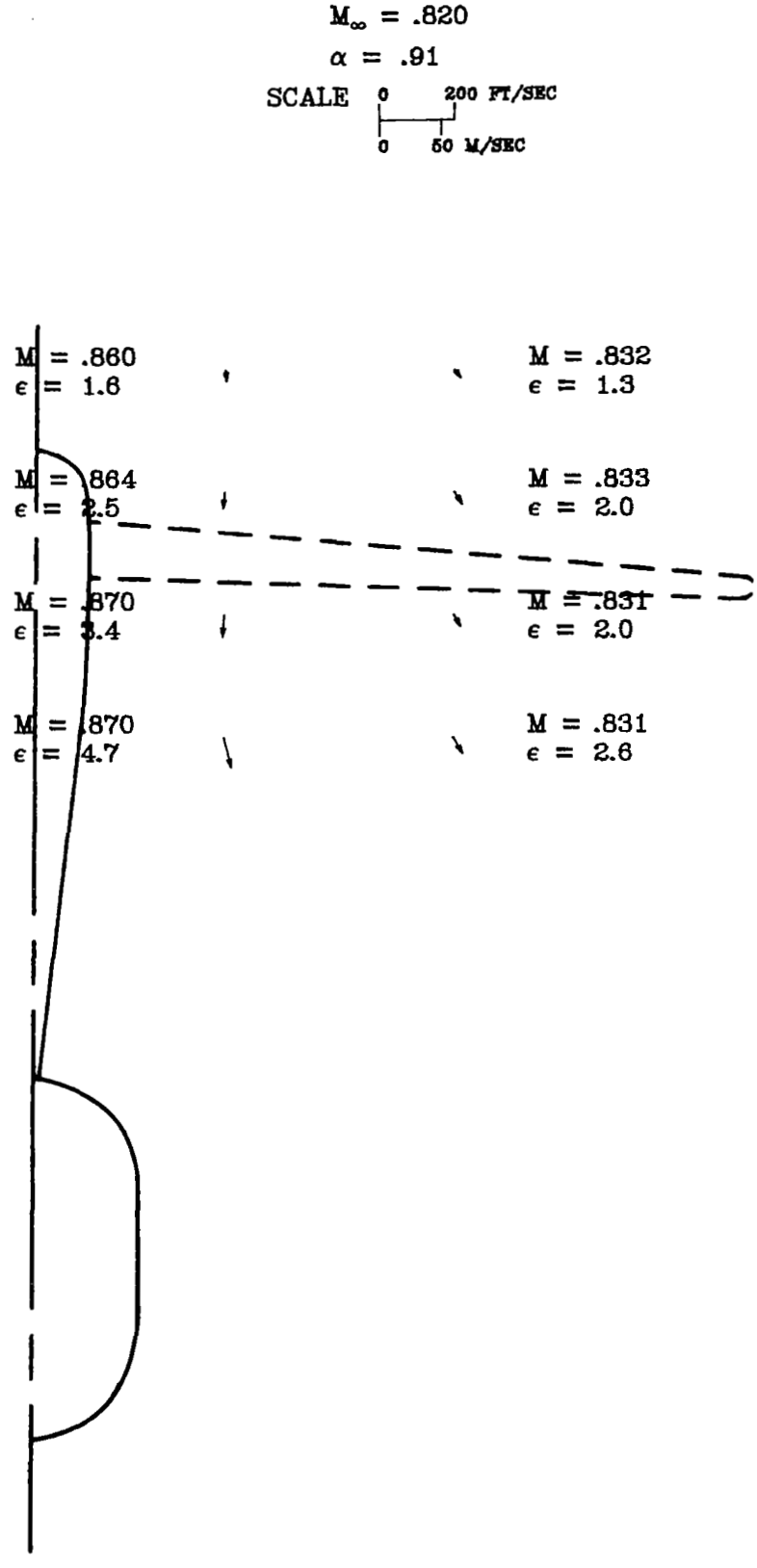

Figure 31.- Continued.

$M_\infty = .820$

$\alpha = 1.40$

SCALE 0 200 FT/SEC

0 60 M/SEC

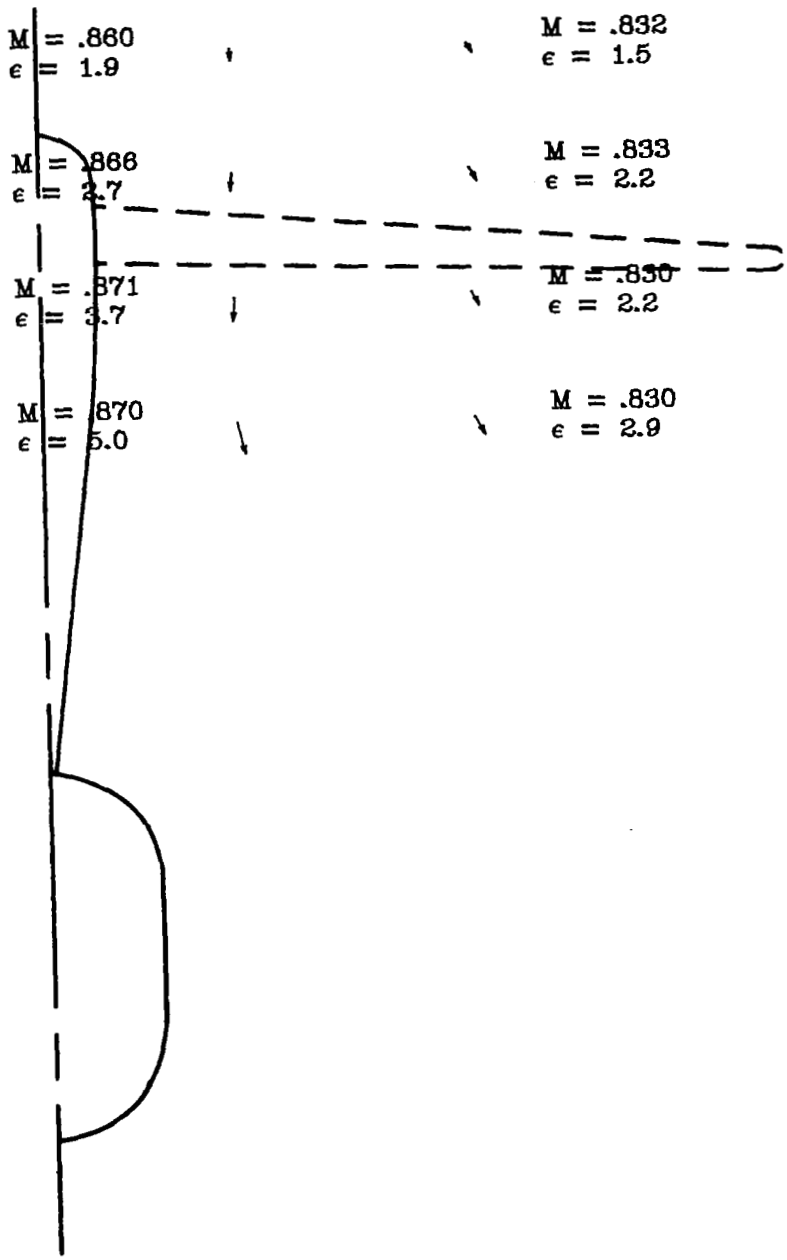

Figure 31.- Continued.

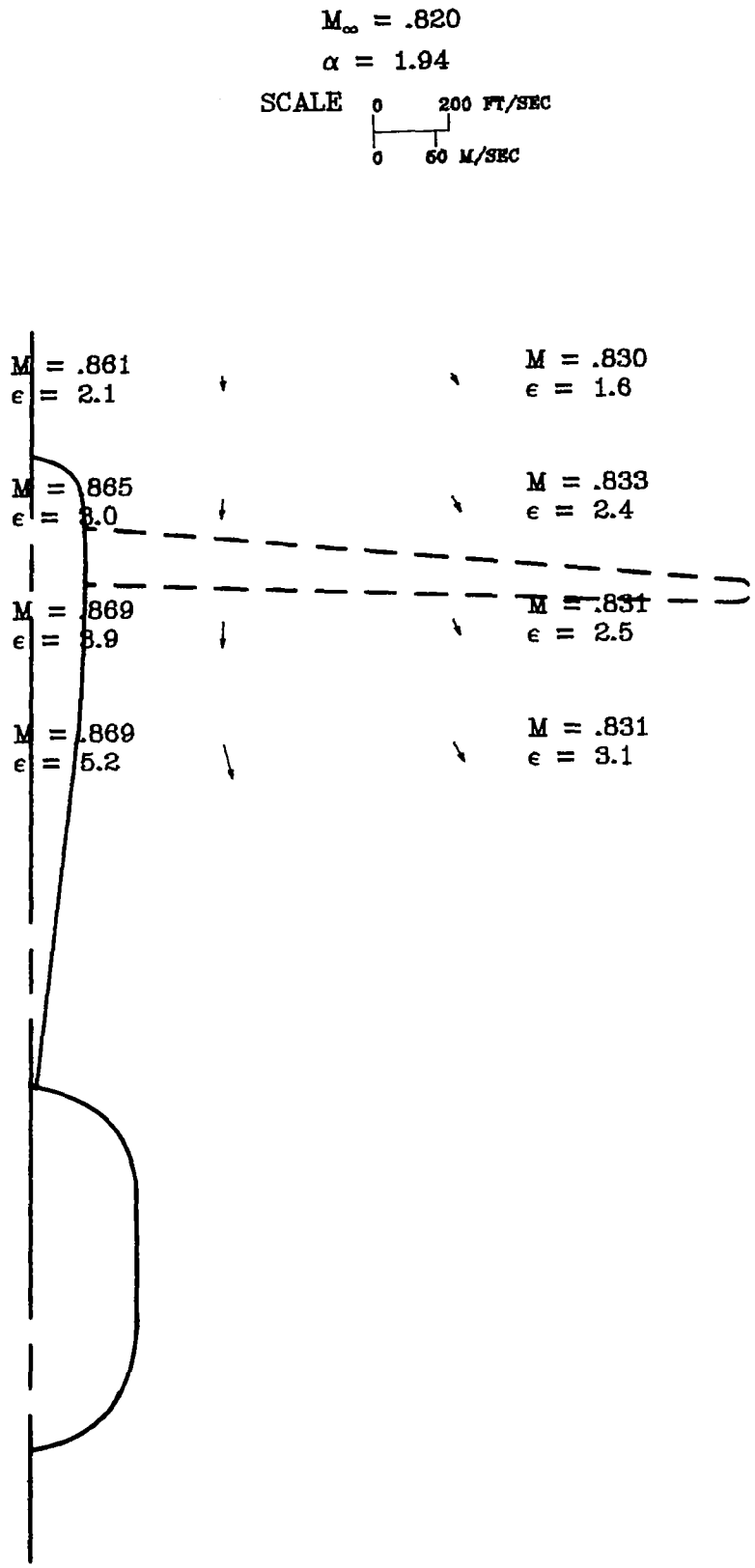

Figure 31.- Continued.

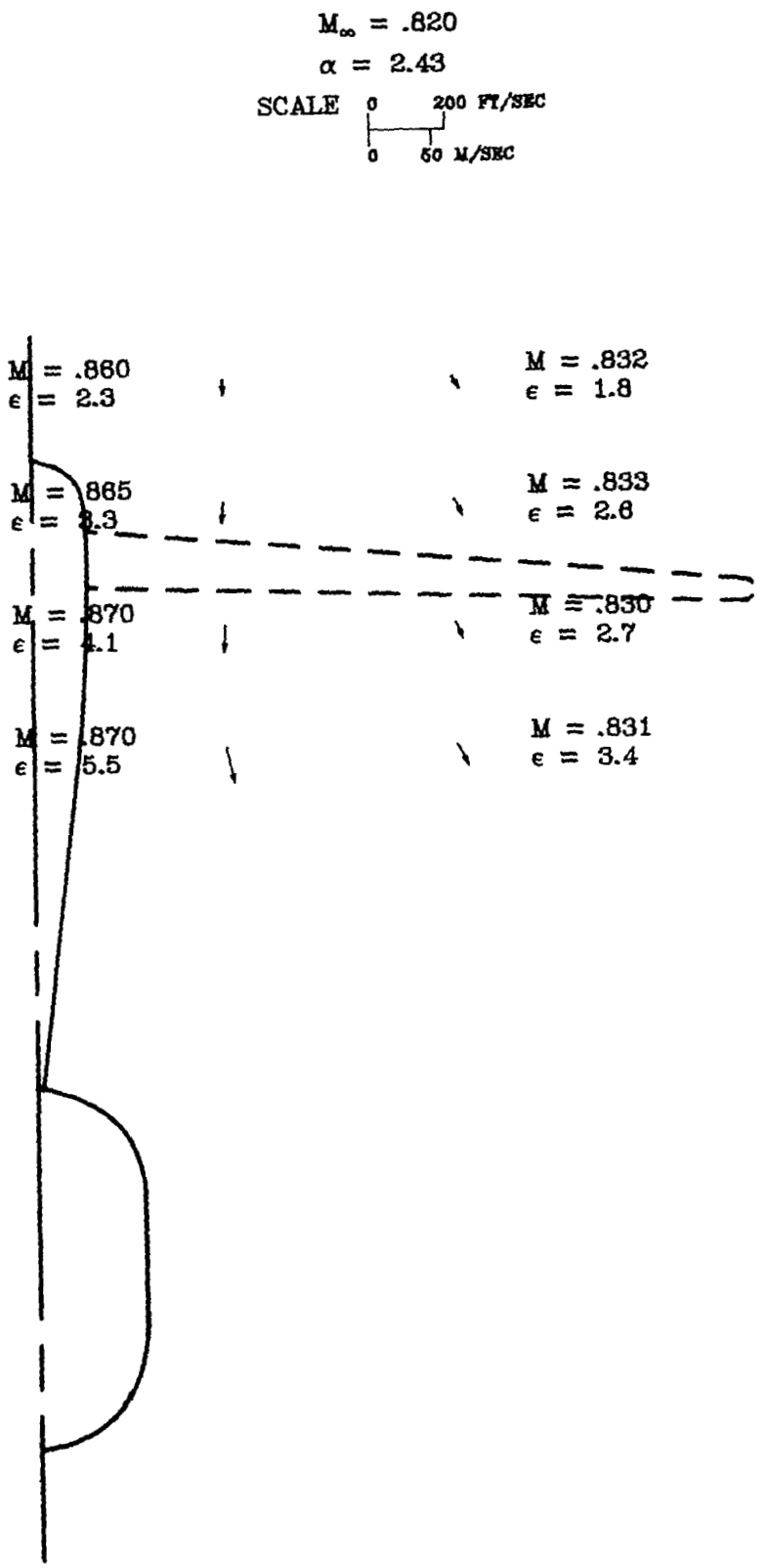

Figure 31.- Continued.

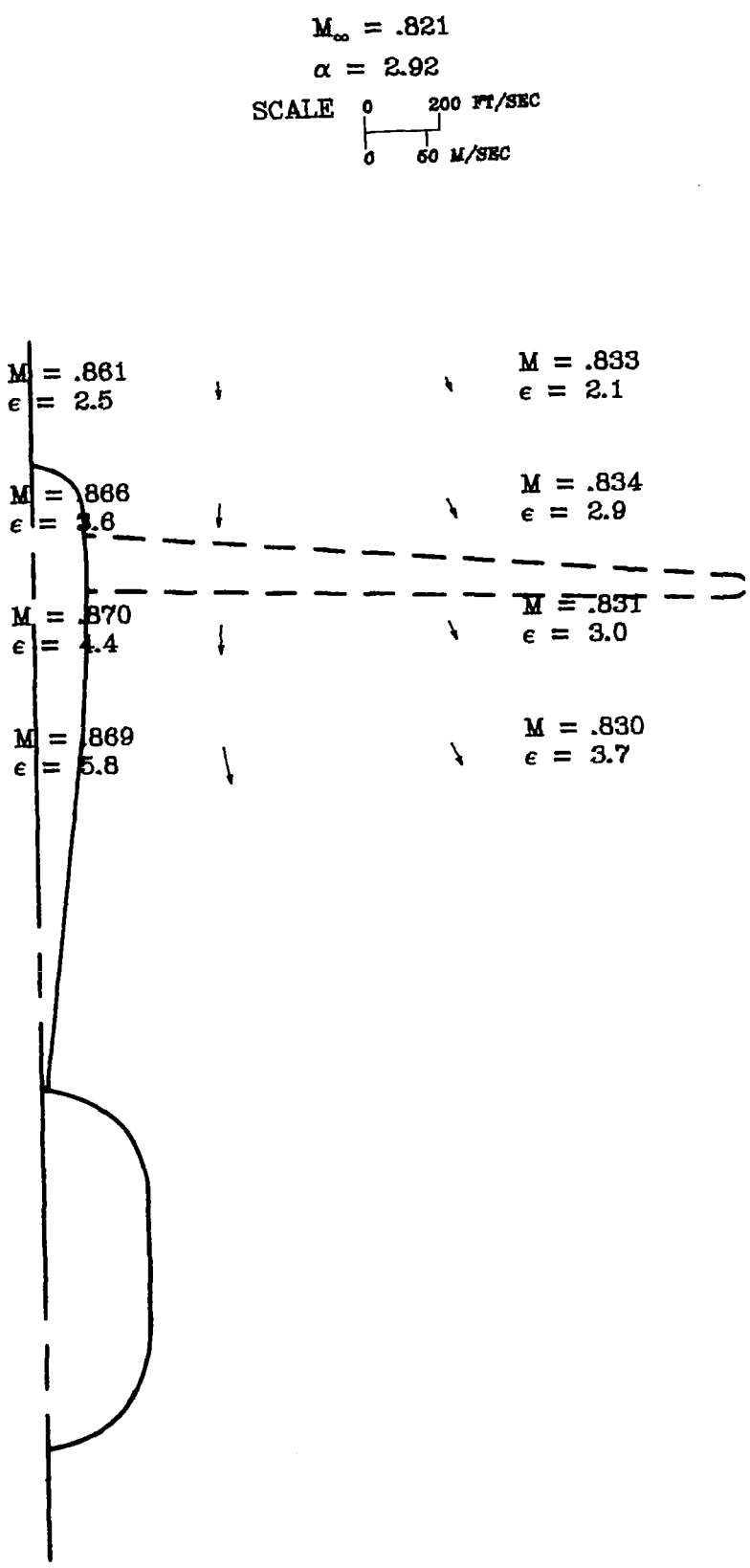

Figure 31.- Continued.

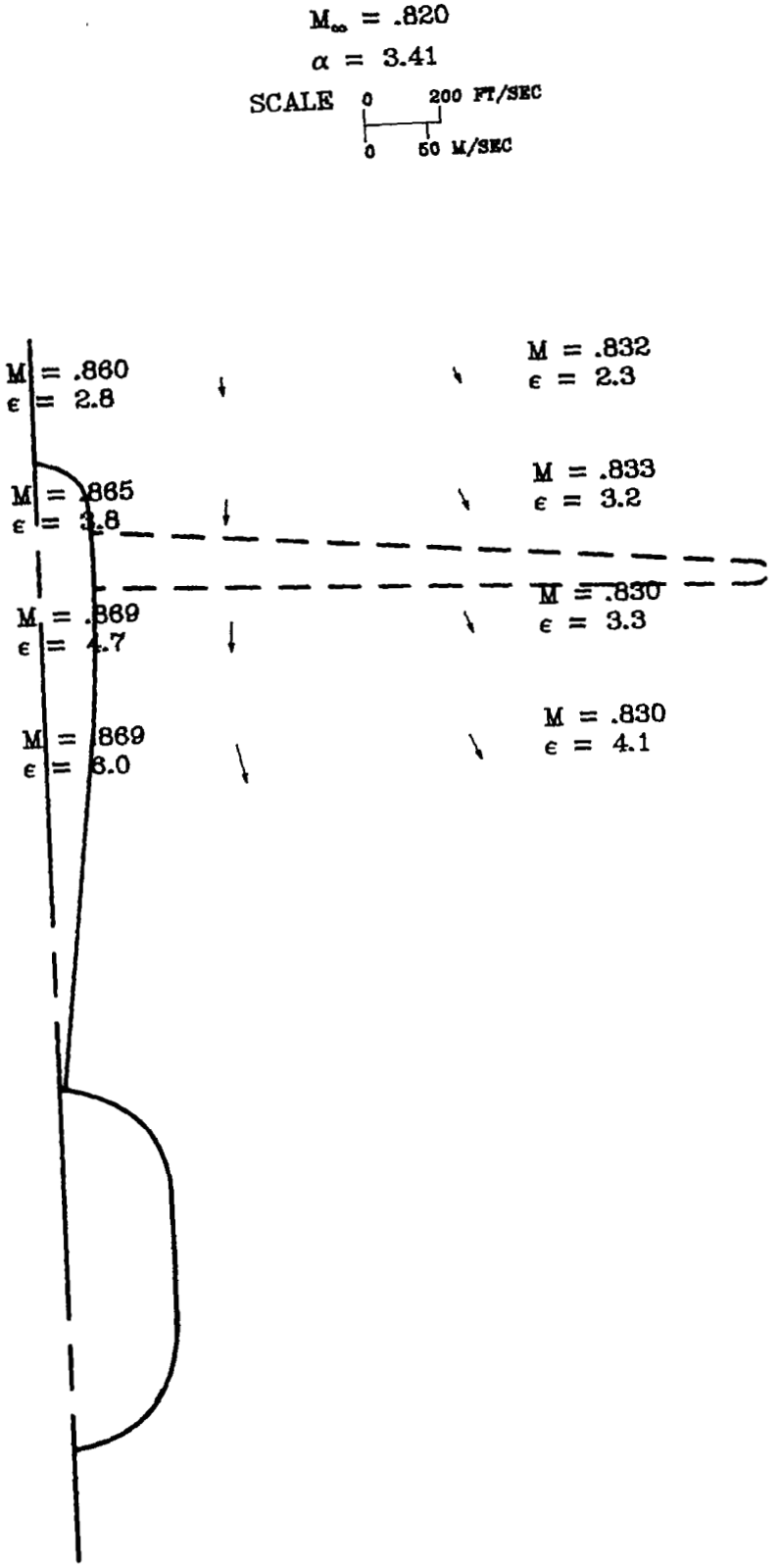

Figure 31.- Continued.

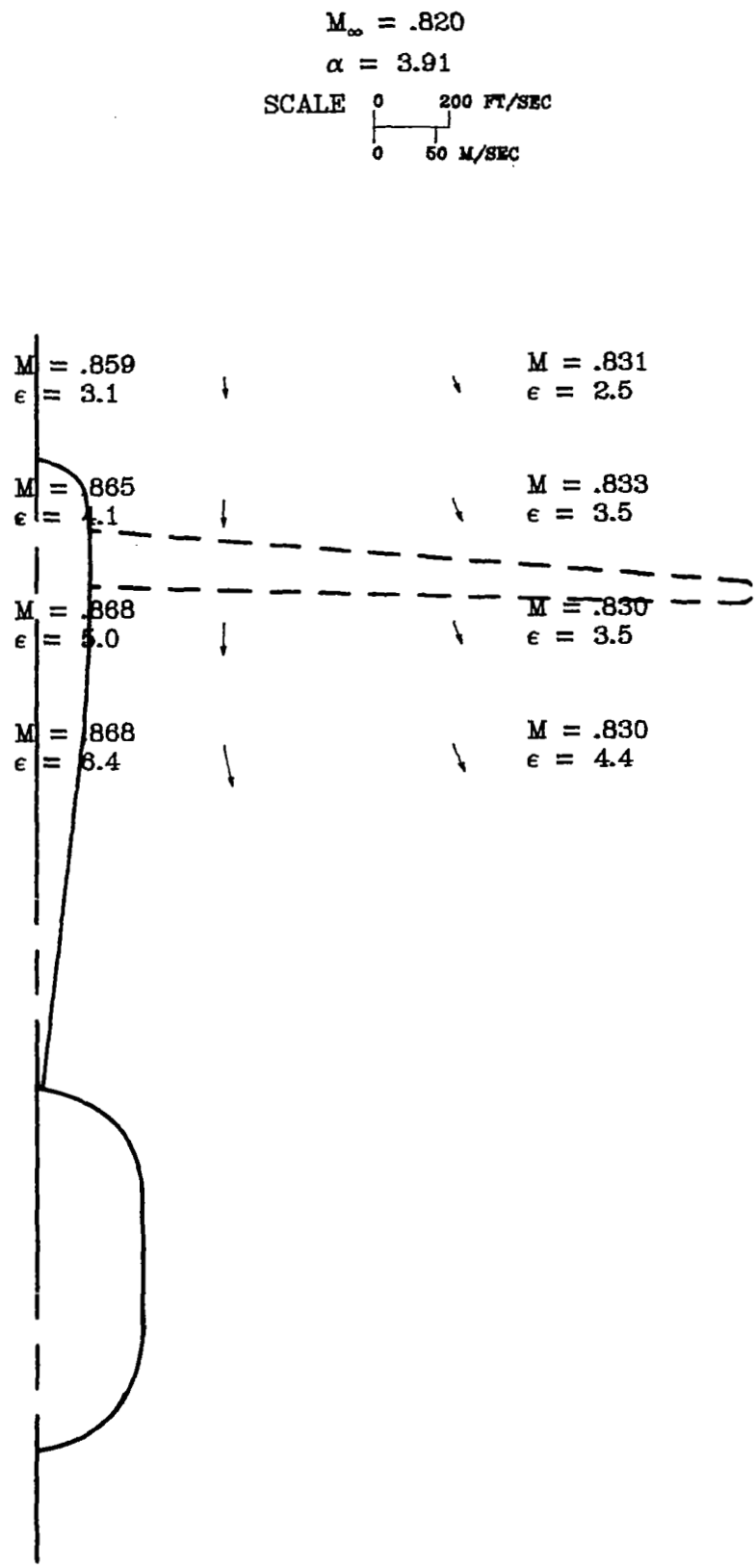

Figure 31.- Continued.

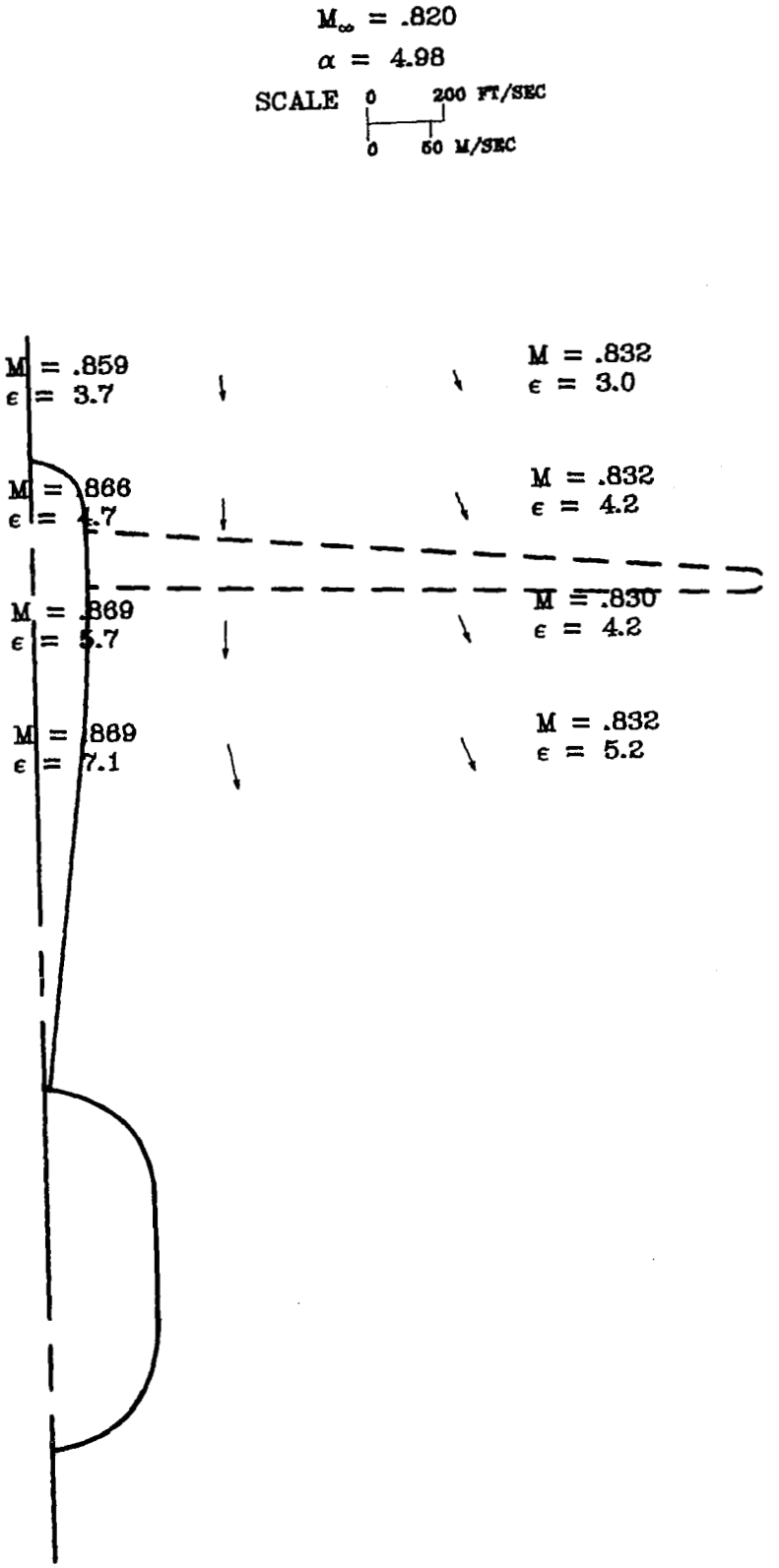

Figure 31.- Continued.

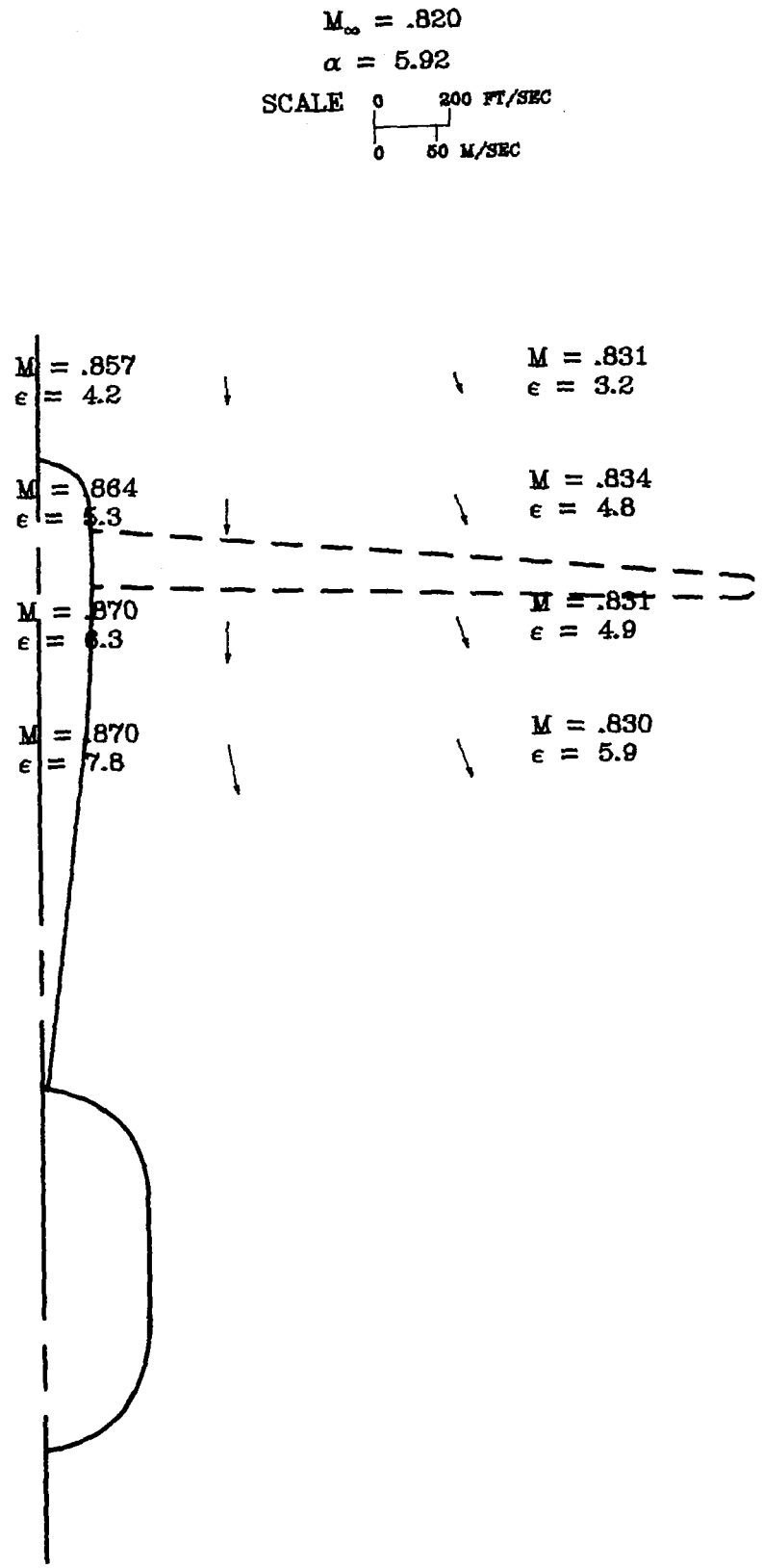

Figure 31.- Continued.

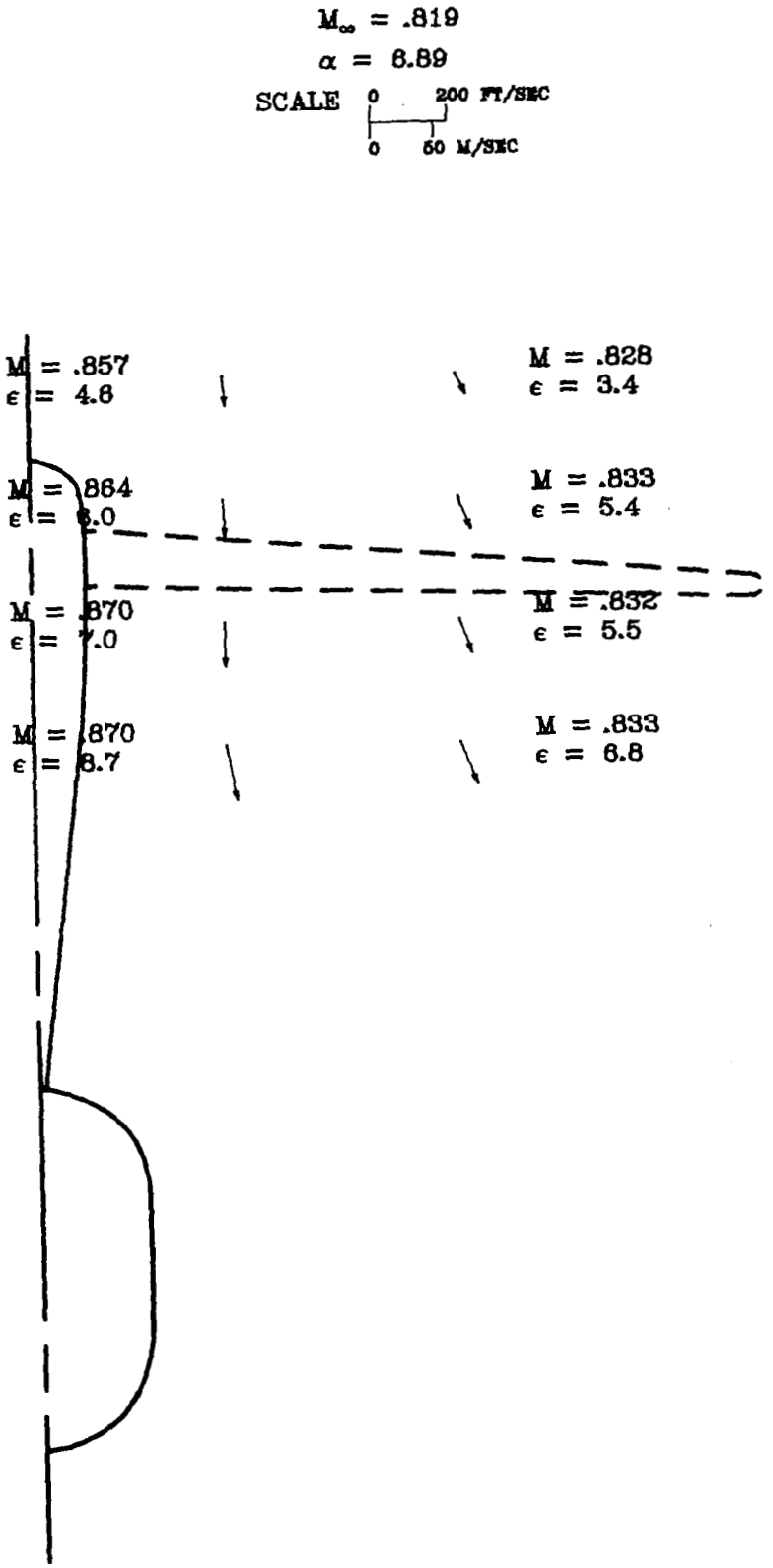

Figure 31.- Continued.

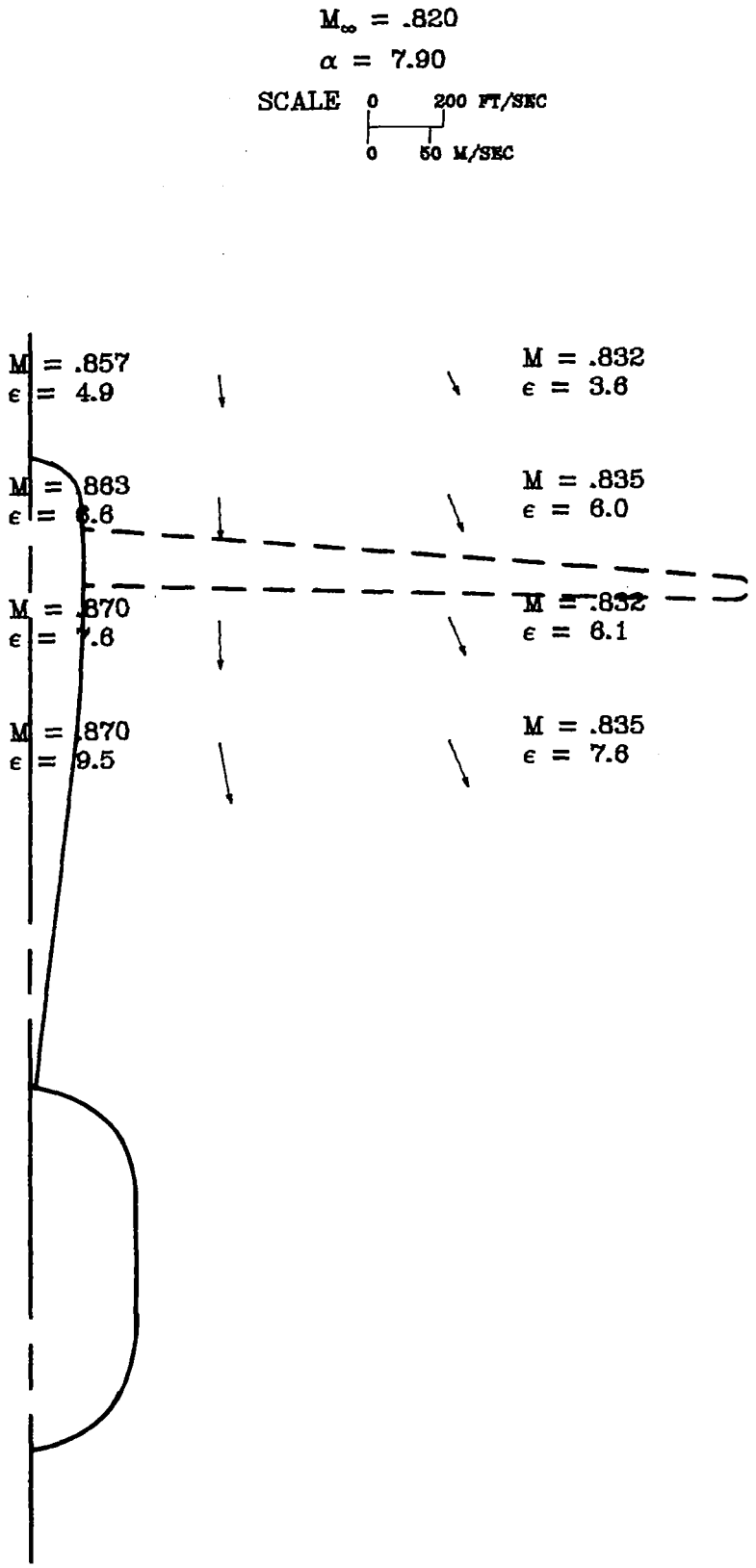

Figure 31.- Concluded.

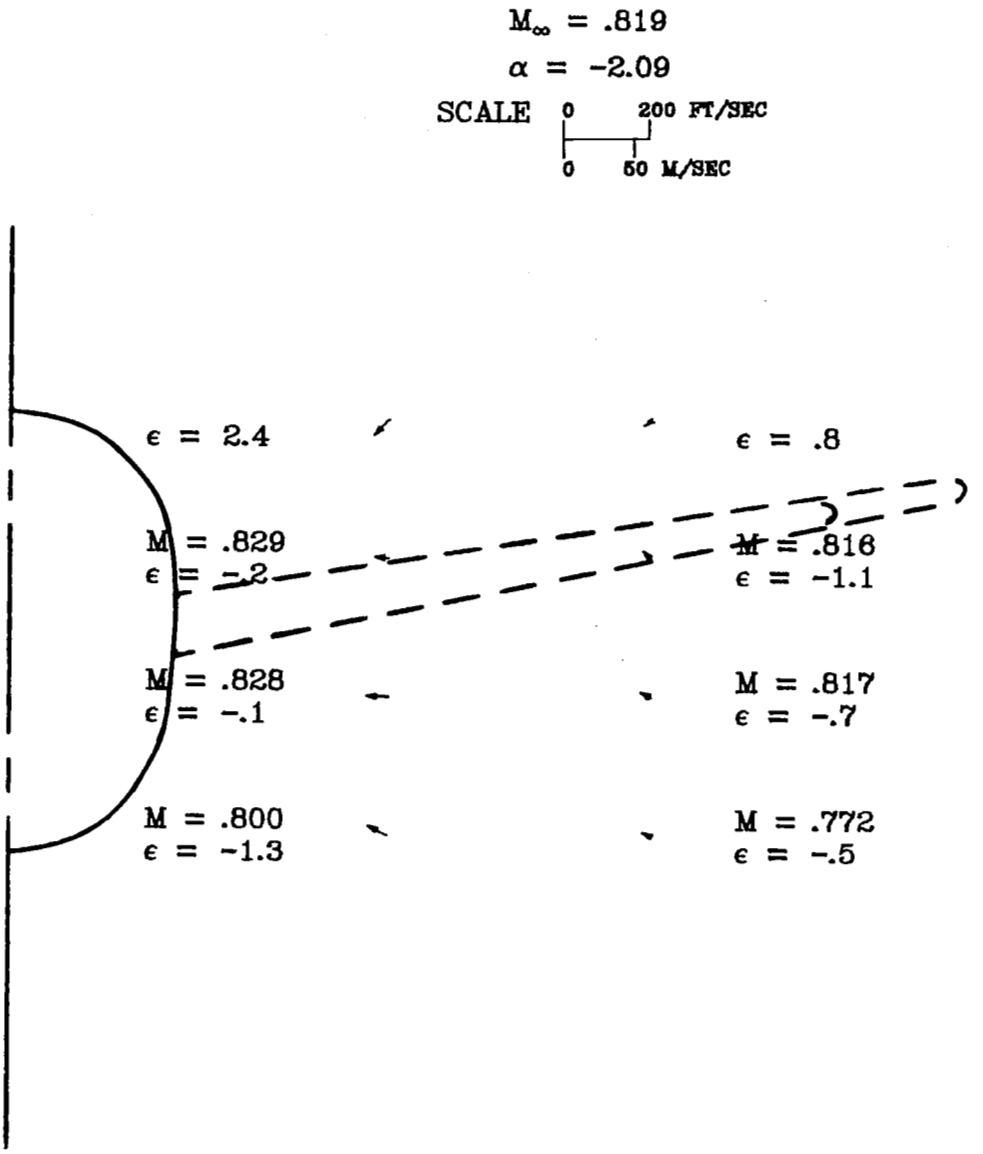

Figure 32.- Local Mach numbers and flow-field velocity vectors behind the supercritical wing with low-tail configuration.

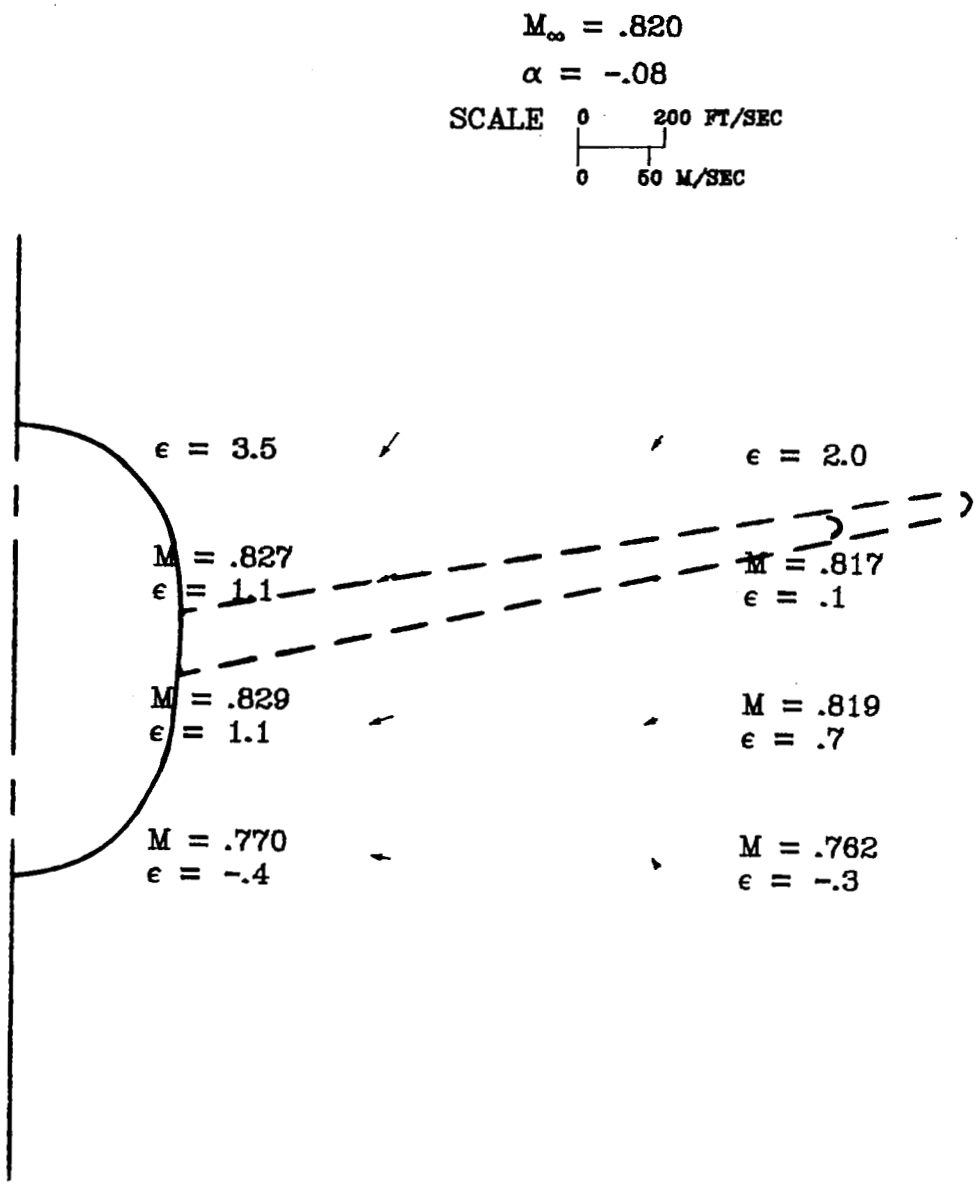

Figure 32.- Continued.

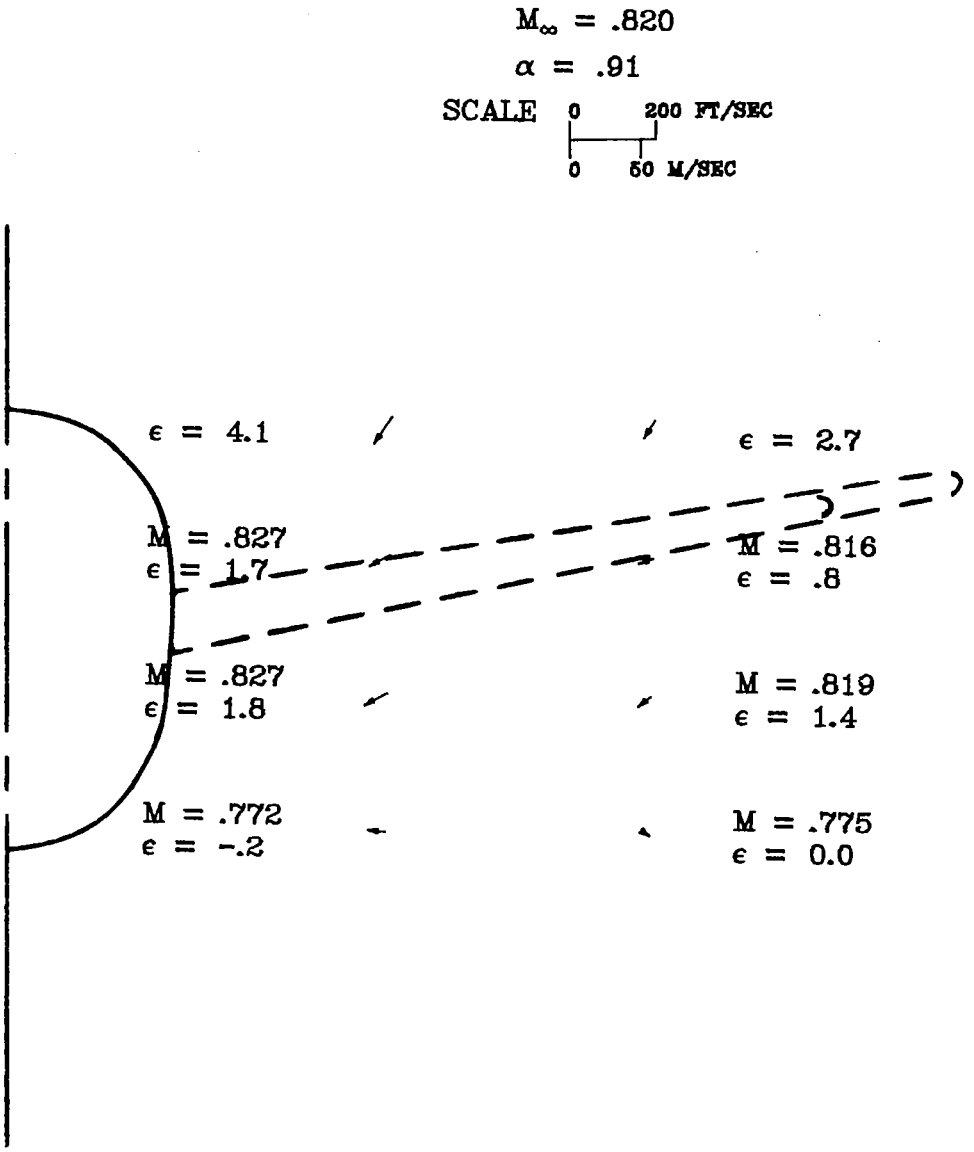

Figure 32.- Continued.

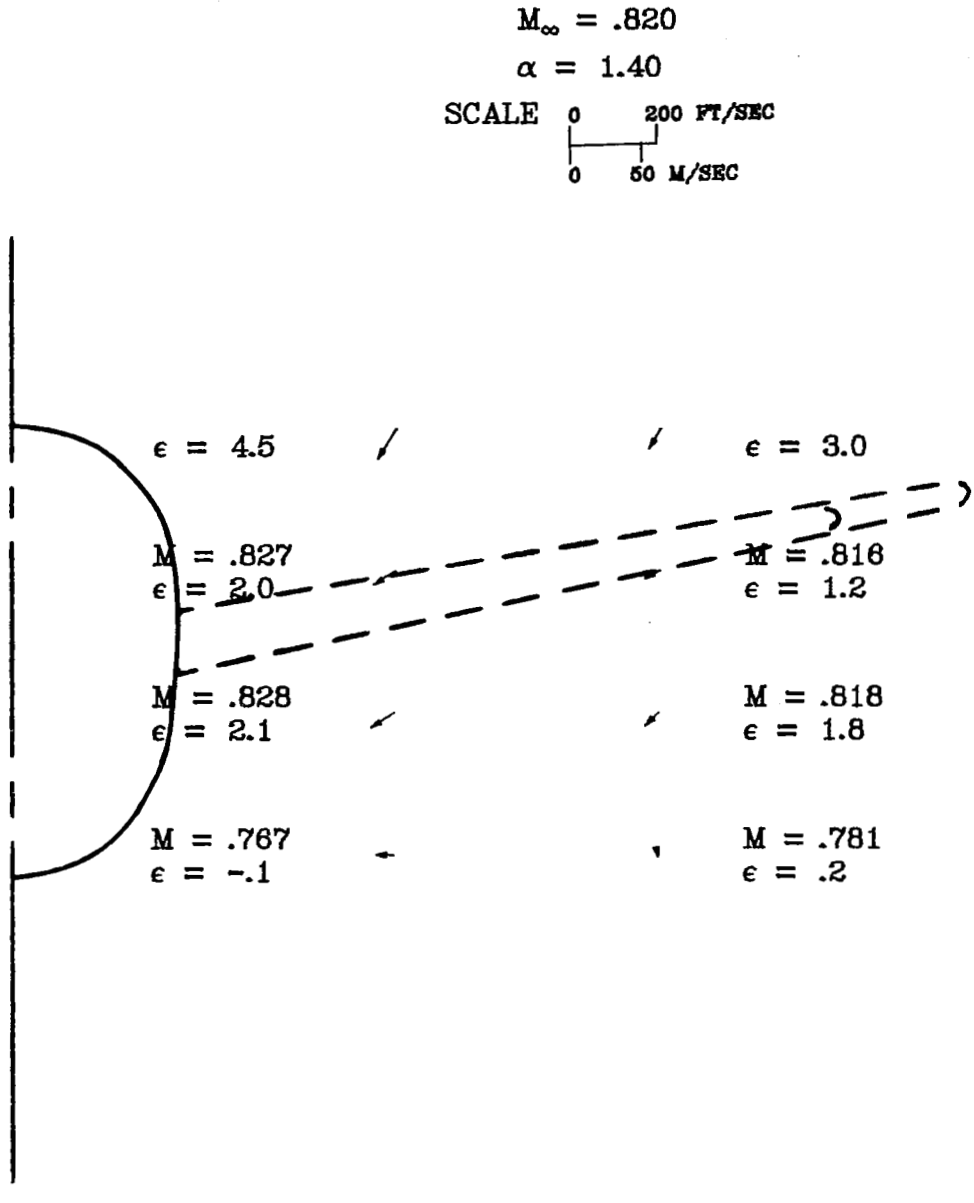

Figure 32.- Continued.

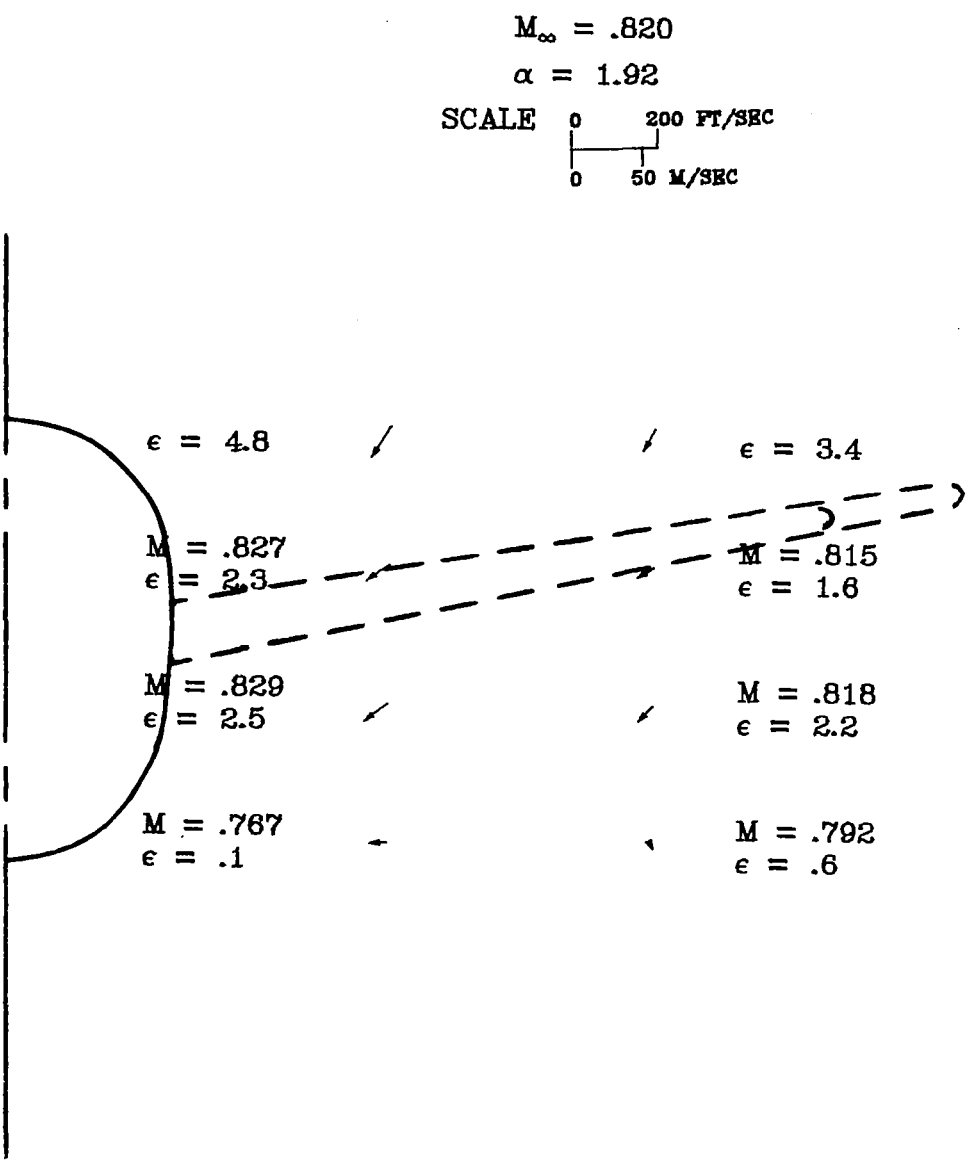

Figure 32.- Continued.

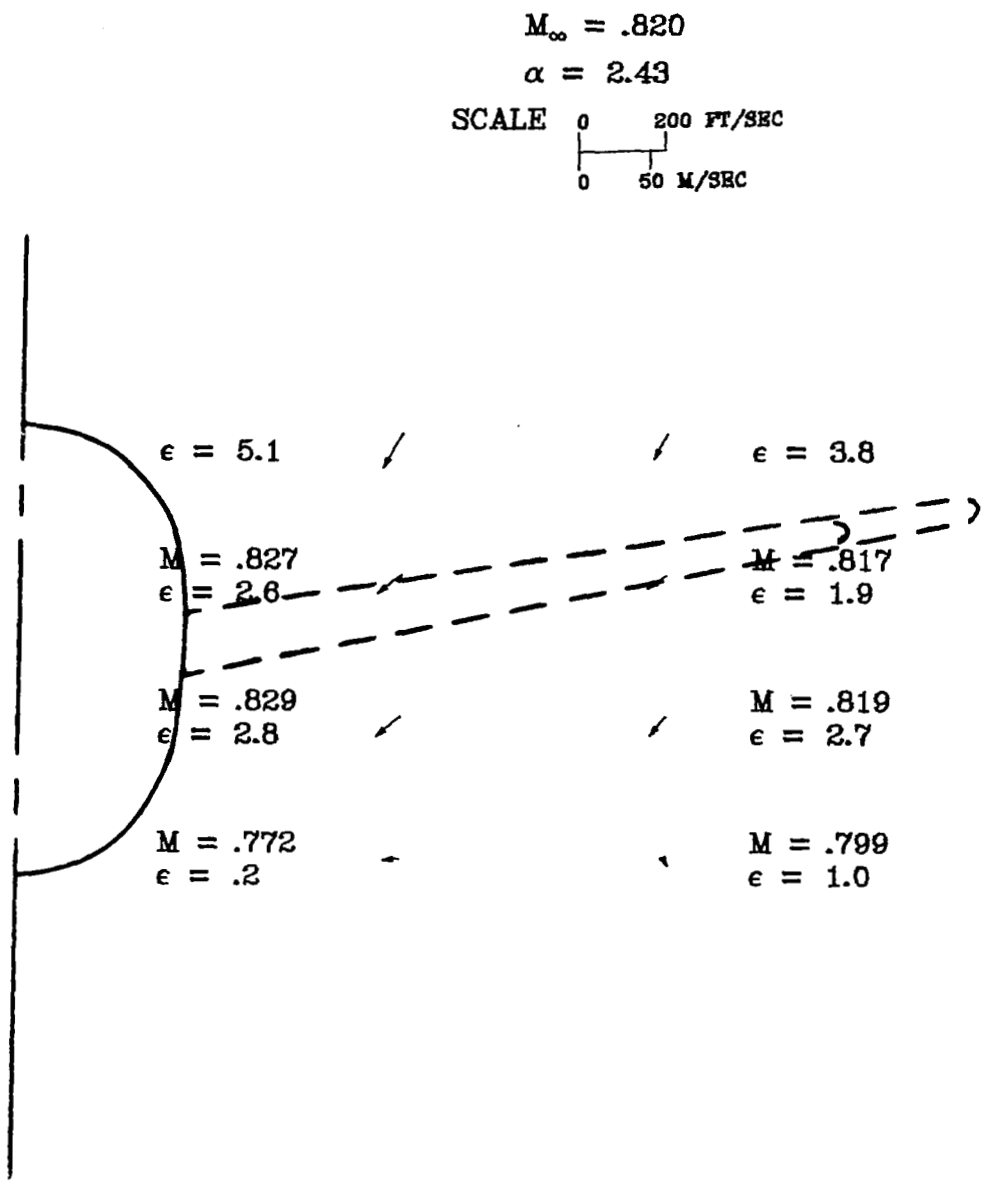

Figure 32.- Continued.

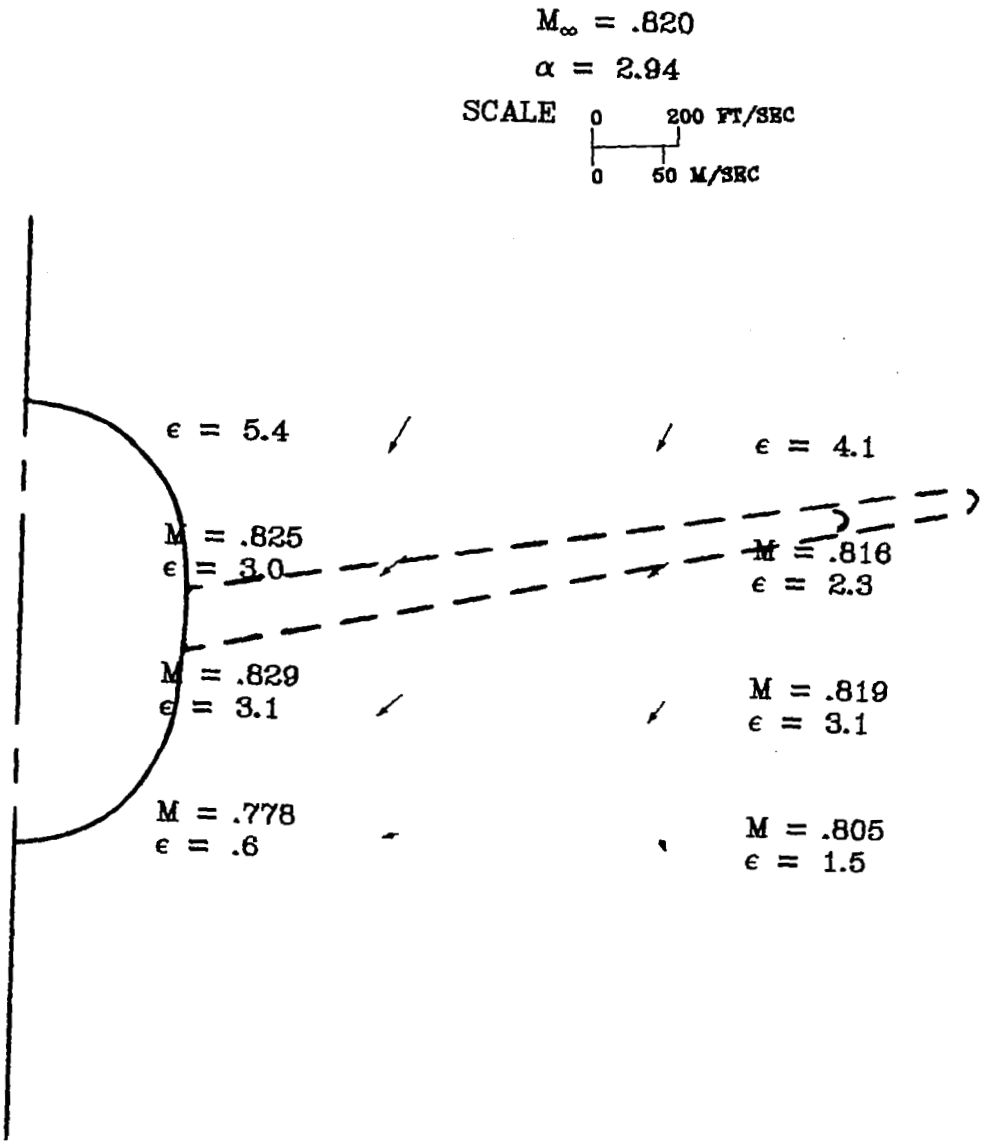

Figure 32.- Continued.

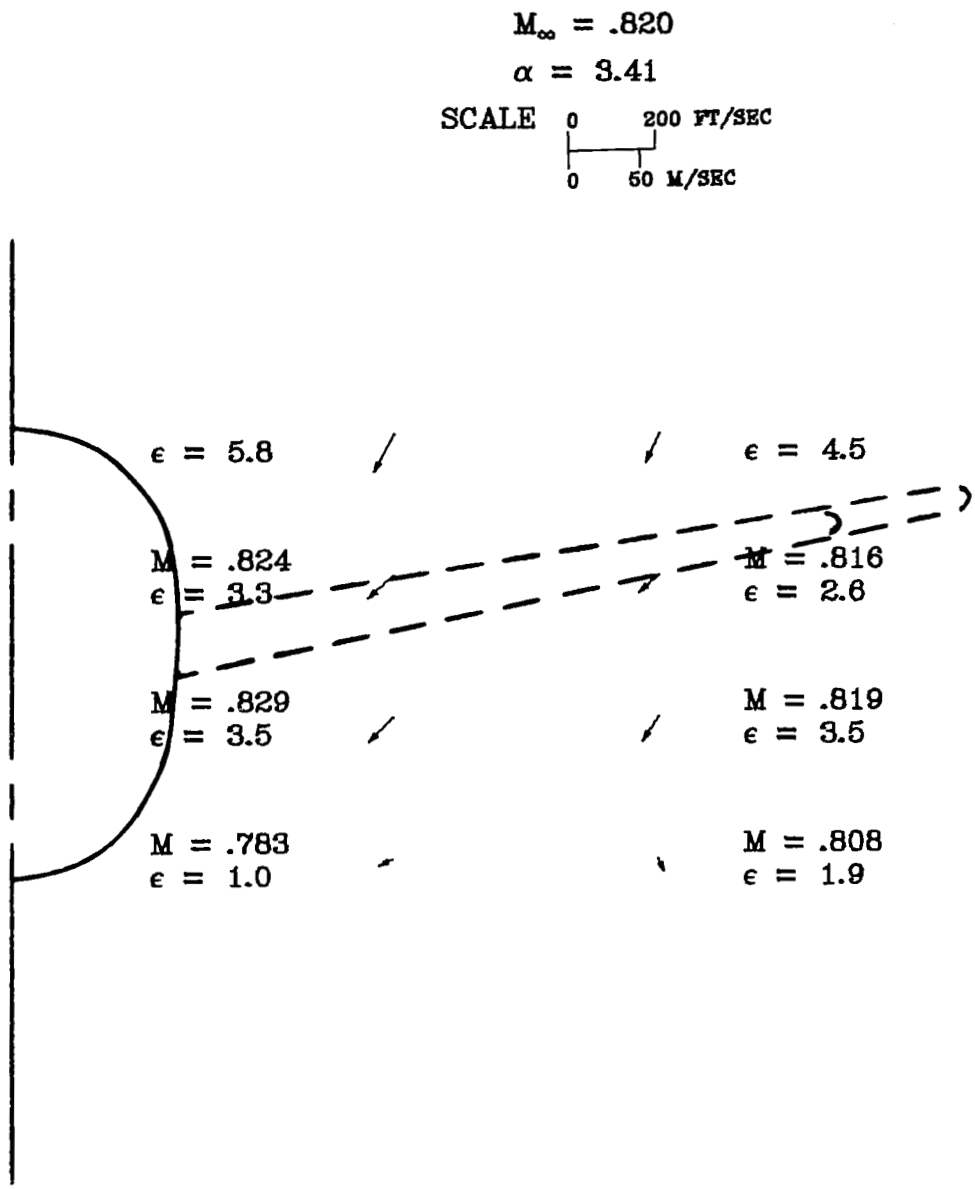

Figure 32.- Continued.

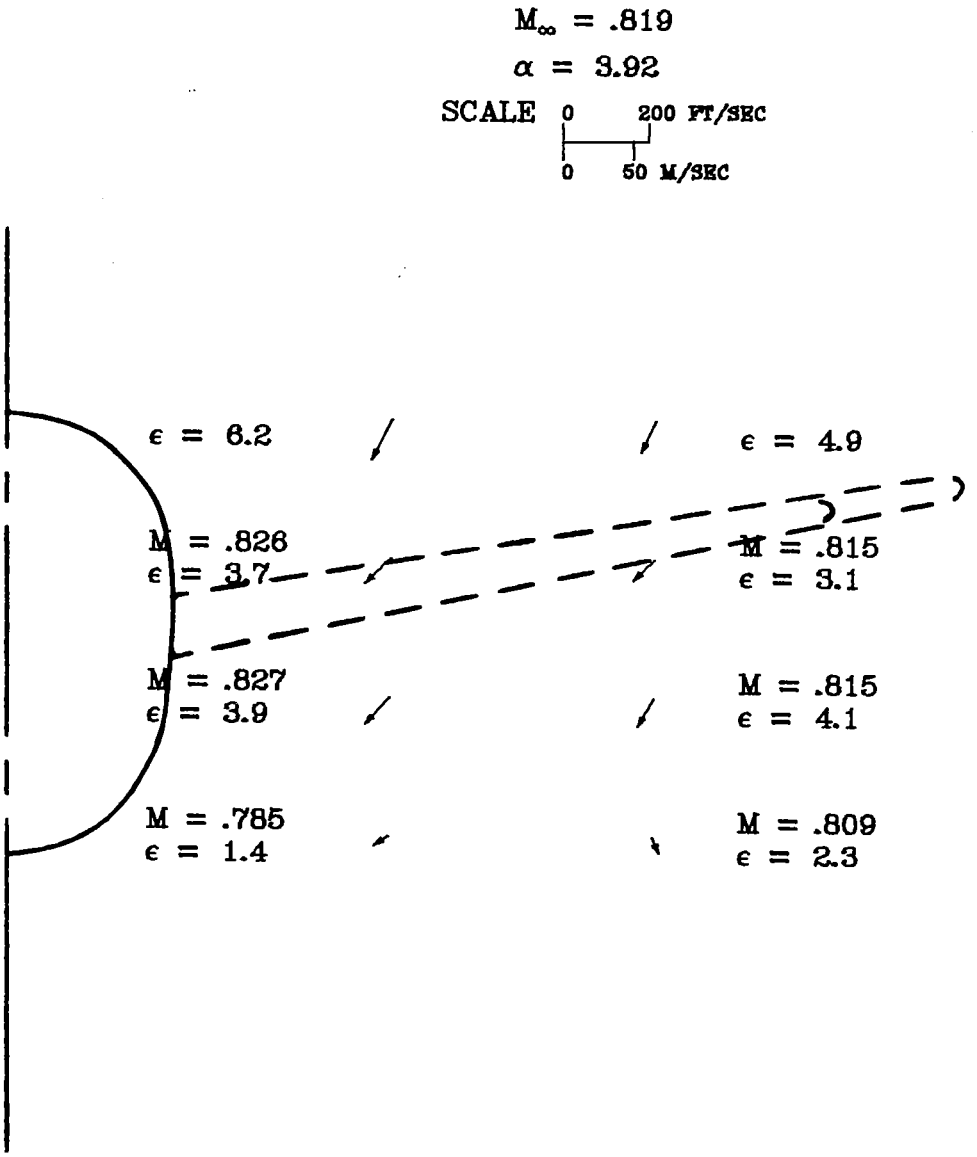

Figure 32.- Continued.

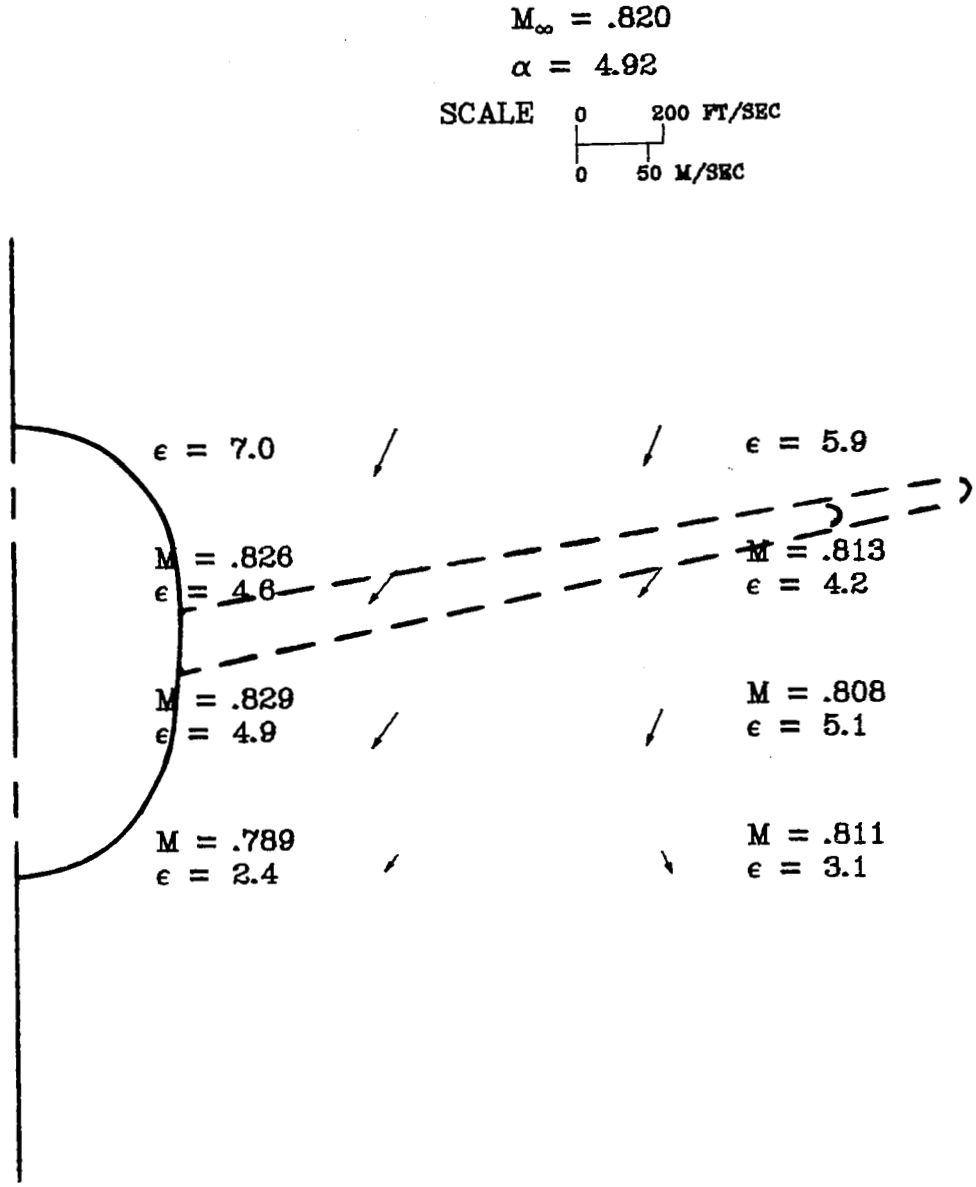

Figure 32.- Continued.

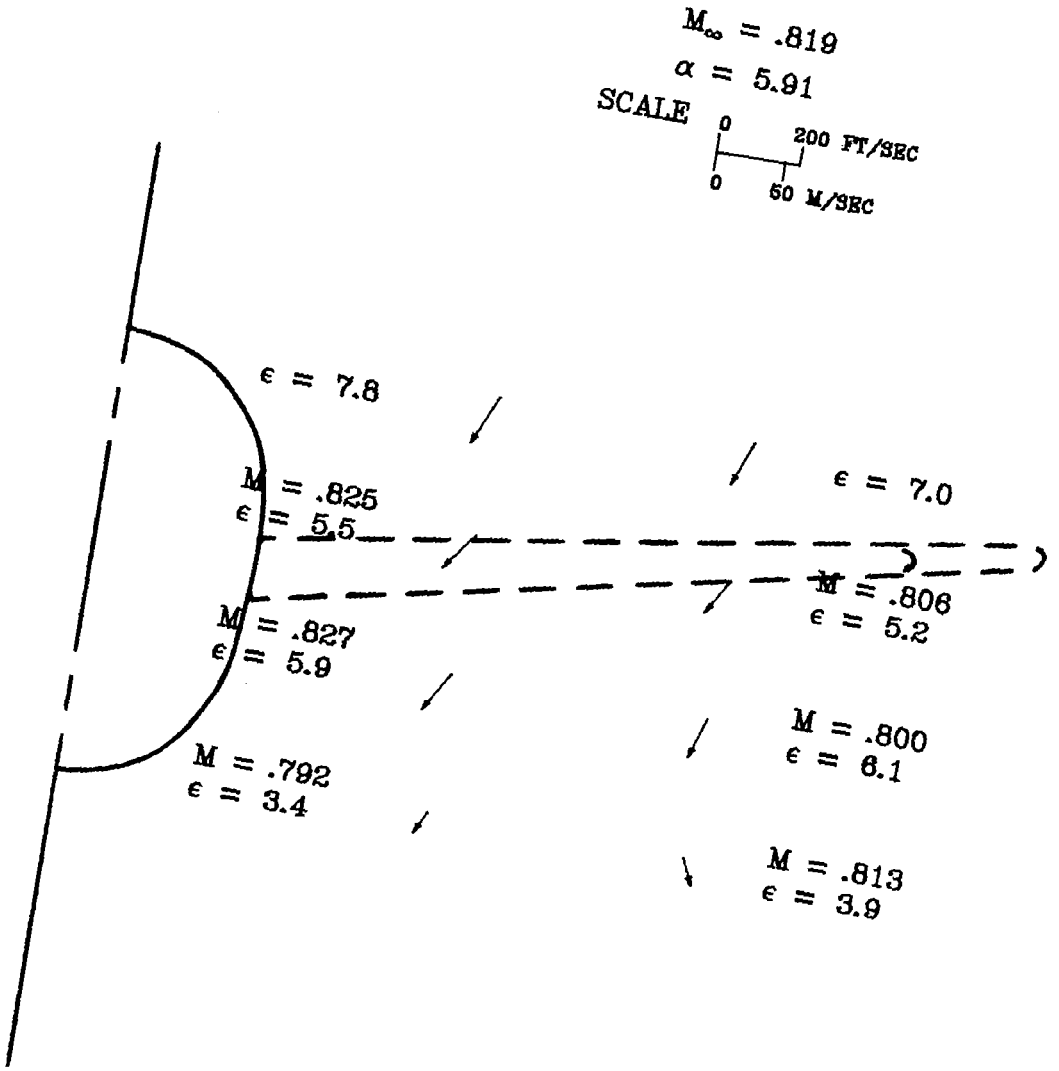

Figure 32.- Continued.

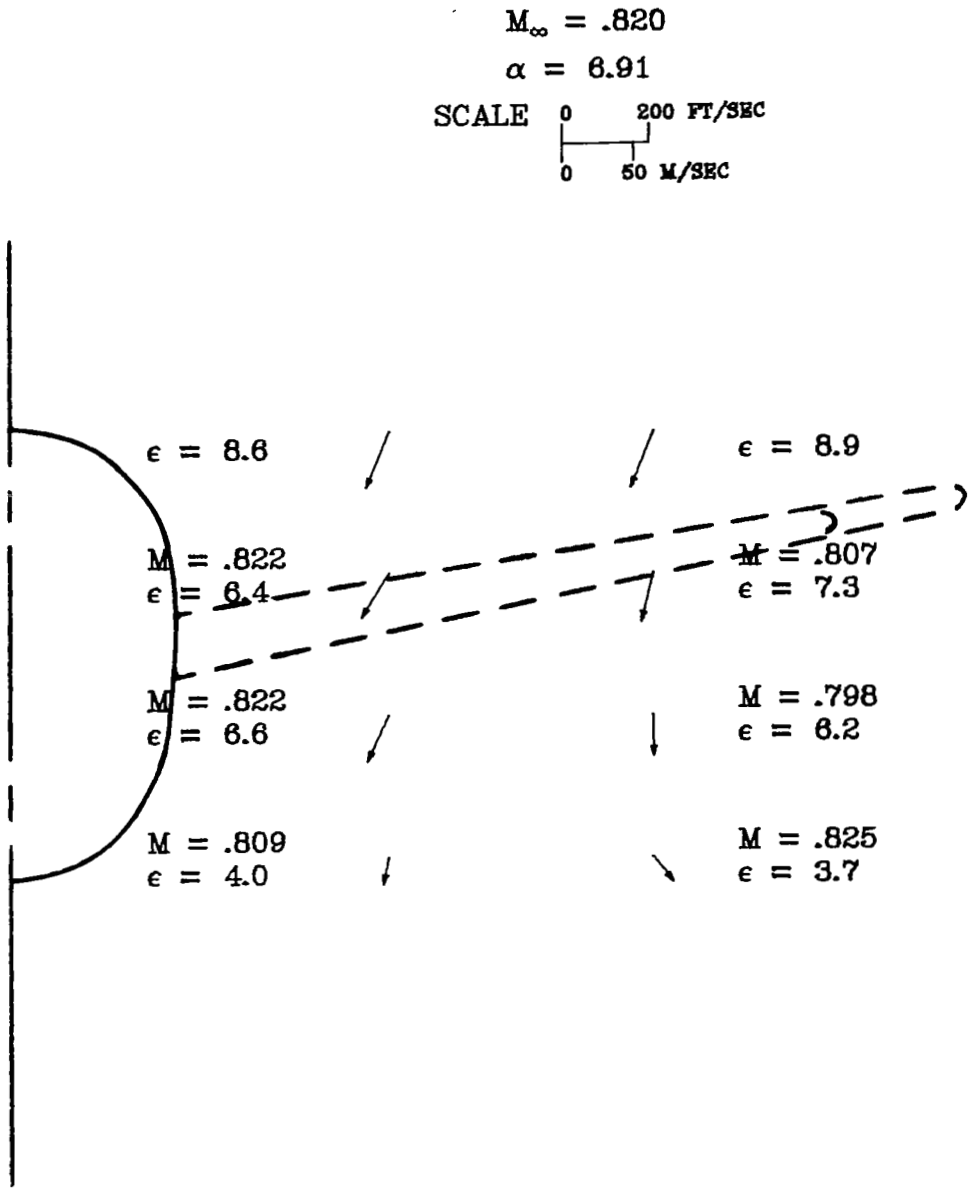

Figure 32.- Continued.

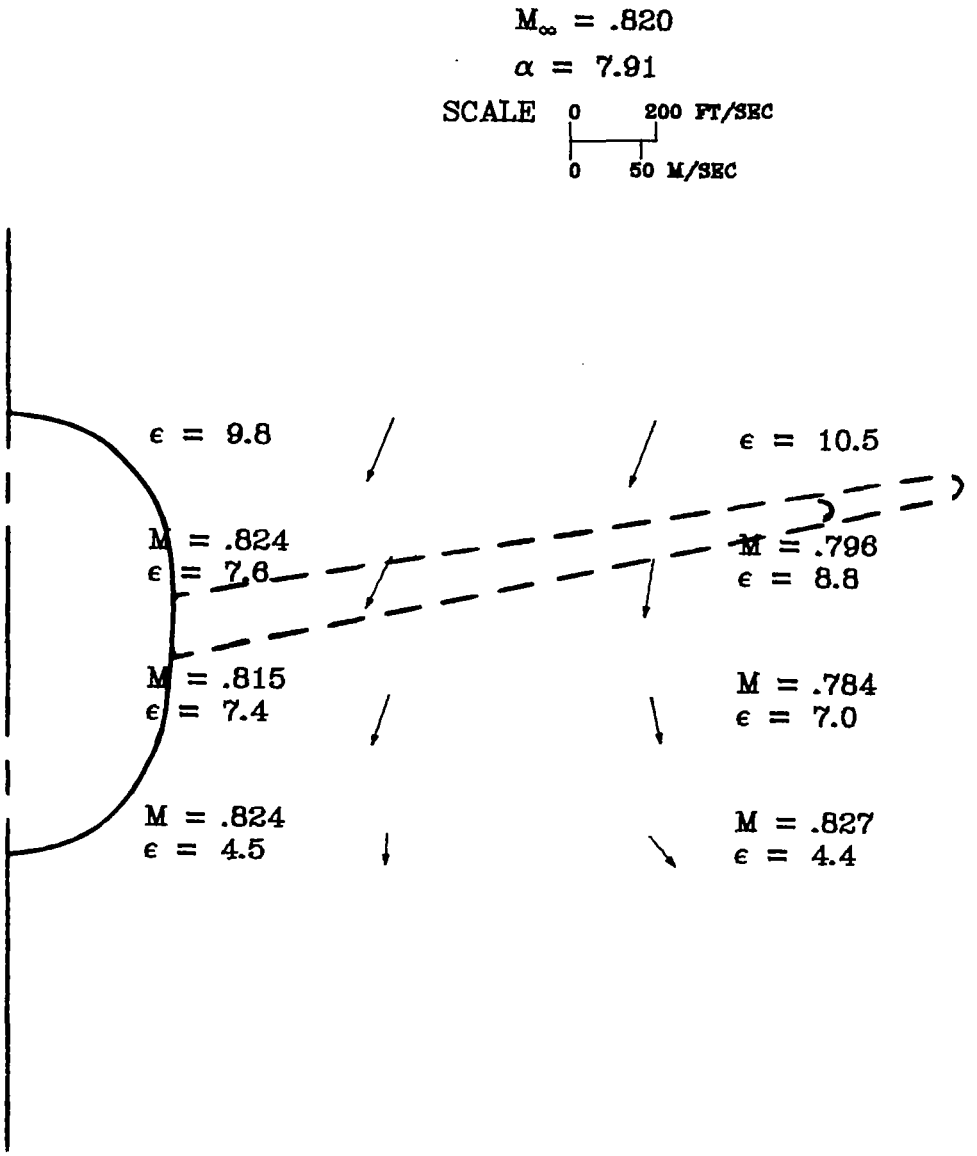

Figure 32.- Concluded.

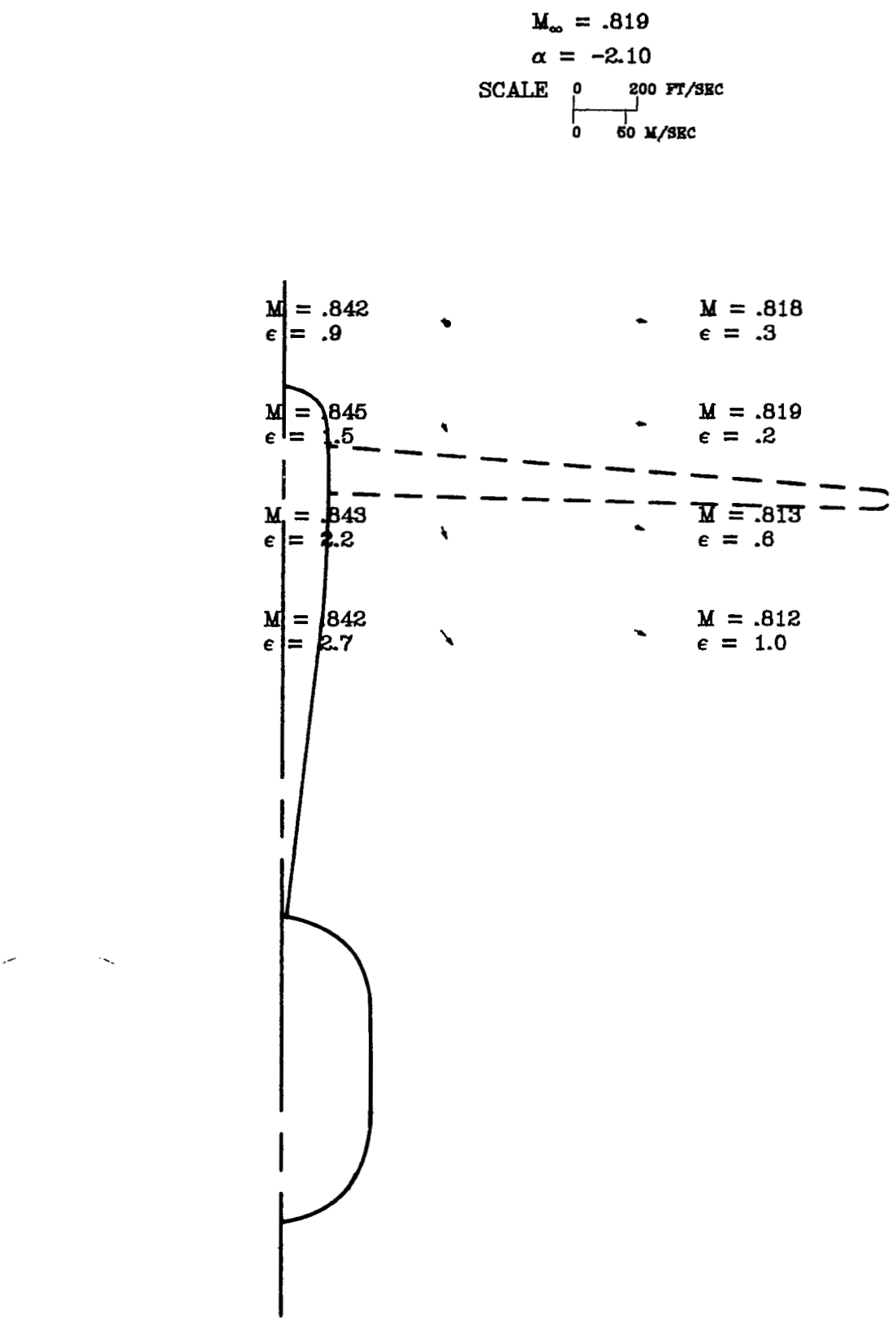

Figure 33.- Local Mach numbers and flow-field velocity vectors behind the supercritical wing with T-tail configuration.

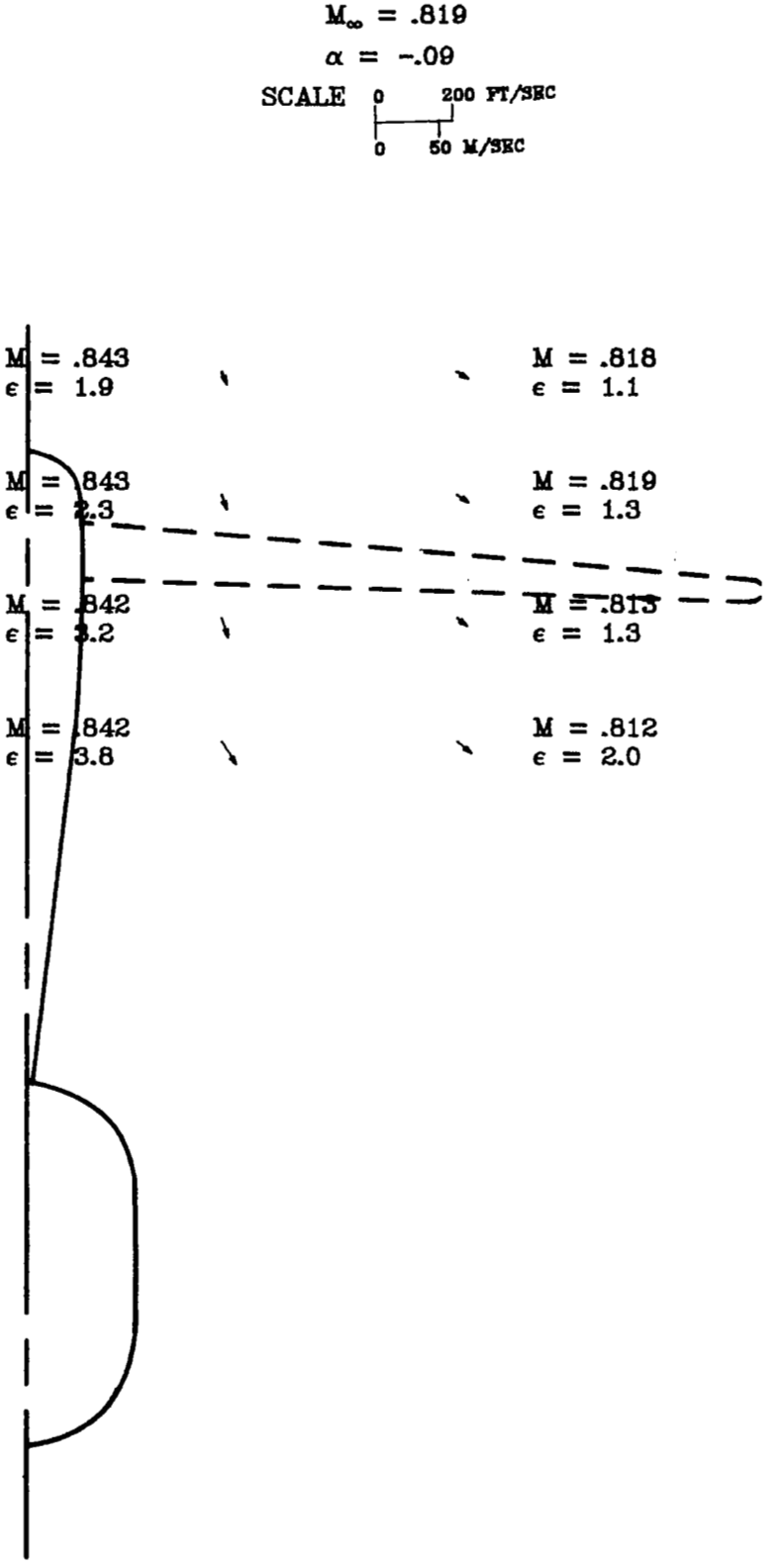

Figure 33.- Continued.

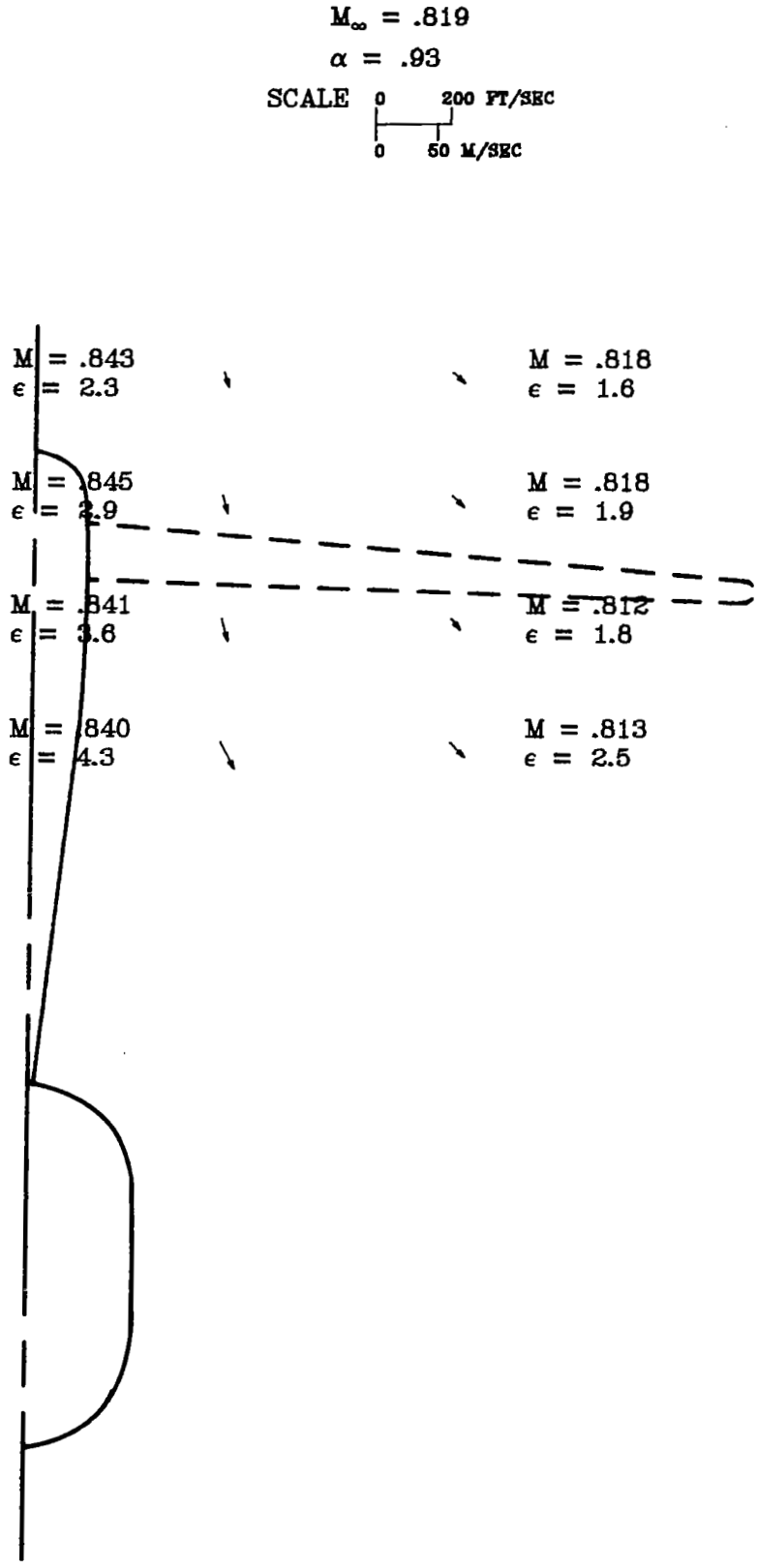

Figure 33.- Continued.

$M_\infty = .819$

$\alpha = 1.44$

SCALE 0 200 FT/SEC
0 50 M/SEC

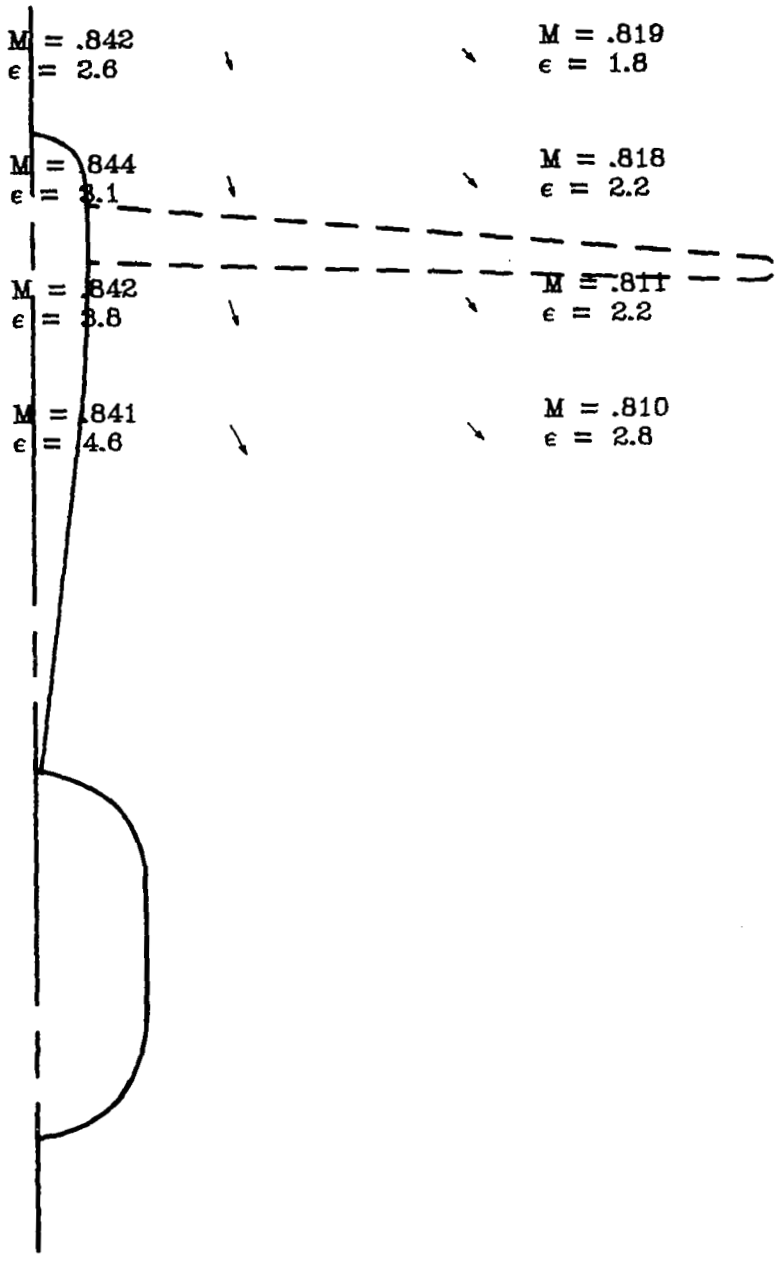

Figure 33.- Continued.

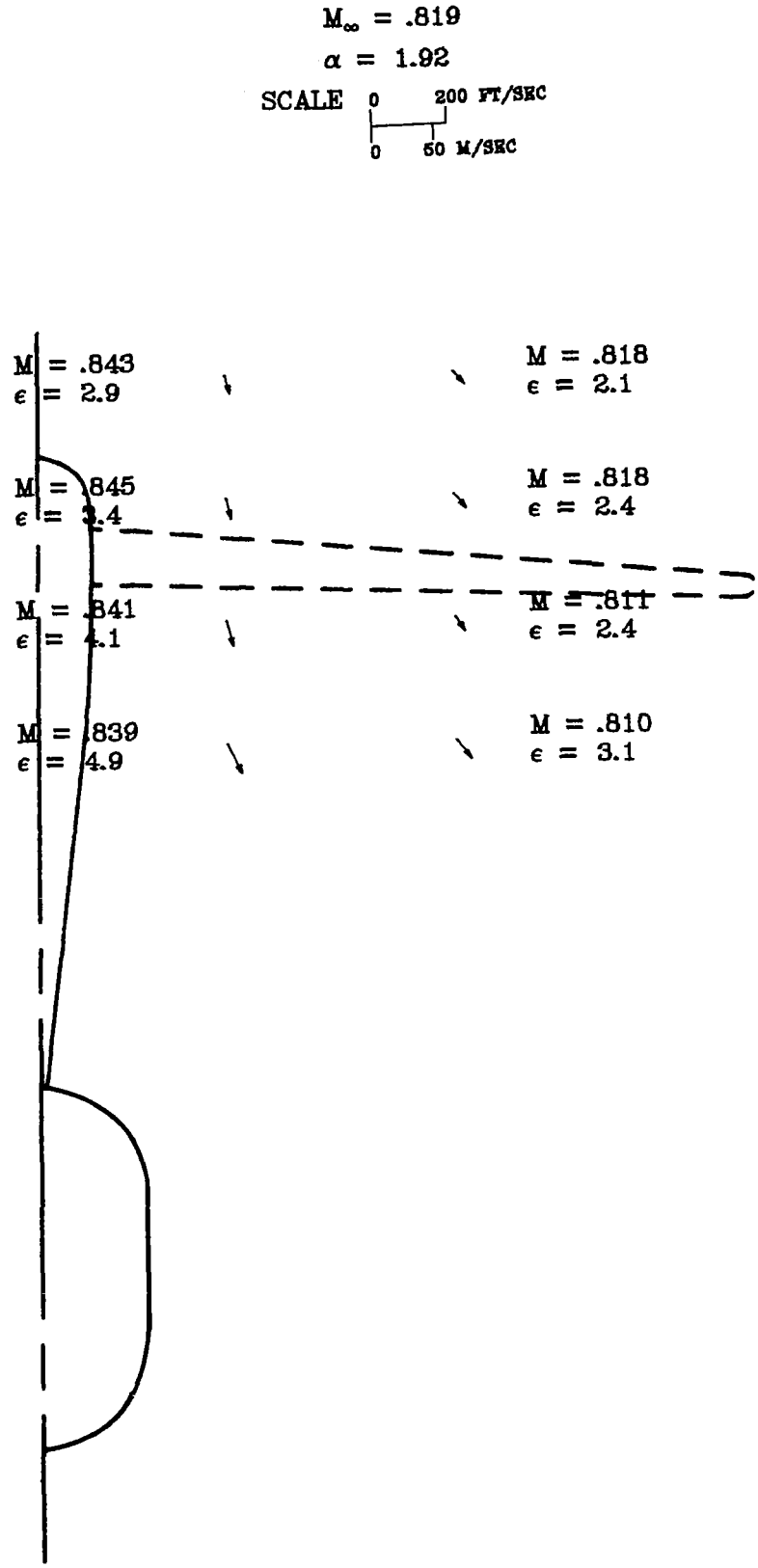

Figure 33.- Continued.

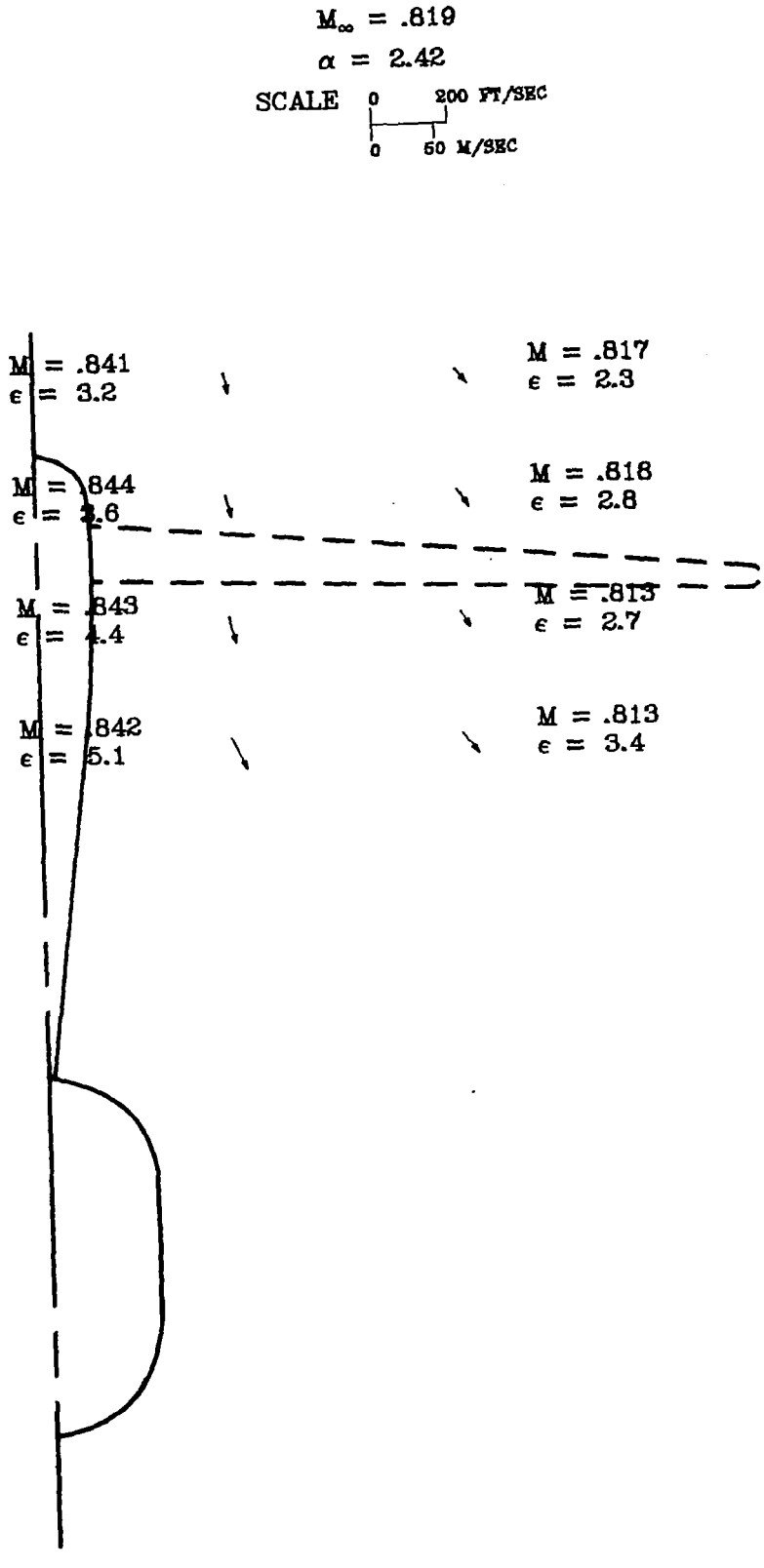

Figure 33.- Continued.

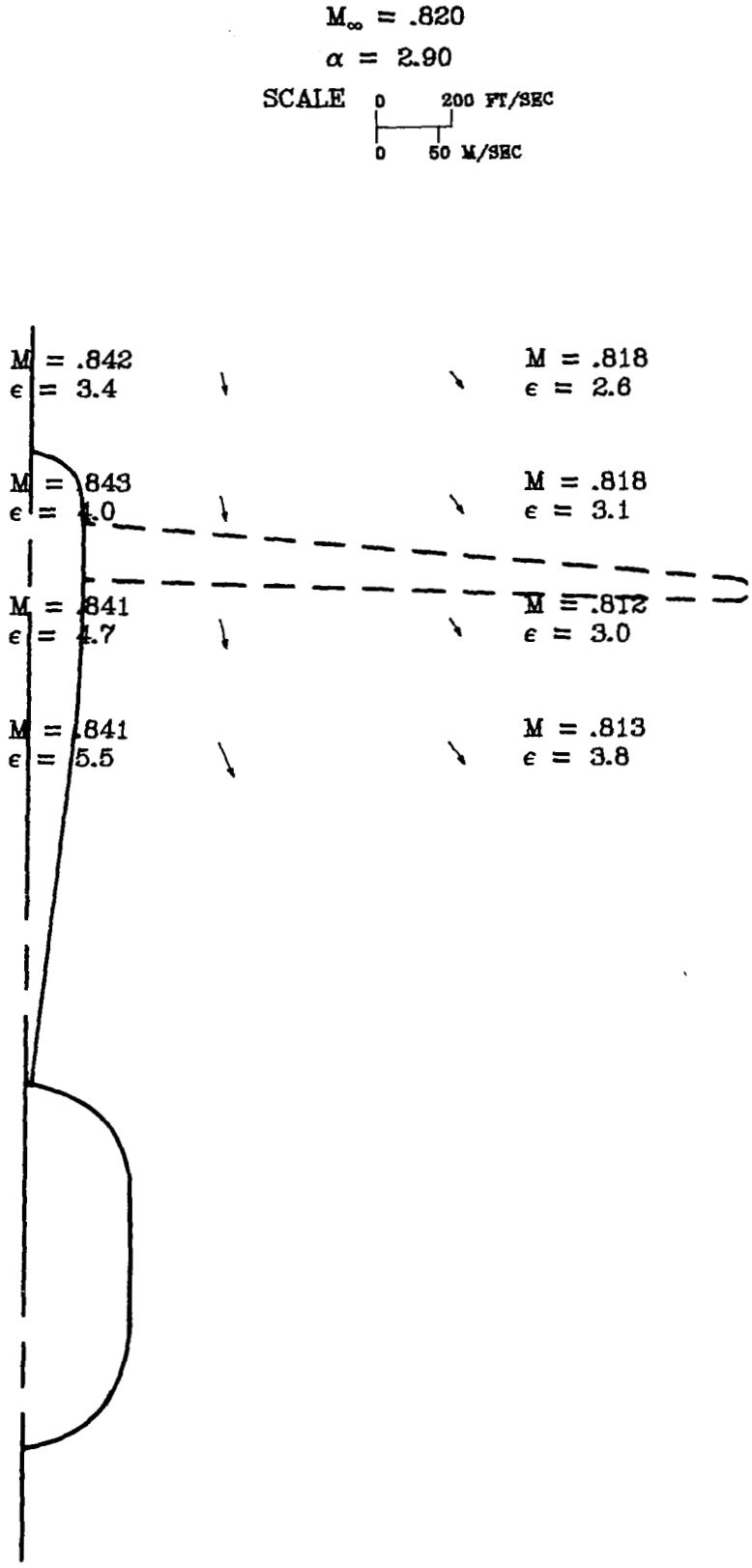

Figure 33.- Continued.

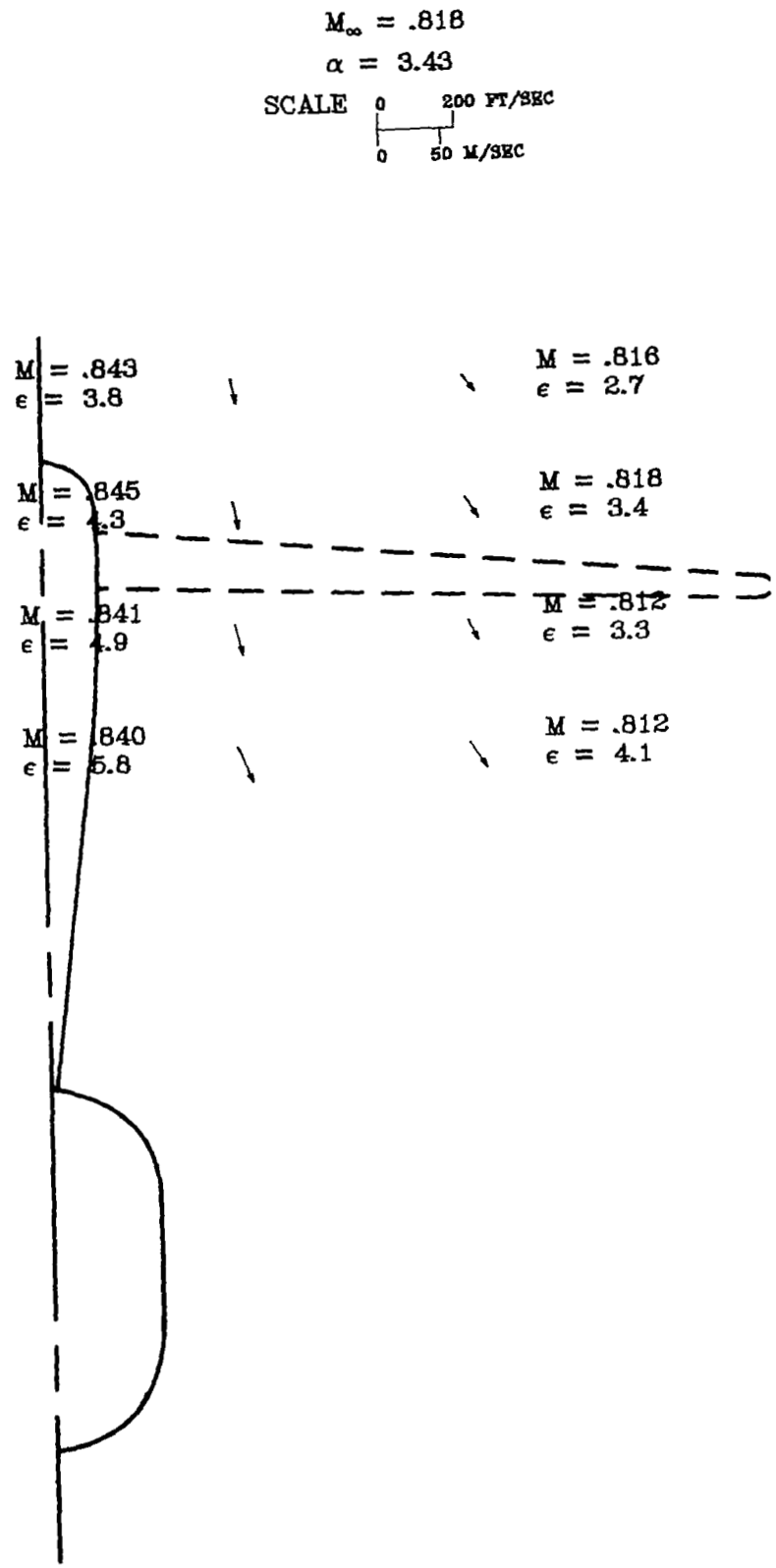

Figure 33.- Continued.

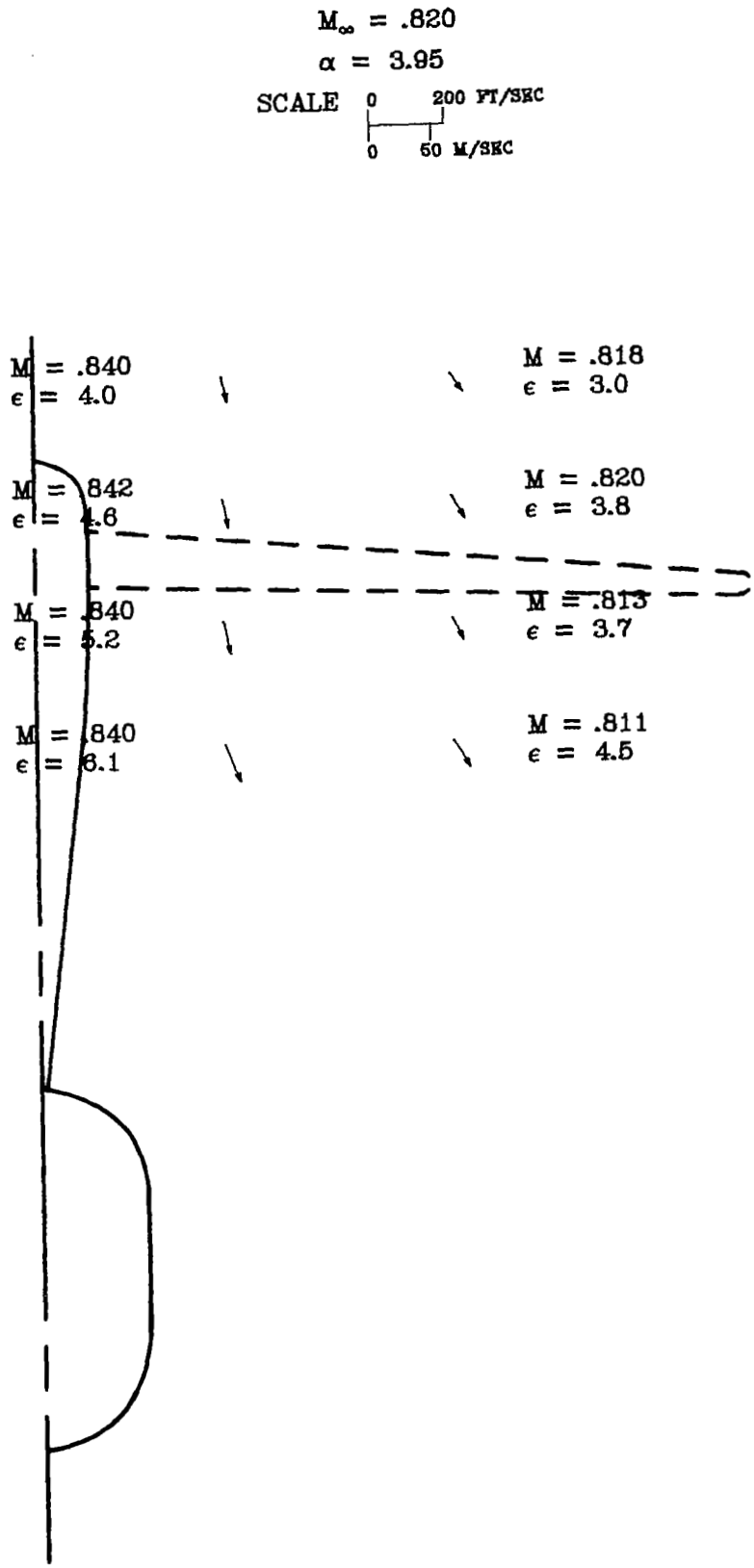

Figure 33.- Continued.

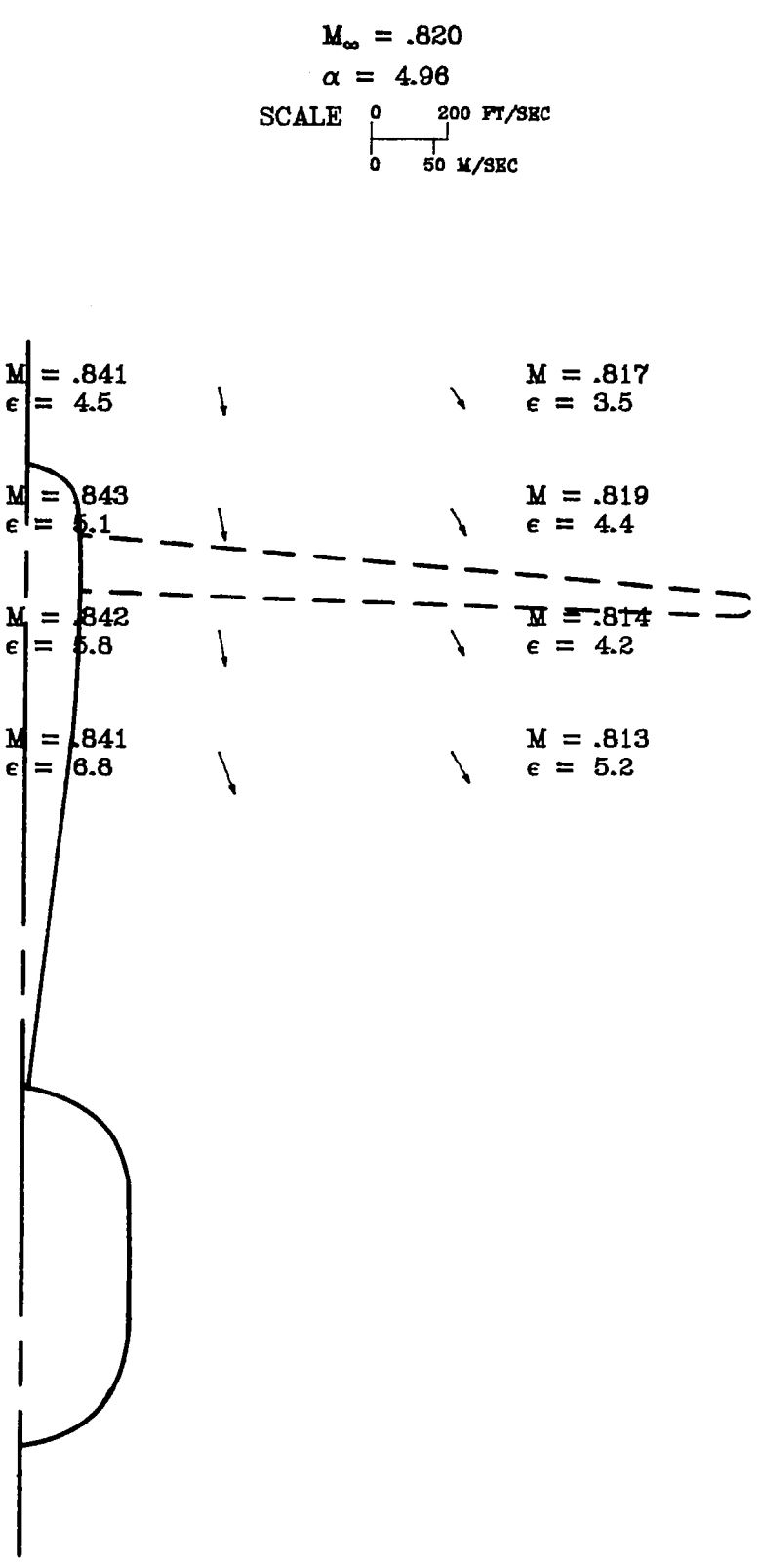

Figure 33.- Continued.

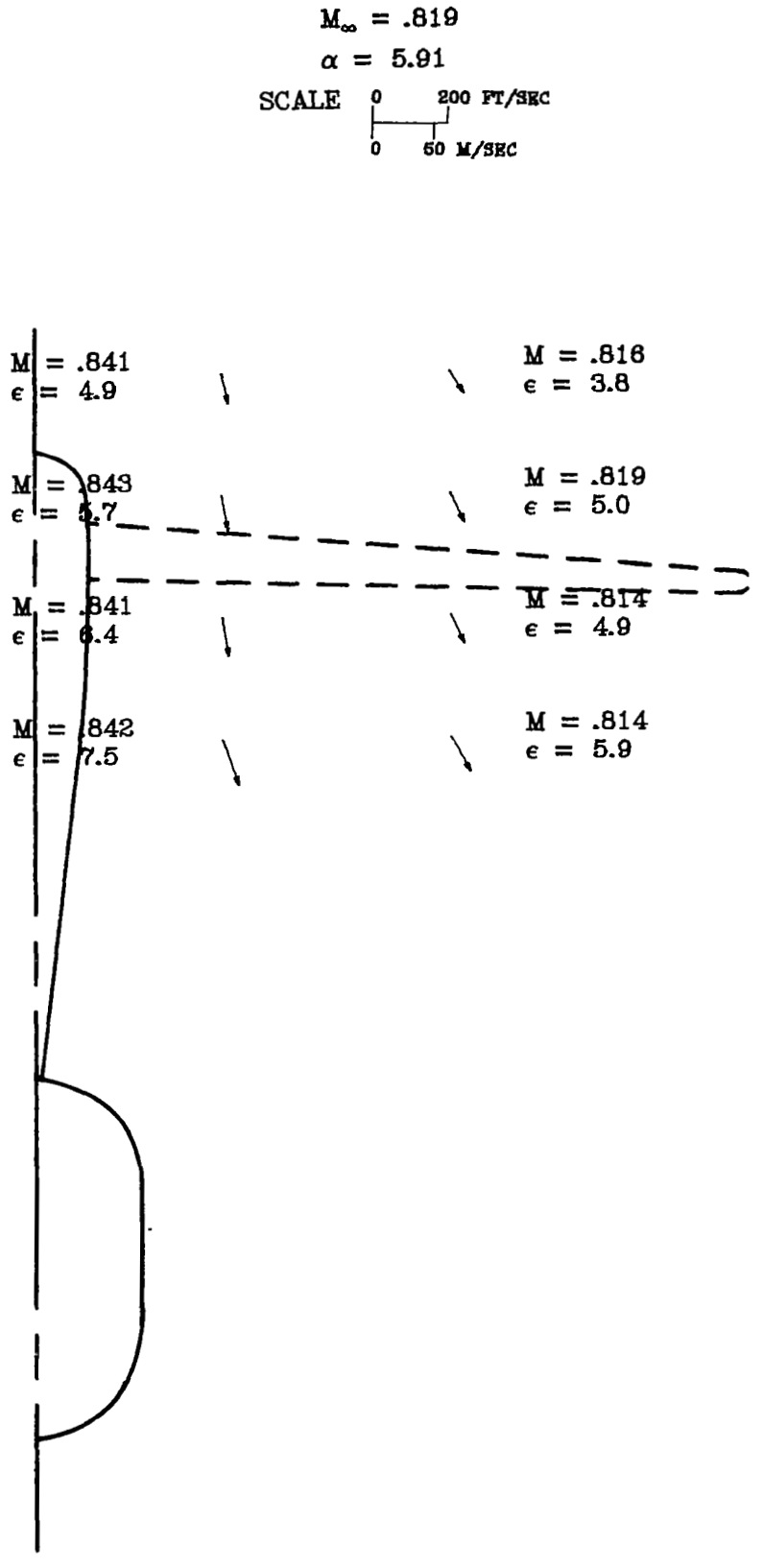

Figure 33.- Continued.

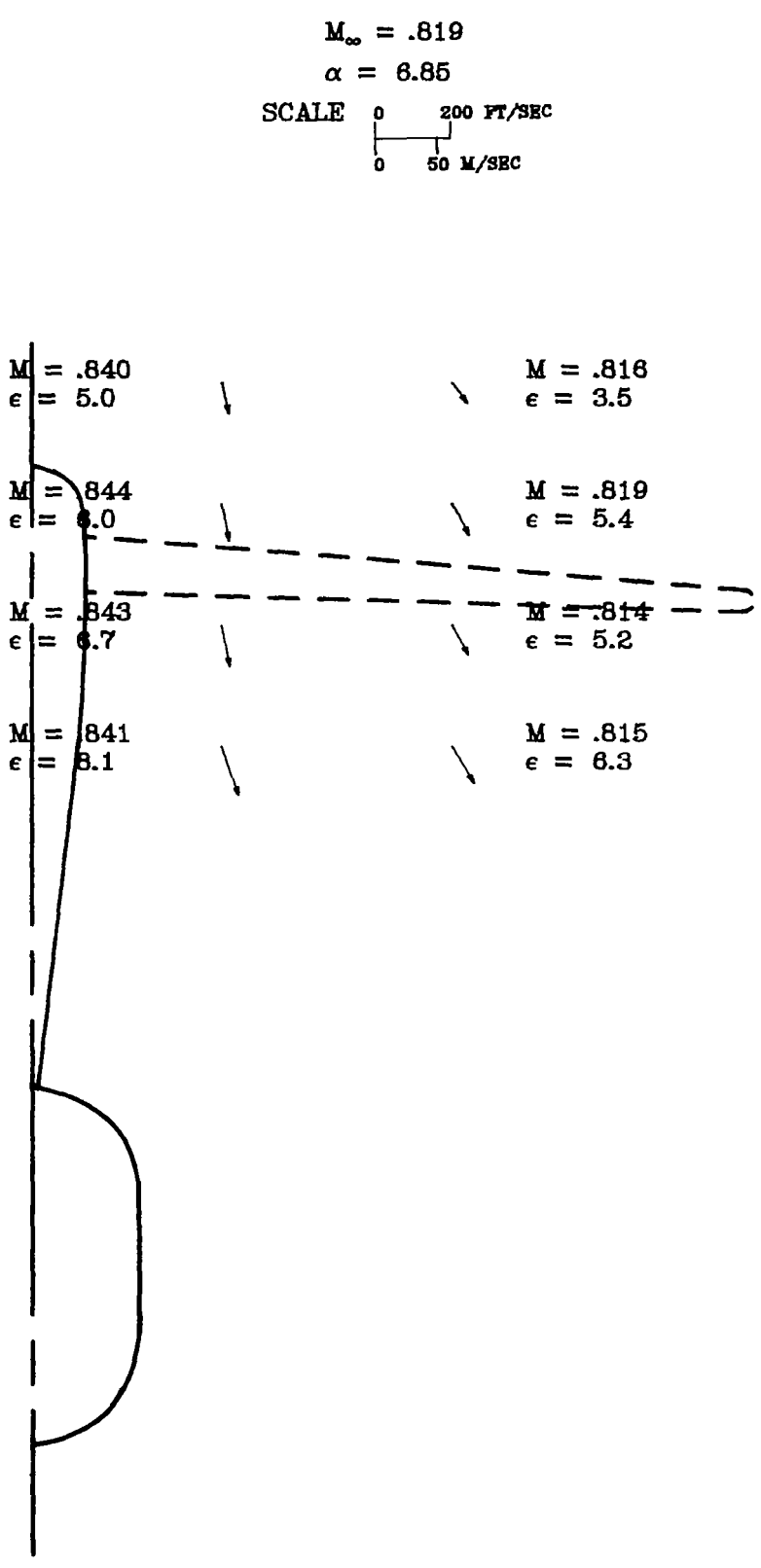

Figure 33.- Concluded.

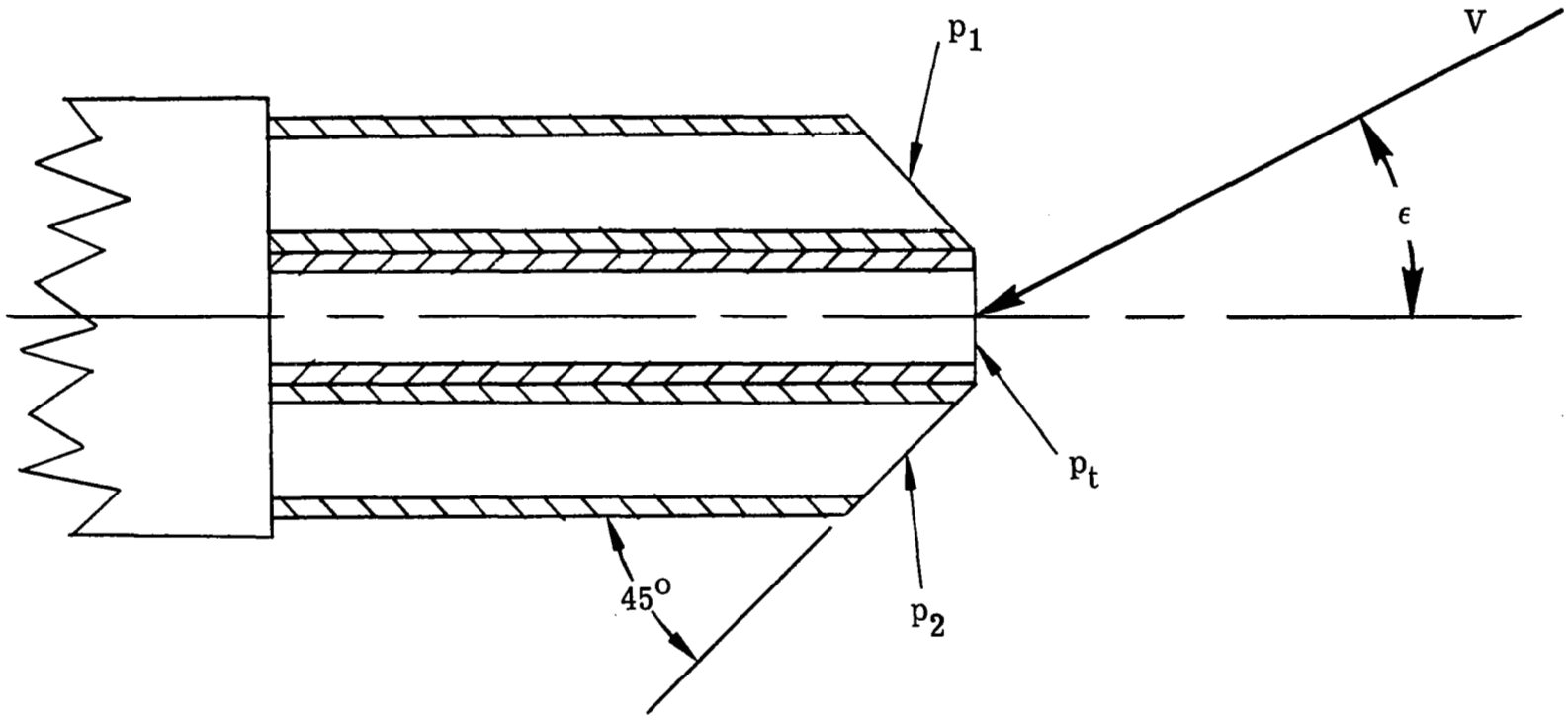

Figure 34.- Schematic drawing of yawhead.

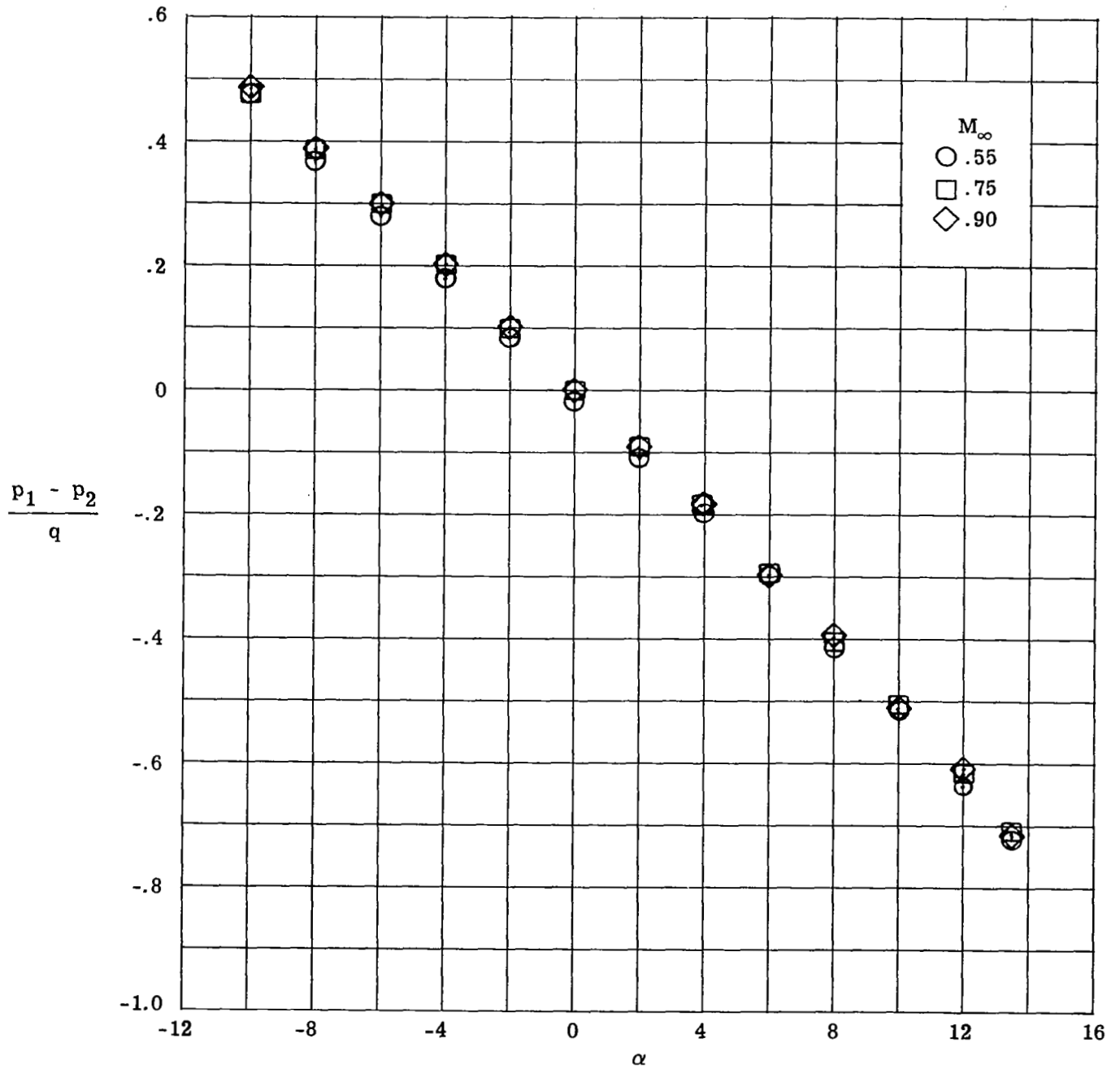

Figure 35.- Variation of nondimensionalized pressure difference with angle of attack for typical yawhead.

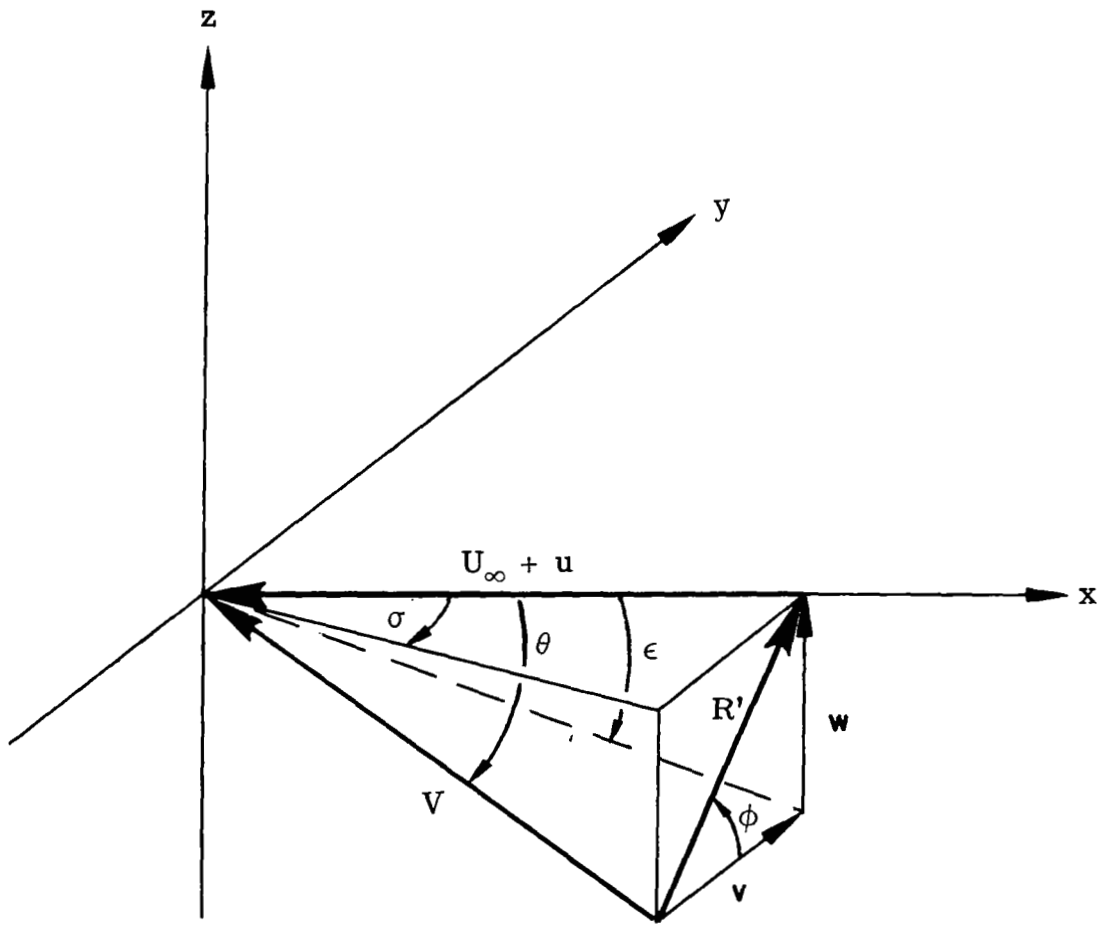

Figure 36.- Schematic drawing of flow-field velocity vectors.

1. Report No.	2. Government Accession No.	3. Recipient's Catalog No.
NASA TP-2071		

4. Title and Subtitle	5. Report Date
EXPERIMENTAL TRIM DRAG VALUES AND FLOW-FIELD MEASUREMENTS FOR A WIDE-BODY TRANSPORT MODEL WITH CONVENTIONAL AND SUPERCRITICAL WINGS	October 1982
	6. Performing Organization Code: 505-31-43-03
7. Author(s): Peter F. Jacobs	8. Performing Organization Report No.: L-15315
	10. Work Unit No.
9. Performing Organization Name and Address: NASA Langley Research Center, Hampton, VA 23665	11. Contract or Grant No.
	13. Type of Report and Period Covered: Technical Paper
12. Sponsoring Agency Name and Address: National Aeronautics and Space Administration, Washington, DC 20546	14. Sponsoring Agency Code

15. Supplementary Notes

16. Abstract

The purpose of this study was to determine if advanced supercritical wings incur higher trim drag values at cruise conditions than current wide-body technology wings. Relative trim drag increments were measured in an experimental wind-tunnel investigation conducted in the Langley 8-Foot Transonic Pressure Tunnel. The tests utilized a high-aspect-ratio supercritical wing and a wide-body aircraft wing, in conjunction with five different horizontal tail configurations, mounted on a representative wide-body fuselage. The three low-tail and two T-tail configurations were designed to measure the effects of horizontal tail size, location, and camber on the trim drag increments for the two wings. Longitudinal force and moment data were taken at a Mach number of 0.82 and design cruise lift coefficients for the wide-body and supercritical wings of 0.45 and 0.55, respectively. The data indicate that the supercritical wing does not have significantly higher trim drag than the wide body wing. A reduction in tail size, combined with relaxed static stability, produced trim drag reductions for both wings. The cambered tails had higher trim drag increments than the symmetrical tails for both wings, and the T-tail configurations had lower trim drag increments than the low-tail configurations.

17. Key Words (Suggested by Author(s))	18. Distribution Statement
Trim drag Supercritical wings Horizontal tails Vertical tails Longitudinal stability	FEDD Distribution Subject Category 02

19. Security Classif. (of this report)	20. Security Classif. (of this page)	21. No. of Pages	22. Price
Unclassified	Unclassified	143	

Available: NASA's Industrial Applications Centers

NASA-Langley, 1982